

2

REPORT DOCUMENTATION PAGE

AD-A238 374



22 1991

| | | | | | |
|--|---|---|----------------|--------------------|----------------------------|
| 1a. RESTRICTIVE MARKINGS | | | | | |
| 3. DISTRIBUTION/AVAILABILITY OF REPORT Approved for public release; distribution unlimited. | | | | | |
| 4. PERFORMING ORGANIZATION REPORT NUMBER(S) | | | | | |
| 5. MONITORING ORGANIZATION REPORT NUMBER(S) ARO 23646.33-EL | | | | | |
| 6a. NAME OF PERFORMING ORGANIZATION University of California, LA Electrical Engineering Dept. | 6b. OFFICE SYMBOL (If applicable) | 7a. NAME OF MONITORING ORGANIZATION U. S. Army Research Office | | | |
| 6c. ADDRESS (City, State, and ZIP Code) 7619 Boelter Hall 405 Hilgard Avenue Los Angeles, CA 90024-1594 | | 7b. ADDRESS (City, State, and ZIP Code) P. O. Box 12211 Research Triangle Park, NC 27709-2211 | | | |
| 8a. NAME OF FUNDING/SPONSORING ORGANIZATION U. S. Army Research Office | 8b. OFFICE SYMBOL (If applicable) | 9. PROCUREMENT INSTRUMENT IDENTIFICATION NUMBER DAAL03-86-K-0104 | | | |
| 8c. ADDRESS (City, State, and ZIP Code) P. O. Box 12211 Research Triangle Park, NC 27709-2211 | | 10. SOURCE OF FUNDING NUMBERS | | | |
| | | PROGRAM ELEMENT NO. | PROJECT NO. | TASK NO. | WORK UNIT ACCESSION NO. |
| 11. TITLE (Include Security Classification) Quantum Devices and Structures Using Si-Based Molecular Beam Epitaxy | | | | | |
| 12. PERSONAL AUTHOR(S) K. L. Wang | | | | | |
| 13a. TYPE OF REPORT Final Technical Rpt. | 13b. TIME COVERED FROM 6/15/86 TO 12/14/89 | 14. DATE OF REPORT (Year, Month, Day) 91/5/15 | | 15. PAGE COUNT | |
| 16. SUPPLEMENTARY NOTATION The view, opinions and/or findings contained in this report are those of the author(s) and should not be construed as an official Department of the Army position, policy, or decision, unless so designated by other documentation. | | | | | |
| 17. COSATI CODES | | 18. SUBJECT TERMS (Continue on reverse if necessary and identify by block number) | | | |
| FIELD | GROUP | SUB-GROUP | | | |
| | | | | | |
| | | | | | |
| 19. ABSTRACT (Continue on reverse if necessary and identify by block number) The final report describes the technical tasks and accomplishments during the contractual period from June 15, 1986 to December 14, 1989 for "Quantum Devices and Structures using Si Molecular Beam Epitaxy". Research findings are summarized in five scientific areas, (a) study of strain in SiGe layers by reflection high energy electron diffraction (RHEED); (b) Silicide/Si quantum well structures, (c) development of theory and design for superlattice device, (d) miniband conduction in SiGe/Si superlattices, and (e) intersubband infrared absorption between valence minibands of symmetrically strained SiGe/Si superlattices. Details of these results may be referenced to the publications listed in Appendix. In addition to scientific publications, the results of this research also help industrial development of Si-based heterostructure devices in the U.S.A. | | | | | |
| 91-05693 | | | | | |
| 20. DISTRIBUTION/AVAILABILITY OF ABSTRACT <input type="checkbox"/> UNCLASSIFIED/UNLIMITED <input type="checkbox"/> SAME AS RPT. <input type="checkbox"/> DTIC USERS | | 21. ABSTRACT SECURITY CLASSIFICATION Unclassified | | | |
| 22a. NAME OF RESPONSIBLE INDIVIDUAL | | 22b. TELEPHONE (Include Area Code) | | 22c. OFFICE SYMBOL | |

Contents

| | |
|--|----|
| 1 Abstract | 0 |
| 2 Introduction | 1 |
| 3 Progress and Accomplishments | 1 |
| 4 Industrial Impact | 10 |
| 5 Publications and Graduate Student Training | 10 |
| 5.1 Publications supported by this contract fund | 10 |
| 5.2 Graduate student training | 13 |
| 6 Appendix | 15 |



| | |
|-------------------|----------------------|
| Accession For | |
| 201 00001 | |
| BRI 100 | |
| ON 100000 | |
| JUL 10 1964 | |
| By | |
| Distribution/ | |
| A allanist; codes | |
| Dist | Level and/or Special |
| A-1 | 20 |

List of Figures

| | | |
|---|-----------------------------------|---|
| 1 | RHEED patterns | 3 |
| 2 | Critical thickness | 3 |
| 3 | Miniband transport | 5 |
| 4 | Intersubband absorption | 6 |
| 5 | Quantum devices | 8 |
| 6 | Schematic of the System | 9 |

QUANTUM DEVICES AND STRUCTURES USING Si BASED MOLECULAR BEAM EPITAXY

1 Abstract

The final report describes the technical tasks and accomplishments during the contractual period from June 15, 1986 to December 14, 1989 for "Quantum Devices and Structures using Si Molecular Beam Epitaxy". Research findings are summarized in five scientific areas, (a) study of strain in SiGe layers by reflection high energy electron diffraction (RHEED), (b) Silicide/Si quantum well structures, (c) development of theory and design for superlattice device, (d) miniband conduction in SiGe/Si superlattices, and (e) intersubband infrared absorption between valence minibands of symmetrically strained SiGe/Si superlattices. Details of these results may be referenced to the publications listed in Appendix. In addition to scientific publications, the results of this research also help industrial development of Si-based heterostructure devices in the U.S.A.

2 Introduction

Recently, strained layer Si-based heterostructures have attracted considerable attention due to possible Si-based heterojunction and superlattice device application. The progress of the research in Si molecular beam epitaxy (MBE) have made it possible to achieve device quality epitaxial layers with controlled strains. The new degrees of freedom offered in advanced layered semiconductor research provide opportunities for engineering many ingenious devices, which are not obtainable from bulk Si. In particular, the SiGe/Si strained layers offer unique opportunity for engineering of devices using the properties of type I and type II heterostructures by controlling the strain. Several attempts have been made to incorporate SiGe/Si strained layer heterostructures into device applications in the areas of heterojunction bipolar transistors, modulation doped field effect transistors, quantum devices, and optical detectors which might be the key to the implementation of integrated high frequency devices and optoelectronics on Si.

In this report, we describe the progress and the scientific findings made upon completion of the contract performed for "Quantum Devices and Structures using Si Molecular Beam Epitaxy". We have executed most of proposed tasks in the areas of study of strain in SiGe layers, silicide/Si heterostructures, transport and optical properties of SiGe quantum wells and superlattices, theory for design and analysis of superlattice device. The progress made in the contractual period is summarized below. Detailed descriptions are referred to the papers published as attached in the appendix.

3 Progress and Accomplishments

With the current ARO support, we have made significant advances in the MBE growth studies of $Si_{1-x}Ge_x/Si$ superlattices and the fabrication of resonant tunneling devices.

In the following we highlight the accomplishments made. Details may be referenced to the publications resulting from the past three years efforts listed in Appendix.

(a) $Si_{1-x}Ge_x/Si$ strained layers

Ge_xSi_{1-x}/Si layers of any Ge alloy composition have been grown for investigation of strain effects. The strain of the film is varied by the Ge composition, x of the film and the buffer layer whose lattice constant is adjusted in between bulk Si and Ge. Raman spectroscopy was used to determine the strain via the shift of the optical phonon energies [1]. The strain of the $Si_{1-x}Ge_x$ layer was also investigated by observing the change of RHEED pattern, from (7×7) to (5×5) reconstruction as the film is strained [2, 3]. The RHEED pattern changes back to (7×7) as the thickness of the film exceeds the critical thickness. Figure 1 shows the change of RHEED patterns from (7×7) to (5×5) when a SiGe film grown on a Si (111) substrate. This provides us a very convenient way of in-situ calibration of the critical thickness of SiGe films. RHEED oscillations were established for precise control and calibration for growth of $Si_{1-x}Ge_x$ superlattices. This is extremely important for the growth of monolayer superlattices with period of only few monolayers. The strain relaxation of the of short period superlattices was also studied [4]. Figure 2 shows the critical thickness as a function of average Ge content in a short period superlattice. Similarly, X-ray rocking curve techniques were used to study the strain and the crystallinity [5, 6, 4]. The investigation of transport and optical properties and testing of several device structures are described in the next few sections.

We highlight a few points below (and details are given in the published papers listed in the Appendix).

- Strain determination of $Si_{1-x}Ge_x$ layers by Raman spectroscopy and X-ray diffraction.
- In-situ determination of critical thickness of SiGe films using change of RHEED patterns due to strain.
- Study of strain in short period superlattices using RHEED.

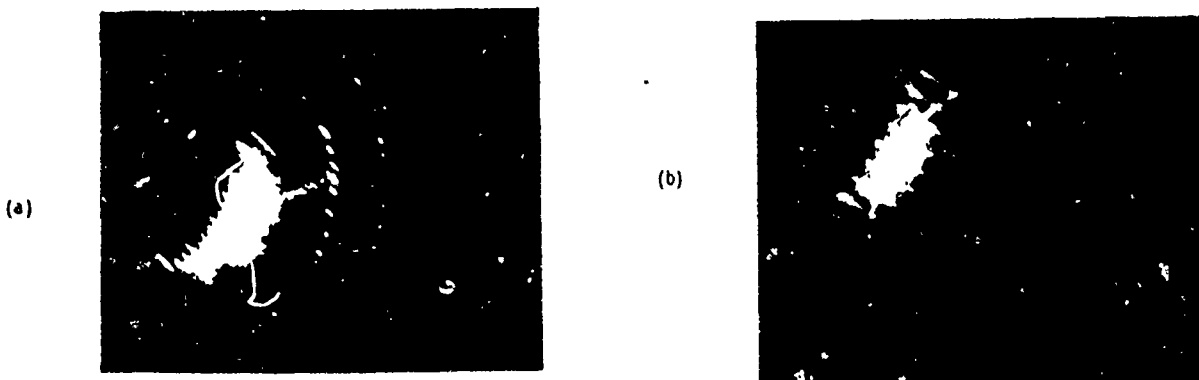


Figure 1: RHEED patterns of a SiGe film grown on Si (111) substrate (a) before relaxation, and (b) after relaxation of strain.

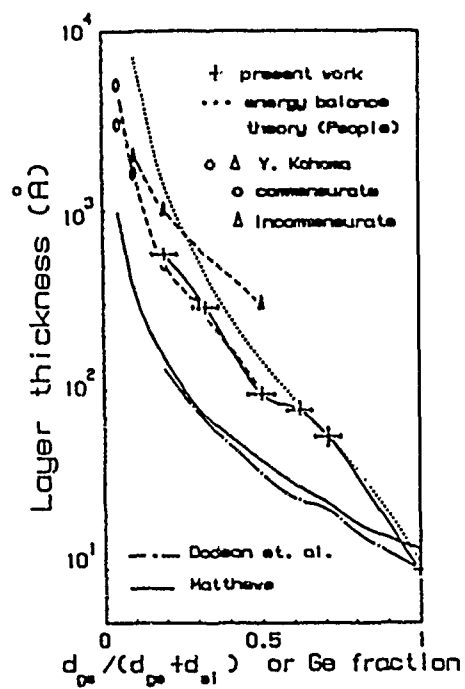


Figure 2: Critical thickness of a monolayer superlattice as a function of average Ge composition.

(b) Silicide/Si quantum well structures

We have also performed the growth studies of $CoSi_2$ in a direction for realization of metal/semiconductor superlattices. Substantial improvement in reducing the pin hole density of $CoSi_2$ films has been done and understanding of $CoSi_2/Si$ strain stability and strain relaxation was obtained.[7] A new approach in growth of strained layers on a patterned substrate was implemented. Permeable transistors and tunneling structures were fabricated. To eliminate the formation of pin holes, a new approach of growth has been employed using room temperature (RT) co-deposition of Si and Co in a stoichiometric ratio (2:1), followed by RT deposition of a thin α -Si capping layer and annealing at an elevated temperature [8]. The α -Si layer prevent the exposure of high-energy $CoSi_2$ surface during the recrystallization and thus, eliminate the pin hole formation. We have characterized the surface reconstruction of $CoSi_2$ during the various steps used during the growth. We outline typical tasks accomplished below:

- Electrical characterization of $CoSi_2/Si$ interface by a forward C(V) technique.
- Successful fabrication and testing of $CoSi_2$ permeable transistor.
- Successful growth of pin hole free $CoSi_2$ films on Si(111) (up to 800Å thick).
- Study of surface reconstruction of $CoSi_2$ using RHEED.

(c) Miniband conductance through $Si_{1-x}Ge_x/Si$ superlattice

The transport properties of holes through minibands of a $Si_{1-x}Ge_x/Si$ superlattice has been investigated [9]. The measured I-V and dI/dV characteristics at 4.2 K, 35 K and 77 K are shown in Fig. 3. Two peaks are observed at 1.1 V and 2.5 V at 77 K with clear negative resistance (NDR). As the temperature of the sample decreased, the peak- to-valley ratio of the peak at 2.5 V increases and the peak at 1.1 V becomes more apparent from the dI/dV curve. The peak to valley current ratio for the peak at 2.5 V decreases as the temperature is reduced, while the peak positions shifts towards higher voltage. Above 100 K, the NDR is no longer clearly observed. The measured I-V and dI/dV data can be understood quantitatively as the light conduction through the

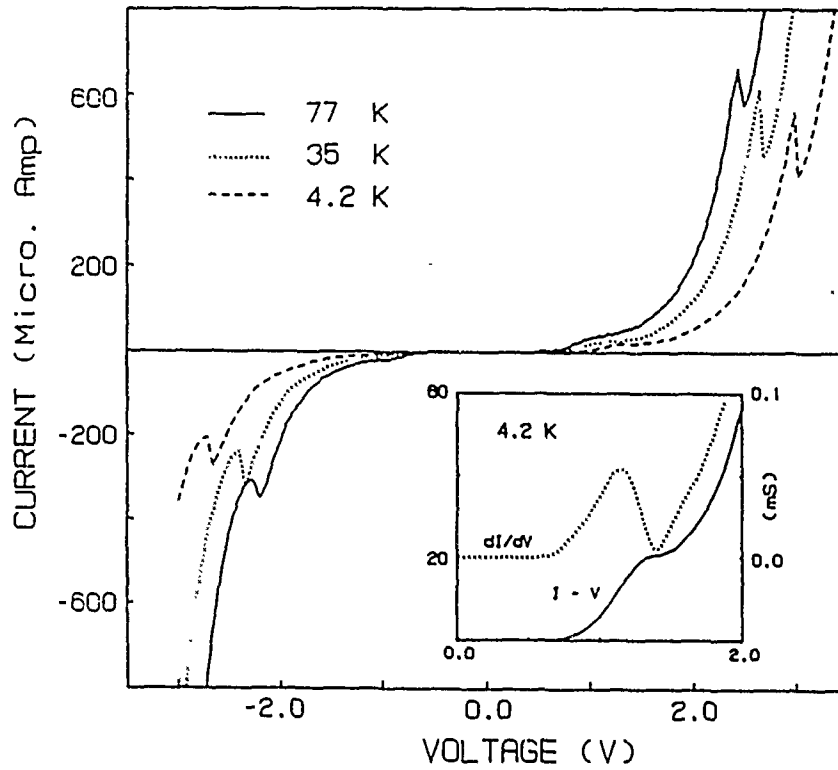


Figure 3: Observed current-voltage (I-V) at 4.2, 35, and 70 K, showing conduction through minibands in the superlattice. Inset of the figure shows the magnified I-V and dI/dV for the first peak.

minibands in the superlattice. The conduction through minibands occurs when the Fermi level in the emitter region is aligned with the bottom of a miniband. The NDR shows up when the Fermi level is moved away from the miniband. The position of the minibands also obtained using temperature dependence measurement at low bias condition. In this case the conduction is dominated by the thermionic emission. The measured values of the miniband positions are in good agreement with the calculated values using envelope function approximation and band offsets under strain condition.

- Observation of hole miniband conduction through a symmetrically strained $Si_{1-x}Ge_x/Si$ superlattice for the first time.
- Demonstration of negative differential resistance.
- Thermionic analysis of the position of the minibands. The results are in good agreement with the calculated values.

(d) Intersubband infrared absorption

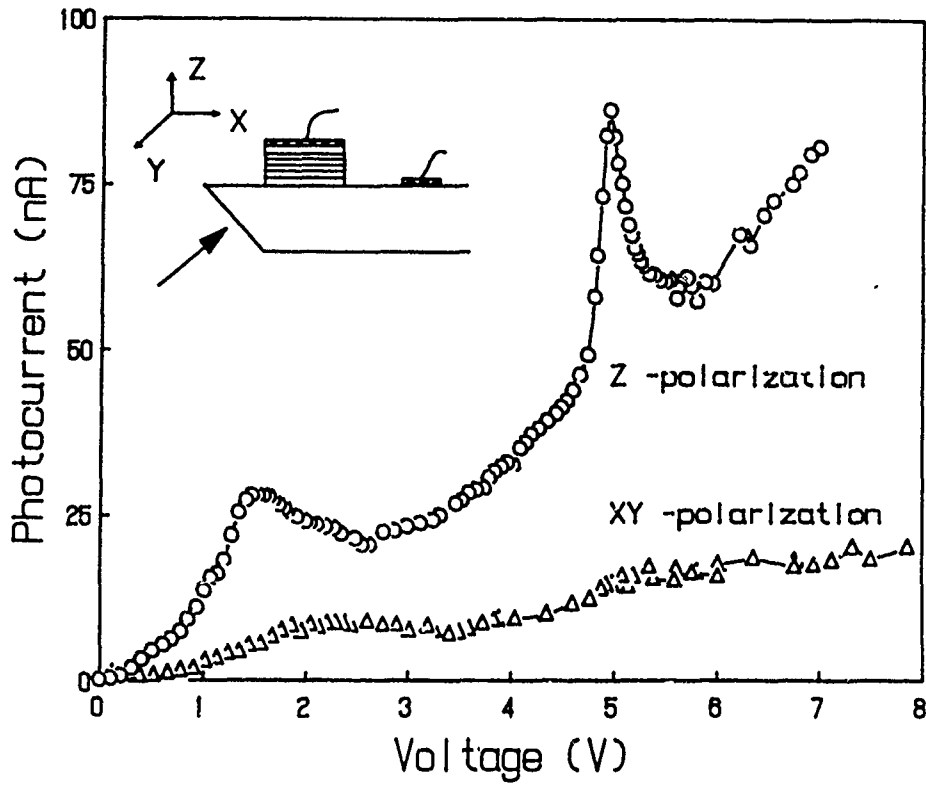


Figure 4: The infrared photoresponse as a function applied bias for xy and z polarizations. The peak at 1.5 and 5 V are due to intersubband infrared absorption between light hole minibands. The conduction voltage characteristic (dashed curve) shows the enhancement of conductivity when the minibands are aligned with the emitter.

The intersubband infrared absorption of holes in a $\text{Si}_{1-x}\text{Ge}_x$ superlattice is observed for the first time [10]. In the experiment, the photocurrent is measured as a function of applied bias which is used to inject holes to the minibands of the superlattice. A CO_2 laser tuned at $10.6 \mu\text{m}$ is used as the infrared source. Figure 4 shows the measured photocurrent as a function of applied bias across the superlattice device for polarization of the infrared beam parallel and perpendicular to the interfaces of the superlattice. Two clear peaks are observed at 1.5 and 5 V when the polarization of the incident beam has a component perpendicular to the interfaces (z polarization). In the case of polarization parallel to the interfaces (xy polarization), the peak at 5 V completely disappeared while the one at 1.5 V became smaller. This polarization dependence is a characteristics of the intersubband transition. It is interesting to note that the peaks in the photoresponse appear very close to the high conductivity regions in the conductance-voltage characteristics as shown in by the dashed line in Fig. 4. We have constructed a band diagram to understand the experimental observations.

The calculations show that only light split-off holes form minibands and heavy holes form only isolated bound states indicating the photoresponse is mainly due to the light hole minibands.

- Observation of the intersubband infrared absorption of holes using photocurrent measurement.
- Construction of a band diagram of the superlattice to identify the transitions.
- Study of the polarization dependence of the absorption to study the nature of the transitions. The polarization data are in good agreement with the selection rules of the intersubband transition.

(e) Design tools for superlattice device synthesis

Many superlattices and MQW devices were conceived during the period of two years under ARO support. These include the formation of the mini-band junctions and the Band Aligned Superlattice (BAS) concepts with a combination of several multilayer superlattices (superlattices with variable basis).[11] The junction concept is shown in Fig. 5(a) in which two different types of superlattices having different well widths are shown. The junction J is formed by two superlattices S1 and S2. The superlattice on the left has two subbands while there is only one subband aligned to the upper subband of S1. Carrier transport occurs only in the upper subbands which are aligned and these structures are thus referred as Band Aligned Superlattices (BAS). The transport in the lower subband is blocked due to the discontinuity of the minibands. Using these new device elements or superstructures, many different device structures ranging from optical detectors to sources are possible.[12, 13, 14] For example, Fig. 5(b) shows a hot hole transistor using a superlattice base and resonant tunneling injector. In order to facilitate the design of such devices, we need easy analytical methods or tools that are, of course, different from those for conventional devices. We have established a formalism for analyzing these structures within the effective mass frame work. The details of these are given in the publications listed in the Appendix.

Mini-band discontinuity
(a)

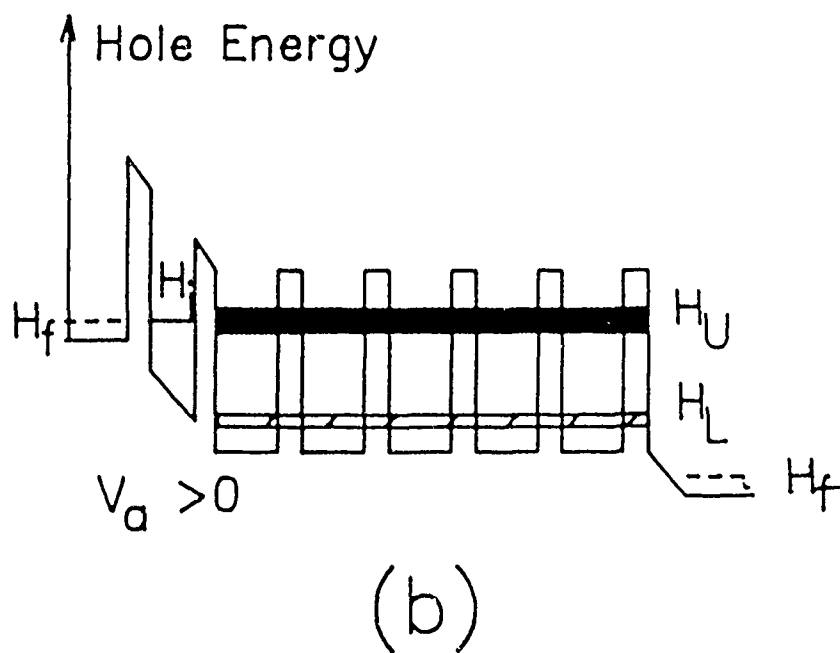


Figure 5: (a) Miniband junction, and (b) hot hole transistor.

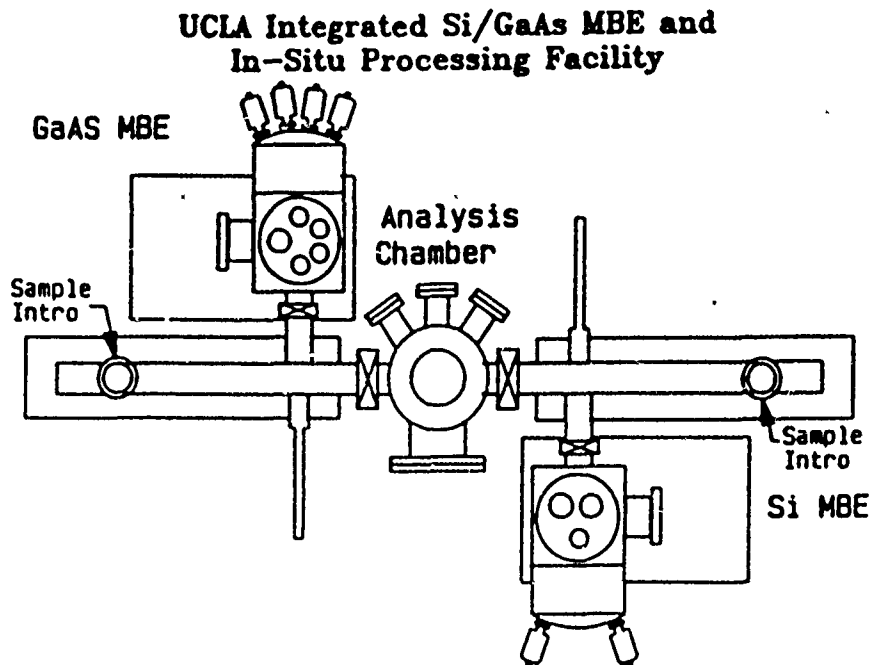


Figure 6: Schematic diagram of the integrated Si and III-V MBE system

(f) Acquisition of additional new MBE facility

In the past, all the superlattices were grown with the MBE system developed at UCLA. Although the system works well for the studies of growth, it is necessary to have the accurate and automated control of layer thickness and other growth parameters for investigation of the properties and device application in the extreme quantum limit. In anticipation of the expanded research and for maintaining the competitive edge, the laboratory has acquired a new integrated MBE system under DoD-URIP support. The system schematic is illustrated in Fig. 6, in which the Si-based growth chamber and III-V chamber are integrated all in ultra high vacuum. There is also an analysis chamber which houses an Auger-ESCA system. In addition, other in-situ processing chambers may be added in the future. The system is being dedicated to studies of the quantum effects as well as synthesis of Si-based superlattices.

4 Industrial Impact

As a result of the successful growth of SiGe/Si heterostructures under controlled strain, several microelectronic manufacturers have requested our experience in MBE growth. We are currently working with Hughes to develop IMPATT diodes and heterojunction bipolar transistors (HBT's). The impact of these developments are indispensable for the future microelectronic devices.

5 Publications and Graduate Student Training

5.1 Publications supported by this contract fund

- Jogai, B., Wang, K. L., and Brown, K. W., "Free Electron Density and Transit Time in a Finite Superlattice," J. of Appl. Phys., 59(8), 2968 (1986).
- Jogai, B., Wang, K. L., and Brown, K. W., "Frequency and Power Limit of Quantum Well Oscillators," Appl. Phys. Lett. 48(15), 1003 (1986).
- de Frésart, E., Kao, Y. C., and Wang, K. L., "Study of Solid Phase and Molecular Beam Epitaxial Cobalt Silicide Films on Si (111) Using Electron Energy Loss Spectroscopy", J. Vac. Sci. Technol. B, 4(2), 645 (1986).
- Lin, T. L., Chen, S. C., Kao, Y. C., Wang, K. L., and Iyer, S., "100 Micron Wide Silicon-on-Insulator (SOI) structures by Si-MBE Growth on Porous Silicon", Appl. Phys. Lett., 48(26), 1793 (1986).
- Lin, T. L. and Wang, K. L., "New Silicon-On-Insulator Technology Using a Two-Step Oxidation Technique", Appl. Phys. Lett., 49(17), 1104 (1986).
- de Frésart, E., Rhee, S.S., and Wang, K. L., "Boron Oxide Interaction with Silicon in Silicon Molecular Beam Epitaxy", Appl. Phys. Lett., 49(14), 847 (1986).
- Yuh, P. and Wang, K. L., "Intersubband Auger Recombination in a superlattice", Phys. Rev. B 37, 1328 (1988).
- de Frésart, E., Wang, K. L., and Rhee, S. S., "Boron Surface Segregation in Silicon Molecular Beam Epitaxy", Appl. Phys. Lett. 53(1), 48 (1988).
- Rhee, S. S., Park, J. S., Karunasiri, R. P. G., Ye, Q., and Wang, K. L., "Resonant Tunneling through a $Si/Ge_xSi_{1-x}/Si$ Heterostructure on a SiGe Buffer Layer," Appl. Phys. Lett., 53(3) 204 (1988).
- Chang, S. J., Wang, K. L., Kallel, M. A., Bowman, R. C., and Chow, P., "Study of Molecular Beam Epitaxy Grown Ge_xSi_{1-x}/Si Layers by Raman Scattering," J. Appl. Phys., 64, 3634, (1988).

- Kang, T. W., Huang, C. F., Karunasiri, R. P. G., Park, J. S., and Wan, K. L., "Rheed Observation of MBE-Grown $\text{Ge}_x\text{Si}_{1-x}$ on Silicon", J. Vac. Sci. Tech. B, 6(2) 721 (1988).
- Mii, Y. J., Lin, T. L., Kao, Y. C., Wu, B. J., Wang, K. L., Neih, C. W., Jamieson, D., and Liu, J. K., "Studies of MBE Growth of GaAs on Porous Si Substrates", J. of Vac. Sci. Tech. B, 6(2) 696 (1988).
- Yuh, P. and Wang, K. L., "Intersubband Optical Absorption in Coupled Quantum Wells Under an Applied Electric Field," Phys. Rev. B, 38 (12), 8382 (1988).
- Karunasiri, R. P. G., and Wang, K. L., "Infrared Absorption in Parabolic Multi-quantum Well Structures", Superlattices and Microstructures, 4, 661 (1988).
- Yuh, P. and Wang, K. L., "Formalism of the Kronig-Penney Model for Superlattices of Variable Basis", Phys. Rev. B, 38, 13307, (1988).
- Chang, S. J., Huang, C. F., Kallel, Wang, K. L., Wang, Bowman, R. C., and Adams, P. M., "Growth and Characterization of Ge/Si Strained Layer Superlattice," Appl. Phys. Lett., 53, 1835 (1988).
- Wang, K. L. and Yuh, P., "Theory and Applications of Band-aligned Superlattices," IEEE J. Quantum Electron., 25, 12 (1989).
- Yuh, P. F., and Wang, K. L., "Large Stark Shift by Transitions from Localized States to Globalized States in Quantum Well Structures", submitted to IEEE J. Quantum Electron., 25, 1671 (1989).
- Yuh, P. F., Wang, K. L., "Optical Transitions in a Step Quantum Well," J. Appl. Phys., 65, 4377 (1989).
- Rhee, S. S., Karunasiri, R. P. G., Chern, C. H., Park, J. S., and Wang, K. L., " $\text{Si}/\text{Ge}_x\text{Si}_{1-x}/\text{Si}$ Resonant Tunneling Diode Doped by Thermal Boron," J. Vac. Sci. Tech., B7, 327 (1989).
- Chang, S. J., Huang, C. F., Kallel, M. A., Wang, K. L., Bowman, R. C., and Adams, P. M., "Study of Ultra Thin Ge/Si Strained Layer Superlattice," J. of Crystal Growth, 95, 451 (1989).
- Park, J. S., Karunasiri, R. P. G., Wang, K. L., Rhee, S. S., and Chern, C. H., "Hole Transport Through Minibands of a Symmetrically Strained $\text{Ge}_x\text{Si}_{1-x}/\text{Si}$ Superlattice," Appl. Phys. Lett., 54, 1564 (1989).

CONTRIBUTIONS TO SEMINARS AND CONFERENCES:

- Wang, K. L. "Silicon Molecular Beam Epitaxy", The Aerospace Corporation Special Conference on Electronic Materials, Los Angeles, October 1-2, 1986.
- Kao, Y. C., Wang, K. L., de Frésart, E., Hull, R., Bai, G., Jamieson, D., and Nicolet, M.-A., "Study of CoSi_2/Si Strained Layers Grown by MBE," Seventh Annual US MBE Workshop, MIT in Cambridge, Massachusetts, October 20-22, 1986.

- Wang, K. L., "Elemental and Compound Semiconductor Devices Today and Beyond: Influence of Advanced Epitaxial Processes", SPIE's Advances in Semiconductors and Semiconductor Structures Conference, Bay Point, Florida, March 22-27, 1987. (Keynote Address)
- Mii, Y. J., Kao, Y. C., Wu, B. J., Wang, K. L., Lin, T. L., Neih, C. W., and Jamieson, D., "Studies of MBE Grown GaAs on Porous Silicon", the 8th MBE Workshop, Los Angeles, California, September 9-11, 1987.
- Kang, T. W., Huang, C. F., Karunasiri, R. P. G., Park, J. S., and Wang K. L., "RHEED Studies of MBE-Grown Ge_xSi_{1-x} on Silicon", the 8th MBE Workshop, Los Angeles, California, September 9-11, 1987.
- Kang, T. W., Huang, C. F., Karunasiri, R. P. G., Park, J. S., Chern, C. H., and Wang, K. L., "Reflection High-Energy Electron Diffraction Observation of Substrate Cleaning During Silicon Molecular Beam Epitaxy", 2nd International Symposium on Silicon Molecular Beam Epitaxy, Honolulu, Hawaii, October 18-23, 1987.
- Rhee, S. S., and Wang, K. L., "Ultraviolet Laser Assisted Silicon Molecular Beam Epitaxy Growth", 2nd International Symposium on Silicon Molecular Beam Epitaxy, Honolulu, Hawaii, October 18-23, 1987.
- Kang, T. W., Park, J. S., Huang, C. F., Karunasiri, R. P. G., Chern, C. H., and Wang, K. L., "Surface Reconstruction of Ge_xSi_{1-x} Observed after Thermal Treatment", MRS Fall Meeting, Boston, 1987.
- Chang, S. J., Kallel, M. A., and Wang, K. L., "Strain Distribution of MBE Grown Ge_xSi_{1-x}/Si Layers by Raman Scattering", Proc. SPIE 946, 163, (1988).
- Yuh, P., and Wang, K. L., "Theory and Application of Band-aligned Superlattices," American Physical Society March Meeting, New Orleans, March 21-25, 1988.
- Chang, S. J., Kallel, M. A., Wang, K. L., Bowman, R. C., and Chow, P., "Raman Study of Ge_xSi_{1-x}/Si Strained-Layer Superlattice," American Physical Society March Meeting, New Orleans, March 21-25, 1988.
- Yuh, P., and Wang, K. L., "The Mini-band Engineering in a Superlattice with Multiple-well-coupling Basis," American Physical Society March Meeting, New Orleans, March 21-25, 1988.
- Wang, K. L., Karunasiri, R. P., Park, J., Rhee, S. S., and Chern, C. H., "Resonant Tunneling of Variously Strained $Si/Ge_xSi_{1-x}/Si$ Heterostructures," 4th International Conference on Superlattices, Microstructures, Microdevices, Trieste, Italy, August 8-12, 1988.
- Chang, S. J., R. Bowman, and Wang, K. L., "Study of Ultrathin Ge_mSi_n Strained Layer Superlattice Grown by MBE", Fifth International Conference on Molecular Beam Epitaxy, Sapporo, Japan, August 26 - September 3, 1988.
- Rhee, S. S., Chern, C. H., Park, J. S., Karunasiri, R. P. G., and Wang, K. L., "Resonant Tunneling of Holes in MBE $Si/Ge_xSi_{1-x}/Si$ Heterostructures Doped by Thermal Boron Source", 9th MBE Workshop, West Lafayette, Indiana, September 21-23, 1988.

- Chang, S. J., Arbet, V., Kallel, M. A., Wang, K. L., Bowman, R. C., and Adams, P. M., "Raman Study of Ge/Si Strained Layer Superlattice Grown on Different Substrate Orientation," SPIE Meeting, Los Angeles, Jan., 1989.
- Bowman, R. C., Adams, P. M., Chang, S. J., and Wang, K. L., "Studies of Interface Mixing in a Symmetrically Strained Ge/Si Superlattice," MRS meeting, San Diego, April, 1989.
- Bowman, R. C., Adams, P. M., Chang, S. J., and Wang, K. L., "Studies of Interface Mixing in a Symmetrically Strained Ge/Si Superlattice," MRS meeting, San Diego, April, 1989.
- Arbet, V., Chang, S. J., and Wang, K. L., "Investigation of Ge_mSi_n Strained Monolayer Superlattices by RHEED, Raman and X-ray Techniques," E-MRS Conference, Strasbourg, France, May, 1989.
- Park, J. S., Karunasiri, R. P. J., and Wang, K. L., "Study of Hole Miniband Transport Through Minbands in Symmetrically Strained $\text{Ge}_x\text{Si}_{1-x}/\text{Si}$ Superlattices," E-MRS Conference, Strasbourg, France, May, 1989.
- S. J. Chang, V. Arbet, K. L. Wang, R. C. Bowman, Jr. and P. M. Adams, "Studies of Interdiffusion in Ge_mSi_n Strained Layer Superlattice", EMC, Boston, June (1989).
- R. P. G. Karunasiri, J. S. Park, K. L. Wang, and P. F. Yuh, "Study of Hole Miniband Transport in $\text{Ge}_x\text{Si}_{1-x}/\text{Si}$ Superlattice", DRC, Boston, June (1989).
- K. L. Wang and R. P. G. Karunasiri, "SiGe Heterostructures and Devices", 12th IEEE/Cornell University Conference, Ithaca, August 7-9, (1989).

5.2 Graduate student training

The research contract funding has been supporting graduate students in their M.S. and Ph.D. dissertation research. During this contractual period, seven Ph.D. students have completed their studies. Currently, they are employed by organizations such as IBM, JPL and Texas Instruments.

| | |
|--------------|-------|
| P. D. Chow | Ph.D. |
| T. L. Lin | Ph.D. |
| M. A. Kallel | M.S. |
| M. Mojaradi | Ph.D. |
| B. Jogai | Ph.D. |
| Y. J. Mii | M.S. |
| Y. C. Kao | Ph.D. |

| | |
|---------------|--------------|
| P. F. Yuh | Ph.D. |
| S. J. Chang | Ph.D. |
| E. de Fresart | Postdoctoral |
| R. Karunasiri | Postdoctoral |

References

- [1] S. J. Chang, M. A. Kallel, K. L. Wang, R. C. Bowman, Jr., and P. Chow. *J. Appl. Phys.*, 64, 3634, 1988.
- [2] T. W. Kang, C. F. Huang, R. P. G. Karunasiri, J. S. Park, C. H. Chern and K. L. Wang. *j. Vac. Sci. Technol.*, 6, 721, 1988.
- [3] F. Huang, R. P. G. Karunasiri, K. L. Wang, and T. W. Kang. Proc. mrs fall meeting. In *Boston*, 1987.
- [4] V. Arbet, S. J. Chang and K. L. Wang. *Thin Solid Films*, 183, 57, 1989.
- [5] S. J. Chang, C. F. Huang, M. A. Kallel, K. L. Wang, R. C. Bowman, J , and P. M. Adams. *J. Crystal Growth*, 95, 451, 1989.
- [6] S. J. Chang, C. F. Huang, M. A. Kallel, K. L. Wang, R. C. Bowman, Jr., and P. M. Adams. *Appl. Phys. Lett.*, 53, 1835, 1988.
- [7] Y. C. Kao, K. L. Wang, B. J. Wu, T. L. Lin, C. W. Nieh, D. Jamieson, and G. Bai. *Appl. Phys. Lett.*, 51(22), 1809, 1987.
- [8] Q. Ye, T. W. Kang, K. L. Wang, G. Bai, and M. A. Nicolet. Rheed study of cosi_2/si multilayer structures. To appear in Proc. of 10th Si-MBE conference (1989).
- [9] J. S. Park, R. P. G. Karunasiri, K. L. Wang, C. H. Chern, and S. S. Rhee. *Appl. Phys. Lett.*, 54, 1564, 1989.
- [10] R. P. G. Karunasiri, J. S. Park, K. L. Wang, and Li-Jen Cheng. *Appl. Phys. Lett.*, 56(14), 1342, 1990.

- [11] P. F. Yuh and K. L. Wang. *Appl. Phys. Lett.*, 51, 1404, 1987.
- [12] P. F. Yuh and K. L. Wang. *Phy. Rev. B*, 38, 8377, 1988.
- [13] P. F. Yuh and K. L. Wang. *J. Appl. Phys.*, 65, 4377, 1989.
- [14] P. F. Yuh and K. L. Wang. *IEEE J. Quantum Electron.*, QE-25, 1671, 1989.

6 Appendix

Free-electron density and transit time in a finite superlattice

B. Jogai and K. L. Wang

Devices Research Laboratory, Electrical Engineering Department, University of California at Los Angeles, Los Angeles, California 90024

K. W. Brown

Sensor Physics Section, Chemistry and Physics Laboratory, The Aerospace Corporation, El Segundo, California 90245

(Received 11 November 1985; accepted for publication 2 January 1986)

In this paper we have calculated the free-electron density in a finite superlattice. Resonant tunneling causes a buildup of particle density in the well regions, giving rise to an accumulation of electrons in those regions. Using our results, we have estimated the change in barrier heights and well depths caused by the electrostatic force. A negligible change is found for a double-well structure having well widths of 40 Å and barrier widths of 20 Å. Our approach could be extended to calculate the tunneling current self-consistently. Additionally we have used a time-dependent solution of Schrödinger's equation to estimate the trapping time of the electrons due to the resonant effect. The results show that the probability density oscillates several times between the two wells, leaking out gradually at each step. After about 2.4×10^{-13} s, most of the waves centered about the resonant energies have been transmitted.

INTRODUCTION

Interest in the finite superlattice, consisting of only a few layers, has been renewed due to the recent quality of thin films grown by molecular-beam epitaxy (MBE). Such a structure has potential device applications since the resonant tunneling phenomenon can lead to negative resistance. This effect had been predicted by Tsu and Esaki,¹ and subsequently verified by Chang *et al.*² Lately, there have been reports on measurements done on MBE-grown samples.^{3,4} The results have included measurements of the current-voltage curve of a double-barrier device. In each case, the calculated tunneling current does not agree with the measured value for reasons that have not yet been clarified. In particular, the large peak-to-valley ratio predicted has not been realized experimentally. Discrepancies are to be expected, however, as the model is very simple. As an example, in the early calculation of the current,¹ the conduction-band edge was modeled in a staircase approximation to account for the applied voltage. Semianalytic expressions were then obtained for the current. A numerical approach⁵ has involved a more realistic treatment of the band edge, but the results are still not close to experiment.

In attempts to refine the model, it has been suggested that the well regions act as dynamic traps for the tunneling electron.⁶ The presence of the electron in the well for some time is therefore expected to modify the potential. Deviation from linearity may occur. As a further refinement to the model, the tunneling current could be calculated self-consistently, taking into account the change in potential caused by the trapped electrons. We outline a way this can be done by calculating the free-electron density in the barrier and well regions, as a result of the accumulation of particle density in the well regions. Solution of Poisson's equation yields the modified potential. Such information can then be used to recalculate the electron density. Also presented is a time-dependent solution of Schrödinger's equation for a double-well, triple-barrier structure. Multiple reflections of the elec-

tron wave packet are seen to increase the tunneling time by an order of magnitude over the classical limit.

METHOD

Figure 1 shows the conduction-band edge of the structure that has been simulated. The free-electron density has been found by first obtaining the one-electron wave function. In the outermost GaAs layers, the wave functions are shown in Fig. 1, in which $k_0^2 = 2m_{GaAs}^*(E - E_{\parallel})/\hbar^2$, $k^2 = 2m_{GaAs}^*(E + eV_a - E_{\parallel})/\hbar^2$, $k_{0\parallel}^2 = 2m_{GaAs}^*E_{\parallel}/\hbar^2$. E_{\parallel} is the energy in the GaAs regions corresponding to motion parallel to the interface plane, E is the total energy, and V_a is the applied voltage. The wave function for the barrier layers is given by

$$\Psi_b = [a \text{Ai}(-t_b) + b \text{Bi}(-t_b)] \exp(ik_{0\parallel} \cdot \rho), \quad (1)$$

$$t_b = x_0^{-1} \gamma^{-1/3} [(E - eV_0 - \gamma E_{\parallel})/eF + z]. \quad (2)$$

Here Ai and Bi are the Airy functions, F is the magnitude of the electric field, γ is the ratio of the effective mass in GaAs to that in $\text{Ga}_{1-x}\text{Al}_x\text{As}$, x_0 is a characteristic length given by $x_0 = (2m_{GaAs}^*eF/\hbar^2)^{-1/3}$, and V_0 is the barrier height. For the well regions the wave function is given by

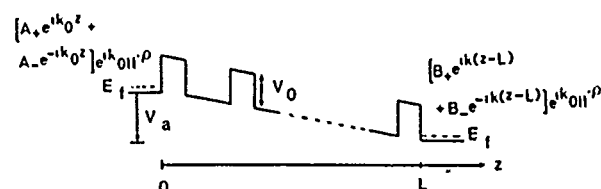


FIG. 1. Conduction-band edge of a multilayered $\text{GaAs}/\text{Ga}_{1-x}\text{Al}_x\text{As}$ structure for an applied voltage V_a . The outermost GaAs layers are assumed to be heavily doped and semi infinite in extent, so that the electric field in those regions can be assumed to be small, enabling the use of plane wave solutions. The rest of the structure is assumed to be intrinsic so that the electric field is taken to be a constant and in the negative z direction. k_0 is the common barrier height.

$$\Psi_w = [c \text{Ai}(-t_w) + d \text{Bi}(-t_w)] \exp(i\mathbf{k}_{0\parallel} \cdot \mathbf{p}), \quad (3)$$

$$t_w = x_0^{-1} [(E - E_{\parallel})/eF + z]. \quad (4)$$

Using the transfer matrix technique,⁶ the constants preceding the linearly independent solutions are found, enforcing in the process, the continuity of flux, and particle current at each interface. Finally, the constant A_+ is determined by requiring delta-function normalization of the incident plane wave, giving $|A_+|^2 = 1/(2\pi)^3$. The free-electron density is then found from

$$n(z) = n_1(z) + n_2(z), \quad (5)$$

where $n_1(z)$ is the electron concentration caused by elec-

trons originating from the left contact region and tunneling through the superlattice; $n_2(z)$ is the concentration due to electrons originating from the right contact region. Explicitly, $n_1(z)$ is given by

$$n_1(z) = 2(2\pi) \iint |\Psi_L(z)|^2 f(E) k_{\parallel} dk_{\parallel} dk_{\perp}, \quad (6)$$

where $f(E)$ is the Fermi-Dirac occupation probability of the left contact region, and $|\Psi_L(z)|^2$ is the density of one electron caused by an electron originating from the left. Ignoring the effective mass variation from layer to layer, i.e., setting $\gamma = 1$ for simplicity, Eq. (6) may be simplified since Ψ_L becomes independent of E_{\parallel} . Using Eq. (5), the total concentration is given by

$$n(z) = \pi kT (2m_{\text{GaAs}}^*/\hbar^2)^{3/2} \left(\int_{l_1(z)}^{\infty} |\Psi_L(z)|^2 \ln[1 + \exp(E_f - E_1)/kT] dE_1/\sqrt{E_1} \right. \\ \left. + \int_{l_2(z)}^{\infty} |\Psi_R(z)|^2 \ln[1 + \exp(E_f - E_1 - eV_a)/kT] dE_1/\sqrt{E_1} \right), \quad (7)$$

where Ψ_R is the wave function due to an electron originating from the right. $l_1(z)$ and $l_2(z)$ are the lower limits of integration. Under the assumption that the voltage is applied as in Fig. 1, $l_1(z)$ is zero for the well regions and is equal to the conduction-band edge for the barrier regions. $l_2(z)$ is given by the conduction-band edge of the respective regions. Included in Eq. (7) is the fact that electrons incident from the right with negative energies may also contribute to the free-electron density.

RESULTS AND DISCUSSION

Equation (7) was solved for a double-well, triple-barrier structure having well widths of 40 Å, barrier widths of 20 Å, and 0.25-eV barrier heights. The structure is assumed to be undoped except for the two outermost GaAs layers whose Fermi levels are assumed to be 0.005 eV above the respective band edges. Figure 2 compares the resulting electron concentration for the case of zero applied voltage with applied voltages of 0.2, 0.5, and 1 V. At 0 V the electron density in the well regions is about $4 \times 10^{16} \text{ cm}^{-3}$. It drops to about 10^{12} cm^{-3} in the barrier regions. Below the barrier level there are two resonant states, occurring at 0.08 and 0.11 eV above the GaAs conduction-band edge for $V_a = 0$. The maximum electron density occurs when the applied voltage is about twice the resonant energies, so that the resonant level is then aligned with the Fermi level. At high applied voltages, the reduced transit time of the electrons causes the overall density to drop. At the same time, the electron density in the barrier regions close to $z = L$ approaches that in the well regions due to the lowering of the barriers by the applied voltage. The principal contribution to the electron density is the incident electrons within a narrow band of energies enclosing the resonant levels. Hence the profile of the electron distribution essentially follows that of the resonant wave functions. Except for small applied voltages, the

contribution of $|\Psi_R(z)|^2$ to the electron density is small, caused by the lowering of the Fermi level. If the applied voltage is greater than about twice the resonant energy, localized levels having negative energies are formed in the wells close to $z = L$. In this case, electrons with negative energies incident from the right may also contribute to the carrier density. In the specific example we have chosen,

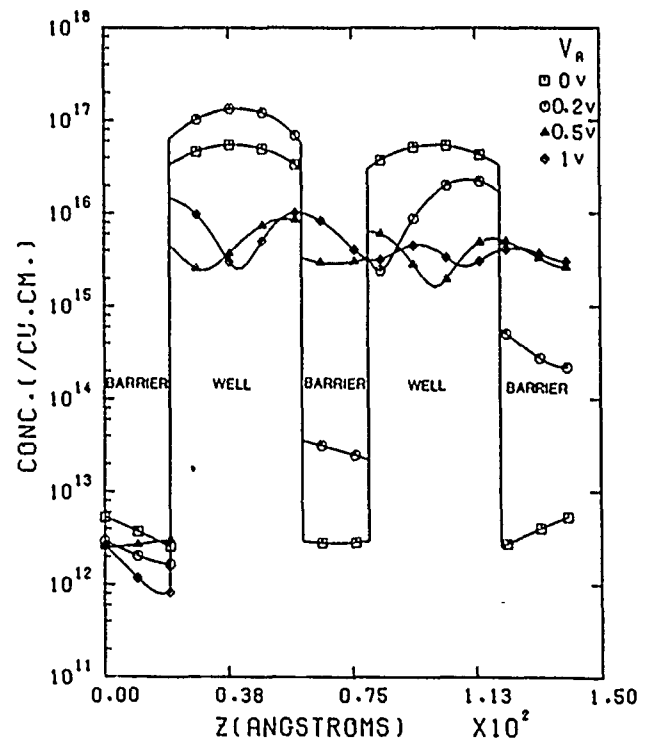


FIG 2 Free electron density as a function of position in a double-well, triple-barrier structure at 300 K. The well widths are 40 Å, the barrier widths 20 Å, and the barrier heights 0.25 eV. The four sets of curves refer to four different applied voltages.

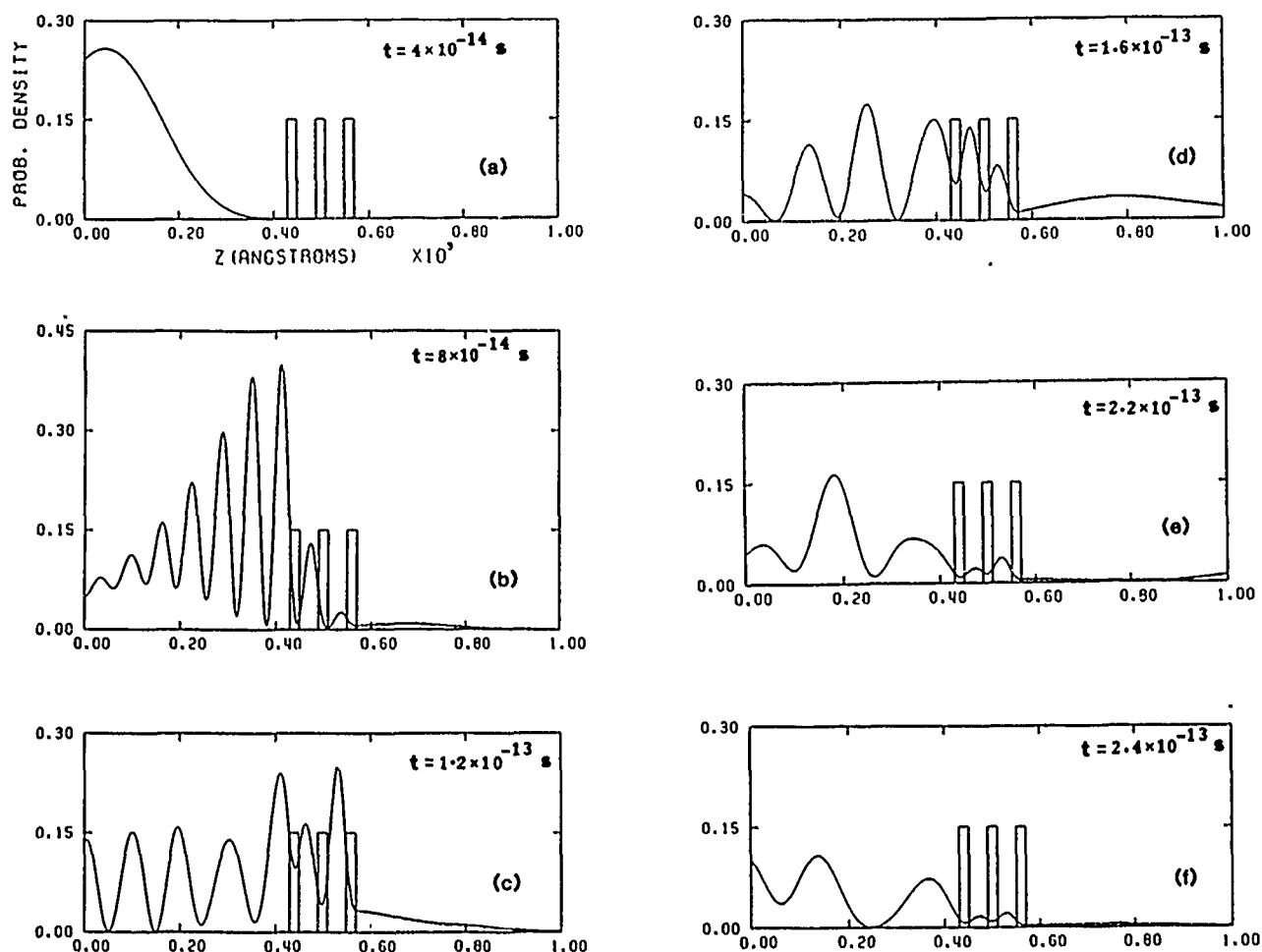


FIG. 3. (a)–(f) show the evolution of a Gaussian wave packet in the vicinity of the double-well structure. The elapsed time is shown in the inset. The average energy is 0.08 eV (near resonance) and the initial half-width is 30 Å.

these states have a negligible effect because of the Fermi level position.

Using the results of Fig. 2, we solved Poisson's equation to find the change in potential. Owing to the small size of the wells and barriers, the edges of the wells were lowered by only 1 meV. It is estimated that a well concentration of about 10^{18} cm^{-3} would be required for a 10 meV change. It appears, therefore, that a linear potential distribution is justified for this particular structure. An improved estimate of the tunneling current may be obtained by repeatedly calculating the charge density and potential until convergence occurs. The current is then estimated according to Vassel *et al.*⁵ Such an approach may be appropriate for heavily doped samples.

As a further investigation of resonant state trapping we have considered the evolution of a Gaussian wave packet as it traverses the finite superlattice. The wave packet has a half-width of about 30 Å at $t = 0$ and an average energy E_0 . At subsequent times the wave function is calculated according to the Crank–Nicolson method⁷ which preserves its normalization. It is assumed that the structure is bounded by infinite potentials which are far removed so as not to influence the wave packet during the time it interacts with the finite superlattice. Figures 3(a)–3(f) show the results for a wave packet having an average energy of 0.08 eV which is close to the resonant energy. The center of the packet takes

approximately $4 \times 10^{-14} \text{ s}$ to reach the first barrier after being launched. Most of the packet is reflected, except for those waves having energies close to the resonant level. The remaining portion oscillates several times between the two wells and gradually leaks out. A significant portion of the wave remains even after about $2.4 \times 10^{-13} \text{ s}$. This is about ten times greater than the classical estimate found by dividing the length of the well regions by the group velocity. A more detailed analysis of the trapping time should include the effect of the incident electrons emitting phonons in the well regions, thereby remaining trapped for a longer time.

ACKNOWLEDGMENTS

Two of the authors, B. J. and K. L. W., wish to acknowledge the support of the U. S. Army Research Office and Semiconductor Research Corporation. K. W. B. acknowledges the support of Aerospace Sponsored Research funds.

¹R. Tsu and L. Esaki, *Appl. Phys. Lett.* **22**, 562 (1973).

²L. L. Chang, L. Esaki, and R. Tsu, *Appl. Phys. Lett.* **24**, 593 (1974).

³T. C. L. G. Sollner, W. D. Goodhue, P. E. Tannenwald, C. D. Parker, and D. D. Peck, *Appl. Phys. Lett.* **43**, 588 (1983).

⁴T. J. Shewchuk, P. C. Chapin, P. D. Coleman, W. Kopp, R. Fisher, and H. Morkoç, *Appl. Phys. Lett.* **46**, 508 (1985).

⁵M. O. Vassel, Johnson Lee, and H. F. Lockwood, *J. Appl. Phys.* **54**, 5206 (1983).

⁶B. Ricco and M. Ya. Azbel, *Phys. Rev. B* **29**, 1970 (1984).

⁷C. F. Gerald, *Applied Numerical Analysis*, 2nd ed. (Addison-Wesley, Reading, MA, 1980).

Frequency and power limit of quantum well oscillators

B. Jogai and K. L. Wang

Device Research Laboratory, Electrical Engineering Department, University of California, Los Angeles, Los Angeles, California 90024

K. W. Brown

Sensor Physics Section, Chemistry and Physics Laboratory, The Aerospace Corporation, El Segundo, California 90245

(Received 30 December 1985; accepted for publication 17 February 1986)

The maximum frequency at which amplification can be obtained from quantum well oscillators is discussed. Intrinsically, the frequency limit for having negative differential resistance (NDR) can be very high, of the order of the inverse of the electron transit time. Owing to the large capacitance of the well and barrier regions, the actual frequency limit at which amplification occurs may be lower than the intrinsic limit because of the capacitance charging time. We have estimated the frequency limit of NDR by considering the electron transit time and have calculated the maximum oscillation frequency from an equivalent circuit model. We have also obtained an expression for the high-frequency power output as a function of frequency, based on a transmission line model.

Negative differential resistance in quantum well devices is of considerable interest since the fast electron transport expected in such devices can result in high-frequency amplification. Tsu and Esaki¹ had predicted NDR in a finite superlattice as a consequence of resonant tunneling. The first experimental results were obtained by Chang *et al.*² Due to high input impedance, high-frequency oscillations were not observed in the early samples. Furthermore, the peak to valley ratio of the current was much too small to produce any workable power. Recent measurements on samples grown by molecular beam epitaxy³⁻⁵ have shown promising results. Sollner *et al.*^{3,6} have obtained a peak to valley ratio of 6:1,⁶ and have also demonstrated mixing and detection at 138 GHz, 761 GHz, and 2.5 THz; these results suggest NDR up to 2.5 THz. In addition, they have used a coaxial resonant cavity to obtain oscillations at 18 GHz. If the electron transit time is the limiting factor for maximum oscillation frequency, an upper limit of about 1 THz seems possible. However, so far there has been no reported oscillation frequency in excess of 18 GHz.

In this letter, we discuss the maximum frequency at which NDR is possible as well as the maximum frequency at which a signal can be amplified by the quantum well device. In particular, we calculate the maximum frequency at which amplification is obtainable within a simple circuit model. We show that the circuit parameters which model the parasitic effects such as device capacitance and series resistance can have serious limitation on the maximum frequency of oscillation.

Previously Ricco and Azbel⁷ have discussed the time development of resonant tunneling in a double barrier device, and have shown that an important quantity in determining frequency behavior is a time constant τ , which is the time required for the probability density to build up in the well when a voltage is applied. Once this amount of time has elapsed, resonant tunneling is fully established. The frequency limit of NDR is expected to be set by the inverse of τ . Luryi⁸ has related the frequency limit of oscillation to the reciprocal of the charging time of a capacitor represented by

the first barrier layer; the second barrier is ignored in the estimate of the charging time. The charging current is assumed to be the single barrier tunneling current. A time constant of about 40 ps for the device of Refs. 3 and 4 is then obtained using the capacitance and positive resistance of the single barrier. In attempting to explain the higher observed detection frequencies,³ Luryi proposed a new model in which the negative resistance is effected by the reduction in density of occupied emitter states allowed for tunneling with increasing applied voltage. When the quasibound level drops below the conduction-band edge of the emitter, there are no occupied emitter states consonant with energy and momentum conservation for tunneling. This effect as pointed out by Luryi, is of course, a generic feature to tunneling from a three-dimensional to a two-dimensional system of states. We note that this situation bears some resemblance to tunneling in a tunnel diode. Although the foregoing model for the existence of NDR is possible, it is not clear to us, however, that Sollner's detection of NDR at 2.5 THz depends upon the origin of the NDR.

An alternative explanation of the oscillation frequency and high-frequency detection may be possible and perhaps more appropriate. We are proposing an equivalent circuit model, based on which the oscillation frequency can be estimated from the magnitude of the NDR. The latter may be extracted from theoretical or experimental current-voltage curves if available. The results are independent of whether the NDR originates from the density of states or from the Fabry-Perot effect.

In quantum well devices where the NDR is accounted for by the Fabry-Perot mechanism, the speed at which the electron wave packet traverses the total structure is expected to govern the maximum frequency of amplification. Under ideal conditions, this maximum frequency should be close to the limit enforced by the transit time, since beyond this limit the NDR is annihilated, i.e., the negative conductance goes to zero. Recently, Barker⁹ has calculated the tunneling time through a double barrier device by solving Wigner's equation. A semiclassical formulation allows the effect of colli-

sions to be included by a Monte-Carlo calculation of the distribution function. Tunneling times of the order of 10^{-14} s are reported in the near hot electron regime. We have obtained a simple estimate of the tunneling time by looking at the time evolution of a Gaussian wave packet in the vicinity of a triple-barrier, double-well device. The packet is approximately monoenergetic if its real space half-width is sufficiently large. For an average energy equal to the resonant state energy, the problem resembles that of an electron at the resonant energy interacting with the structure. The time-dependent Schrödinger equation was solved numerically. We find that for a structure having barrier widths of 20 Å and well widths of 40 Å, most of the incident wave packet has been reflected or transmitted after about 3×10^{-13} s. This estimate is quite consistent with the Barker's results since the extra well causes additional interference. Furthermore, the average electron energy is much smaller than that of Ref. 9. We have ignored the effect of the charge buildup in modifying the potential, having previously found it to be small for sufficiently narrow wells and barriers.¹⁰ Based on these interaction times we expect the intrinsic frequency limit of NDR to be of the order of a few hundred GHz for a double-well device, and much higher for a single-well structure. Single-barrier conduction yields an even higher frequency limit of NDR than Fabry-Perot conduction owing to the reduced tunneling time.

Using an equivalent circuit model similar to that of the tunnel diode,¹¹ we show that the measured amplification frequency may be much lower than that anticipated from the electron transit time. This model is shown in Fig. 1(a) where R represents the ideal dynamic NDR (ac) caused by coherent tunneling either of the Fabry-Perot or the single-barrier type, C is the total capacitance of the barrier and well regions, and R_s is the series resistance of the substrate. R_p

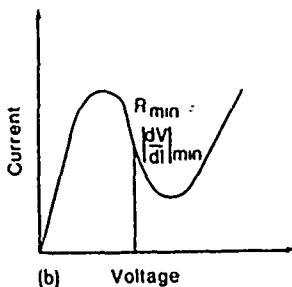
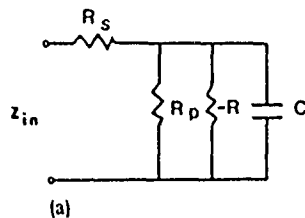


FIG. 1 (a) Equivalent circuit of the quantum well device. R is nonlinear resistance representing the resonant tunneling current. R_p represents the leakage currents, R is the substrate resistance, and C is the capacitance of the well and barrier regions. (b) Tunneling current of the device showing the minimum NDR.

represents an excess current caused by leakage processes. The input impedance Z_{in} of this circuit has a negative real part as long as

$$f < \frac{1}{2\pi RC} \left[\frac{R}{R_s} - 1 + \frac{R}{R_p} \left(2 - \frac{R}{R_p} - \frac{R}{R_s} \right) \right]^{1/2}. \quad (1)$$

The maximum frequency occurs when R (ac) is replaced by R_{min} , i.e., when the bias point is at the steepest part of the current-voltage curve [Fig. 1(b)] so long as the dynamic NDR still exists. In the limit as $R_s \rightarrow 0$, the frequency is expected to approach the intrinsic limit set by the electron trapping (or transit) time. For the device shown in Ref. 4, we obtain a maximum frequency of about 200 GHz based on the reported NDR of 400 Ω. This value of NDR already accounts for the effects of excess currents. A series resistance of 10 Ω was assumed, based on the dopant density and cross-sectional area given. If the theoretical current-voltage curves of Ref. 1 are used, much higher oscillation frequencies are obtainable. The effect of the excess currents is to lower the oscillation frequency by smearing out the NDR. The circuit shown in Fig. 1(a) is consistent with the high-frequency detection of Ref. 3, provided that R_s is small. Then the second derivative of the terminal current is independent of frequency as in Sollner's case, as long as the NDR remains the same at the detection frequency. It is noted that the RC time constant loses its meaning as a conventional charging time when the resistance value is a negative differential resistance. As f_{max} approaches the characteristic cutoff, the dynamic NDR becomes weaker and finally disappears.

Apart from the maximum attainable frequency, other quantities of interest include the available rf power and the power-frequency relation. Although the available power is related to the product of the maximum current and voltage swing, the actual power that can be extracted may be governed by external conditions. As an example, we consider the coaxial resonator of Ref. 4. By balancing the loss and gain of the resonator, the output power P is found to be directly proportional to $(|\rho|^2 - 1)$, where the reflection coefficient ρ is given by

$$|\rho(\omega, R)|^2 = \frac{(R_{in} - Z_0)^2 + X_{in}^2}{(R_{in} + Z_0)^2 + X_{in}^2}. \quad (2)$$

Thus the power is found from

$$P(\omega, R) \propto 4R_{in}Z_0 / [(R_{in} + Z_0)^2 + X_{in}^2]. \quad (3)$$

R_{in} and X_{in} are, respectively, the real and imaginary parts of the input impedance, and Z_0 is the characteristic impedance of the resonator. From Fig. 1(a), R_{in} is given by

$$R_{in} = R_s + R_T / (1 + \omega^2 \tau_c^2), \quad (4)$$

where R_T is the parallel combination of R_p and R , and $\tau_c = R_T C$. In addition to the explicit frequency dependence of R_{in} , there is also an intrinsic dependence on frequency, since the NDR is expected to be smeared out as $1/\omega$ approaches the trapping time of an electron in the resonant state. The exact dependence can, of course, be found from a time dependent solution of the tunneling current, but may be approximated phenomenologically by the expression $R = R_0(1 + \omega^2 \tau^2)$, where τ represents a time constant related to the electron transit time and R_0 is the low-frequency

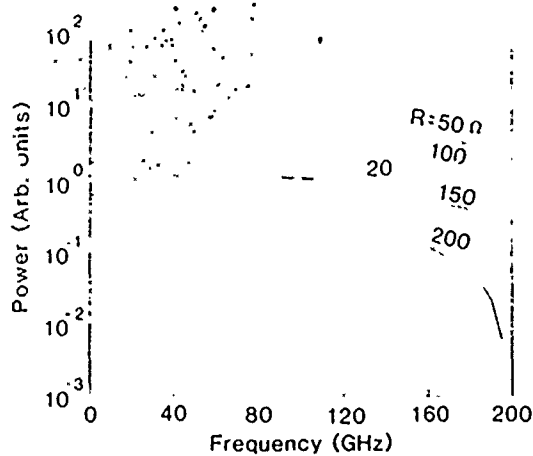


FIG. 2. rf power as a function of frequency of operation of the quantum well device in a coaxial resonator. Several values of NDR are indicated.

NDR. The power (in arbitrary units) is calculated as a function of frequency from Eq. (3), assuming $Z_0 = 50 \Omega$. Figure 2 shows the results for several values of NDR. At low frequencies, maximum power occurs when $R \approx R_0 + Z_0$. This is shown in Fig. 3 where the power is plotted as a function of R for several frequencies. At very high frequency, the device terminal resistance is positive so that the resonator becomes lossy. For the low frequencies shown, the anticipated smear out of the NDR with increasing frequency is negligible and therefore has little effect on the power. A large value of NDR is undesirable¹² as it results in a reflection coefficient of less than 1.

In summary, we have estimated the oscillation frequency and power limitation of a quantum well oscillator from an equivalent circuit in which the nonlinearity of the current-voltage curve is included phenomenologically in a parameter R . We have shown that previously ignored external conditions can severely limit the oscillation frequency and ac power output.

B. J. and K. L. W. acknowledge the support of the Office of Naval Research and the Army Research Office. K. W. B.

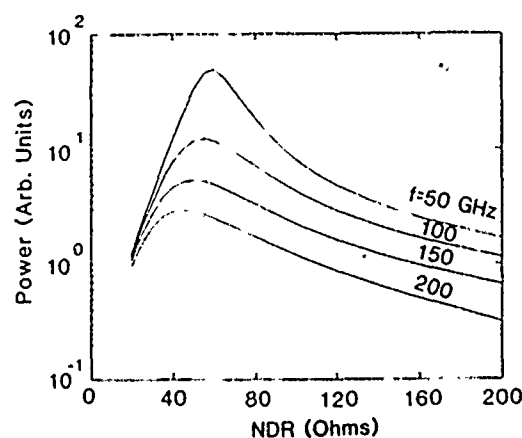


FIG. 3. Power as a function of NDR for several frequencies.

acknowledges the support of Aerospace Sponsored Research Funds.

¹R. Tsu and L. Esaki, *Appl. Phys. Lett.* **22**, 562 (1973).

²L. L. Chang, L. Esaki, and R. Tsu, *Appl. Phys. Lett.* **24**, 593 (1974).

³T. C. L. G. Sollner, W. D. Goodhue, P. E. Tannenwald, C. D. Parker, and D. D. Peck, *Appl. Phys. Lett.* **43**, 588 (1983).

⁴T. C. L. G. Sollner, P. E. Tannenwald, D. D. Peck, and W. D. Goodhue, *Appl. Phys. Lett.* **45**, 1319 (1984).

⁵T. J. Shewchuk, P. C. Chapin, P. D. Coleman, W. Kopp, R. Fisher, and H. Morkoc, *Appl. Phys. Lett.* **46**, 508 (1985).

⁶Recently Sakaki has reported a peak to valley ratio of 10.1. See, for example, H. Sakaki, *International Electron Devices Meeting*, 2-5 Dec. 1985, Washington DC.

⁷B. Ricco and M. Ya. Azbel, *Phys. Rev. B* **29**, 1970 (1984).

⁸Serge Luryi, *Appl. Phys. Lett.* **47**, 490 (1985).

⁹J. R. Barker (private communication).

¹⁰B. Jogai, K. L. Wang, and K. W. Brown, *J. Appl. Phys.* **59**, 15 Apr. (1986).

¹¹"Standards on Definitions, Symbols, and Methods of Test for Semiconductor Tunnel (Esaki) Diodes and Backward Diodes," *IEEE Trans. Electron Devices* **ED-12**, 374 (1965).

¹²A large value of NDR indicates the disappearance of negative conductance. Thus it appears more appropriate in power considerations to use negative differential conductance (NDC).

Study of solid phase and molecular beam epitaxial cobalt silicide films on Si(111) using electron energy loss spectroscopy

E. de Fresart, Y. C. Kao, and K. L. Wang

Device Research Laboratory, Electrical Engineering Department, University of California, Los Angeles, Los Angeles, California 90024

(Received 23 September 1985; accepted 11 December 1985)

Very thin cobalt silicide films of several atomic compositions from Co to CoSi_2 have been grown by thermal reaction of Co deposited at room temperature and by molecular beam epitaxy on Si(111) substrates under ultrahigh vacuum conditions. They were analyzed by electron energy loss spectroscopy. Loss spectra characteristic of the Co-rich silicides, CoSi, and CoSi_2 phases were found to be quite different, first by the energy of the bulk plasmons, around 22 eV for Co-rich silicides, 20.6 and 19.5 ± 0.7 eV for CoSi and CoSi_2 , respectively, second by the interband and surface-state transitions. In the CoSi and CoSi_2 spectra, two transitions were interpreted as related to the excitation of bonding $\text{Co}(3d)\text{-Si}(3p)$ and nonbonding $\text{Co}(3d)$ electronic states. A transition at 1.7 eV obtained on CoSi_2 grown both by the solid phase and molecular beam epitaxy techniques was found to be sensitive to the surface conditions and was attributed to a surface state. This result was correlated to the surface morphology and film crystallinity checked by scanning electron microscopy and electron channeling. Energy loss spectra were correlated to the alloy composition ratios obtained by Auger spectroscopy and Rutherford backscattering spectrometry.

I. INTRODUCTION

In situ characterization of cobalt silicide films is essential for controlling the growth of CoSi_2/Si heterostructures used in the engineering of novel devices. Among potential applications of these heterostructures in microelectronics technology, metal base transistors and permeable base transistors have been proposed using the epitaxial silicide film as buried layers.^{1,2} Transistor action in $\text{Si}/\text{CoSi}_2/\text{Si}$ structures has recently been demonstrated.³ The growth of epitaxial CoSi_2 on Si in ultrahigh vacuum (UHV) conditions has already been studied for its structural properties, kinetics of formation, and morphology using Rutherford backscattering spectroscopy (RBS), transmission and scanning electron microscopy (TEM, SEM), and x-ray rocking curve.⁴⁻⁹ Electronic properties were investigated by angle-resolved ultraviolet photoemission spectroscopy (ARUPS), x-ray photoemission spectroscopy (XPS), and low-energy electron diffraction (LEED).¹⁰ The electrical properties of $\text{CoSi}_2/\text{Si}(111)$ Schottky barriers were studied by current and capacitance versus voltage (I - V and C - V) and deep-level transient spectroscopy (DLTS).^{11,12} In this work, we aimed to obtain additional information on the cobalt silicide/Si system using only two *in situ* techniques, the Auger electron spectroscopy (AES) and the electron energy loss spectroscopy (EELS). Furthermore, after *in situ* analysis each sample was next studied by RBS to obtain the alloy composition, and by SEM for the surface morphology and uniformity. These studies were correlated with the AES and EELS results. Electron channeling patterns were also taken to check the film crystallinity.

II. EXPERIMENTAL PROCEDURE

In this work, we use *n*-type (111) oriented Si wafers with a resistivity of about 4–10 Ω cm. Prior to loading the sample

into the UHV chamber, the Si wafer was chemically cleaned by the method of Ishizaka *et al.*,¹³ leaving at the last step of cleaning a protective thin oxide coating on the surface. After loading the sample in the UHV system, this oxide layer was thermally evaporated by flash heating to 900–950 °C for 5–10 min to provide an atomically clean (7 \times 7) Si(111) surface prior to growth. The (7 \times 7) reconstruction has been identified by the presence of characteristic surface-state transitions¹⁴ in the EELS spectra. Two techniques, the solid phase epitaxy (SPE) and the molecular beam epitaxy (MBE) techniques, were used to grow silicide films. In the SPE method, a 100 Å cobalt film was evaporated on the substrate at room temperature (RT), then annealed for 10 min at a fixed temperature (T_a) in order to achieve the silicide formation of a given composition. The range of T_a was from RT up to 900 °C. Surface substrate temperature was measured with a calibrated optical infrared pyrometer. The Co growth rate was about 10 Å/min, monitored by a quartz microbalance. The vacuum pressure during growth never exceeded 4×10^{-9} Torr. In the MBE technique, Co and Si were simultaneously deposited on the sample held at 540 °C with a Si/Co flux ratio of about 2 at the pressure of 2×10^{-8} Torr and a growth rate of 19 Å/min. The growth chamber was equipped with a cylindrical mirror analyzer (CMA) from Perkin-Elmer Company. Auger and EELS spectra were taken in the derivative mode using a lock-in amplifier. Two electron primary energies used in EELS measurements were $E_p = 500$ and 80 eV. At $E_p = 500$ eV, strong signals from plasmons and core level excitations were obtained. At $E_p = 80$ eV, an increase of the energy resolution ($\Delta E = 0.7$ eV), measured at full width at half-maximum, allowed the observation of the low energy interband transitions and, at the same time, of the surface state transitions due to the short electron inelastic mean free path.

III. RESULTS AND DISCUSSION

A. Surface morphology and film crystallinity

The surface morphology of each sample was examined by SEM. For Co and for Co-rich silicide films obtained with annealing temperatures ranging from RT to 350 °C, very smooth surface films were obtained.

At higher annealing temperatures, films were found to consist of perforated silicide. For 400–650 °C annealing range, the hole diameter remained unchanged, about 0.5 μm . The hole density relative to the whole sample surface did not exceed 10%. At $T_a = 730$ °C, 16% of the surface was covered by perforations and at 900 °C, cobalt disilicide islands were always observed. These observations are in agreement with those of Refs. 4 and 8, in which uniformity and stoichiometry of SPE CoSi₂ films have been studied by RBS and SEM as a function of the annealing temperature.

SEM from the MBE CoSi₂ film revealed no holes or any other defect features. Very smooth and uniform epitaxial layers were grown by this method, as already reported in a previous study.⁶⁻⁹

Qualitative information concerning the film's crystallinity was also checked by observing the quality of electron channeling patterns taken at $E_p = 20$ keV using SEM. No pattern was observable for Co-rich silicide and CoSi, in accordance to cobalt silicides/silicon epitaxial relationships indicating that only the CoSi₂ phase can grow epitaxially on Si(111).¹⁵ For SPE and MBE CoSi₂ films, electron channeling patterns were shown broad and diffuse for the former, and sharp and bright for the latter. This result confirms the superior MBE technique for the growth of epitaxial CoSi₂ films for Si(111).

B. Silicide atomic composition ratio measurements

One part of this work was to compare the atomic concentration ratio $C[\text{Si}/\text{Co}]$ measured by AES, to that obtained by RBS. The AES technique is known only as a semiquantitative analytical technique, but well adapted to UHV systems. RBS has been used extensively as a quantitative technique in the characterization and the study of the kinetics of formation of silicides.¹⁶ In this study, SEM information was used for correcting the measured Si/Co ratios obtained by AES and RBS by subtracting the Si substrate contribution due to the holes in the silicide layers from the total Si signal. The composition ratios of the SPE samples after the area correction by SEM picture are shown in Table I. In the AES measurements, the concentration ratios have been calculated using the element sensitivity factors given in Ref. 17.

It appears from Table I that the calculated ratios by the two methods are very close for Co-rich silicides and monosilicide samples. For CoSi₂, the RBS technique gives a ratio of about 30% higher than in AES. These results must be correlated to the surface morphology observed by SEM. The concentration ratios obtained by both techniques coincide only when the films are uniform and the surface smooth, as seen in the former case. In the latter case, however, the comparison is not meaningful because of the uncertainty in the RBS results caused by the film thinness, the presence of perforations, or the formation of islands. Therefore, Auger spectroscopy

TABLE I. Calculated Si/Co concentration ratios obtained from AES and RBS results on SPE samples annealed at different temperatures T_a .

| T_a (deg C) | AES $C[\text{Si}/\text{Co}]$ | RBS $C[\text{Si}/\text{Co}]$ |
|------------------|---------------------------------|---------------------------------|
| 300 | 0.22 | 0.22 |
| 340 | 0.37 | ~0.34 |
| 470 | 1.1 | 1.2 |
| 440 | 1.0 | 1.0 |
| 650 | 1.7 | 2.1 |
| 730 | 1.9 | 2.5 |

copy was used to give the more reliable composition information for those samples which were nonuniform.

C. EELS results

Figures 1 and 2 show the EELS spectra of Co, Si, and three silicide phases, taken at $E_p = 500$ and 80 eV, respectively. All the spectra are presented in the derivative mode. The transition energies, measured at the half-height of the peaks,

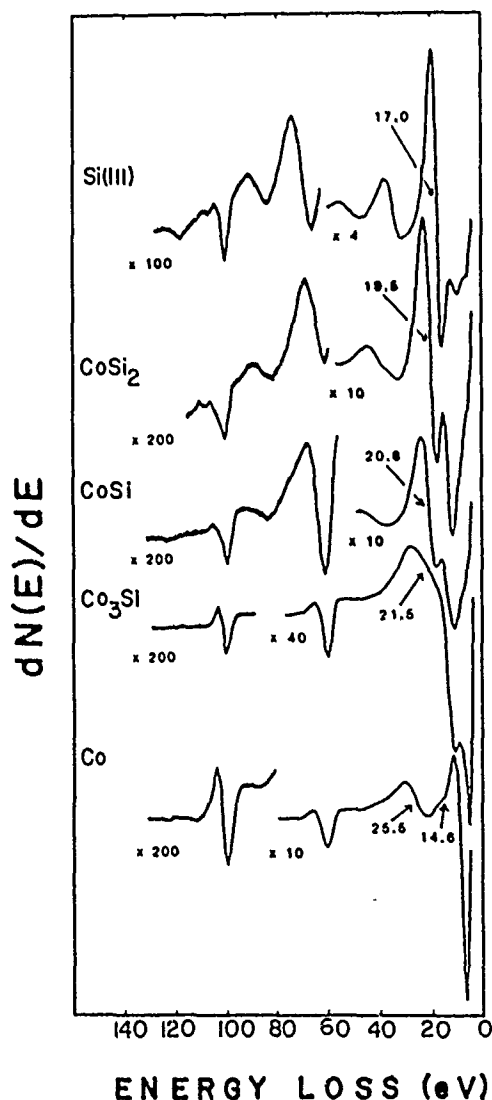


FIG. 1. EELS spectra of Co, Si, and SPE silicides taken at primary energy $E_p = 500$ eV. Spectra are presented in the derivative mode.

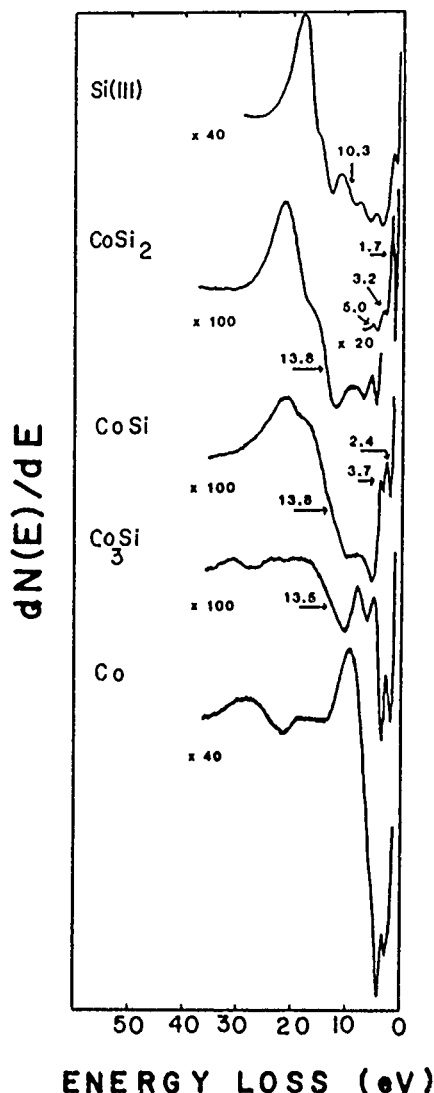


FIG. 2. EELS spectra of Co, Si, and SPE silicides taken at primary energy $E_p = 80$ eV. Spectra are presented in the derivative mode.

have been collected in Table II, for $E_p = 500$ eV, and in Table III for $E_p = 80$ eV.

Consider, first, the evolution of plasmon energies (Fig. 1) with the composition variation. For pure Co, two components of bulk plasmons are assumed, corresponding to the excitation of $4s$ and $3d$ electrons.^{18,19} As discussed in Ref. 19, using primary energy $E_p = 900$ eV, plasmon losses from polycrystalline Co surface's sample were found at 15.8 and 11 eV, respectively, associated to $3d$ and $4s$ collective electron oscillations. In our measurements, the shoulder at 14.6 eV is attributed to the $3d$ plasmon. No peak at 11 eV is observed, possibly due to the low excitation energy used. The peak at 25.5 eV is interpreted as a multiple scattering of ($4s + 3d$) plasma. For silicides only one bulk plasmon is observed and its energy decreases with increase of the Si concentration, from around 22 eV (Co-rich silicides), 20.6 (CoSi), and 19.5 ± 0.7 eV (CoSi₂). No variation of the surface plasmon energy has been found with the change of the Si concentration: $\hbar\omega_s = 13.6 \pm 0.7$ eV. The assignment of this transition to the surface plasmon was deduced from the approximate relation $\hbar\omega_s \cong \hbar\omega_p / \sqrt{2}$. For silicon, bulk and sur-

TABLE II. Transition energy values observed from EELS spectra obtained at $E_p = 500$ eV, as shown in Fig. 1.

| C[Si/Co] | | AES | | | | |
|-----------------------|------|--------|--------|--------|-----------------|-----------------|
| | | Si(2p) | Co(3s) | Co(3p) | $\hbar\omega_b$ | $\hbar\omega_s$ |
| Co | Co | | 101.3 | 61.6 | 25.5 | 14.6 |
| ~Co ₃ Si | 0.37 | | 101.5 | 61.8 | 21.7 | 13.5 |
| CoSi | 1.0 | 101.2 | | | 20.7 | 13.7 |
| SPE CoSi ₂ | 1.7 | 103.0 | | | 19.5 | 13.6 |
| MBE CoSi ₂ | 2.1 | 103.0 | | | 19.5 | 13.7 |
| Si | Si | 101.5 | | | 17.0 | 10.3 |

face plasmons are found at 17.0 and 10.3 ± 0.7 eV, respectively, the latter corresponding to the value characteristic of the (7×7) Si(111) superstructure.¹⁴

Transitions resulting from the inner shells were observed near 101 eV for Co(3s), and at about the same energy for the Si(2p) levels. The Co(3s) transition, optically forbidden, is interpreted as a quadrupole-allowed process. Multiple transitions are often well observed with electrons as primary excitation, especially if they are slow and they lose a large fraction of their energy.²⁰ The transition near 62 eV for Co and Co-rich silicides was from Co(3p). Si(2p) and Co(3s) cannot be separated with the single-pass CMA analyzer, but they can be distinguished by their shape, symmetric for Co(3s) and asymmetric for Si(2p) (Fig. 1).

Interband and surface-state transitions are best observed in Fig. 2, using a low primary energy $E_p = 80$ eV. All the transitions characteristic of the (7×7) Si(111) surface are apparent: S_1 (1.9) eV, S_2 (7.2 eV), and S_1' (14.5 eV) are related to intrinsic surface states.¹⁴ E_2 (4.8 eV) is a bulk transition. Spectra of low energy transitions from Co and silicides are rather different, and can be used as "signatures" to determine the silicide phase on the surface. The interpretation of these spectra taken at $E_p = 80$ eV, as shown in Fig. 2, was made with the help of self-consistent calculations of the CoSi₂ electronic band structure²¹ supported by ARUPS experimental investigation of the CoSi₂/Si(111) interface.¹⁰ These calculations predict a strong peak in the density of states (DOS) at 1.7 eV coming from the nonbonding states of essentially Co(3d) orbitals, and a second peak near 3.7 eV attributing to the bonding states between Co(3d) and Si(3p) orbitals. Just above E_F , the calculated s and p components of the DOS show an enhancement of the Si(3s) character.

TABLE III. Transition energy values observed from EELS spectra obtained at $E_p = 80$ eV, as shown in Fig. 2.

| C[Si/Co] | | AES | | Interband and surface-state transitions | |
|-----------------------|------|-------|-----------------|---|--------------------|
| | | S_1 | $\hbar\omega_s$ | | |
| Co | Co | | | 7.2 | 4.5/3.1 |
| ~Co ₃ Si | 0.37 | | 13.5 | 7.1 | 4.2/2.5 |
| CoSi | 1.0 | | 13.8 | ~8.2 | 6.2/3.7/2.4 |
| SPE CoSi ₂ | 1.7 | | 13.6 | ~8.8 | 7.5 |
| MBE CoSi ₂ | 2.1 | | 13.7 | ~8.7 | 7.2 |
| Si | Si | 14.5 | 10.3 | 7.2 | 4.8/1.9 |
| | | | | (S_2) | (E_2)(S_1) |

From these calculated data, we therefore interpreted the peaks at 3.2 and 5.0 eV in our CoSi₂ EELS spectra as respectively related to the electronic excitation from the nonbonding Co(3*d*) and bonding Co(3*d*)-Si(3*p*) levels to the empty Si(3*s*) level. The spectra of MBE CoSi₂ are similar to those obtained on SPE CoSi₂. In both cases the amplitude of the 1.7 eV transition is sensitive to the surface conditions, as seen by SEM and electron channeling patterns. We attribute its origin to a surface-state related transition. As shown in Ref. 10 for CoSi the nonbonding Co(3*d*) and bonding Co(3*d*)-Si(3*p*) peaks are closer in energy and shift towards the Fermi level. We thus attribute the 2.4 and 3.7 eV peaks on our CoSi spectrum to the same origins of the nonbonding and bonding states. The 2.5 eV transition on Co₃Si has been associated to the excitation of the *d* band of Co metal. Several band structures of bulk Co have been published.^{22,23} However, no obvious correlation with our EELS results could be obtained.

IV. CONCLUSION

The systematic characterization of cobalt silicide films grown by SPE and MBE on the Si(111) substrate has yielded sufficient information to enable the *in situ* composition determination by AES and EELS alone.

The atomic concentration ratio C[Si/Co] obtained by AES and RBS has been compared for different compositions. The accuracy of the RBS technique was found poorer than AES for nonuniform samples. Therefore, Auger spectroscopy was used to give the more reliable composition information for these nonuniform samples. Quite different EELS spectra were obtained for Co-rich silicides, CoSi and CoSi₂, providing an easy assessment to unambiguously distinguish the phases. The distinction between silicides was observed, first by the bulk plasmon energy value, shifting from around 22 eV (Co-rich silicides) to 20.6 (CoSi) and 19.5 ± 0.7 eV (CoSi₂), and second by the interband and surface-state transitions. For CoSi and CoSi₂ two energy transitions from our EELS spectra have been determined as excitation from filled unbonding to Co(3*d*) and Co(3*d*)-Si(3*p*) states to the empty Si(3*s*) level. Qualitative information on the surface morphology and film crystallinity for SPE and MBE CoSi₂ has been obtained by inspection of the EELS 1.7

eV transition intensity and correlated to SEM and electron channeling patterns information.

ACKNOWLEDGMENTS

This work is in part supported by the Army Research Office, the Semiconductor Research Office, and the National Science Foundation.

- ¹C. O. Bozler, G. D. Alley, R. A. Murphy, D. C. Flanders, and W. T. Lindley, IEDM Tech. Dig. 1979, 384.
- ²K. L. Wang, Solid State Technol. 28 (10), 137 (1985).
- ³J. C. Hensel, A. F. J. Levi, R. T. Tung, and J. M. Gibson, Appl. Phys. Lett. 47, 151 (1985).
- ⁴K. Ishibashi and S. Furukawa, Appl. Phys. Lett. 43, 660 (1983).
- ⁵R. T. Tung, J. C. Bean, J. M. Gibson, J. M. Poate, and D. C. Jacobson, Appl. Phys. Lett. 42, 888 (1983).
- ⁶A. H. Hamdi, M.-A. Nicolet, Y. C. Kao, M. Tejwani, and K. L. Wang, Mater. Res. Soc. Symp. Proc. 41, 355 (1985).
- ⁷L. J. Chen, J. W. Mayer, and K. N. Tu, Thin Solid Films 93, 135 (1982).
- ⁸F. Arnaud d'Avitaya, S. Delage, E. Rosencher, and J. Derrien, J. Vac. Sci. Technol. B 3, 770 (1985).
- ⁹Y. C. Kao, M. Tejwani, T. H. Xie, T. L. Lin, and K. L. Wang, J. Vac. Sci. Technol. B 3, 596 (1985).
- ¹⁰C. Pirri, J. C. Peruchetti, G. Gewinner, and J. Derrien, Phys. Rev. B 29, 3391 (1984).
- ¹¹E. Rosencher, S. Delage, and F. Arnaud d'Avitaya, J. Vac. Sci. Technol. B 3, 762 (1985).
- ¹²Y. C. Kao, Y. Y. Wu, and K. L. Wang, in Proceedings of the First International Symposium on Si Molecular Beam Epitaxy, Toronto, Canada, May 12-17, 1985 (to be published).
- ¹³A. Ishizaka, K. Nakagawa, and Y. Shiraki, in Proceedings of the Conference on Molecular Beam Epitaxy and Clean Surface Techniques (Japanese Society of Applied Physics, Tokyo, 1982), p. 183.
- ¹⁴J. E. Rowe and H. Ibach, Phys. Rev. Lett. 31, 102 (1973).
- ¹⁵A. Zur, T. C. McGill, and M.-A. Nicolet, J. Appl. Phys. 57, 600 (1985).
- ¹⁶R. T. Tung, J. M. Poate, J. C. Bean, J. M. Gibson, and D. C. Jacobson, Thin Solid Films 93, 77 (1982).
- ¹⁷Handbook of Auger Electron Spectroscopy (Physical Electronics Industries, Eden Prairie, 1978).
- ¹⁸D. L. Misell and A. J. Atkins, Philos. Mag. 27, 95 (1973).
- ¹⁹H. B. Kolodziej and B. Rozenfeld, Acta Phys. Pol. A 48, 765 (1975).
- ²⁰E. Colavita, M. De Crescenzi, L. Popagno, R. Searmozzino, L. S. Caputi, R. Rosei, and E. Tosatti, Phys. Rev. B 25, 2490 (1982).
- ²¹J. Tersoff and D. R. Hamann, Phys. Rev. B 28, 1168 (1983).
- ²²J. F. Janak, Solid State Commun. 25, 53 (1978).
- ²³D. Bagayoko, A. Ziegler, and J. Callaway, Phys. Rev. B 27, 7046 (1983).

100- μm -wide silicon-on-insulator structures by Si molecular beam epitaxy growth on porous silicon

T. L. Lin, S. C. Chen, Y. C. Kao, and K. L. Wang

Device Research Laboratory, Electrical Engineering Department, University of California, Los Angeles, California 90024

S. Iyer

IBM Thomas J. Watson Research Center, P. O. Box 218, Yorktown Heights, New York 10598

(Received 14 February 1986; accepted for publication 5 May 1986)

100- μm silicon-on-insulator structures have been achieved by first utilizing silicon molecular beam epitaxial (Si MBE) growth on porous silicon and subsequently oxidizing the porous silicon through the patterned Si MBE film windows. A Si beam method is used for the low-temperature surface cleaning of porous silicon prior to Si MBE growth. By using a two-step growth technique, the Si MBE film shows good crystallinity checked by Rutherford backscattering channeling spectroscopy and cross-sectional transmission electron microscopy. An electron mobility of 1300 $\text{cm}^2 \text{V}^{-1} \text{s}^{-1}$ with a doping concentration of $6 \times 10^{15} \text{cm}^{-3}$ has been achieved.

Silicon-on-insulator (SOI) technology is very attractive for very large scale integrated circuit (VLSI) applications because of its potential for high speed and high package density. It has been reported that porous silicon prepared from a crystalline substrate retains its crystallinity so that an epitaxial layer can be grown onto it.¹ However, if porous silicon was exposed to temperatures above 800 °C, such as during the conventional chemical vapor deposition (CVD) epitaxial growth, the structure of pores collapses and the oxidation rate is dramatically reduced.² Since silicon molecular beam epitaxy (Si MBE) can grow epifilms at temperatures as low as 600 °C,³ the technique is ideal for preparing epifilms while maintaining the porosity of the porous silicon. By using Si MBE growth on porous silicon and subsequently oxidizing the porous silicon through lithographically patterned Si windows, porous silicon can be oxidized rapidly and laterally underneath the Si MBE film due to the high oxidation rate of porous silicon; a SOI structure is then accomplished.⁴ In this letter, we report a low-temperature silicon beam surface cleaning method for porous silicon sample prior to the Si MBE growth, and a two-step Si-MBE growth technique that are used to achieve 100- μm -wide SOI islands.

Porous silicon samples are prepared as follows. *p*-type (100) wafers with resistivity of 0.01–0.02 Ωcm are chemically etched repeatedly in boiling nitric acid followed by HF dip to remove a few nanometers of surface layer. Porous silicon layers are then uniformly formed by anodizing Si samples in an HF electrolyte. Before being loaded into the ultrahigh vacuum (UHV) chamber, a protective SiO_2 layer is grown on top of the porous silicon surface using a $\text{H}_2\text{SO}_4\text{:H}_2\text{O}_2\text{:H}_2\text{O} = 4\text{:}1\text{:}4$ solution.

An atomically clean sample surface is essential for a successful epitaxial growth in MBE. After being loaded in the UHV chamber, the sample is usually preheated to a temperature higher than 800 °C prior to MBE growth so that a clean surface is obtained.⁵ However, this method is not suitable for porous Si samples since temperatures higher than 700 °C can result in the change of pore structure. A revised method using a low flux Si beam to *in situ* clean the porous silicon surface has been developed. It has been reported that below a critical flux, the Si beam reacts with SiO_2 to form SiO

which desorbs from Si/SiO₂ surface at a temperature as low as 700 °C due to its high vapor pressure.⁶ By carefully adjusting the Si beam flux, clean surface can be achieved for subsequent MBE growth. In the Si beam surface cleaning process, Si beam with a flux of $7 \times 10^{13} \text{cm}^{-2} \text{s}^{-1}$ is used and the porous silicon sample is held at 750 °C. The effectiveness of this method is checked by Auger electron spectroscopy (AES) and by the etch pit density of as-grown MBE films using Schimmel etch. Figure 1 shows the AES peak to peak amplitude ratios of both oxygen and carbon to silicon as a function of cleaning time. The oxygen peak is markedly reduced but a small value remains after even 6 min of cleaning. It should be noted, however, when this method is used to clean single-crystal Si sample, both oxygen and carbon signals reduce below the AES detection limit. We believe that these signals for the porous Si case come from the oxygen and carbon sitting on the sidewalls of the pores. They remain on the sidewall surfaces since they cannot be reached by the Si beam, and consequently should not have any effect on the following MBE growth. This is confirmed by the Rutherford backscattering spectrum (RBS) of a typical Si MBE film on porous silicon sample as shown in the inset of Fig. 2. It shows that the oxygen is present from near the MBE Si layer and porous silicon interface 0.5 μm deep into the porous silicon layer. We propose the behavior of C signal as followed.

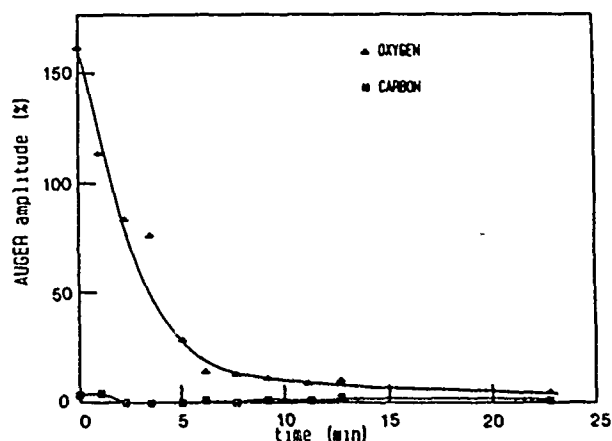


FIG. 1. Auger spectroscopy of oxygen and carbon contaminants on the surface as a function of silicon beam cleaning time.

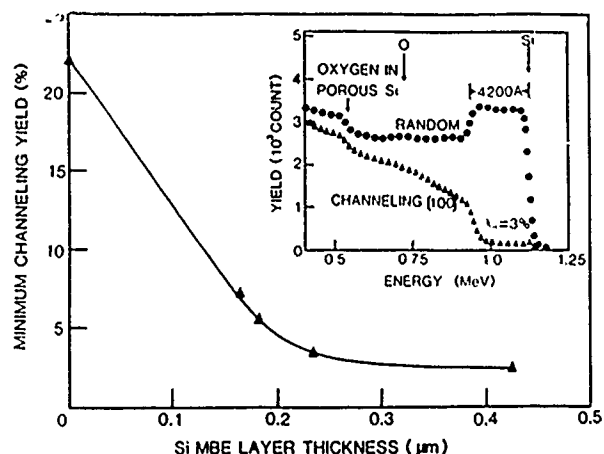


FIG. 2. Rutherford backscattering (RBS) minimum channeling yield for various silicon molecular beam epitaxial (Si MBE) film thicknesses. Inset is the RBS of a sample with 4200-Å-thick Si MBE film on porous silicon. Oxygen is observed in the porous silicon region.

When the surface layer of oxide is being etched by Si beam, the carbon sitting on it is removed. However, since the thickness of remaining oxide still exceeds the depth resolution of AES, the carbon existing in porous silicon cannot be observed. Consequently, carbon signal drops. As the oxide is getting thinner due to the etching of impinging Si beam, carbon can now be observed by AES, resulting in the increase of the carbon signal, which will eventually go down again as the oxide layer is etched and the Si epitaxial growth begins. The as-grown MBE samples are Schimmel etched for 30 s and the etch pit density is observed by Nomarski microscopy. An etch pit density of $1.7 \times 10^3 \text{ cm}^{-2}$ is obtained. Thus we demonstrate that the Si beam method is very effective for surface cleaning porous silicon in ultrahigh vacuum.

Si MBE layers are then grown on porous silicon at 750 °C immediately following the surface cleaning to avoid any recontamination by the residual gases in the UHV chamber. A two-step growth technique is used for the first layer of 500-Å thickness grown at a lower rate (0.2 Å s^{-1}) followed by a second layer at a higher growth rate (2 Å s^{-1}). The base pressure of the MBE system is 2×10^{-10} Torr and the pressure during the growth is below 2×10^{-9} Torr. Figure 2 shows the minimum channeling yield of the Rutherford backscattering channeling spectra as a function of Si MBE film thickness. The inset illustrates the RBS channeling spectrum for a sample having a 0.42-μm-thick Si MBE film grown on porous silicon; a minimum yield X_m of 3% is identical to that of single-crystal silicon. The minimum channeling yield is greatly improved after a Si MBE layer was grown on the porous silicon compared to the virgin porous silicon which has a minimum yield of 22.4%. The film crystallinity improves further as the Si MBE film thickens, as the thickness of the Si MBE film exceeds 0.24 μm, the minimum yield indicates that the crystallinity of the Si MBE film is close to that of ideal single-crystal Si. Figure 3(a) shows the cross-sectional transmission electron microscopy (TEM) picture of the interface of the Si MBE film and porous silicon. The Si MBE film is shown to have a high crystallinity although some microdefects are present near the interface. The electron mobility of the *n*-type Si MBE film which is electrically isolated from the *p*-type porous silicon

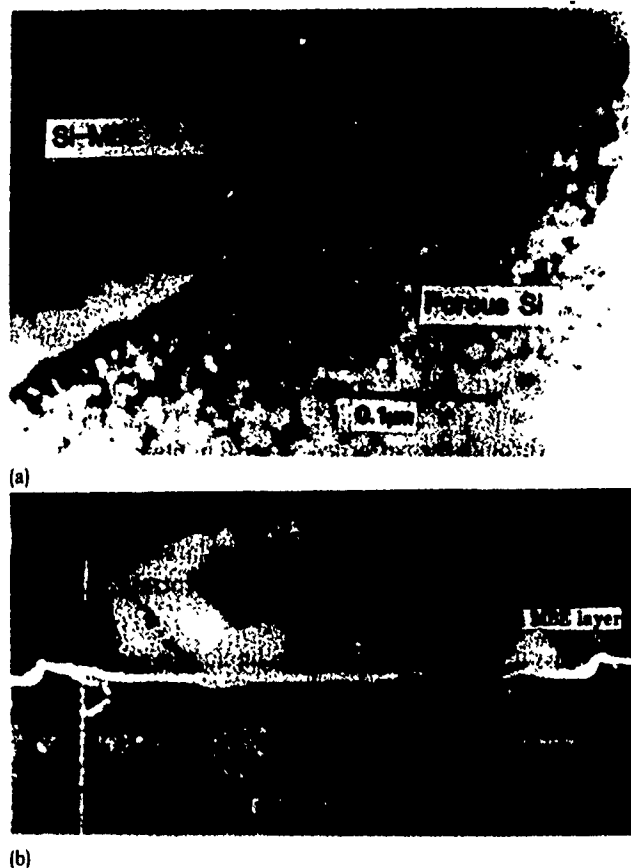


FIG. 3. (a) Cross-sectional TEM picture of the interface between the Si MBE film and porous silicon. (b) A 100-μm-wide Si MBE island is completely isolated by the oxidized porous silicon.

substrate is measured by the van der Pauw method. An electron mobility as high as $1300 \text{ cm}^2 \text{ V}^{-1} \text{ s}^{-1}$ was obtained for an antimony-doped Si MBE film with a doping concentration of $6 \times 10^{15} \text{ cm}^{-3}$ which is accomplished during Si MBE growth with a Sb Knudsen cell heated at 430 °C.

The SOI structure is fabricated as followed. The samples are wet oxidized at 750 °C to grow a 500-Å-thick SiO_2 layer. Then, 2000-Å-thick Si_3N_4 is deposited on the SiO_2 layer by low pressure chemical vapor deposition (LPCVD). After lithographical patterning, Si islands are formed by removing Si_3N_4 , SiO_2 , and the Si MBE film using plasma etching, buffered hydrofluoric acid, and reactive ion etching, respectively. Then the samples are wet oxidized at 900 °C for 4 h. During the oxidation, the porous silicon is oxidized through the window openings and the oxidation fronts moved laterally and rapidly underneath the Si MBE film until they met. Therefore, the Si MBE islands are completely isolated by SiO_2 and the SOI structures are accomplished. A cross-sectional scanning electron microscope (SEM) picture of a 100-μm-wide SOI structure is shown in Fig. 3(b). The nonplanarity near the window openings is mainly due to the volume expansion of the porous silicon after oxidation. This effect can be minimized by adjusting the porosity of the porous silicon to 0.55, so that the pore volume is completely filled by SiO_2 after oxidation. The dimensions of the SOI structures are limited by the drastic reduction of porous silicon oxidation rate due to the collapse of porous structure during the 900 °C oxidation process. An alternative oxida

tion technique which consists of two oxidation stages is now under study to further extend the dimensions of SOI structures.

In conclusion, a silicon beam method has been successfully used as a low-temperature surface cleaning method for porous silicon prior to Si MBE growth. RBS shows that the tail of the AES oxygen signal is due to residual oxygen sitting on the pore walls which cannot be reached by Si beam, and consequently should not have any effect on the following Si MBE growth. The etch pit density of the as-grown Si MBE film is below $1.7 \times 10^3 \text{ cm}^{-2}$. The RBS channeling spectrum of the Si MBE film on porous silicon has a minimum yield of 3% indicating a good crystallinity. The crystallinity of the Si MBE film on porous silicon samples improves as the Si MBE

film thickens. An electron mobility of $1300 \text{ cm}^2 \text{ V}^{-1} \text{ s}^{-1}$ is measured by the van der Pauw method for an antimony doping concentration of $6 \times 10^{15} \text{ cm}^{-3}$. SOI islands as large as $100 \mu\text{m}$ wide are successfully fabricated.

This work is supported in part by the Army Research Office and the Semiconductor Research Cooperation.

¹T. Unagami and M. Seki, J. Electrochem. Soc. **125**, 1339 (1978).

²T. Unagami, Jpn. J. Appl. Phys. **19**, 231 (1980).

³M. Tabe, K. Arai, and H. Nakamura, Jpn. J. Appl. Phys. **20**, 703 (1981).

⁴S. Konaka, M. Tabe, and T. Sakai, Appl. Phys. Lett. **41**, 86 (1982).

⁵A. Ishizaka, K. Nakagawa, and Y. Shiraki, *Proceeding of Conference on Molecular Beam Epitaxy and Clean Surface Techniques* (Japanese Society of Applied Physics, Tokyo, Japan, 1982), p. 183.

⁶M. Tabe, Jpn. J. Appl. Phys. **21**, 534 (1982).

New silicon-on-insulator technology using a two-step oxidation technique

T. L. Lin and K. L. Wang

Device Research Laboratory, Department of Electrical Engineering, University of California, Los Angeles, California 90024

(Received 19 May 1986; accepted for publication 29 August 1986)

Large silicon-on-insulator (SOI) structures have been obtained using a new two-step oxidation technique on a silicon molecular epitaxial film grown onto a porous silicon sample. The first low-temperature oxidation step oxidizes the large-pore silicon underlayer to avoid the collapse of the porous structure and thus secure the lateral oxygen supply channels in the porous oxide. In the second step, a higher temperature is used to oxidize the remaining porous silicon and the bottom part of the Si molecular beam epitaxy overlayer with the oxygen supplied through the oxidized porous silicon underlayer. A new porous silicon structure used is composed of a top porous silicon layer which has a smaller porosity for the ease of subsequent silicon epitaxial growth, and a second layer with a larger porosity which not only gives oxygen supply channels during the SOI oxidation but also allows the volume expansion of the porous silicon oxide to be accommodated. SOI sizes of $325\ \mu\text{m} \times 2\ \text{mm}$ have been successfully fabricated. The breakdown voltage of the SOI structures is about 400 V and the leakage current densities between the SOI layer and the substrate are below $3\ \text{nA cm}^{-2}$ with a 10-V bias. *n*-channel metal-oxide-silicon field-effect transistors have been fabricated on the SOI structures with good characteristics, indicating that this technology may be suitable for very large scale integrated circuits applications.

Silicon-on-insulator (SOI) structures have been fabricated by utilizing the high oxidation properties of porous silicon.¹ However, the widths of the SOI structures are limited by the isotropic nature of porous silicon formation. Some approaches have been taken to increase anisotropy formation of porous Si for larger SOI structures, either by introducing a p^+ epilayer² or by utilizing the electrical breakdown phenomenon between the hydrofluoric acid electrolyte and an n^+ epilayer³ to confine the formation of porous Si inside the p^+ or n^+ epilayer. The width of structures has been thus improved to $45\ \mu\text{m}$.³ An alternative approach utilizing silicon molecular beam epitaxial (Si MBE) growth on porous Si has been used to increase the SOI size.^{4,5} In the latter approach, porous silicon is first uniformly formed by anodizing p^+ silicon wafer in hydrofluoric acid electrolyte. Since porous Si remains single crystalline after being made, an epitaxial Si layer can be grown onto the porous Si. After patterning the Si islands, the samples are wet oxidized and SOI structures as wide as $100\ \mu\text{m}$ are obtained.⁵ Si MBE is utilized so that Si epitaxial layers can be grown on porous Si at a low temperature (750°C). Since the porous structure collapses after exposure to temperatures higher than 800°C , the complete oxidation of porous silicon becomes difficult.⁶ With its unique attribute of low growth temperature,⁷ Si MBE is thus ideal for the Si epitaxial growth on porous silicon. Integrated circuits as well as discrete devices fabricated in Si MBE layers have been reported.⁸⁻¹² Si MBE films grown on porous silicon have been previously demonstrated to have a good crystallinity and low dislocation densities.⁵

In all the previous oxidized porous silicon (OPS) SOI approaches, the porous silicon is oxidized to form the insulating oxide of the SOI structure. This process often results in excessive wafer warpage and defect development in the silicon islands due to the volume expansion of the porous

silicon oxide.⁸ Since the porous silicon layers are formed prior to Si MBE growth in our approach, the porous silicon structures can be optimized to allow proper oxygen flow and thus the SOI size can be increased. Similarly, the volume expansion of the porous silicon oxide can be reduced. In this study, a new two-layer porous silicon structure is used. The top porous silicon layer has a smaller porosity for the ease of the subsequent epitaxial growth and forms a dense oxide layer after the SOI oxidation as part of the insulating layer. The second porous silicon layer has a larger porosity ($> 55\%$) and oxygen flows readily through the pores during oxidation so that the bottom part of the Si MBE overlayer can be uniformly oxidized. The specific thicknesses and the porosities of the porous silicon layers can be selected by the anodizing time, the HF (hydrofluoric acid) concentration, and the anodizing current density. Figure 1 shows the porosities of the porous silicon layers fabricated from p^+ wafers for various anodizing current densities and HF concentra-

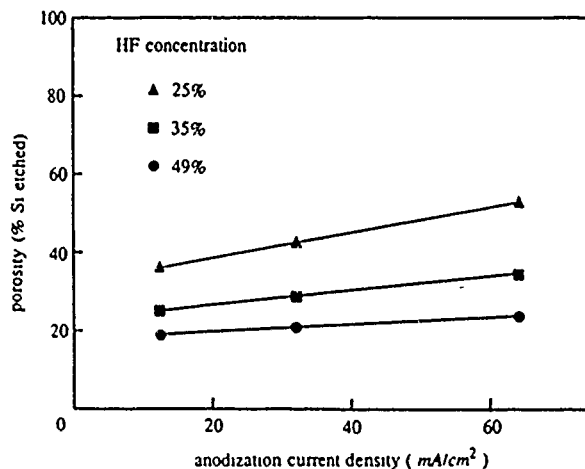


FIG. 1 Porosity of porous Si for various anodizing current density and HF concentrations.

tions. By proper control of the porosity, larger SOI sizes can be accomplished. The volume expansion of the porous silicon oxide can also be accommodated in this porous silicon layer due to its large porosity. To accomplish this goal, a two-step oxidation technique is used. The first low-temperature oxidation step oxidizes the porous silicon underlayer to avoid the collapse of the porous structure and thus the lateral oxygen supply channels in the porous oxide are secured. In the second oxidation step, a higher temperature is used to oxidize the bottom part of the Si MBE overlayer with oxygen flowing through the porous oxide. SOI structures as wide as $325\text{ }\mu\text{m}$ have been successfully fabricated, and the size is apparently limited by the largest mask feature available. Ultimately, the size is limited by the lateral diffusion of oxygen through the porous layers.

The porous silicon samples are fabricated as followed. Si (100) wafers with a resistivity of $0.01\text{--}0.02\text{ }\Omega\text{ cm}$ are anodized in 30% HF electrolyte. The porosity of the porous Si can be varied by adjusting either the HF concentration or the anodizing current density as shown in Fig. 1. The two porous Si layers are prepared by using two different anodizing current densities. First, an anodizing current density of 13 mA cm^{-2} is used for 30 s and then the anodizing current density is increased to 130 mA cm^{-2} . After the formation of the porous silicon layers, a protective thin oxide is chemically grown on the sample surface and the sample is loaded into the ultrahigh vacuum (UHV) MBE chamber.

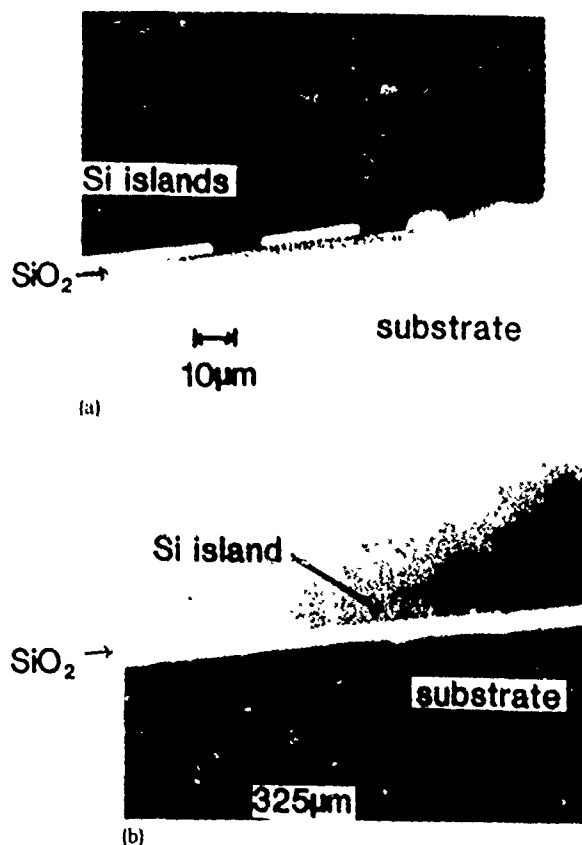


FIG. 2. (a) $325\text{-}\mu\text{m}$ -wide Si MBE island is completely isolated by the oxidized porous Si. (b) Cross-sectional picture of SOI structures with various widths.

A Si MBE layer $1.75\text{ }\mu\text{m}$ thick is grown on the porous Si in the UHV chamber with a base pressure of 2×10^{-10} Torr and a growth pressure below 2×10^{-9} Torr. A growth temperature of $750\text{ }^{\circ}\text{C}$ is used to assure that the high oxidation rate of porous Si is preserved. A low-temperature surface cleaning method⁵ which involves the use of a low flux S molecular beam is employed to clean the porous silicon surface. The MBE growth immediately follows the surface cleaning to avoid any recontamination by residue gases inside the UHV chamber. The Si MBE layer is then patterned to form Si islands 2 mm long and of various widths by reactive ion etching, and part of the porous silicon is exposed for subsequent oxidation. The SOI structures are formed by wet oxidizing the samples at $750\text{ }^{\circ}\text{C}$ for 2 h, followed by a second oxidation step at $950\text{ }^{\circ}\text{C}$ for two more hours. After oxidation, the sample is annealed in N_2 for 20 min. Metal-oxide-silicon field-effect transistors (MOSFET's) are fabricated on the SOI islands using standard n^+ polycrystalline silicon polysilicon gate process with a 40-nm -thick gate oxide.

The cross-sectional view of the SOI structure is shown in Fig. 2(a). SOI structures $325\text{ }\mu\text{m}$ wide and 2 mm long are completely isolated by SiO_2 . In Fig. 2(b), SOI structures with widths of 5, 10, 25, and $50\text{ }\mu\text{m}$ are shown. Figure 2(b) clearly demonstrates that the surfaces of the SOI structures are planar. In Fig. 3(a), the cross-sectional scanning electron microscope (SEM) picture shows that the bottom part of the Si MBE layer near the porous silicon interface is uniformly oxidized and, as a consequence, the Si/ SiO_2 interface moves from the epi-Si/porous silicon interface into the bulk of Si MBE layer, resulting in improved electrical properties of the Si/ SiO_2 interface. This is demonstrated by the low source-drain leakage currents ($<1\text{ pA}$) of the SOI MOSFET's with channel width and length of $20\text{ }\mu\text{m}$ and $5\text{ }\mu\text{m}$, respectively.

As shown in Fig. 3(b), the lower portion of the oxide is porous due to its original large porosity. This porous oxide provides channels for oxygen supply during the SOI oxidation process, so that the bottom of the Si MBE layer can be uniformly oxidized. As a result, identical oxide thicknesses of the top part and the bottom part of the Si MBE layer are obtained ($0.33\text{ }\mu\text{m}$). The uniformity of the oxide at the Si MBE bottom layer across the SOI structures is shown in Fig. 3(a). The maximum SOI dimension ($325\text{ }\mu\text{m}$) accomplished in this study is only limited by the largest feature of the present mask size, and by no means presents the ultimate size limit of the SOI dimension achievable by this approach. The maximum size of SOI structures will thus depend on the oxygen supply capability of the porous oxide during the SOI fabrication process, which in turn is determined by the porous structures of the porous Si as well as by the oxidation conditions.

However, the porous property of the underlying oxide may cause some problems during subsequent IC fabrication processes since it can be etched off easily by HF. Lift-off of the SOI Si MBE layer has been occasionally observed during the oxide etching process because of the high etching rate of the porous oxide. This problem is solved by depositing a protective Si_3N_4 layer on the porous oxide.

A breakdown voltage of 400 V was measured for all the

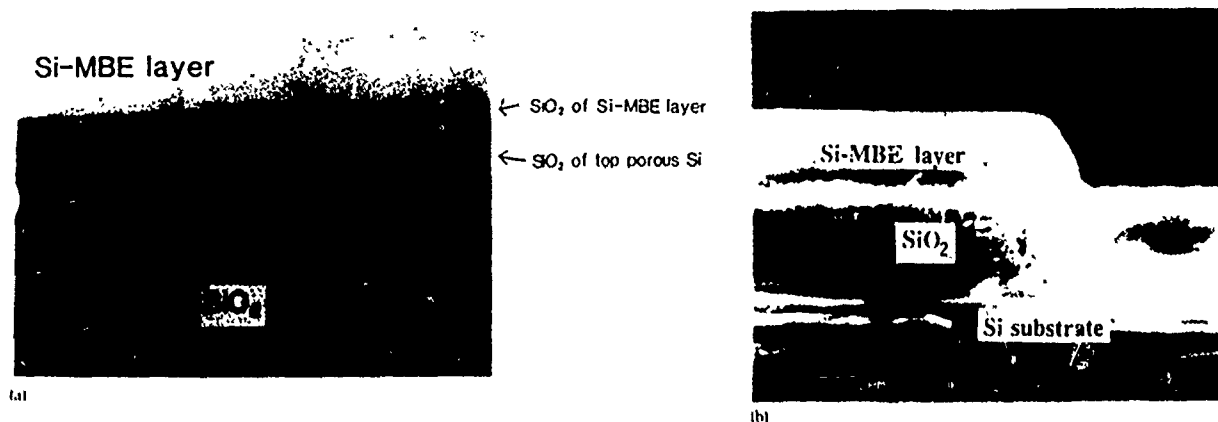


FIG 3 (a) Cross-sectional SEM picture shows that the bottom of Si MBE layer is uniformly oxidized. (b) The oxide of the second layer is porous.

SOI structures on the substrate. Leakage current densities between the SOI structure and the substrate are below 3 nA cm^{-2} with a 10-V bias measured for SOI structures of $325 \mu\text{m} \times 2 \text{ mm}$. The results indicate good insulating properties of the insulating layers which consist of both the porous silicon oxide and the oxide of the Si MBE bottom layer.

Figure 4 shows the current-voltage characteristics of a fabricated SOI *n*-channel MOSFET with channel width and length of $20 \mu\text{m}$ and $5 \mu\text{m}$, respectively. The gate oxide thickness is 40 nm. The source to drain leakage current is below 1 pA with V_{ds} of 0.05 V. The "kink" effect observed at higher values of V_{ds} is typical of the SOI device with a floating substrate. The electron field-effect mobility calculated by the conductance in the triode region is $730 \text{ cm}^2 \text{ V}^{-1} \text{ s}^{-1}$.

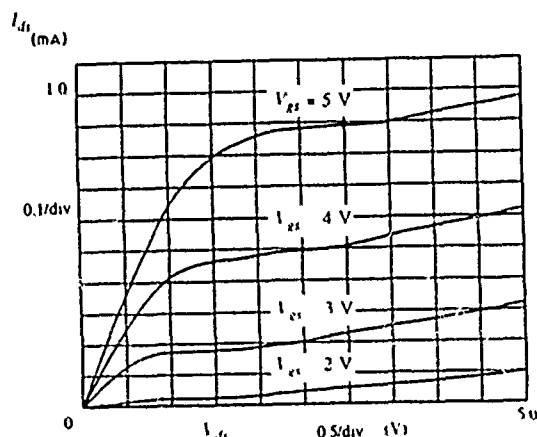


FIG. 4. Current-voltage characteristics of an SOI *n*-channel MOSFET with a channel width and channel length of $20 \mu\text{m}$ and $5 \mu\text{m}$, respectively.

In conclusion, SOI structures with dimensions of $325 \mu\text{m} \times 2 \text{ mm}$ have been successfully fabricated. The cross-sectional view shows that the surfaces of both SOI islands and insulating oxide are flat, suggesting volume expansion during oxidation is accommodated by the pores. The porous oxide provides adequate channels for oxygen supply during the SOI oxidation, so that the bottom part of the Si MBE layers is uniformly oxidized. The result suggests that still larger SOI dimensions could be accomplished by using this two-step oxidation technique. A breakdown voltage of 400 V and leakage current densities below 3 nA cm^{-2} with a 10-V bias indicate good insulating properties. MOSFET's have been fabricated on the SOI islands with good characteristics suggesting that this technology is suitable for very large scale integrated circuit applications.

This work is supported in part by the Semiconductor Research Corporation and the Army Research Office.

- ¹K. Imai, IEEE Trans. Electron Devices ED-31, 297 (1984).
- ²L. A. Nesbit, Int. Electron. Devices Meeting Tech. Dig. 800 (1984).
- ³R. P. Holmstrom and J. Y. Chin, Appl. Phys. Lett. 42, 386 (1983).
- ⁴S. Konaka, M. Tabe, and T. Sakai, Appl. Phys. Lett. 41, 86 (1982).
- ⁵T. L. Lin, S. S. Chen, Y. C. Kao, K. L. Wang, and S. Iyer, Appl. Phys. Lett. 48, 1973 (1986).
- ⁶T. Unagami and M. Seki, J. Electrochem. Soc. 125, 1339 (1978).
- ⁷J. C. Bean, Int. Electron. Devices Meeting Tech. Dig. 6 (1981).
- ⁸R. G. Swartz, G. M. Chin, A. M. Voshchenkov, P. Ko, B. A. Wooley, S. N. Finegan, and R. H. Bosworth, IEEE Electron Device Lett. EDL-5, 29 (1984).
- ⁹C. A. Goodwin and Y. Ota, IEEE Trans. Electron Devices ED-26, 1796 (1979).
- ¹⁰Y. Katayama, Y. Shiraki, K. L. I. Kobayashi, K. F. Komatsubara, and N. Hashimoto, Appl. Phys. Lett. 34, 740 (1979).
- ¹¹R. G. Swartz, J. H. McFee, P. Grabbe, and S. N. Finegan, IEEE Electron Device Lett. EDL-2, 293 (1979).
- ¹²W. C. Ballamy and Y. Ota, Appl. Phys. Lett. 39, 629, (1981).

Boron oxide interaction with silicon in silicon molecular beam epitaxy

E. de Frésart, S. S. Rhee, and K. L. Wang

Device Research Laboratory, Electrical Engineering Department, University of California at Los Angeles, Los Angeles, California 90024

(Received 13 May 1986; accepted for publication 7 August 1986)

B_2O_3 decomposition by reaction with Si has been studied *in situ* by Auger electron spectroscopy in a Si molecular beam epitaxy environment as a function of the silicon flux ($0 < J_{Si} < 14.5 \text{ Å/min}$) and the growth temperature ($25^\circ\text{C} < T_s < 800^\circ\text{C}$). Quantitative analysis of Auger signals indicates that oxygen is associated with both SiO_2 and B_2O_3 . Below a critical substrate temperature ($T_s < 500^\circ\text{C}$), no reaction occurs between B_2O_3 and Si. When the substrate temperature is higher than 500°C , the atomic fraction of Si and B increases while that for SiO_2 and B_2O_3 decreases. The chemical reaction which causes the signal changes is thermally activated, as shown by the dependence of the oxygen on boron concentration ratio, $I[O/B]$, which drops rapidly according to an Arrhenius relation with an activation energy $E_a = 4.5 \pm 1.0 \text{ eV}$. From the experimental results, we propose a model which involves B_2O_3 reduction by Si to form the (Si-B) and SiO_2 phases. SiO_2 is then decomposed by Si bombardment on the surface to produce SiO which subsequently desorbs.

Recently, it has been reported that boron doping of Si in molecular beam epitaxy can be accomplished using B_2O_3 as a source material from an effusion cell.^{1,2} The authors have demonstrated the ability of using this technique to obtain films having a high doping level ($7 \times 10^{19} \text{ cm}^{-3}$) with an abrupt doping profile. Furthermore, the oxygen content observed in the epilayers was shown to be below the secondary ion mass spectroscopy detection limit ($1 \times 10^{18} \text{ cm}^{-3}$). In these studies, the sticking coefficient and boron incorporation probability were found constant in the growth temperature range between 550 and 800°C .

In this work, we investigated the decomposition reaction of B_2O_3 by Si and the escape of oxygen during growth as a function of the silicon flux (J_{Si}) and the substrate temperature (T_s). The films have been grown in a Si molecular beam epitaxy system (Si MBE) under ultrahigh vacuum conditions (base pressure 1×10^{-10} Torr). Surface atomic fractions were probed *in situ* by Auger electron spectroscopy (AES) using a single pass cylindrical mirror analyzer from

Physical Electronics.

In experiments, *n*-type (100) Czochralski silicon wafers with resistivities ranging from 1 to 20 Ω cm were used. The wafers were chemically cleaned in a series of degreasing, oxidizing, and reducing solutions.¹ A protective oxide layer was left prior to transferring the sample into the MBE system. The oxide layer was then *in situ* thermally removed by heating the sample at 900°C for 10 min . The substrate temperature was measured using an optical pyrometer itself being calibrated by detecting the melting point of an aluminum piece stuck on a Si sample. The silicon deposition source is a 12 kW electron beam evaporator from Temescal Company. The Si flux was monitored by a quartz crystal sensor. Boron oxide was evaporated from an effusion cell. In all the measurements, the system pressure never exceeded 5×10^{-9} Torr.

Two sets of experiments were performed on two different substrates to study the dependence of the atomic surface concentrations on the silicon flux and the growth tempera-

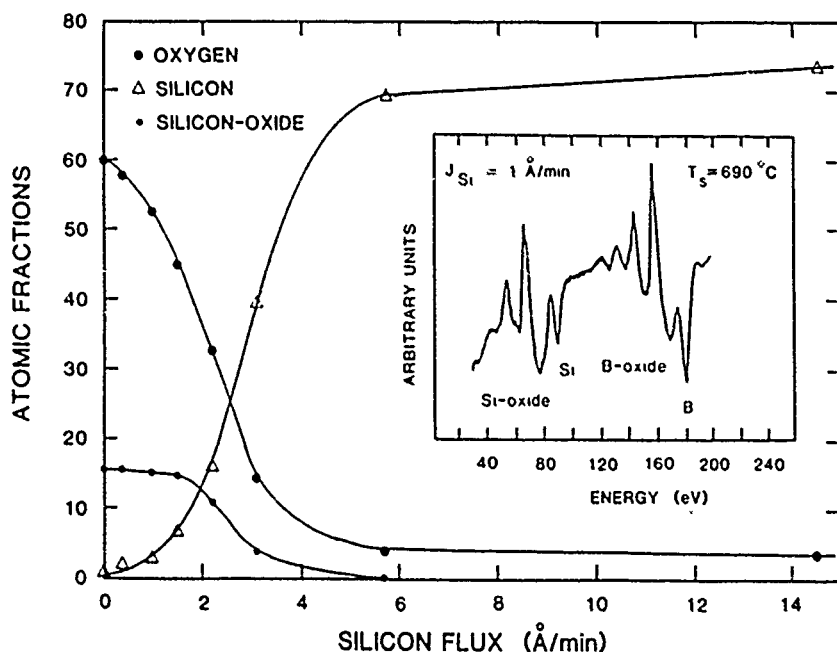


FIG 1. Evolution of the Si, Si oxide, and O atomic fractions (in percent) as a function of the silicon flux ($0 < J_{Si} < 14.5 \text{ Å/min}$). The growth temperature ($T_s = 690^\circ\text{C}$) and the boron oxide flux ($J_B \approx 0.6 \text{ Å/min}$) were kept constant. Inset: Auger spectrum, taken for $J_{Si} = 1 \text{ Å/min}$, showing the Si oxide (76 eV), Si (92 eV), B oxide (171 eV), and B (182 eV) transitions. The residual oxygen signal observed for high Si fluxes is probably due to surface contamination during AES data acquisition.

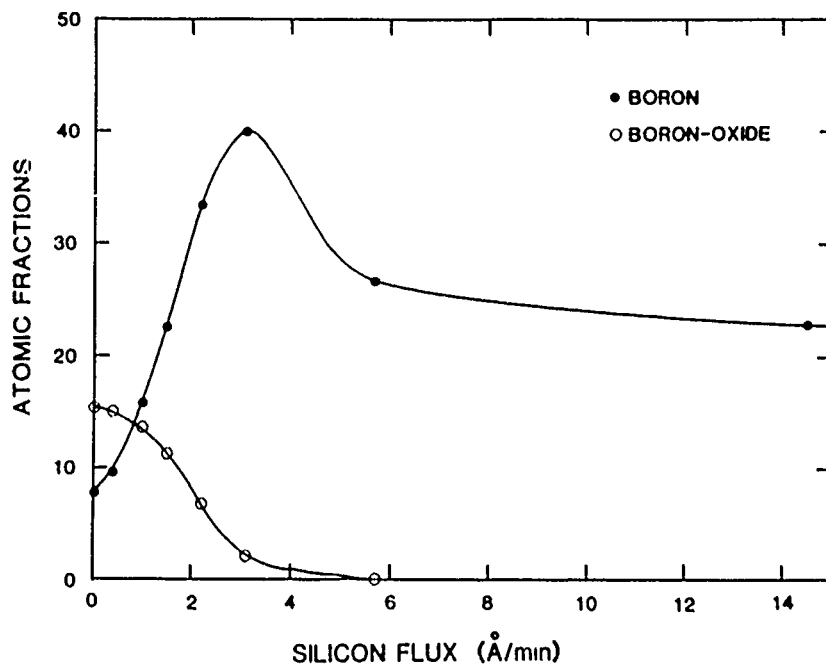


FIG. 2. Evolution of the B and B oxide atomic fractions (in percent) as a function of the silicon flux. The growth conditions are the same as in Fig. 1.

ture. In the first set, J_{Si} was varied from 14.5 to 0 Å/min, while the dopant flux J_d and the substrate temperature T_s were kept constant (boron oxide cell temperature $T_c = 1040^\circ\text{C}$, $J_d \approx 0.6$ Å/min, $T_s = 690^\circ\text{C}$). In the second set, Si and dopant fluxes are kept constant ($J_{Si} = 14$ Å/min, $T_c = 1070^\circ\text{C}$) while T_s is varied from 800 to 25 °C. In both cases, a pure silicon layer (with a thickness of 30–10 Å and 60 Å for the first and second cases, respectively) was deposited in order to separate the previously co-deposited layers ($\text{Si-B}_2\text{O}_3$) to ensure a reproducible fresh starting condition for the subsequent experiments. All the Auger data were obtained after quenching the sample to near room temperature.

A typical Auger spectrum is shown in the inset of Fig. 1 for the first set of experiments with $J_{Si} = 1$ Å/min and $T_s = 690^\circ\text{C}$. We can clearly discriminate the transitions of pure (92 eV) and oxidized (76 eV) silicon⁴ as well as elemental (182 eV) and oxidized (171 eV) boron.⁵ From these

spectra, atomic fractions of silicon and boron, as well as their oxides and oxygen, have been calculated using the sensitivity factors given in Refs. 4 and 5. Results have been plotted as a function of the silicon flux as shown in Fig. 1 for Si, Si oxide and O, and in Fig. 2 for B and B oxide. At this growth temperature (690 °C) and for $J_{Si} = 0$ Å/min, B_2O_3 reacts with the substrate and decomposes to form Si oxide (16% of the total surface concentration) and elemental boron (8%) phases. When J_{Si} increases, B_2O_3 decomposition accelerates and the atomic fraction values change as shown in Fig. 2. Practically, for this set of experimental conditions, ... the reaction between Si and B_2O_3 is completed for the Si flux below 3 Å/min. For $J_{Si} = 3$ Å/min, B oxide, oxygen, and Si oxide represent only a few percent of the surface composition. At this low flux range, the boron fraction first increases along with that of silicon at the expense of the boron oxide concentration, then passes through a maximum, and, finally decreases as illustrated in Fig. 2. The maximum is due to the

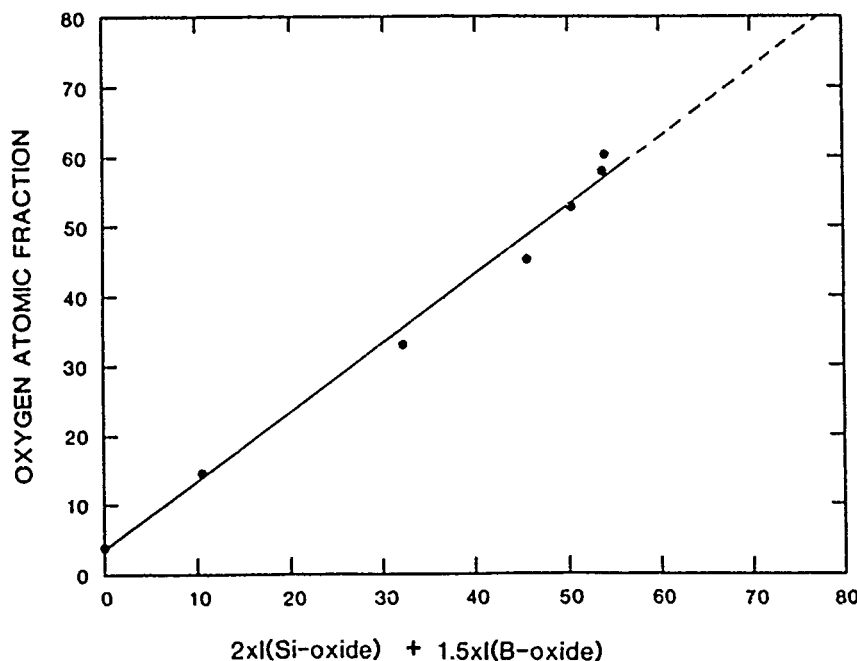


FIG. 3. Relation between the oxygen atomic fraction (in percent) and the sum of $2 \times I[\text{Si oxide}] + 1.5 \times I[\text{B oxide}]$, assuming that the Auger Si oxide and B oxides transitions are associated to SiO_2 and B_2O_3 . Results are calculated from Figs. 1 and 2.

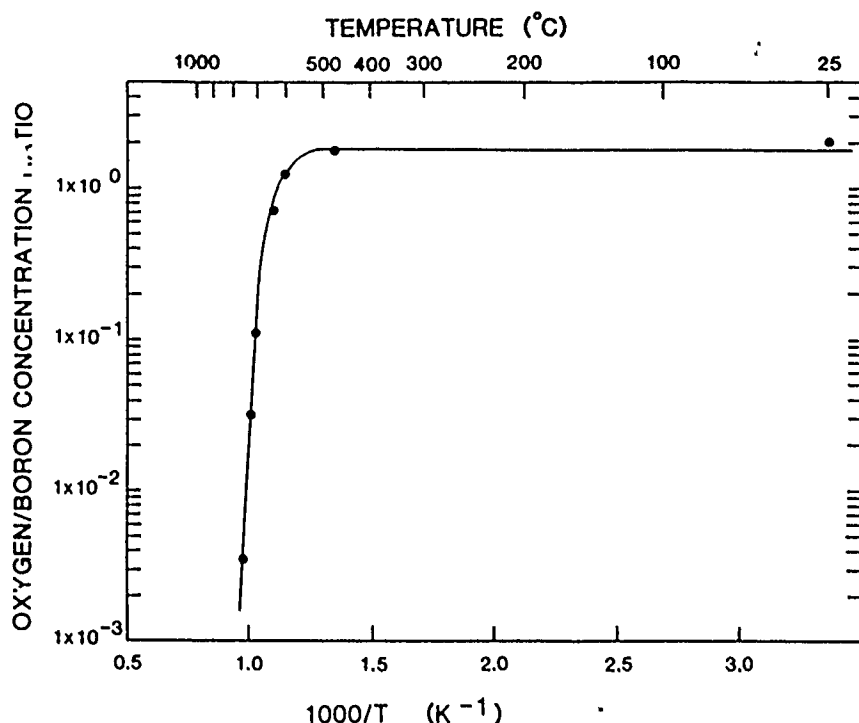


FIG. 4. Arrhenius plot of the oxygen/boron concentration ratio for the growth temperature range $25^{\circ}\text{C} < T_s < 800^{\circ}\text{C}$. The Si/dopant flux ratio was kept constant around the value $J_s/J_d \approx 20$.

fact that B_2O_3 is completely reduced by the silicon flux. This oxygen and Si oxide removal from the surface is most probably realized by desorption of SiO , after decomposition of the SiO_2 phase into SiO by Si. The removal of SiO_2 resulting from the reaction with the impinging Si or with substrate Si has already been studied⁶ and this technique is presently used in Si MBE as a low-temperature cleaning method.⁷ Oxygen is distributed between SiO_2 and B_2O_3 , as evidenced from the Auger transitions at 76 eV and 171 eV which are associated with Si oxide and B oxide, respectively. The oxygen concentration can be plotted as a function of the relation: $2 \times I[\text{Si oxide}] + 1.5 \times I[\text{B oxide}]$. Figure 3 shows a linear relation with a unity slope, suggesting that almost all the oxygen is associated with SiO_2 and B_2O_3 . An apparent residual oxygen concentration at the origin of Figure 3, i.e., a gap of 3.5% on the surface concentration observed between the fitted line and a line passing by the origin, is probably due to oxygen contamination during data acquisition.

The temperature effect on the reduction of B_2O_3 by Si was studied by the same AES technique. Results are presented in Fig. 4 where the oxygen/boron concentration ratio $I[\text{O/B}]$ is plotted as a function of the inverse of the growth temperature. The sum of the two boron phases (B + B oxide) was taken for the boron concentration. In this measurement, the dopant-to-silicon flux ratio was approximately 1/20. In the low-temperature region ($T_s < 500^{\circ}\text{C}$), $I[\text{O/B}] = 1.5$ remains constant. Its value corresponds to the stoichiometric B_2O_3 ratio. No chemical reaction is seen between Si and B_2O_3 and the oxide is imbedded in the silicon layer. In the second temperature region ($T_s > 500^{\circ}\text{C}$), $I[\text{O/B}]$ decreases rapidly according to an Arrhenius relation. The activation energy has been calculated to be $E_a = 4.5 \pm 1.0$ eV. Several kinetic phenomena are accountable for this activation energy. B_2O_3 decomposition and SiO_2 formation by chemical reaction with Si, SiO_2 decomposition and SiO desorption.

In conclusion, a study of B_2O_3 reduction resulting from

reaction with the silicon beam has been performed as a function of the silicon flux and the growth temperature. The Auger observations show the following. (1) Distinct Auger peaks for elemental and oxide phases. Oxygen when detected is essentially associated with SiO_2 and B_2O_3 . (2) Below a critical temperature ($T_s < 500^{\circ}\text{C}$), no chemical reaction occurs between Si and B_2O_3 . (3) For $T_s > 500^{\circ}\text{C}$, B_2O_3 is reduced by chemical reaction with impinging Si and substrate Si to form the (Si-B) and SiO_2 phases. (4) Both phases evolve according to a sigmoidal reaction curve as a function of J_s , increasing for (Si-B) and decreasing for SiO_2 . (5) SiO_2 is decomposed by the Si bombardment to produce SiO which in turn desorbs. (6) The overall decomposition/desorption kinetics is thermally activated above the critical temperature as shown by the Arrhenius behavior of the $I[\text{O/B}]$ concentration ratio. The activation energy is found to be $E_a = 4.5 \pm 1.0$ eV. (7) Extrapolation of the data for sufficient high temperature ($T_s > 600^{\circ}\text{C}$) and high Si flux, such as these used in realistic Si MBE growth conditions, indicates that only the (Si-B) phase remains in the layer. This makes the B_2O_3 effusion cell source a good candidate to grow high-doped p-type epilayer in Si molecular beam epitaxy.

This work is supported in part by the Semiconductor Research Corporation and the Army Research Office.

¹H. Aizaki and T. Tatsumi, *Extended Abstracts of the 17th Conference on Solid State Devices and Materials* (The Japan Society of Applied Physics, Tokyo, 1985), p. 297.

²R. M. Ostrom and F. G. Allen, *Appl. Phys. Lett.* **48**, 221 (1986).

³A. Ishizaka, K. Nagakawa, and Y. Shiraki, *Proceedings of the 2nd International Symposium on Molecular Beam Epitaxy and Related Clean Surface Techniques*, Tokyo, Japan, 1982, p. 183.

⁴L. E. Davis, N. C. MacDonald, P. W. Palmberg, G. E. Riach, and R. E. Weber, *Handbook of Auger Electron Spectroscopy*, 2nd ed. (Physical Electronics, Eden Prairie, 1976).

⁵D. J. Joyner and D. M. Hercules, *J. Chem. Phys.* **77**, 1095 (1980).

⁶M. Tabe, *Jpn. J. Appl. Phys.* **21**, 534 (1982).

⁷Y. Hirofujii, N. Matsuo, and K. Kugimiya, *Extended Abstracts of the 17th Conference on Solid State Devices and Materials* (The Japan Society of Applied Physics, Tokyo, 1985), p. 297.

Summary Abstract: Reflection high-energy electron diffraction observation of molecular-beam epitaxially grown $\text{Ge}_x\text{Si}_{1-x}$ on Si(111)

T. W. Kang, C. F. Huang, R. P. G. Karunasiri, J. S. Park, C. H. Chern, and K. L. Wang
Device Research Laboratory, University of California, Los Angeles, Los Angeles, California 90024-1600

(Received 5 September 1987; accepted 14 December 1987)

The growth of $\text{Ge}_x\text{Si}_{1-x}$ thin films on silicon has received much attention recently because of both fundamental interest in overlayer ordering as well as potential device applications using the tunable band gap.¹⁻³ Although progress has made it possible to grow high-quality pseudomorphic Si/ $\text{Ge}_x\text{Si}_{1-x}$ multilayer structures,¹ the initial stage of growth of $\text{Ge}_x\text{Si}_{1-x}$ thin films and their surface structures still remains relatively unknown. This motivated us to investigate the surface reconstruction of $\text{Ge}_x\text{Si}_{1-x}$ /Si(111) during growth using reflection high-energy electron diffraction (RHEED).

Surface reconstruction of $\text{Ge}_x\text{Si}_{1-x}$ /Si(111) films after growth have been examined by a number of authors⁴⁻⁷ using low-energy electron diffraction (LEED). A 7×7 LEED pattern was observed by Gossmann *et al.*⁴ for thin films (~ 65 Å) of Ge grown by molecular-beam epitaxy (MBE) on the Si(111)- 7×7 substrate and the $\text{Ge}_{0.5}\text{Si}_{0.5}$ film clearly showed a 5×5 LEED pattern. Furthermore, McRae⁵ and Shoji *et al.*⁶ studied the epitaxy of Ge on Si(111) vicinal surfaces and observed the formation of 5×5 LEED patterns after annealing. However, to our best knowledge, no RHEED studies concerning $\text{Ge}_{0.5}\text{Si}_{0.5}$ on Si(111) vicinal surfaces have been reported. As far as *in situ* characterization of thin films during the growth is concerned, RHEED provides information regarding both crystallinity and surface reconstruction. In this paper, we report for the first time the studies of the surface reconstruction of $\text{Ge}_{0.5}\text{Si}_{0.5}$ on Si(111) during the initial stage of growth using RHEED.

Thin films of $\text{Ge}_{0.5}\text{Si}_{0.5}$ alloy were grown in a MBE system with a base pressure less than 3×10^{-10} Torr. The system has electron-beam evaporators for silicon and germanium, and a RHEED for *in situ* characterization of films. The acceleration voltage of the RHEED apparatus was 10 kV. The fluxes from the Si and Ge sources were separately sensed and monitored by an Inficon Sentinel III deposition controller and calibrated using a quartz thickness monitor. Both Si and Ge thicknesses from the quartz monitor were calibrated by measuring the actual thickness using a Dektak II thickness profiler. The substrate temperature and the substrate heater power were cross checked using an optical pyrometer.

Prior to loading the samples into the growth chamber, silicon substrates were precleaned by Shiraki's method.⁸ Then, the protective oxide film was removed *in situ* by a silicon-beam self-cleaning method with a Si flux of 2×10^{13} $\text{cm}^{-2}\text{s}^{-1}$ at 750°C for 3 min. After the Si flux cleaning, a 1000-Å Si buffer layer was grown on the substrate at 750°C to further improve the quality of the surface. Then, a $\text{Ge}_{0.5}\text{Si}_{0.5}$ layer was grown on the substrate at 550°C . The growth rate was ~ 1 Å/s and the pressure during the growth

was $2-5\times 10^{-9}$ Torr. The $\text{Ge}_x\text{Si}_{1-x}$ film thickness (80 Å) was kept under the critical thickness in order to prevent the development of misfit dislocations.⁹ The RHEED patterns were continuously monitored using a video camera.

Figure 1 shows a clear 7×7 surface structure after a 1000-Å-thick undoped Si buffer layer is grown on the substrate. The RHEED pattern of the $\text{Ge}_{0.5}\text{Si}_{0.5}$ epitaxial layer grown on Si(111) shows a 5×5 superstructure as shown in Fig. 2. The $\text{Ge}_{0.5}\text{Si}_{0.5}$ (111)- 5×5 pattern is analogous to the ones previously reported⁴ using LEED for MBE-grown $\text{Ge}_{0.5}\text{Si}_{0.5}$ films.

There is little understanding as to why the surface structure of $\text{Ge}_{0.5}\text{Si}_{0.5}$ /Si(111) is 5×5 . Gossmann *et al.*⁴ proposed that the formation of $\text{Ge}_{0.5}\text{Si}_{0.5}$ alloy due to Ge indiffusion during the Ge epitaxy on Si(111) is responsible for the formation of the 5×5 reconstruction, while Philips¹⁰ suggested that strain existing in the $\text{Ge}_x\text{Si}_{1-x}$ /Si film is a contributing factor in determining the surface reconstruction from 7×7 to 5×5 . This also agrees with the fact that the surface reconstruction of a relaxed Ge film on Si(111) shows a 7×7 LEED pattern.⁶



FIG. 1. A 7×7 RHEED pattern after a 1000-Å-thick Si buffer layer was grown on a Si(111) substrate (obtained from (110) azimuth)



FIG. 2. A 5×5 RHEED pattern during $\text{Ge}_x\text{Si}_{1-x}$ film growth (obtained from $\langle 110 \rangle$ azimuth, $x = 0.5$ and the film thickness $\approx 80 \text{ \AA}$).

In summary, we have observed a $7 \times 7 \rightarrow 5 \times 5$ RHEED reconstruction pattern transition during $\text{Ge}_{0.5}\text{Si}_{0.5}$ film growth on $\text{Si}(111)$ substrate. Further studies of the surface reconstructions of $\text{Ge}_x\text{Si}_{1-x}$ films may provide important clues for the understanding of the strain dependence of RHEED patterns and the origin of the different reconstruction.

Acknowledgments: This work is supported in part by the Office of Naval Research and by the U. S. Army Research Office.

¹J. C. Bean, L. C. Feldman, A. T. Fiory, S. Nakahara, and I. K. Robinson *J. Vac. Sci. Technol. A* **2**, 436 (1984).

²K. L. Wang, *Solid State Technol.* **28** (No. 10), 137 (1985).

³R. People, *IEEE J. Quantum Electron.* **22**, 1696 (1986).

⁴H. J. Gossmann, J. C. Bean, L. C. Feldman, and W. M. Gibson, *Surf. Sci.* **158**, L175 (1984).

⁵E. G. McRae and R. A. Malic, *Surf. Sci.* **163**, L702 (1985).

⁶K. Shoji, M. Hyodo, H. Ueba, and C. Tatsuyama, *Jpn. J. Appl. Phys.* **22**, L200 (1983).

⁷J. M. Seo, D. L. Doering, D. S. Black, and J. E. Rowe, *J. Vac. Sci. Technol. A* **4**, 894 (1986).

⁸A. Ishizuka and Y. Shiraki, *J. Electrochem. Soc.* **133**, 666 (1986).

⁹R. People and J. C. Bean, *Appl. Phys. Lett.* **47**, 322 (1985).

¹⁰J. C. Philips, *Phys. Rev. Lett.* **45**, 905 (1980).

Intersubband Auger recombination in a superlattice

Perng-fei Yuh and K. L. Wang

*Device Research Laboratory, Department of Electrical Engineering,
University of California, Los Angeles, California 90024-1600*

(Received 19 August 1987)

It is known that the recombination mechanism in narrow-band-gap semiconductor lasers is dominated by the Auger process. An attempt to use the intersubband transitions in the superlattice for lasers is thus restricted by the Auger recombination process. The intersubband Auger recombination process is different from the conduction to valence-band Auger process since the subbands have different band structures, resulting in a different overlap integral and probability weighting function. The probability weighting function is comparable to that of the valence to conduction-band Auger process for narrow-band-gap (≤ 0.3 eV) bulk material. The overlap integral can be reduced by adjusting the miniband bandwidth. However, there is a tradeoff in controlling the bandwidth for a lower Auger rate (requiring narrower bandwidth) and for a larger carrier injection (requiring wider bandwidth). A closed form of the intersubband Auger rate is derived. It gives a much weaker band-gap and temperature dependence. Due to the adjustable overlap integral, the intersubband Auger rate can be made much lower than that of the conventional conduction to valence-band transition of the same band gap.

I. INTRODUCTION

The physics of intersubband optical transitions in quantum well structures and the device applications have been extensively studied by many authors.¹⁻¹⁰ The term "intersubband transitions" is used to refer to the subband-to-subband transitions occurring within only the condition subbands or within only the valence subbands. The intersubband optical transitions have many unique features as compared to the usual valence-to-conduction-band transitions. First, the absorption or gain coefficient is sharp, analogous to an atomic two-level system. Second, the subband-to-subband energy gaps as well as the bandwidths can be tuned. The intersubband in superlattices can be treated as a man-made narrow-band-gap material with almost arbitrarily controllable parameters. Indirect-band-gap material such as Si and Ge can be used for lasing and it occurs as "direct" transition regardless of the nature of the host bulk material.

In order to access the merits of the intersubband transition for lasers, two problems remain to be solved. One is the pumping for population inversion; the other is the reduction of nonradiative recombination rates. The formal will be discussed briefly later. As for the nonradiative recombination process, we first consider the transition energies of intersubband transitions, which are typically on the order or less than a few tenths of eV, corresponding to the transition frequency in the infrared range. In narrow-band-gap semiconductor laser material however, the nonradiative decay of the injected carriers at the lasing condition is dominated by the band-to-band Auger recombination.¹¹ It is thus important to study the Auger process in the intersubband transition in superlattices. This paper proceeds to analyze the dominant nonradiative Auger recombination process.

The fundamental theory of the Auger recombination

was first treated by Beattie and Landsberg.¹² Since then several authors have calculated the band-to-band Auger rates involving the light hole¹³ and the split-off band hole.¹⁴ More complex calculations for phonon-assisted, trap Auger and second-Auger processes have taken into account nonparabolic bands, Fermi statistics, and screening effects in the case of bulk semiconductors.¹⁵⁻¹⁸ In this paper the intersubband Auger recombination was treated. It, however, is different from the above calculations in that the intersubband case has different band structures and a different overlap integral and a probability weighting function. The probability weighting function is shown to be comparable to the conduction-to-valence Auger process for narrow-band-gap cases; while the overlap integral can be reduced by adjusting the miniband bandwidth. An analytic form has been obtained for the intersubband Auger process, and it shows that the recombination has a much less band-gap and temperature dependence. From this formulation we show that the intersubband transition has a significantly lower Auger rate than the conventional semiconductor lasers of the same bandgap due to the adjustable overlap integral, although the Auger remains to be the dominant recombination process.

II. MATRIX ELEMENT

For a two-level system, all the possible Auger interactions are depicted in Fig. 1. In Fig. 1, 1(a) and 1(b) are the recombination processes, while 1(c) and 1(d) are their corresponding inverse processes, the impact ionization. If we consider the upper (*U*) level as a conduction band (*C*) and the lower level (*L*) as heavy-hole valence band (*H*), then processes 1(a) and 1(c) involve three states in the conduction band and one in the heavy-hole valence band, and are conventionally called the *CHCC* process. Similarly, 1(b) and 1(d) are called the *CHHH* process.

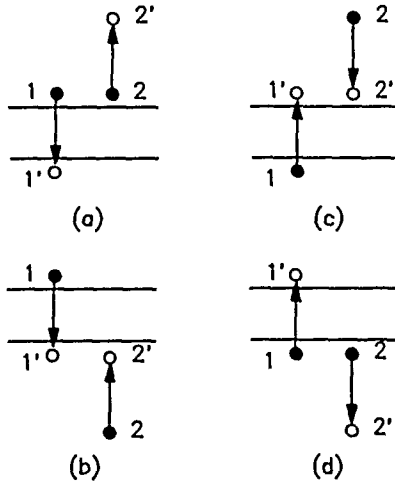


FIG. 1. All the possible transitions of two electron interaction in a two-level system. (a) and (c) are the CHCC process. (b) and (d) are the CHHH process. Each pair consists of one Auger process and one impact ionization. 1 and 2 are the initial states. 1' and 2' are the final states.

For the intersubband cases, they are referred as ULUU and ULLL, respectively.

Since the Auger recombination is a two-electron interaction via their Coulomb potential and it is a short-range interaction, the screened Coulomb potential is used.¹⁹ The matrix element after summing over the singlet and triplet states of electrons 1 and 2 is of the following form:¹²

$$M_{if} = \int \int [\Phi_1^*(r_1)\Phi_2^*(r_2)\Delta_{21} - \Phi_2^*(r_1)\Phi_1^*(r_2)\Delta_{12}] \times [e^2 \exp(-\lambda r_{12}) / \epsilon r_{12}] \Phi_1'(r_1) \times \Phi_2'(r_2) d^3r_1 d^3r_2, \quad (1)$$

where $\Phi_1(r_1), \Phi_2(r_2)$ denote the initial states of electrons 1 and 2, and $\Phi_1'(r_1), \Phi_2'(r_2)$ denote their final states. The quantities $\Delta_{21} = \Delta_{12} = 1$ when electrons 1 and 2 have the same spins, preserved in the transition, $\Delta_{21} = 1, \Delta_{12} = 0$ when they have opposite spins preserved in the transition and $\Delta_{21} = 0, \Delta_{12} = 1$ when they have opposite spins but are both changed by the transition; $\Delta_{21} = \Delta_{12} = 0$ otherwise. The quantity λ in the screened Coulomb potential is the reciprocity of the Debye length which is given by¹⁵

$$\lambda_B = \left[\frac{4\pi e^2 n}{\epsilon kT} \right]^{1/2}, \quad \lambda_F = \left[\frac{12m_e e^2 n}{\epsilon \hbar^2} \right]^{1/2} \left[\frac{n}{9\pi} \right]^{1/6}, \quad (2)$$

for the Boltzmann and Fermi statistics, respectively. All the symbols have their usual definition. Using a two-band envelope function²⁰ in the growth direction \hat{z} , the superlattice wave function becomes

$$\Phi(k, q, r, z) = [F_s(q, z)u_s(k, q, r, z) + F_p(q, z)u_p(k, q, r, z)]e^{ik \cdot r}, \quad (3)$$

where \mathbf{k} is the two-dimensional wave vector in the trans-

verse direction, q is the wave vector along \hat{z} , and u_s and u_p are the periodic parts of the host Bloch functions for the conduction and light-hole bands, respectively. F_s and F_p are the envelope functions along \hat{z} . Using the Fourier expansion in the transverse direction as was done in Ref. 12, and neglecting the terms which have a product of two vanishing small (zero) terms in the overlap integrals, the matrix element for the ULUU process of the intersubband transition becomes

$$M_{if} = \frac{2\pi e^2}{\epsilon} \int \int \left[\frac{\Delta_{21} V(1, 1') V(2, 2')}{(g^2 + \lambda^2)^{1/2}} - \frac{\Delta_{12} V(2, 1') V(1, 2')}{(h^2 + \lambda^2)^{1/2}} \right] \times \delta(k_1 + k_2 - k'_1 - k'_2) dz_1 dz_2, \quad (4)$$

where $g = |k_1 - k'_1|$, $h = |k_1 - k'_2|$, and the quantities $V(i, j)$ are defined by

$$\begin{aligned} V(1, 1') &= F_U^*(q_1, z_1) F_L(q'_1, z_1), \\ V(2, 2') &= F_U^*(q_2, z_2) F_U(q'_2, z_2), \\ V(2, 1') &= F_U^*(q_2, z_1) F_L(q'_1, z_1), \\ V(1, 2') &= F_U^*(q_1, z_2) F_U(q'_2, z_2), \end{aligned} \quad (5)$$

where F 's are the F_s in Eq. (3) with U, L denoting the upper and lower levels, respectively. The terms involved with F_p are negligibly small, i.e., the one-band model is valid. For the conduction- to valence-band transition in quantum wells, $V(i, j)$ have the same definition as in Eq. (5) with F_U and F_L replaced by U_s and U_p and the integration is over r_1 and r_2 . Thus the conduction- to valence-band transition in a quantum well has the same overlap integral as the bulk case¹⁷ while the intersubband transition has an overlap integral determined only by the envelope functions, which can be easily tuned. In deriving Eq. (4), we have assumed that most of the contribution to the integral arises from small z_{12} (Ref. 17), i.e.,

$$\begin{aligned} & \int \frac{\exp[-\lambda(r_{12}^2 + z_{12}^2)]^{1/2}}{(r_{12}^2 + z_{12}^2)^{1/2}} \exp(-i\mathbf{r}_{12} \cdot \mathbf{g}) r_{12} dr_{12} d\theta \\ & \approx \int \frac{\exp(-\lambda r_{12})}{r_{12}} \exp(-ir_{12} g \cos\theta) r_{12} dr_{12} d\theta \\ & = \frac{2\pi}{(g^2 + \lambda^2)^{1/2}}. \end{aligned} \quad (6)$$

For the ULLL process, the matrix element is the same as Eq. (4) except that $V(i, j)$ are replaced by

$$\begin{aligned} V(1, 1') &= F_U^*(q_1, z_1) F_L(q'_1, z_1), \\ V(2, 2') &= F_L^*(q_2, z_2) F_L(q'_2, z_2), \\ V(2, 1') &= F_L^*(q_2, z_1) F_L(q'_1, z_1), \\ V(1, 2') &= F_U^*(q_1, z_2) F_L(q'_2, z_2). \end{aligned} \quad (7)$$

In the discussion above, we have considered only the transitions involving two minibands, i.e., an ideal two-level system. If, however, either one of the four states involved in the process are in the third band, there will be a product of two negligible small terms in the overlap integral. The transitions involving three bands are thus treated as forbidden in the first-order approximation.

As discussed in Ref. 21, an upper bound for the matrix element of Eq. (4) may be written as

$$|M_{if}|^2 \leq 8 \left[\frac{2\pi e^2}{\epsilon} \right]^2 \frac{\left| \int \int V(1,1')V(2,2')dz_1dz_2 \right|^2}{g^2 + \lambda^2}, \quad (8)$$

where g may be replaced by k'_2 for the most probable transition so that the integration can be evaluated easily.

III. OVERLAP INTEGRAL

The overlap integral in Eq. (8) can be evaluated by constructing the superlattice envelope function $F(q,z)$ in terms of the isolated quantum well wave function $f_0(z)$ by a tight-binding scheme,²⁰

$$F(q,z) = \frac{1}{\sqrt{N}} \sum_{j=-\infty}^{\infty} e^{iqjd} f_0(z-jd), \quad (9)$$

where d is the period of the superlattice and N is the number of periods in the superlattice. The conservation of momentum is required for nonzero results; thus we may write the overlap integral as

$$\begin{aligned} \int V(1,1')dz_1 &= \int F_U^*(q_1,z_1)F_L(q'_1,z_1)dz_1 \\ &= \int F_U^*(q_1,z_1)F_L(q'_1,z_1)\delta(q_1-q'_1)dz_1 \\ &= \sum_p 2 \cos(pq_1d) \int f_{U0}(z_1)f_{L0} \\ &\quad \times (z_1+pd)dz_1. \end{aligned}$$

Similarly, we have

$$\int V(2,2')dz_2 = \int F_U^*(q_2,z_2)F_U(q'_2,z_2)dz_2 \approx 1. \quad (10)$$

We notice that the miniband bandwidth is approximated to be²⁰

$$B = 4 \int_{-\infty}^{\infty} f_0(z)V_c(z)f_0(z-d)dz, \quad (11)$$

where V_c is the conduction-band offset of the heterojunc-

tion making up the superlattice. For a square-well superlattice, the overlap integral can then be approximated by

$$\int \int V(1,1')V(2,2')dz_1dz_2 \approx \frac{\sqrt{B_U B_L}}{2V_c} \cos(q_1d), \quad (12)$$

where B_U, B_L is the miniband bandwidth for the upper and lower bands, respectively. For a parabola well as in the doped superlattice, the wave function may be approximated by the simple harmonic-oscillator model,²²

$$F_j(z) = \pi^{-1/4} \alpha^{-1/2} e^{-z^2/2\alpha^2} (2^j j!)^{-1/2} H_j \left[\frac{z}{\alpha} \right], \quad (13)$$

where $\alpha^2 = \hbar/m_c \omega_0$, $\omega_0 = (e^2 N_d / \epsilon m_c)^{1/2}$, and N_d is the doping. The two lower-order Hermite polynomials are $H_0(x) = 1, H_1(x) = 2x$. Then the overlap integral becomes

$$\int \int V(1,1')V(2,2')dz_1dz_2 = \frac{\sqrt{2}d}{\alpha} e^{-\alpha^2/4\alpha^2} \cos(q_1d). \quad (14)$$

IV. PROBABILITY WEIGHTING FUNCTION

Using Fermi's golden rule, the Auger rate is

$$\begin{aligned} R &= \frac{2\pi}{\hbar} \left[\frac{1}{8\pi^3} \right]^4 \int |M_{if}|^2 P(1,1',2,2') \delta(E_i - E_f) \\ &\quad \times d^2 k_1 d^2 k_2 d^2 k'_1 d^2 k'_2 dq_1 \\ &\quad \times dq_2 dq'_1 dq'_2, \end{aligned} \quad (15)$$

where P is the difference of the probabilities of the Auger process and the inverse process. In the following we will derive the most probable transition probability for different intersubband as well as the conventional band cases.

A. Case 1: CHCC for conventional band

Let us assume that all the energy levels are referenced to the valence-band maximum. For a conventional band in Fig. 2(a), the probability weighting function is

$$\begin{aligned} P &= (1 \text{ occupied})(2 \text{ occupied})(1' \text{ empty})(2' \text{ empty}) \\ &\quad - (1 \text{ empty})(2 \text{ empty})(1' \text{ occupied})(2' \text{ occupied}) \\ &= \frac{1 - \exp[-(E_{f_2} - E_{f_1})/kT]}{(1 + \exp(E_1 - E_{f_2})/kT)[1 + \exp(E_2 - E_{f_2})/kT][1 + \exp(-(E'_1 - E_{f_1})/kT)]}, \end{aligned} \quad (16)$$

where Fermi-Dirac distributions are assumed for quasiequilibrium, and E_{f_2}, E_{f_1} are the quasi-Fermi-levels for the upper and lower levels, respectively. In the non-degenerate limit, Eq. (16) reduces to

$$P = e^{-E'_2/kT} e^{2E_{f_2}/kT} (1 - e^{-(E_{f_2} - E_{f_1})/kT}). \quad (17)$$

The maximum of P is obtained by minimizing E'_2 with the constraint that both energy and momentum are con-

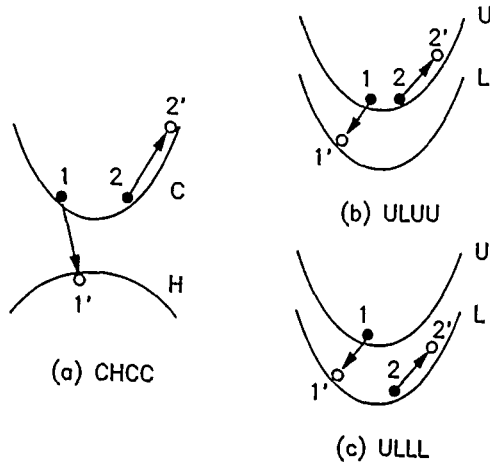


FIG. 2. (a) CHCC process in conventional band. (b) ULUU process in intersubband, corresponding to the CHCC process in the bulk case. (c) ULLL process in intersubband, corresponding to the CHHH process in the bulk case.

served. The result for the nondegenerate case is¹²

$$P_{\max} = \exp \left[-\frac{\mu}{\mu+1} E_G / kT \right] e^{-2(E_G - E_{f_2})/kT} \times (1 - e^{-(E_{f_2} - E_{f_1})/kT}), \quad (18)$$

where $\mu = m_c/m_v$ is the ratio of effective masses of electrons and holes. The prefactor $\exp[-(\mu/\mu+1)E_G/kT]$ is the major cause of the band-gap and temperature dependence of the Auger rate. The rate of CHCC is usually larger than CLCC, where L stands for the light hole, simply because μ is smaller in CHCC. For the degenerate case, one may also assume that P_{\max} occurs at the same condition as in the nondegenerate case such that

$$E'_1 = -\frac{\mu}{(2\mu+1)(\mu+1)} E_G, \quad (19)$$

$$E_2 = E_1 = E_G + \frac{\mu^2}{(2\mu+1)(\mu+1)} E_G.$$

B. Case 2: ULUU for intersubband

For the band shown in Fig. 2(b), in the lasing condition we will assume states 1,2 in degenerate while states 1',2' in nondegenerate for simplicity. This case corresponds to the CHCC process in the conventional band. The probability function is

$$P = \frac{1 - \exp(-(E_{f_2} - E_{f_1})/kT)}{[1 + \exp(E_1 - E_{f_2})/kT][1 + \exp(E_2 - E_{f_2})/kT]}, \quad (20)$$

whose maximum value P_{\max} occurs at $E_2 = E_1 = E_G$, $E'_2 = 3/2 E_G$, $E'_1 = 1/2 E_G$. In the nondegenerate limit, we have

$$P_{\max} = e^{-2(E_G - E_{f_2})/kT} (1 - e^{-(E_{f_2} - E_{f_1})/kT}). \quad (21)$$

Compared to Eq. (18), the intersubband transition has a much larger probability than the conduction- to valence-band transition, especially for wide band-gap material at low temperature. However, for the narrow band-gap material in the lasing condition (usually in degenerate case), they are comparable. For example, for $E_G = 0.1$, $\mu = 0.15$, and $E_{f_2} - E_G = 0.05$ eV, the ratio of P_{\max} for interband and conventional band transitions are 1.3 at 300 K and 1 at 77 K.

C. Case 3: ULLL for intersubband

For the ULLL process shown in Fig. 2(c), which corresponds to the CHHH process in the bulk case, the probability is

$$P = \frac{\exp(-(E_2 - E_{f_1})/kT)}{1 + \exp(E_1 - E_{f_2})/kT} [1 - \exp(-(E_{f_2} - E_{f_1})/kT)]. \quad (22)$$

Here we assume that electrons in state 1 are degenerate while those in others are treated as nondegenerate. P_{\max} occurs at $E_1 = E_G$, $E_2 = 0$,

$$P_{\max} = \frac{e^{E_{f_1}/kT}}{1 + e^{-(E_G - E_{f_2})/kT}} \ll 1. \quad (23)$$

If $E_{f_1} \ll 0$, then P_{\max} for the ULLL process is much smaller than P_{\max} for ULUU. This condition is usually valid in the intersubband transition. In the following calculation, we will consider only the ULUU process.

V. AUGER RATE AND DISCUSSION

The Auger rate is given by Eq. (15), where the matrix element $|M_{if}|^2$ is evaluated by Eq. (8) for the most probable transition, such that $g^2 \approx k_2'^2 \approx k_G^2/2$, where $E_G = \hbar^2 k_G^2/2m_c$. Then the remaining part of the integration in Eq. (15) is

$$I = \int P(1, 1', 2, 2') \delta(E_i - E_f) \delta(k_1 + k_2 - k'_1 - k'_2) \times \delta(q_1 - q'_1) \delta(q_2 - q'_2) d^2 k_1 d^2 k_2 d^2 k'_1 d^2 k'_2 \times dq_1 dq_2 dq'_1 dq'_2, \quad (24)$$

where P is given by Eq. (20), and is only a function of E_1 and E_2 , and all the delta functions come in when $|M_{if}|^2$ was evaluated. The difference of the initial and final energies taking the miniband energy into consideration is

$$E_i - E_f = E_1 + E_2 - E'_1 - E'_2 = \frac{\hbar^2}{2m_{c2}} (k_1^2 + k_2^2 + k_G^2 + k_q^2 - \mu k_1'^2 - \mu k_2'^2), \quad (25)$$

where $\mu = m_{c2}/m_{c1}$, $\mu_t = m_{c2}/m_{c1}$, and m_{c1} is the effective mass at the lower subband E_1 , and m_{c2} and m_{c1} are those at E_2 and E'_2 , respectively; k_q is defined by

$$k_q = \left[\frac{m_c^2}{\hbar^2} (B_U + B_L) \cos q_1 d \right]^{1/2}. \quad (26)$$

For the convenience of integration, two new variables $h = k_1' + k_2'$ and $j = k_1' - k_2'$ are introduced, and $m_{c1} = m_{c2} = m_{cl} = m_c$ are assumed. Then Eq. (25) becomes

$$\frac{\hbar^2}{2m_c} [k_1^2 + k_2^2 + k_G^2 + k_q^2 - \frac{1}{2}(|j|^2 + |k_1 + k_2|^2)]. \quad (27)$$

The integration is then performed under the constraint

$$|j_0|^2 = 2(k_1^2 + k_2^2 + k_G^2 + k_q^2) - |k_1 + k_2|^2 \geq 0, \quad (28)$$

which is always true if $E_G > B_U + B_L$. After integration with respect to k_1 and k_2 , the final result for I becomes

$$I = \frac{32\pi^5 m_c N_{2D}^2}{\hbar^2} (1 - e^{-(E_{f2} - E_{f1})/kT}), \quad (29)$$

where N_{2D} is the two-dimensional injected carrier concentration given by

$$N_{2D} = \frac{m_c kT}{\pi \hbar^2} \ln(1 + e^{(E_{f2} - E_G)/kT}). \quad (30)$$

Combining Eqs. (8), (12), and (29), the Auger rate (/sec·m²) for the intersubband transition is then

$$R = \frac{m_c e^4}{\hbar^3 \epsilon^2} \frac{B_U B_L}{V_c^2} \frac{N_{2D}^2}{\lambda^2 + k_2'^2} (1 - e^{-(E_{f2} - E_{f1})/kT}). \quad (31)$$

There again, B_U, B_L are the miniband bandwidth for the upper and lower bands, respectively, V_c is the conduction-band offset, λ is the reciprocal Debye length, and $k_2'^2$ is evaluated at the most probable transition such that $k_2'^2 \approx k_G^2/2$. The Auger recombination lifetime τ_{au} , defined by

$$R = \frac{N_{2D} - N_0}{\tau_{au}} \approx \frac{N_{2D}}{\tau_{au}}$$

is shown in Fig. 3 as a function of the subband band gap and N_0 is the equilibrium value. It is a linear function of the band gap, where the slope is inversely proportional to the injection carrier concentration. Compared to the conduction- to valence-band Auger recombination time, which has an exponential dependence of the band gap and the temperature, the intersubband Auger time has a smaller band-gap dependence and is constant in temperature. As a result the threshold current for intersubband laser transitions will have a much weaker temperature dependence. The spontaneous emission lifetime, given by the expression²³

$$\frac{1}{\tau_{sp}} = \frac{2n^3 \mu^2 \omega^3 g_1}{\epsilon \hbar c^3} \quad (32)$$

is also plotted in Fig. 3, where n is the index of refraction, g_1 is the degeneracy factor, and μ is the dipole moment given by

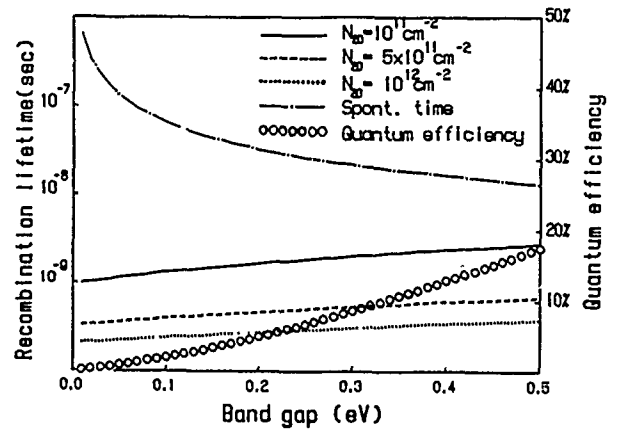


FIG. 3. The recombination lifetime vs energy band gap. Three lines are for intersubband Auger recombination time with different injection levels. They are increasing functions of the band gap. The spontaneous lifetime is a decreasing function of the band gap. The quantum efficiency is defined by Eq. (34) using the data of $N_{2D} = 10^{11}/\text{cm}^2$. All other parameters not specified in the text are assumed to be for GaAs.

$$\mu^2 = \frac{\hbar e^2}{2m_0 \omega} f_{ij}, \quad (33)$$

where f_{ij} is the oscillator strength, assumed to be unity here. The spontaneous quantum efficiency η defined by

$$\eta = \frac{\tau_{au}}{\tau_{sp} + \tau_{au}} \quad (34)$$

is also plotted in Fig. 3 as a function of energy. The Auger recombination time as well as the quantum efficiency could be tailored by adjusting the miniband bandwidth. Here we assume that $B_U = 10$ meV, $B_L = 1$ meV, and $V_c = 0.24$ eV. However, the miniband bandwidth is limited by the accuracy of the growth parameters. Also, the choice of bandwidth is limited by the requirement for efficient injection. The effective mass in the growing direction of a superlattice is estimated to be $m_z = 2\hbar^2/Bd^2$.²⁴ As the bandwidth becomes small, the effective mass increases and the mobility drops. In the limiting case of quantum wells, the miniband bandwidth becomes zero and the Auger rate is zero. However, the current injection will then be impossible in this case since the mobility of the structure is zero.

As for the pumping in the intersubband lasing transition, one possible way is shown in Fig. 4.²⁵ The population inversion is achieved by current injected through the aligned superlattice minibands in the right-hand side. While in the left-hand side, the injected carriers are

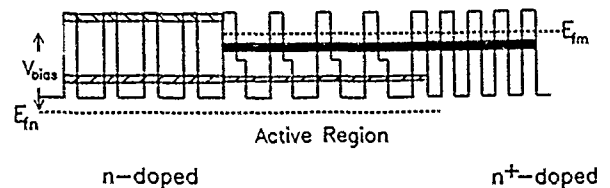


FIG. 4. Band-aligned superlattice laser using intersubband optical transition and miniband alignment.

blocked by the miniband discontinuity there. Such a band alignment scheme allows convenient current injection for the intersubband lasing.

VI. CONCLUSION

In conclusion, we have calculated the intersubband Auger recombination rate in superlattices. An analytic form is derived which shows much smaller band-gap and temperature dependence. With the promising of an adjustable Auger rate by choosing the superlattice parameters (composition, dopant, thickness, etc.), the intersubband Auger rate could be two orders of magnitude

smaller than the conventional narrow band-gap material. High gain coefficient, smaller threshold current, less temperature dependence of the threshold current, and better tunability could be expected for the applications in long-wavelength lasers using intersubband transition in superlattices.

ACKNOWLEDGMENTS

The authors are indebted to Dr. J. Schulman for calculations relating to the superlattice miniband. This work is in part supported by the U.S. Office of Naval Research and the Semiconductor Research Corporation and the U.S. Army Research Office.

-
- ¹B. Jogai and K. L. Wang (to be published).
 - ²D. D. Coon and R. P. G. Karunasiri, *Appl. Phys. Lett.* **45**, 649 (1984).
 - ³L. C. West and S. J. Eglash, *Appl. Phys. Lett.* **46**, 1156 (1985).
 - ⁴D. D. Coon, R. P. G. Karunasiri, and L. Z. Liu, *Appl. Phys. Lett.* **47**, 289 (1985).
 - ⁵D. D. Coon, R. P. G. Karunasiri, and L. Z. Liu, *J. Appl. Phys.* **60**, 2636 (1986).
 - ⁶B. F. Levine, R. J. Malik, J. Walker, K. K. Choi, C. G. Bethea, D. A. Kleinman, and J. M. Vandenberg, *Appl. Phys. Lett.* **50**, 273 (1987).
 - ⁷D. Ahn and S. L. Chuang, *Phys. Rev. B* **35**, 4149 (1987).
 - ⁸Alex Harwit and J. S. Harris, Jr., *Appl. Phys. Lett.* **50**, 685 (1987).
 - ⁹B. F. Levine, K. K. Choi, C. G. Bethea, J. Walker, and R. J. Malik, *Appl. Phys. Lett.* **50**, 1092 (1987).
 - ¹⁰K. K. Choi, B. F. Levine, C. G. Bethea, J. Walker, and R. J. Malik, *Appl. Phys. Lett.* **50**, 1814 (1987).
 - ¹¹Yoshiji Horikoshi, in *Semiconductors and Semimetals*, edited by R. K. Willardson and A. C. Beer (Academic, London, 1985), Vol. 22, part C, pp. 93-151.
 - ¹²A. R. Beattie and P. T. Landsberg, *Proc. R. Soc. London Ser. A* **249**, 16 (1959).
 - ¹³A. R. Beattie and G. Smith, *Phys. Status Solidi* **19**, 577 (1967).
 - ¹⁴M. Takeshima, *J. Appl. Phys.* **43**, 4114 (1972).
 - ¹⁵Albert Haug, *Solid-State Electron.* **21**, 1281 (1978).
 - ¹⁶N. K. Dutta and R. J. Nelson, *J. Appl. Phys.* **53**, 74 (1982).
 - ¹⁷N. K. Dutta, *J. Appl. Phys.* **54**, 1236 (1983).
 - ¹⁸R. I. Taylor, R. W. Kelsall, and R. A. Abram, *Surf. Sci.* **174**, 169 (1986).
 - ¹⁹A. Haug, *Theoretical Solid State Physics* (Pergamon, Oxford, 1972), Vol. 2.
 - ²⁰G. Bastard, in *Molecular Beam Epitaxy and Heterostructures*, Vol. 87 of *NATO Advanced Study Institute, Series E: Applied Sciences*, edited by L. I. Chang and K. Ploog (Nijhoff, Dordrecht, 1985), pp. 381-423.
 - ²¹Akira Sugimura, *J. Appl. Phys.* **51**, 4405 (1980).
 - ²²Gottfried H. Dohler and Peter Paul Ruden, *Phys. Rev. B* **30**, 5932 (1984).
 - ²³Amnon Yariv, *Quantum Electronics*, 2nd Ed. (Wiley, New York, 1975), Chap. 8.
 - ²⁴J. N. Schulman (private communication).
 - ²⁵Peng-fei Yuh and K. L. Wang, *Appl. Phys. Lett.* **51**, 1404 (1987).

Boron surface segregation in silicon molecular beam epitaxy

E. de Frésart,^{a)} K. L. Wang, and S. S. Rhee

Device Research Laboratory, Electrical Engineering Department, University of California at Los Angeles, Los Angeles, California 90024

(Received 16 October 1987; accepted for publication 5 May 1988)

Boron surface segregation in Si molecular beam epitaxy has been measured on Si(111) substrate as a function of the growth temperature ($400^\circ\text{C} \leq T_s \leq 900^\circ\text{C}$) by Auger electron spectroscopy. Boron oxide (B_2O_3) was used as dopant material to achieve a boron concentration level of about $1 \times 10^{19} \text{ cm}^{-3}$. Three temperature regions are observed for the behavior of the ratio $r_d = I_s/I_b$ of the surface (I_s) to the bulk (I_b) dopant atomic fractions. At low temperature, $T_s = 400\text{--}570^\circ\text{C}$ the ratio maintains at the value $r_d \approx 1.5$. For $570^\circ\text{C} < T_s \leq 720^\circ\text{C}$, r_d increases to a plateau $r_d \approx 5.5$, and then jumps to $r_d = 42$ in the $720\text{--}750^\circ\text{C}$ region. At higher temperature, $T_s > 750^\circ\text{C}$, r_d decreases according to a relation which can be approximated by the classical equilibrium segregation theory. In that region, the boron Gibbs free energy of surface segregation is calculated from data to be $\Delta G^s = -0.33 \pm 0.02$ eV. Evolution of r_d is closely correlated to the etch pit count and electron channeling results revealing amorphous, polycrystalline, and epitaxial growth, when going from low to high growth temperature.

Engineering of *p-n* junctions having carrier concentrations as high as 10^{20} cm^{-3} and profile abruptness in the $100 \text{ \AA}/\text{decade}$ range is desired for application in conventional or novel devices based on multilayered structures. In the Si molecular beam epitaxy technique (Si-MBE), such specifications strongly depend on two fundamental parameters: the dopant incorporation probability (σ_d) and the segregation coefficient (r_d), which in turn depend on the growth parameters.¹ In this letter, we show the evolution of the boron surface segregation with the growth temperature and its correlation with the film morphology.

The films were grown in a Si-MBE system with a base pressure of 2×10^{-10} Torr. The details of the system have been described in a previous paper.² Boron oxide was evaporated by heating B_2O_3 in a boron nitride effusion cell crucible. *n*-type ($5\text{--}10 \text{ } \Omega \text{ cm}$) Czochralski Si(111) sample substrates were used. They were chemically cleaned by the usual oxidation/reduction method leaving a protective thin oxide layer prior to the transfer to the system.³ The thin oxide layer was then thermally removed *in situ* by annealing the sample at 900°C for 10 min. The surface temperature was monitored by an infrared pyrometer ($\lambda \approx 2 \text{ } \mu\text{m}$). Absolute temperature was known to $\pm 40^\circ\text{C}$. During evaporation, the growth rate was maintained in the $1.1\text{--}1.4 \text{ \AA/s}$ range, as measured by a quartz crystal monitor. The Si/B flux ratio was kept constant and adjusted to obtain a B doping concentration $N_d \approx 1 \times 10^{19} \text{ cm}^{-3}$. The doping cell temperature was 882°C .

Two sets of experiments have been done as a function of the growth temperature, in the range $400^\circ\text{C} \leq T_s \leq 900^\circ\text{C}$.

In the first set, films $1 \text{ } \mu\text{m}$ thick have been grown, one for each temperature, by step of 50°C . Their morphology and defect density have been analyzed by the defect etch technique, using a diluted Schimmel solution.⁴ Optical micrographs of the etched films show three growth temperature regions. At low temperature, $400^\circ\text{C} \leq T_s \leq 550^\circ\text{C}$, no

patterns are observable. The films are thought to be amorphous or polycrystalline with polycrystal sizes smaller than $0.1 \text{ } \mu\text{m}$. For $550^\circ\text{C} < T_s < 700^\circ\text{C}$ an intermediate region is observed and nucleation of grains is clearly visible on the etch patterns. The size of the nuclei increases with T_s , from about $0.5 \text{ } \mu\text{m}$ at 550°C to about $2 \text{ } \mu\text{m}$ at 650°C . Electron channeling patterns, obtained by scanning electron microscopy (SEM), indicate that the grains are crystalline. Figure 1 shows a micrograph of such defect etch pattern taken from $T_s = 600^\circ\text{C}$, indicating the polycrystalline nature of the film. At high temperature, $700^\circ\text{C} < T_s \leq 900^\circ\text{C}$, epitaxial growth is obtained, as seen on pictures in Fig. 2 taken on a film grown at 800°C . Defects are mainly identified as stacking faults and the defect density is in the 10^5 cm^{-2} range. The carrier concentration, measured by the Hall effect in the region where epitaxial growth is observed, increases slightly with T_s , from $p = 6.0 \times 10^{18} \text{ cm}^{-3}$ for $T_s = 700^\circ\text{C}$ to $6.3 \times 10^{18} \text{ cm}^{-3}$ for $T_s = 900^\circ\text{C}$. The high level of defects is

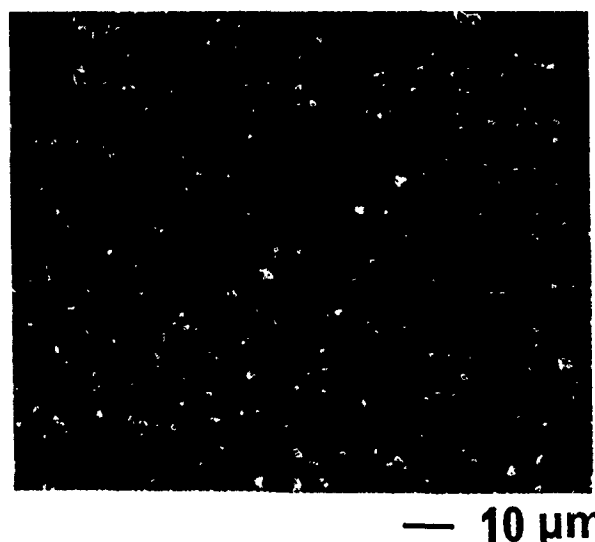


FIG 1 Defect structure of a diluted Schimmel etched Si:B film (doping concentration $N_d \approx 10^{19} \text{ cm}^{-3}$) grown at 600°C . Grain size $\approx 1 \text{ } \mu\text{m}$.

^{a)} Present address: IBM Research Division, Thomas J. Watson Research Center, Yorktown Heights, NY 10598.

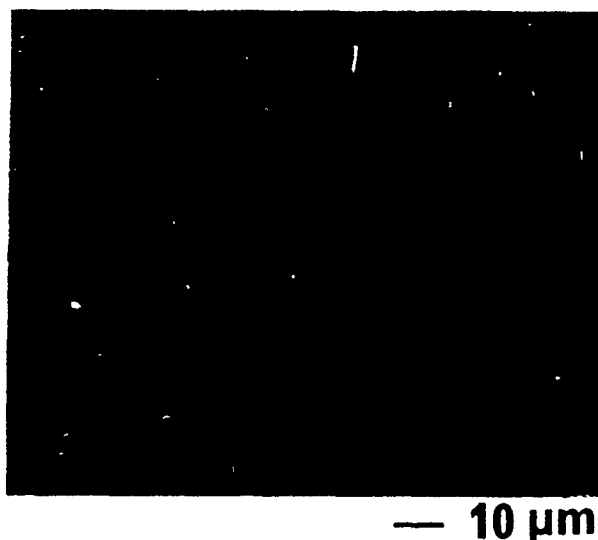


FIG. 2. Optical micrograph of a Si:B film (doping concentration $N_a \approx 10^{19} \text{ cm}^{-3}$) grown at 800°C , after diluted Schimmel etch. Defect density $\approx 10^5 \text{ cm}^{-2}$.

attributed to the chemical reaction of B_2O_3 and Si, where B_2O_3 is reduced by Si to form SiO_2 , BO_x ($x < 1.5$), B or B_2 , and a Si-B compound. SiO_2 is subsequently reduced by Si and thermally desorbed in the SiO form for $T_s > 550^\circ\text{C}$ as shown in our previous work.⁵ The transition between the first (amorphous) and the second (polycrystalline) region which occurs around $550\text{--}600^\circ\text{C}$ can be related to the removal of the oxygen from the film, which starts in this temperature range. In the low-temperature regions, the maximum oxygen concentration into the films is in the 10^{19} cm^{-3} range, since no removal of oxygen occurs yet. This explains the amorphous/polycrystalline nature of the film.

In the second set of experiments, the surface atomic composition of the films was measured *in situ* by Auger electron spectroscopy (AES). The analysis was performed on a codeposited Si:B film of 2000 \AA thickness (doping concentration $N_a \approx 10^{19} \text{ cm}^{-3}$) on the substrate, by probing the $\text{Si}_{L_{VV}}$ (91 eV) and B_{KLL} (182 eV) Auger transitions after

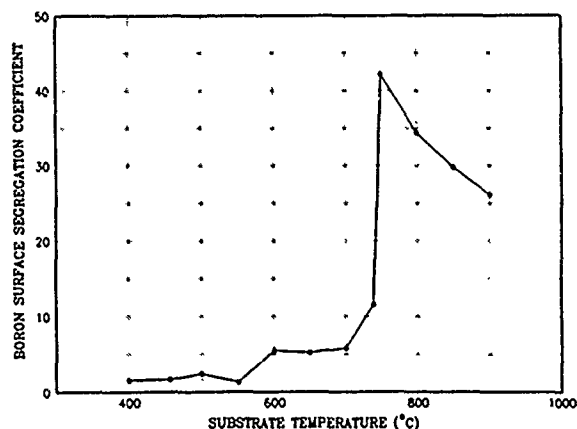


FIG. 3. Evolution of the boron surface segregation ratio r_d , measured *in situ* by Auger electron spectroscopy on a Si:B film, as a function of the growth temperature.

cooling the sample down near room temperature. The thickness value (2000 \AA) of the doped layers was chosen to ensure that during growth the steady-state value of the incorporated dopant fraction was reached. After Auger measurements, every Si:B film was annealed at 900°C for 10 min to remove all remaining oxides, and a 2000 \AA pure Si film was evaporated in order to reproduce the same starting conditions. The measurements were repeated on the same substrate as a function of the deposition temperature. The boron surface segregation ratio r_d , calculated from the Auger data, is plotted in Fig. 3 as a function of the growth temperature $400^\circ\text{C} \leq T_s < 900^\circ\text{C}$. The surface segregation ratio is defined as $r_d = I_s/I_b$, where I_s and I_b are respectively the surface and the bulk boron atomic fractions. I_s was directly measured by AES. The value of I_b , when the growth is epitaxial, can be calculated by fitting the Auger data to the following:

$$\frac{I_s}{1 - I_s} = \frac{I_b}{1 - I_b} \exp\left(-\frac{\Delta G^S}{kT_s}\right), \quad (1)$$

where k is the Boltzmann constant and ΔG^S the Gibbs free energy of boron surface segregation. Figure 3 again shows three temperature regions for r_d . Two plateau values are observed at low temperature with $r_d \approx 1.5$ and intermediate temperature with $r_d \approx 5.5$, corresponding to the amorphous or polycrystalline and polycrystalline regions. We have associated the third (high temperature) region to the epitaxial growth. The transition between the polycrystalline and the epitaxial growth is characterized by an abrupt jump of r_d from 5.5 to 42 in the range $700\text{--}750^\circ\text{C}$. In the epitaxial region, r_d decreases with increasing T_s according to Eq. (1) provided by the classical theory of segregation.^{1,6} This is demonstrated in Fig. 4 where the expression $I_s/(1 - I_s)$ is plotted as a function of the inverse of the temperature. The use of this relation to fit our data is justified by the following: Sachtler and van Santen⁷ have demonstrated that, for binary alloys as well as diluted solutions, surface segregation is a general phenomenon in conditions of thermodynamic equilibrium. However, in cases where no equilibrium is achieved, no segregation appears. This case is applicable to our experiments at low growth temperatures where $r_d < 6$ is measured. In cases with material deposition, a recent theory has been

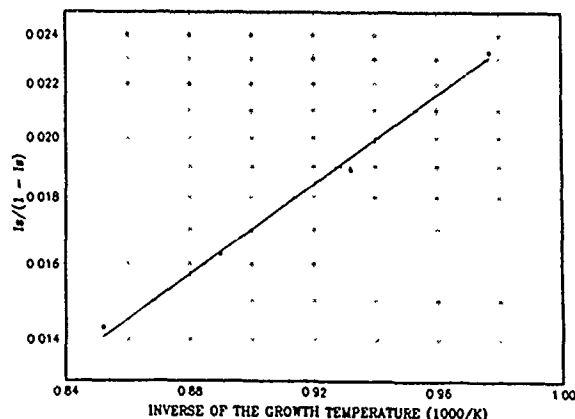


FIG. 4 Arrhenius plot of the calculated expression $I_s/(1 - I_s)$ obtained in the temperature range $750\text{--}900^\circ\text{C}$, where the growth is epitaxial. The boron surface atomic fractions (I_s) were measured by Auger spectroscopy.

developed by Barnett and Greene.¹ It predicts that the surface segregation ratio increases with increasing growth temperature T_s up to a critical temperature T^* characterizing the nonequilibrium regime. This regime is not observed in our measurements, since the trend in r_d behavior at low temperature is most probably controlled by the morphology changes rather than due to kinetics limitations. For $T_s > T^*$, r_d decreases with increasing T_s , and the authors demonstrate that in this particular case, the equation reduces to the classic relation [Eq. (1)] for diluted solutions. This case is applicable to our observations for $T_s > 750^\circ\text{C}$ (epitaxial region), and is explained by the fact that, at high growth temperatures, diffusion and segregation rates are much larger than the film growth rate. By fitting the Auger data ($T_s > 750^\circ\text{C}$) to Eq. (1), we have determined the value of the boron bulk atomic fraction $I_b = 5.4 \times 10^{-4}$, corresponding to a doping concentration of $N_a = 2.7 \times 10^{19} \text{ cm}^{-3}$, and to the free energy $\Delta G^S = -0.33 \pm 0.02 \text{ eV}$. The value of I_b has been used to calculate the segregation coefficient $r_d = I_s/I_b$, whose temperature behavior is presented in Fig. 3. The calculated value of N_a ($2.7 \times 10^{19} \text{ cm}^{-3}$) compared to the carrier concentration ($6.3 \times 10^{18} \text{ cm}^{-3}$) measured by Hall effect suggests that about 23% of the boron is electrically activated in this case. The difference is attributed to the presence into the film of B_2 or BO_x ($x < 1.5$) due to the incomplete reduction of the boron oxide. It is also interesting to note that no boron segregation has been reported in the work where doping was obtained by evaporation of pure boron,⁸ or sublimation of saturated boron-doped silicon.⁹ In the case where these experiments would be confirmed, the

boron segregation should be related to the B_2O_3 decomposition step at the surface.

In conclusion, the boron surface segregation ratio (r_d) in Si-MBE is measured by Auger spectroscopy as a function of the growth temperature T_s . The ratio r_d passes through a maximum ($r_d \approx 40$) near $T_s = 750^\circ\text{C}$, separating the epitaxial growth ($T_s > 750^\circ\text{C}$) from the polycrystalline growth ($T_s < 750^\circ\text{C}$). In the epitaxial region, r_d decreases with T_s , following a relation provided by the classical theory of segregation. In the polycrystalline region, r_d drops to two plateaux, whose values are determined by the morphology changes of the film.

This work is in part supported by the Semiconductor Research Corporation and the Army Research Office. We thank M. Arienzo, S. S. Iyer, and S. S. Delage for useful discussions.

¹S. A. Barnett and J. E. Greene, *Surf. Sci.* **151**, 67 (1985).

²Y. H. Xie, K. L. Wang, and Y. C. Kao, *J. Vac. Sci. Technol. A* **3**, 1035 (1985).

³A. Ishizaka, K. Nagakawa, and Y. Shiraki, *Proceedings of the 2nd International Symposium on Molecular Beam Epitaxy and Related Clean Surfaces Techniques*, Tokyo, Japan, 1982, p. 183.

⁴Y. Ota, *Thin Solid Films* **106**, 3 (1983).

⁵E. de Frésart, S. S. Rhee, and K. L. Wang, *Appl. Phys. Lett.* **49**, 847 (1986).

⁶M. J. Kelley and V. Ponec, *Prog. Surf. Sci.* **11**, 139 (1981).

⁷W. M. H. Sachtler and R. A. van Santen, *Appl. Surf. Sci.* **3**, 121 (1979).

⁸R. A. A. Kubiak, W. Y. Leong, and E. H. C. Parker, *J. Vac. Sci. Technol. B* **3**, 592 (1985).

⁹R. M. Ostrom and F. G. Allen, *Appl. Phys. Lett.* **48**, 221 (1986).

Resonant tunneling through a $\text{Si}/\text{Ge}_x\text{Si}_{1-x}/\text{Si}$ heterostructure on a GeSi buffer layer

S. S. Rhee, J. S. Park, R. P. G. Karunasiri, Q. Ye, and K. L. Wang

Device Research Laboratory, 7619 Boelter Hall, Electrical Engineering Department, University of California, Los Angeles, California 90024

(Received 14 April 1988; accepted for publication 19 May 1988)

Resonant tunneling of holes through an unstrained GeSi well between two strained Si barriers on a relaxed GeSi buffer layer has been observed for the first time. The peak-to-valley ratios of 2.1/1 at 4.2 K and 1.6/1 at 77 K in current-voltage characteristics were attained for light holes. Resonant tunneling from heavy-hole states was also observed at room temperature, as well as 77 and 4.2 K by conductance measurement. The positions of the resonance peaks are in good agreement with the light- and heavy-hole bound states in the quantum well.

Recent developments in Si molecular beam epitaxy (MBE) have made it possible to achieve device-quality epitaxial layers with controlled strain. The potential applications of $\text{Ge}_x\text{Si}_{1-x}/\text{Si}$ strain layer heterostructures and superlattices have been recently studied in the development of electronic¹⁻⁴ as well as optical⁵⁻⁷ devices. In spite of the importance of vertical transport through the potential barriers, no tunneling phenomena have been reported in Si-based heterostructures until recently by Liu *et al.*⁸ In device applications that take advantage of band-gap engineering, the double-barrier diode grown on a silicon buffer has limitations due to the limited critical thickness of the strained $\text{Ge}_x\text{Si}_{1-x}$ layers. For the realization of device applications, it is essential to grow $\text{Ge}_x\text{Si}_{1-x}/\text{Si}$ heterostructures on a relaxed $\text{Ge}_x\text{Si}_{1-x}$ buffer layer so that the vertical dimensions of the devices are not restricted to below the critical thickness. In that case, symmetrically strained superlattices may be grown.⁹ In this letter, we report the observation of tunneling of holes in $\text{Si}/\text{Ge}_x\text{Si}_{1-x}/\text{Si}$ double-barrier diodes on an unstrained $\text{Ge}_x\text{Si}_{1-x}$ buffer layer.

In the experiment, the $\text{Si}/\text{Ge}_x\text{Si}_{1-x}$ tunneling structures were grown in a Si MBE chamber with a base pressure of 7×10^{-11} Torr. Low-resistivity ($0.01 \Omega \text{ cm}$) Si(100) wafers were used in this experiment. The sample was cleaned by the Shiraki method¹⁰ prior to loading to the chamber, and the protective oxide layer was removed *in situ* by heating the wafer at 950°C for about 10 min. The sample was kept at 530°C during the epitaxial growth. The Si and Ge growth rates were 45 and $30 \text{ \AA}/\text{min}$, respectively. The Ge was evap-

orated using a conventional Knudsen cell, and *p*-type doping was obtained using a thermal boron source. The schematic band diagram of the double-barrier diode is shown in Fig. 1. First, a 7000-\AA -thick $\text{Ge}_{0.4}\text{Si}_{0.6}$ buffer layer was grown on the Si substrate, and then the double-barrier structure was grown on the buffer. The buffer layer was doped with B at about $5 \times 10^{18} \text{ cm}^{-3}$. The double-barrier structure consists of an undoped 40 \AA $\text{Ge}_{0.4}\text{Si}_{0.6}$ quantum well between two 50 \AA Si barriers. On top of the double barrier, a 7000-\AA -thick unstrained $\text{Ge}_{0.4}\text{Si}_{0.6}$ contact layer was grown with a B doping concentration of about $5 \times 10^{18} \text{ cm}^{-3}$. Just outside two Si barriers, 150-\AA -thick $\text{Ge}_x\text{Si}_{1-x}$ layers were intentionally undoped to prevent dopant diffusion into the quantum well structure. In our structure two Si barriers are coherently strained and the quantum well and the top contact layers as well as the buffer were unstrained.

Tunneling diodes $25\text{--}100 \mu\text{m}$ in diameter were fabricated using conventional lift-off and mesa-etching techniques, and Al was evaporated on mesas to make the contacts. The data presented in this letter were obtained using $50\text{-}\mu\text{m}$ -diam diodes, and the diodes with different sizes showed almost the same characteristics except for higher current for larger diodes. The current-voltage ($I(V)$) and the first and the second derivatives were measured using a computer-controlled tunneling spectroscopy system at 4.2, 77 K, and at room temperature. The $I(V)$, dI/dV , and d^2I/dV^2 of

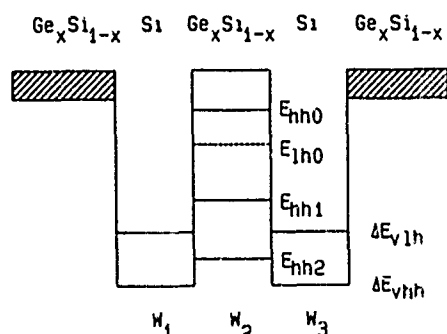


FIG. 1 Schematic band diagram of the double barrier diode. For the structure used in this experiment, $W_{1,3} = 50 \text{ \AA}$, $W_2 = 40 \text{ \AA}$, and $x = 0.4$.

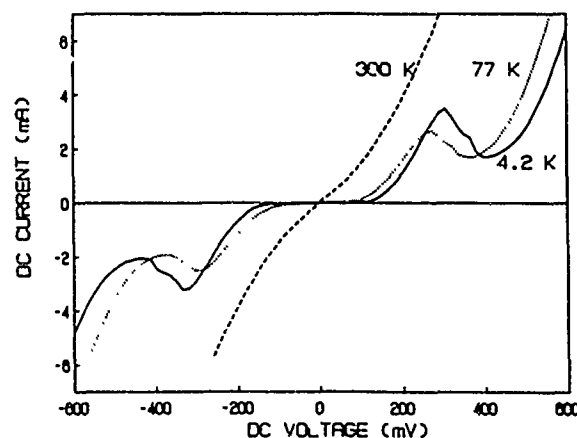


FIG. 2 Observed current-voltage characteristics for the structure shown in Fig. 1 at three different temperatures.

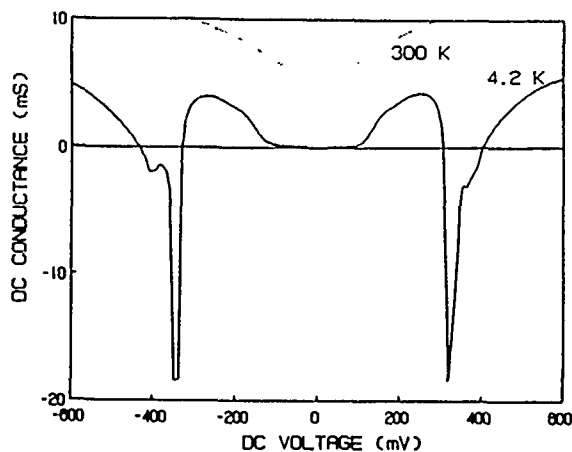


FIG 3 Conductance-voltage curves at 4.2 K and room temperature

the double-barrier diode are shown in Figs. 2, 3, and 4, respectively. The current peak-to-valley ratios were 2.1 and 1.6 at 4.2 and 77 K, respectively. Additional $I(V)$ and conductance data at higher bias, as shown in Fig. 5, were also obtained using a HP4145 parameter analyzer since the current at larger bias is substantially higher than that specified in our tunneling spectrometry setup. At liquid-nitrogen temperature, two peaks were observed at 350 and 900 mV as seen in the Fig. 5. At room temperature no differential negative resistance was observed. However, the resonance tunneling was clearly seen from the dI^2/d^2V data in Fig. 4. The oscillations seen on the dI^2/d^2V curve are due to the instabilities in the circuit when the resistance becomes negative.

The results of this experiment can be quantitatively analyzed using the band offsets,¹¹ and light-hole and heavy-hole states in the quantum well due to quantization. In Fig. 1, the valence-band offsets and possible bound state energies of light and heavy holes are shown schematically. In the unstrained $\text{Ge}_{0.4}\text{Si}_{0.6}$ layers, light-hole and heavy-hole bands are degenerate. However, in the strained Si barriers the light-hole band moves upwards because of tensile strain, while the heavy-hole band moves downwards. This light-hole and

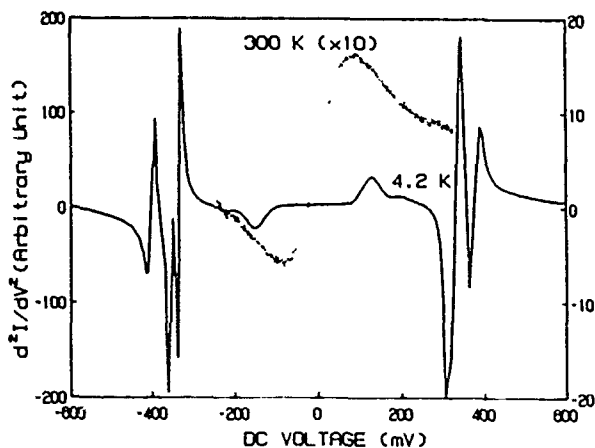


FIG 4 Second derivative of the $I(V)$ at 4.2 K and room temperature showing a peak near the origin due to the resonant tunneling through heavy-hole ground state. The oscillations in the negative resistance regions appear as a result of the instabilities of the circuit

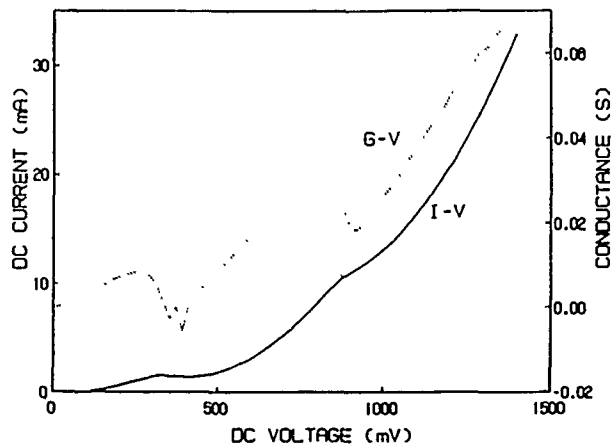


FIG 5. Current-voltage and first derivative at 77 K measured using a HP 4145 parameter analyzer showing the second peak at 900 mV due to the tunneling through first excited heavy-hole state.

heavy-hole band splitting in the coherently strained Si barriers is about 100 mV in our case.

In order to calculate the bound state energies in the quantum well for light and heavy holes, the envelope function approximation was used, including different effective masses in the well and the barriers. Linear interpolation of Si and Ge bulk data was used to estimate the effective masses of light hole and heavy hole in the tunneling structure. The estimated values of the light-hole and heavy-hole band offsets are $\Delta E_{v,th} = 211$ mV and $\Delta E_{v,hh} = 313$ mV, respectively. For the heavy hole there are three bound states in the quantum well at energies $E_{hh0} = 33$ mV, $E_{hh1} = 132$ mV, and $E_{hh2} = 277$ mV, and for the light hole only the ground state at $E_{lh0} = 67$ mV. All the values were measured downward from the band edge of the unstrained $\text{Ge}_{0.4}\text{Si}_{0.6}$ quantum well. The $I(V)$ characteristics shown in Figs. 2 and 5 can be understood quantitatively by considering the barrier heights and the bound states in the quantum well for the light and heavy hole, as discussed above. In Fig. 2 negative differential resistance due to resonant tunneling through the light-hole ground state (E_{lh0}) is clearly seen at 77 and 4.2 K. The resonant tunneling through the heavy-hole ground state is not visible in $I(V)$ and dI/dV , but is clearly seen in the d^2I/d^2V curve even at room temperature (see Fig. 4). The peak current for the resonance increased with decreasing temperature, while the valley current remained almost the same for different temperatures. The peak position of the resonance voltage also increased with decreasing temperature as a result of a larger voltage drop outside the double-barrier region caused by higher current flowing through the contacts. Both of the $I(V)$ and dI/dV in Fig. 5 show another resonant tunneling feature at 900 mV at 77 K and is due to the first excited heavy-hole state (E_{hh1}). The resonant tunneling through the second excited heavy-hole state (E_{hh2}) was not observed because of large leakage current, since the state lies above the light-hole band edge.

We have also fabricated different tunneling diodes on various types of GeSi substrates. The data showed general agreement with the interpretation given here. In the present case the well is unstrained while the barriers are strained and

others have different strains in the layers. The results show that the devices with the controllable strains in both the barrier and the well can be fabricated at will. More important, symmetrically strained superlattices can also be made for studying transport phenomena under controlled strain.

In conclusion, we have observed resonant tunneling through a double-barrier structure grown on a relaxed $\text{Ge}_x\text{Si}_{1-x}$ buffer layer. All the peaks appeared in the $I(V)$, dI/dV , and d^2I/dV^2 assigned to tunneling via the light-hole and heavy-hole bound states in the quantum well. From second derivative of the $I(V)$, the resonant tunneling at room temperature was also observed in $\text{Si}/\text{Ge}_x\text{Si}_{1-x}/\text{Si}$ heterostructures for the first time.

This work is in part supported by the Semiconductor Research Corporation, the Army Research Office, and the Office of Naval Research.

- ¹T. P. Pearsall, J. C. Bean, R. People, and A. T. Fiory, in Proceedings of the International Symposium on Silicon Molecular Beam Epitaxy, Pennington, NJ, 1985, p. 366.
- ²H. Daembks, H. J. Herzog, H. Jorke, H. Kibbel, and E. Kasper, IEEE Trans. Electron. Devices ED-33, 633 (1986).
- ³H. Temkin, J. C. Bean, A. Antreasyan, and R. Leibenguth, Appl. Phys. Lett. 52, 1089 (1988).
- ⁴T. Tatsumi, H. Hirayama, and N. Aizaki, Appl. Phys. Lett. 52, 895 (1988).
- ⁵H. Temkin, T. P. Pearsall, J. C. Bean, R. A. Logan, and S. Luryi, Appl. Phys. Lett. 48, 963 (1986).
- ⁶T. P. Pearsall, J. Bevk, L. C. Feldman, J. M. Bonar, and J. P. Mannacerts, Phys. Rev. Lett. 58, 729 (1987).
- ⁷S. Froyen, D. M. Wood, and A. Zunger, Phys. Rev. B 36, 4547 (1987).
- ⁸H. C. Liu, D. Landheer, M. Buchanan, and D. C. Houghton, Appl. Phys. Lett. 52, 1809 (1988).
- ⁹E. Kasper, Surf. Sci. 176, 630 (1986).
- ¹⁰A. Ishizaka and Y. Shiraki, J. Electrochem. Soc. 133, 666 (1986).
- ¹¹R. People, Phys. Rev. B 32, 1405 (1986).

Study of molecular-beam epitaxially grown $\text{Ge}_x\text{Si}_{1-x}/\text{Si}$ layers by Raman scattering

S. J. Chang, M. A. Kallel, and K. L. Wang

Device Research Laboratory, Electrical Engineering Department, University of California, Los Angeles, California 90024

R. C. Bowman, Jr.

The Aerospace Corporation, M1-109, P. O. Box 92957, Los Angeles, California 90009

Peter Chow

Perkin-Elmer, MBE Division, Eden Prairie, Minnesota 55344

(Received 11 April 1988; accepted for publication 13 June 1988)

The strain distribution of a $\text{Ge}_x\text{Si}_{1-x}/\text{Si}$ strained layer superlattice (SLS) as a function of the distance from the superlattice/substrate interface has been studied by Raman spectroscopy. A small-angle bevel was made by angle lapping on a given thick $\text{Ge}_x\text{Si}_{1-x}/\text{Si}$ SLS so that it is possible to probe the structure at different thicknesses. The Raman spectrum as a function of the distance from interface is then obtained. The results indicate that, as we move away from the substrate interface, the compression strain in the alloy layers decreases while the tensile strain in the Si layers increases. From linewidth measurement of the Raman peaks, it appears that there is an improved crystal quality and a lower concentration of defects going away from the substrate interface.

I. INTRODUCTION

Recently, the successful growth of a $\text{Ge}_x\text{Si}_{1-x}/\text{Si}$ strained layer superlattice¹ has led to some potentially useful photonic and electronic applications. The built-in strain induced by the 4.2% lattice mismatch between Ge and Si has been investigated by various authors.¹⁻³ It is generally recognized that the band offset at the $\text{Ge}_x\text{Si}_{1-x}/\text{Si}$ interface will depend on the distribution of strain between the two layers.^{2,4}

In order to grow a dislocation-free $\text{Ge}_x\text{Si}_{1-x}/\text{Si}$ SLS, both the total superlattice thickness and the individual layer thickness have to be smaller than their respective critical thicknesses, T_c and h_c .⁵ A very thick $\text{Ge}_x\text{Si}_{1-x}/\text{Si}$ SLS with equal individual $\text{Ge}_x\text{Si}_{1-x}$ and Si layer thicknesses will eventually relax to a structure with a lattice constant equal to that of unstrained $\text{Ge}_{x/2}\text{Si}_{1-x/2}$ and become symmetrically strained even without a thick $\text{Ge}_{x/2}\text{Si}_{1-x/2}$ buffer layer. In such a case, the upper layers of the superlattice could be used for subsequent device fabrication while the lower layers of the superlattice act as a buffer.^{6,7}

Raman scattering has been a powerful technique to characterize $\text{Ge}_x\text{Si}_{1-x}/\text{Si}$ structures. For a bulk $\text{Ge}_x\text{Si}_{1-x}/\text{Si}$ alloy, there are three main peaks at around 300, 400, and 500 cm^{-1} ascribed respectively to the vibrations of Ge-Ge, Ge-Si, and Si-Si pairs.⁸ The dependence of the peak positions and the linewidth in the $\text{Ge}_x\text{Si}_{1-x}$ alloy on the fractional composition x has been studied. The $\text{Ge}_x\text{Si}_{1-x}/\text{Si}$ structure has also been studied with the focus being mainly on determining the strain and the critical thickness.⁹ In this paper, the objective is to study the strain distribution in the superlattice as a function of the distance from the interface using the technique of Raman scattering.

II. EXPERIMENT

The Raman experiments were performed at room temperature in the near backscattering geometry. The samples

were excited with the 514.5-nm line from a Spectra Physics 2020 argon ion laser and the scattered light was analyzed with a Spex 1404 double spectrometer and an EG&G 941 photon counter. In order to study the crystal properties of the layers close to the interface of thick $\text{Ge}_x\text{Si}_{1-x}/\text{Si}$ SLS, a small-angle bevel of 0.0035 rad was made on the samples by angle lapping, as shown in the inset of Fig. 1.¹⁰ The laser light was focused with a cylindrical lens to give a narrow line with a width of 12 μm and a length of 60 μm . The Raman spectra were obtained by successively moving the sample in the direction perpendicular to the bevel edge with a micrometer. With the known bevel angle and the distance between the focused laser light and the bevel edge, the effective superlattice thickness t of the laser probing position could be calculated.

The $\text{Ge}_x\text{Si}_{1-x}/\text{Si}$ superlattice samples used in this study are listed in Table I. Samples were grown by an ultra-

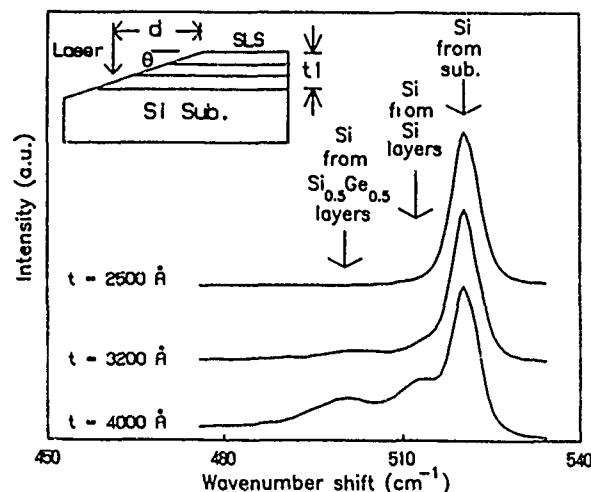


FIG. 1. Raman spectra for sample 62-4 at Si region with laser probing at positions with different superlattice thickness. The inset shows the schematic diagram for bevel etched samples, where $\theta = 0.0035$ rad is the bevel angle and $t = t_1 - d\theta$ is the effective superlattice thickness.

4-layer superlattice samples this work.

| Number of periods | Buffer layer |
|-------------------|---------------------------------------|
| 40 | Si |
| 40 | Ge _{0.25} Si _{0.75} |
| 50 | Si |

ay system with a buffer 2°C and a superlattice typical surface Raman 100 superlattice sample. The arrow positions in encies of our measure- gle-alloy-layer sample. of this SLS sample as- Ge—Ge, Ge—Si, and e all clearly shifted up- i strain while the peak ating from the Si layers eral tensile strain.

on for sample 62-4 with ent superlattice thick- 1 with three peaks, the o Si-Si vibrations from one from Si layers, and decreases, the signals and eventually merge ter peak at 520 cm⁻¹. -Si vibrational Raman

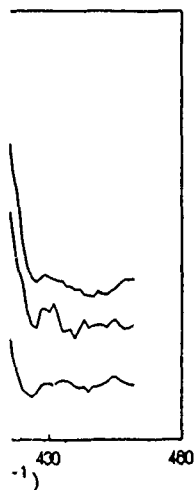


FIG. 3. Ge-Ge Raman spectra for sample 62-4 at different depths. Two competing signals with different intensities are seen as the laser probing at different sample positions.

spectra as a function of the distance t from the superlattice/substrate interface for the same sample. It can be seen that as we get closer to the interface, the Ge-Si peak becomes broader, more asymmetric, and the peak position shifts to the higher-frequency side. This indicates that the compression strain in the alloy layers is larger and that the crystal quality becomes worse as we approach the interface in accord with the fact that misfit dislocations are created at the interface as the SLS relaxes. Similarly, in Fig. 3, we obtain the signal corresponding to the Ge-Ge vibrational mode for the same sample 62-4. In this case, the silicon two transverse acoustic phonon scattering peak¹¹ from the X point at 300 cm⁻¹ becomes dominant as we approach the interface such that it is not possible to determine the actual position or linewidth of the Ge-Ge Raman peak.

Figure 4 shows the peak positions of the Ge-Si Raman peak as a function of t that were obtained from sample 62-4. Although the uncertainty of the peak position is relatively large due to the broad Raman lines, an increasing peak shift of 2 cm⁻¹ is observed near the interface. Several thin Ge_{0.5}Si_{0.5}/Si SLS samples with the same individual layer thickness (i.e., 50 Å) but different total superlattice thickness (i.e., 300, 600, and 1000 Å) were also tested. The surface Ge-Si Raman peak positions as a function of the total superlattice thickness of these samples are also shown in Fig. 4 for comparison. It can be seen that for the bevel-etched thick sample, the Ge-Si Raman peak positions did shift to higher frequency for layers close to the interface. However, these values are still not as high as those from the thin Ge_{0.5}Si_{0.5}/Si samples with the same total thickness. This can be understood by the fact that, for a thick Ge_xSi_{1-x}/Si SLS, the strain on the superlattice layers is relieved by dislocations generated near the superlattice/substrate interface. In order to make a quantitative estimate of the strain distribution, we assume (1) the sample 62-4 is 100% relaxed at the surface such that the Ge_{0.5}Si_{0.5} and Si layers furthest from the Si substrate are both strained by approximately 1.05%, and (2) the linear relationship between strain and peak frequency shift,¹²

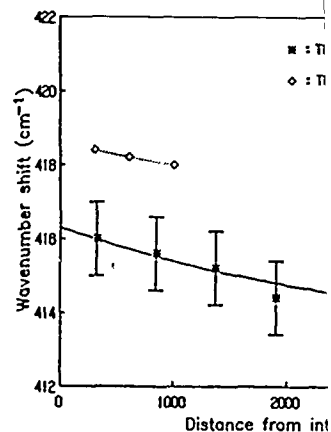


FIG. 4. Depth profiles of Ge-Si Raman strain for sample 62-4. These results are compared with the same individual layer thickness.

$$\delta\omega = b \times \epsilon,$$

is valid, where $b = 4.55 \times 10^2$ cm⁻¹ for Ge_xSi_{1-x} alloy and ϵ is the strain in the Ge_xSi_{1-x} layers. The amount of strain at different distances from the interface for the Ge-Si peak for sample 62-4 is shown in Fig. 4. The strain is found to be smaller than the strain in bulk Ge_{0.5}Si_{0.5} and Si layers, indicating that dislocations generated near the interface relieve the strain.

To investigate the crystal quality near the interface, we obtained the Raman spectrum of the Ge-Si peak as shown in Fig. 3. The peak is broader and broader linewidth as the distance from the interface decreases. These results confirm that the crystal quality near the interface is poorer.

Similar results are obtained for sample 94-1 with $x = 0.5$, which has less Ge in the alloy layers for the same total thickness. Thus for this sample the change in peak position is not as easy to measure. The Si peak from sample 94-1 was found to be broader than the Si peak from sample 62-4, indicating that the Si peak is having a Ge_{x/2}Si_{1-x/2} buffer layer. The peak position is symmetrically strained with the linewidth. Unfortunately, the prediction from the present study is that the superlattice/buffer interface is the underlying buffer region over which the strain is relieved. From the Raman spectrum (Fig. 3), four different peaks at the silicon two transverse acoustic phonon scattering peak are going from lower- to higher-frequency as the distance from the alloy layers, from the Si substrate, and from the surface. As the distance from the surface increases, the intensities of

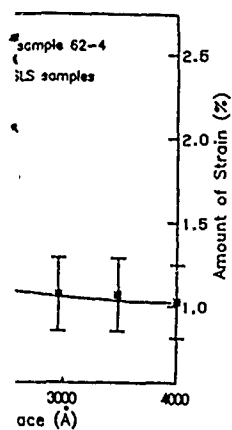


FIG. 4. Peak position and the amount of strain compared to the thin SLS samples.

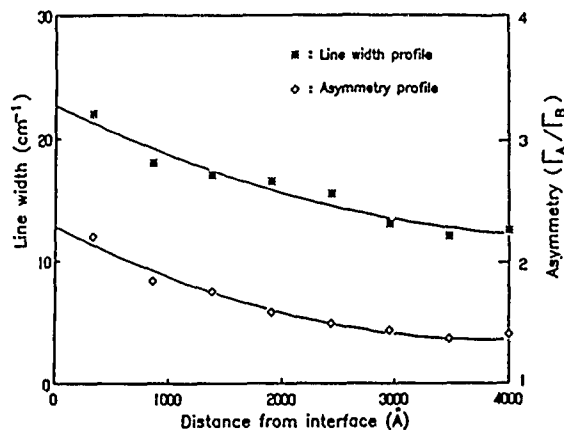


FIG. 5. Depth profiles of linewidth and asymmetry measurement for sample 62-4. The narrower and more symmetric Raman peak taken at layers close to surface suggests a better crystallinity for those layers away from substrate.

(1) Γ^{-1} for the Ge-Si peak of the amount of strain on the amount of strain calculated at different using the measured shifts of Γ illustrated with the coordinate of Fig. 4. The maximum of the 2.1% lattice mismatch which is attributed to the interface.¹⁰

quality distribution for the new width and asymmetry of 5, where greater asymmetry surface is approached. These data for the $\text{Ge}_{0.5}\text{Si}_{0.5}$ layers

and from the Ge-Si Raman shift of 0.3. However, since there is more variation in the strain or is not possible to verify this profile, since as we probe close to the interface, the signal from the unstrained SLS. (As shown), we can observe a region corresponding to, energy shift, the Si-Si modes of the buffer layer, from the Si layer the distance from the interface. The two signals from the SLS

increase, while that of the two signals from the buffer layer and the substrate decrease.

In summary, the Raman spectra taken on small-angle beveled strained-layer superlattice structures provide an effective way to determine quantitatively the distribution of strain and qualitatively the depth profile of crystallinity throughout the layers of interest. It is found that for a thick $\text{Ge}_x\text{Si}_{1-x}/\text{Si}$ SLS, the compression strain on the $\text{Ge}_x\text{Si}_{1-x}$ alloy layers increases and the crystal quality degrades for layers close to the substrate.

ACKNOWLEDGMENTS

The authors want to thank Dr. T. L. Lin and Dr. R. P. G. Karunasiri for their valuable discussion. The support of the Office of Naval Research and the Army Research Office is acknowledged. This work is also partially supported by The Aerospace Sponsored Research program.

- ¹R. People, IEEE Trans. Quantum Electron. QE-22, 1696 (1986).
- ²G. Abstreiter, H. Brugger, and T. Wolf, Phys. Rev. Lett. 54, 2441 (1985).
- ³R. People, J. C. Bean, and D. V. Lang, J. Vac. Sci. Technol. A 3, 846 (1985).
- ⁴R. People and J. C. Bean, Appl. Phys. Lett. 48, 538 (1986).
- ⁵R. Hull, J. C. Bean, F. Cerdeira, A. T. Fiory, and M. Gibson, Appl. Phys. Lett. 48, 56 (1986).
- ⁶E. Kasper, H. J. Herzog, H. Jorke, and G. Abstreiter, Superlatt. Microstruct. 3, 141 (1987).
- ⁷C. G. Tuppen, C. J. Gibbing, S. T. Davey, M. H. Lyons, M. Hockly, and M. A. Halliwell, Proceedings of the 2nd International Symposium on Silicon MBE (1987), p. 36.
- ⁸W. J. Brya, Solid State Commun. 12, 253 (1973).
- ⁹F. Cerdeira, A. Pinzuk, J. C. Bean, B. Batlogg, and B. A. Wilson, J. Vac. Sci. Technol. B 3, 600 (1985).
- ¹⁰H. Huang, P. Y. Yu, M. Charasse, Y. Lo, and S. Wang, Appl. Phys. Lett. 51, 192 (1987).
- ¹¹P. A. Temple and C. E. Hathaway, Phys. Rev. B 7, 3685 (1973).
- ¹²F. Cerdeira, A. Pinzuk, J. C. Bean, B. Batlogg, and B. A. Wilson, Appl. Phys. Lett. 45, 1138 (1984).

Studies of molecular-beam epitaxy growth of GaAs on porous Si substrates

Y. J. Mii

Device Research Laboratory, University of California, Los Angeles, Los Angeles, California 90024

T. L. Lin

Jet Propulsion Laboratory, California Institute of Technology, Pasadena, California 91109

Y. C. Kao, B. J. Wu, and K. L. Wang

Device Research Laboratory, University of California, Los Angeles, Los Angeles, California 90024

C. W. Nieh and D. N. Jamieson

California Institute of Technology, Pasadena, California 91125

J. K. Liu

Jet Propulsion Laboratory, California Institute of Technology, Pasadena, California 91109

(Received 5 September 1987; accepted 14 December 1987)

GaAs has been grown on porous Si directly and on Si buffer layer-porous Si substrates by molecular-beam epitaxy. In the case of GaAs growth on porous Si, transmission electron microscopy (TEM) reveals that the dominant defects in GaAs layers grown on porous Si are microtwins and stacking faults, which originate from the GaAs/porous Si interface. GaAs is found to penetrate into the porous Si layers. By using a thin Si buffer layer (50 nm), GaAs penetration diminishes and the density of microtwins and stacking faults is largely reduced and localized at the GaAs/Si buffer interface. However, there is a high density of threading dislocations remaining. Both Si (100) aligned and four degree tilted substrates have been examined in this study. TEM results show no observable effect of the tilted substrates on the quality of the GaAs epitaxial layer.

I. INTRODUCTION

Because of the potential in integration of GaAs and Si circuits monolithically, the GaAs on Si technology has recently drawn a great deal of interest. However, the 4% mismatch between GaAs and Si lattice constants causes the generation of a large density of misfit dislocations. The problem is exacerbated by the large difference of the thermal expansion coefficients between GaAs and Si which results in a very large postgrowth tensile stress in the grown GaAs layers.

Several approaches, such as the use of strained-layer superlattice,¹ rapid thermal annealing,² and tilted substrates,³ have been utilized to suppress the propagation of threading dislocations toward the GaAs active region. To date, however, the total defect density of the epitaxial layers grown on Si substrates is still much higher than that on GaAs substrates.

Recently, a possible approach for growing defect-free materials on lattice mismatched substrates has been suggested by Luryi and Suhir⁴ in which a substrate having small seed pads of a lateral dimension about 10 nm is used. However, this small size of seed pads is extremely difficult to achieve if not impossible by present lithography techniques. Alternatively, porous Si substrates which have surface pads with dimensions ranging from 3 to 20 nm appear to be an ideal substrate with seed pads for epitaxial growth.

Based on this idea, lattice mismatched GaAs⁵ and CoSi₂⁶ films have been previously grown on porous Si showing good crystallinity and surface morphology. The dominant defects in the GaAs layers are found to be microtwins and stacking faults. In this study, a thin Si buffer layer is grown on top of porous Si substrates to examine its effects on defect struc-

ture. Tilted Si substrates as well as aligned (100) Si substrates are used to study their effects on the GaAs layer grown both directly on porous Si and on buffer layer-porous Si substrates.

II. EXPERIMENT

Porous Si is formed by anodizing single-crystalline Si substrates in HF electrolyte.⁶ The porosity is determined by the anodizing current density, HF concentration, and substrate doping density. P-type Si (100) substrates with a resistivity of 0.02 Ω cm are first cleaned by repeatedly boiling in nitric acid and dipping in HF. Then, the porous Si layers are formed by anodizing the substrates in a 30% HF electrolyte. After anodization, a protective oxide layer is formed immediately in a H₂SO₄:H₂O₂:H₂O = 4:1:4 solution.

To grow the Si buffer layer, the substrate is loaded into the Si molecular-beam epitaxy (MBE) growth chamber. The protective oxide layer is removed by the Si beam self-cleaning method at 750 °C.⁷ The Si buffer layer is grown at a growth rate of 3 nm/min. Then, the substrate is unloaded from the Si MBE chamber and another protective oxide layer is formed on the Si substrates.

Prior to GaAs growth, the substrate is dipped in 49% HF in N₂ ambient⁸ to remove the protective oxide. No further high temperature treatment except outgassing at 700 °C is performed on the substrates so as to prevent the collapse of the porous Si structure. GaAs epitaxial growth is performed by a two-step growth technique. The first layer is grown at 500 °C for 20 nm with 0.4 μ m/h growth rate and the second layer is grown at 650 °C for 1- μ m thickness with 1 μ m/h growth rate.

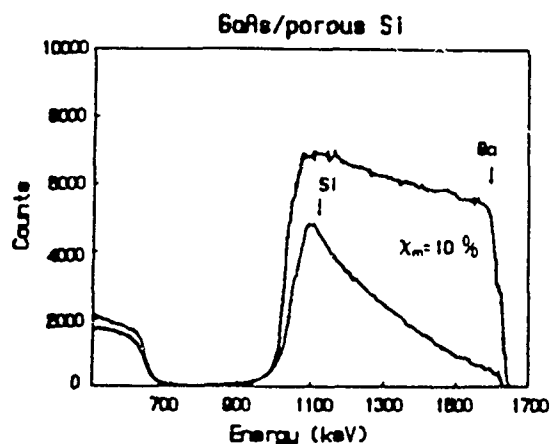


FIG. 1. (a) RBS of GaAs on porous Si (aligned substrate) (b) RBS of GaAs on single-crystalline Si (aligned substrate)

III. RESULTS AND DISCUSSION

Surface morphologies of the GaAs on porous Si and GaAs or Si layers are found to be generally similar and smooth although some features are found with a density of $2 \times 10^8 \text{ cm}^{-2}$. The roughness of the porous Si surface does not seem to deteriorate the surface morphology of the GaAs on porous Si samples when compared to that of the GaAs on Si samples grown at the same time.

The crystallinity of the GaAs layers is examined by Rutherford backscattering spectroscopy (RBS). As shown in Fig. 1, the minimum channeling yield x_m of the GaAs on porous Si is 10%, a little smaller than x_m of 16% for the GaAs on Si samples. Furthermore, the comparison of the dechanneling behaviors of Figs. 1(a) and 1(b) indicates that the crystallinity of GaAs grown on porous Si substrates improves more rapidly than GaAs on Si as the epitaxial GaAs thickness increases.

From cross-section TEM, the dominant defects in GaAs on porous Si layers are microtwins and stacking faults as shown in Fig. 2. Both microtwins and stacking faults originate from the GaAs/porous Si interface. The majority of

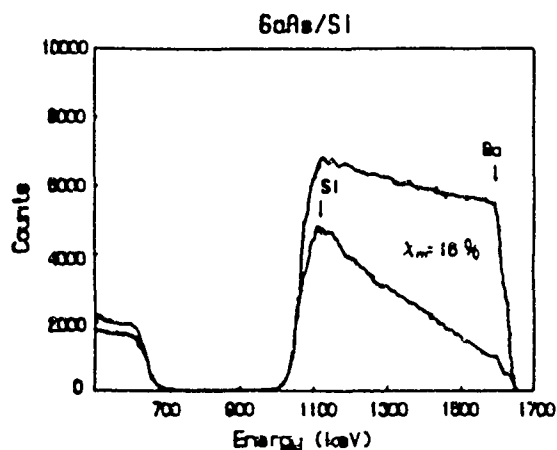


FIG. 2. Cross-section TEM of GaAs on porous Si (aligned substrate), showing that the dominant defects in GaAs layer are microtwins and stacking faults which originate from the GaAs/Si interface.



FIG. 3. Lattice-image TEM of GaAs/porous Si interface (aligned substrate). GaAs is shown to penetrate into the pores.

microtwins terminate within the first 190 nm of the epitaxial layer and the defect density is reduced to $2 \times 10^9 \text{ cm}^{-2}$ at the GaAs surface. GaAs is observed to penetrate into the pores as in Fig. 3. The nucleation of GaAs in the pores is suspected to cause the formation of microtwins and stacking faults.

To eliminate the penetration of GaAs and to reduce the high density of microtwins and stacking faults, a 50-nm thickness of Si buffer layer is grown on the porous Si substrate. The Si buffer layer is shown to bridge over the pores and to smooth the surface of porous Si in Fig. 4. The defect structure of the GaAs layer grown on this Si buffer is shown in Fig. 5, where the dominant defects are threading dislocations instead of microtwins and stack faults. The difference of defect structures for GaAs grown on porous Si and on buffer layer-porous Si samples suggests that the surface roughness of porous Si indeed results in the formation of microtwins and stacking faults.

Samples are also grown on the tilted substrates with and without Si buffer layers. From TEM micrographs, no significant difference between the tilted and aligned substrates is

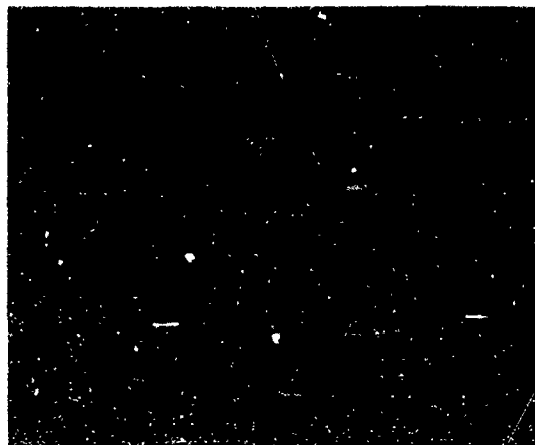


FIG. 4. Lattice-image TEM of GaAs/Si buffer/porous Si interface (aligned substrate). The Si buffer layer of 50-nm thickness has bridged over the pores. Microtwins and stacking faults are largely reduced and localized at the GaAs/Si buffer interface.



FIG. 5. Cross-section TEM of GaAs on Si buffer/porous Si (aligned substrate) showing the remaining large density of threading dislocations.



FIG. 6. Cross-section TEM of GaAs on Si buffer/porous Si (four tilted substrates). The defect structure and density are similar to those for aligned substrates as in Fig. 5.

observed in our present study. Figure 6 shows the TEM micrograph of the GaAs layer grown on the Si buffer layer on the tilted porous Si substrate. The defect structure and density are similar to those for aligned substrates.

To further reduce the defect density, several parameters have to be optimized. The growth conditions, porosity, and buffer layer thickness should be varied for examination of the effect of each parameter on grown GaAs epitaxial layers. Alternatively, a heterobuffer system such as GaAs/Si_{1-x}Ge_x/porous Si can be adopted. By tuning the Ge percentage of the buffer layer, defects may be confined in the heterobuffer layer.

IV. SUMMARY

GaAs layers have been grown on (100) aligned and tilted porous Si substrates and no significant difference of the qualities between them are observed. The GaAs growth is also done either directly on porous Si or on a thin Si buffer layer on porous Si. In the former, the dominant defects are found to be microtwins and stacking faults which originate from the roughness of porous Si surface. For the latter, the thin Si buffer layer of 50-nm thickness is shown to effectively smooth the porous Si surface and to reduce microtwins and stacking faults. There remains a high density of threading dislocations in the buffered samples. It is expected that the density may be reduced further by optimizing the growth conditions, porosity, and buffer layer thickness. Alternatively, a heterobuffer system such as GaAs/Si_{1-x}Ge_x/porous Si may also be used to further suppress the defect density of GaAs epitaxial layers.

ACKNOWLEDGMENTS

The work performed by University of California, Los Angeles is supported in part by the Office of Naval Research and the Army Research Office. The research described in this paper was carried out in part by the Jet Propulsion Laboratory (JPL), California Institute of Technology, and was sponsored by the Strategic Defense Initiatives Organization, Innovative Science and Technology office, and the National Aeronautics and Space Administration. The work was performed as part of JPL's Center for Space Microelectronics Technology. One of us (C.W.N.) acknowledges the support of the National Science Foundation under Grant No. DMR-842119.

¹R. Fischer, D. Neyman, H. Zabel, H. Morkoç, C. Choi, and N. Otsuka, *Appl. Phys. Lett.* **48**, 1223 (1986).

²J. W. Lee, H. Shichijo, H. L. Tsai, and R. J. Matyi, *Appl. Phys. Lett.* **50**, 31 (1987).

³S. Luryi and E. Suhir, *Appl. Phys. Lett.* **49**, 140 (1986).

⁴T. L. Lin, L. Sadwick, K. L. Wang, S. S. Rhee, Y. C. Kao, C. W. Nieh, D. N. Jamieson, and J. K. Liu, in *Heteroepitaxy on Silicon*, edited by J. C. C. Fan, J. M. Philips, and B. Y. Tsau (Materials Research Society, Pittsburgh, PA, 1987), p. 113.

⁵Y. C. Kao, D. Jamieson, G. Bai, C. W. Nieh, T. L. Lin, B. J. Wu, H. Y. Chen, and K. L. Wang, in *Heteroepitaxy on Silicon*, edited by J. C. C. Fan, J. M. Philips, and B. Y. Tsau (Materials Research Society, Pittsburgh, PA, 1987), p. 473.

⁶T. Unagami and M. Seki, *J. Electrochem. Soc.* **125**, 1339 (1978).

⁷T. L. Lin, S. C. Chen, Y. C. Kao, and K. L. Wang, *Appl. Phys. Lett.* **48**, 1793 (1986).

⁸P. J. Grunthaner and F. J. Grunthaner (to be published).

Intersubband optical absorption in coupled quantum wells under an applied electric field

Perng-fei Yuh and K. L. Wang

Device Research Laboratory, Department of Electrical Engineering, University of California, Los Angeles, California 90024-1600

(Received 18 March 1988)

The very large tunability of the transition energy when an electric field is applied is found in the intersubband optical transition in two strongly coupled semiconductor quantum wells. The energy of the absorption peak can shift to red or blue and is very sensitive to the electric field, in contrast to the single-well case, which has only a small blue shift. The oscillator strengths and the selection rule depend on the degree of coupling and are quite different from the single-well case. The method we use to characterize the energy levels and the wave functions of the coupled quantum wells has several advantages over the previous theoretical calculations in that the effective-mass difference, the finiteness of the barrier height, and arbitrary structure of the quantum wells can be taken into account by using a transfer-matrix technique.

I. INTRODUCTION

The electric field dependence of the absorption coefficient in semiconductor quantum wells and superlattices has been studied extensively for possible electro-optical applications.¹⁻⁴ The exciton absorption peak of the interband transition (valence-to-conduction-band transition) in quantum-wells shifts to long wavelength (red shift) when the electric field is applied and is known as the quantum confined Stark effect. The quantum confined Stark effect in quantum wells is more significant than the Franz-Keldysh effect in the bulk semiconductor due to the confinement of the wave functions in the quantum wells.³ On the other hand, the absorption edge of the intersubband transition (subband to subband transitions within the conduction band) in quantum wells shift to short wavelength (blue shift) under an applied electric field.^{5,6} This intersubband Stark shift is small and cannot be used in optical modulation applications since the relative energies of the sublevels in a single well do not change much by the electric field.

The energy levels originated from different wells in coupled quantum wells, however, can be tuned individually by applying electric field. The strength of this interwell transition is small because the wave functions are partially overlapped.⁷ The coupled quantum wells are defined as the quantum-well structure comprising more than one quantum well with interwell spacings and barriers sufficiently small so that significant amount of interaction takes place.⁸ The energy states and wave functions of the coupled quantum wells in the absence of electric field were calculated by several authors.⁸⁻¹⁰ We have calculated the energy states for a superlattice consisting of coupled-well basis.¹¹ Experimental investigation of the interband transition of the coupled quantum wells is also carried out.^{7,12-14}

In this paper a formalism of the dispersion relation is developed for a general quantum well structure in the presence of the electric field. The effective-mass difference, coupling of the conduction band to the valence and split-off bands, and the finite height of the

barriers are also taken into account. As a special case, the intersubband optical transitions in coupled quantum wells are analyzed by this approach. The Stark shift in the coupled wells is considerably larger than that in the single-well case while the oscillator strength is smaller for the former, depending on the degree of coupling. The selection rule also depend on how the wells are coupled. For example, the $1 \rightarrow 3$ transition, which is forbidden in the single-well case, is possible in the coupled well case.

II. METHOD

The dispersion relation of an isolated quantum well is derived here. Figure 1 shows the conduction-band edge of an arbitrary quantum-well structure consisting of a finite number of layers with the total length L . The quantum-well structure is bounded by two infinitely thick potential barriers with height eV_l and eV_r on the left and right, respectively. The energies of interest are between the bottom of the wells and the minimum of eV_l and eV_r . The wave functions Ψ_l and Ψ_r on the left and right contacts, respectively, are

$$\begin{aligned}\Psi_l &= Ae^{\kappa_l z}, \quad z \leq 0 \\ \Psi_r &= Be^{-\kappa_r(z-L)}, \quad z \geq L\end{aligned}\quad (1)$$

where

$$\begin{aligned}\kappa_l^2 &= -(2m_l^*/\hbar^2)(E - eV_l - E_1), \\ \kappa_r^2 &= -(2m_r^*/\hbar^2)(E - eV_r - E_1),\end{aligned}$$

E is the total energy and $E_1 = \hbar^2 k_1^2 / 2m^*$, k_1 is the wave vector normal to the z direction, and m^* is the effective mass in the corresponding region. Using the transfer-matrix technique,¹⁵ Ψ_l and Ψ_r are related by

$$\begin{bmatrix} \Psi_r \\ \Psi_r' \\ m_r \end{bmatrix} = S(L, 0) \begin{bmatrix} \Psi_l \\ \Psi_l' \\ m_l \end{bmatrix}, \quad (2)$$

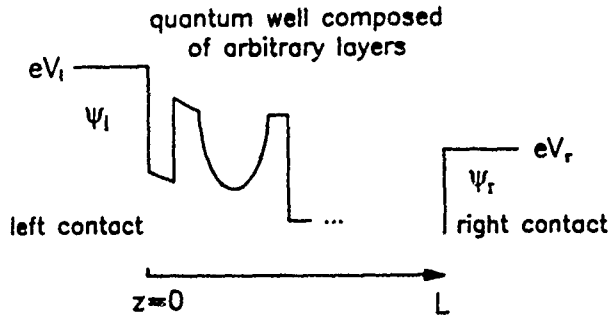


FIG. 1. Conduction-band edge of an arbitrary quantum well consisting of a finite number of layers with the total length L . Ψ_l and Ψ_r are conduction-band envelope functions along the z direction for the left and right contacts with potential eV_l and eV_r , respectively.

where S is a 2×2 transfer matrix. From Eqs. (1) and (2), the constant A and B can be eliminated and the dispersion relation is readily obtained as

$$-\frac{m^*}{\kappa_r} = \frac{S_{11} + (\kappa_l/m_l^*)S_{12}}{S_{21} + (\kappa_l/m_l^*)S_{22}} \quad (3)$$

In calculating an arbitrary potential, the quantum well is divided into several sublayers. Each sublayer contains only a linear potential (tilted or constant). The transfer matrix S is the product of transfer matrices of the sublayers. The explicit expressions of the subtransfer matrix are given in Ref. 11 for a linear potential by the effective mass, two- and three-band models, respectively. The dispersion relations for two- and three-band models are obtained by substituting κ/m^* in Eq. (3) with

$$\begin{aligned} \frac{\kappa}{m^*} &\rightarrow \frac{\kappa}{E - V_p}, \\ \frac{\kappa}{m^*} &\rightarrow \kappa \left[\frac{2}{E - V_p} + \frac{1}{E - V_o} \right], \end{aligned} \quad (4)$$

where V_p and V_o are the light-hole band and split-off band maximum, respectively.¹¹ The wave functions can be constructed once the energy states are determined.

The absorption coefficient of the intersubband transition from initial state n to the final state n' in the dipole approximation is given by

$$\alpha = \frac{\pi e^2 \hbar c \mu_0}{2m^* n_r} f_{n'n} J_{n'n}(\omega) \times \Delta N, \quad (5)$$

where μ_0 is the permeability and c is the speed of light. The index of refraction n_r and the effective mass m^* are considered to be the average values in the quantum-well structure. The oscillator strength $f_{n'n}$ is given by

$$f_{n'n} = \frac{2}{m^* \hbar \omega} P_{n'n}^2 = \frac{2m^*}{\hbar^2} E_g \langle n' | z | n \rangle^2, \quad (6)$$

where $P_{n'n}$ is the momentum matrix element and $E_g = E_{n'} - E_n$ is the transition energy. The joint density of states $J_{n'n}$ in intersubband transitions is a δ function

$$J_{n'n} = 2\delta(\hbar\omega - E_g).$$

The broadening effect can be incorporated by experimental linewidth and then the density of states can be written as

$$J_{n'n} = \frac{2}{\pi} \frac{\hbar/T_2}{(E_g - \hbar\omega)^2 + (\hbar/T_2)^2}, \quad (7)$$

where T_2 is of the order 10^{-13} sec by recent experiments.^{5,16} The population difference ΔN of the initial state to the final state at finite temperature can be obtained,

$$\Delta N = N_n - N_{n'} = \frac{4\pi m^*}{h^2 L} kT \ln \frac{1 + e^{-(E_n - E_f)/kT}}{1 + e^{-(E_{n'} - E_f)/kT}}, \quad (8)$$

where L is the width of the quantum well and E_f is the Fermi energy. The peak absorption occurs at $\hbar\omega = E_g$ and is

$$\alpha = (4.3686 \times 10^4) f_{n'n} \frac{T_2}{10^{-13} \text{ sec}} \frac{\Delta N}{10^{18} \text{ cm}^{-3}} (\text{cm}^{-1}) \quad (9)$$

for the material parameters of GaAs.

III. RESULTS

The coupled quantum well structure comprising two wells A and B of dimension $W_A = 100 \text{ \AA}$ (35 monolayers) and $W_B = 50 \text{ \AA}$ (17 monolayers) and a barrier of dimension 30 \AA (11 monolayers) inserted between A and B is investigated. This coupled-quantum-well structure is bounded by thick n^+ barriers such that the voltage drops only in the wells and the thin barrier. All the wells are assumed GaAs and the barriers $\text{Al}_{0.3}\text{Ga}_{0.7}\text{As}$. The 0.6:0.4 rule is used for the ratio of the conduction-band offset to the valence-band offset in $\text{Al}_x\text{Ga}_{1-x}/\text{GaAs}$ heterojunctions.

In the discussion that follows, first the energy states and wave functions are calculated to illustrate how the wells are coupled. It is instructive to relate the energy states of the double well coupling case to the original single-well states. The term "interwell transition" refers to the intersubband transition whose initial state and final state are originated from different wells, while the term "intrawell transition" is for the transition between two states in the same well. The transition energy of the interwell transition is a strong function of the applied electric field. However, the oscillator strength of the interwell transition is in general smaller than that of the intrawell transition. The oscillator strength as a function of the well dimension, the barrier dimension, and the electric field is discussed secondly.

A. Energy states and wave functions

The energy states versus the well dimension of the B well is shown in Fig. 2(a). The two states at around 30 and 120 meV are originated from the A well and are labeled as $n_A = 1_A$ and 2_A in Fig. 2. The three falling states come from the B well and are labeled as $n_B = 1_B$, 2_B , and 3_B . For example, the $1 \rightarrow 2$ transition corre-

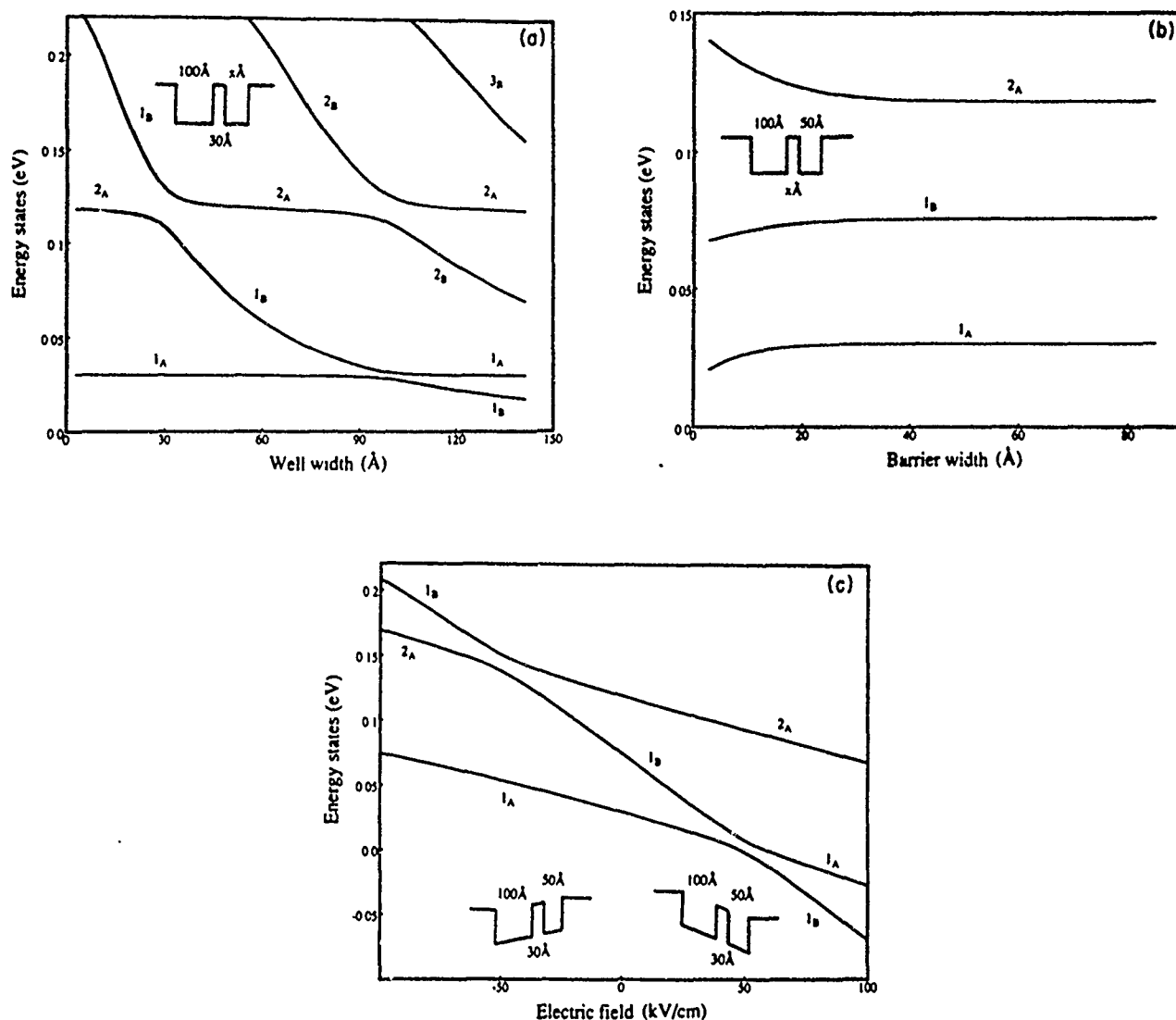


FIG. 2. Energy states as a function of (a) the well width, (b) the barrier width, and (c) the applied electric field for the coupled quantum wells comprising two wells A and B and a thin barrier in between. (a) Energy states as a function of the width of the B well when the A well is 100 Å and thin barrier is 30 Å. The energy states originated from the A well are labeled as $n_A = 1_A$ and 2_A and those from the B well are labeled as $n_B = 1_B$, 2_B and 3_B in order to distinguish the interwell transitions from the intrawell transitions. (b) Energy states as a function of the width of the thin barrier when the A well is 100 Å and B well is 50 Å. (c) Energy states as a function of the electric field when the A well is 100 Å, the B well is 50 Å, and thin barrier is 30 Å. The 1_B state intersects the 2_A state at the field -50 kV/cm, while it intersects the 1_A states at 50 kV/cm. The transition energies of the $1_A \rightarrow 1_B$ and the $1_B \rightarrow 2_A$ transitions is very sensitive to the applied electric field.

sponds to the $1_A \rightarrow 1_B$ interwell transition when the B well is 50 Å while it corresponds to the $1_A \rightarrow 2_A$ intrawell transition when the B well is 20 Å.

The energy states versus the barrier dimension is shown in Fig. 2(b). The barrier dimension has small effect on the energy states when the barrier width is larger than 30 Å.

The electric field dependence of the energy states is shown in Fig. 2(c). The polarity of the electric field is shown in the inset. The energy states originated from the A well and the B well are labeled in a way as in Fig. 2(a). The transition energy of the $1_A \rightarrow 2_A$ intrawell transition does not change much by the electric field but the $1_A \rightarrow 1_B$ interwell transition does. Depending on the po-

larity of the applied field, the transition energy can shift to small energy (red shift), or large energy (blue shift).

Shift of the absorption peak as large as 75 meV is predicted for the interwell transition case (the $1_A \rightarrow 1_B$ or equivalently, the $1 \rightarrow 2$ transition between the field -50 and 50 kV/cm). For comparison, the single well case has only a shift of 1.6 meV under an applied field of 36 kV/cm.⁵ According to the recent intersubband experiments,¹⁶ the full width at half maximum (FWHM) of the absorption coefficient is about 19 meV, which is much smaller than the shift of this interwell transition in coupled quantum wells by applying an electric field.

The wave functions of the lowest three states are shown in Fig. 3, for the zero field, -50 and 50 kV/cm,

respectively. The wave function oscillates in its own original well and decays in the other well in the zero field or small field cases. Thus the overlap of the interwell wave functions is considerably smaller than that of the intrawell wave functions. The -50 kV/cm fields are chosen such that the 1_B and 2_A states are mixed, thus the

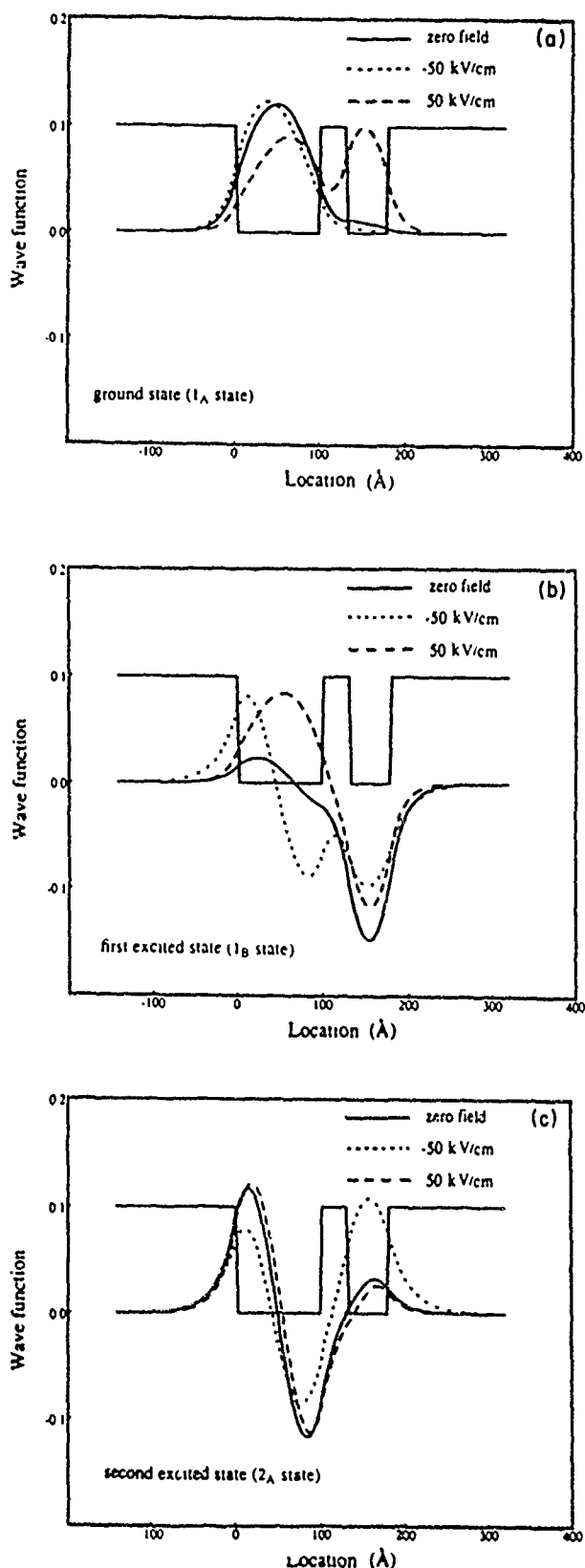


FIG. 3. Wave functions of the lowest three states in the coupled quantum wells described in Fig. 2(c) for the zero field, and ± 50 kV/cm, respectively.

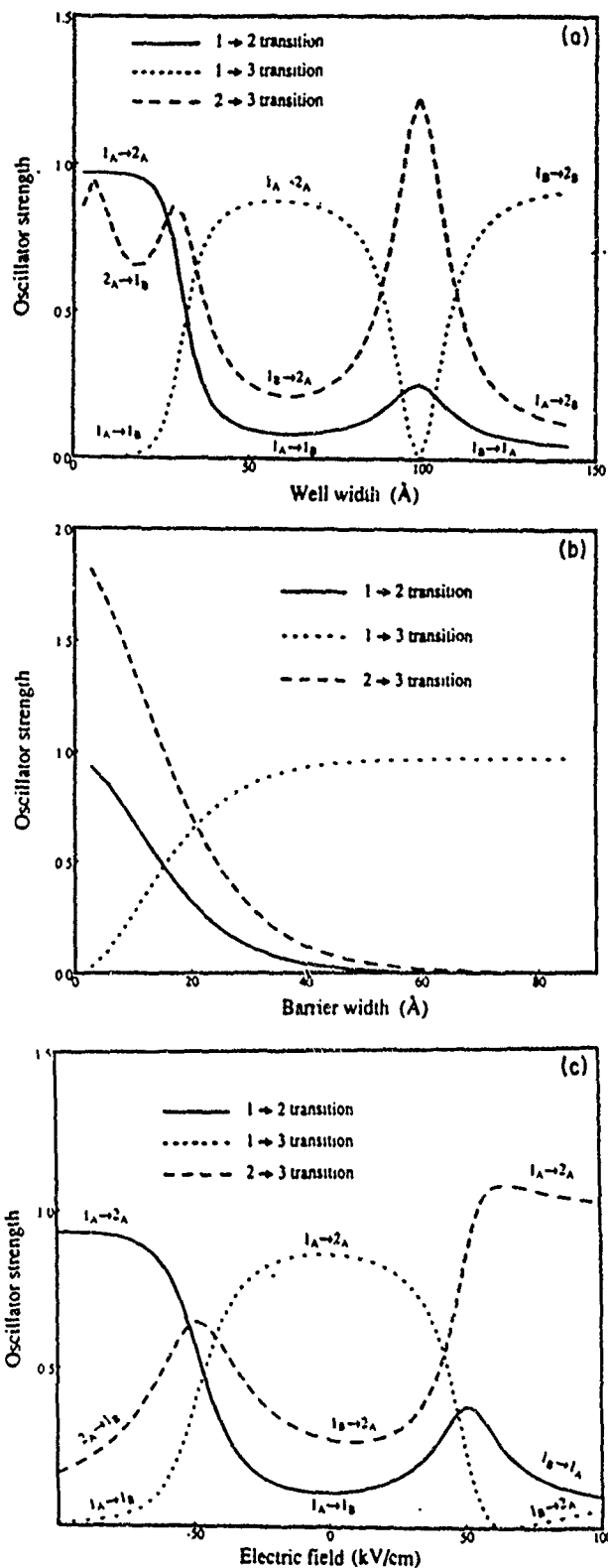
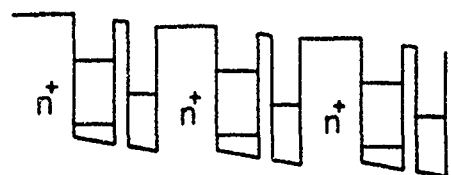
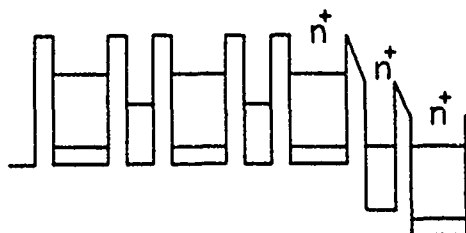


FIG. 4. Oscillator strength as a function of (a) the well width, (b) the barrier width, and (c) the applied electric field for the coupled quantum wells described in Fig. 2. (a) Oscillator strength as a function of the width of the B well. The oscillator strength is labeled in each section as the $1_A \rightarrow 1_B$, $1_A \rightarrow 2_A$ transitions, etc., according to the labeling in Fig. 2(a). The interwell transitions usually have small strength. (b) Oscillator strength as a function of the width of the thin barrier. The interwell transition $1_A \rightarrow 1_B$ has large strength when the thin barrier is smaller than 30 Å. (c) Oscillator strength as a function of the electric field. The oscillator strength is proportional to the absorption coefficient by Eq. (9).



(a) Multiple quantum wells doped in the thick barriers



(b) Superlattice doped in the wells

FIG. 5. Arrangement of the coupled quantum wells for electro-optical applications. (a) Multiple-quantum-well case: the undoped coupled quantum wells are inserted between heavily doped thick barriers. The electric field is distributed only in the coupled quantum wells. Thus the result in Sec. III can be directly applied. The peak absorption energy of the interwell transition can shift to red or blue by the electric field. (b) Superlattice case: a superlattice incorporates the coupled quantum wells as its basis. Only the well regions are heavily doped. High-electric-field domains are expanding well by well in the barrier regions so that the energy levels in each well are aligned. The transition energy of the interwell transition does not change with the electric field. But the absorption magnitude decreases as the domains expand since the absorbent wells available are decreasing.

wave functions of the 1_B and 2_A states are oscillatory in both wells. While at the field 50 kV/cm, the 1_B and 1_A states are mixed, where the wave functions of the 1_B and 1_A states are oscillatory in both wells.

B. Oscillator strength and absorption coefficient

To show that the intrawell transitions are usually stronger than the interwell transition, the oscillator strength versus the well dimension of the B well is plotted in Fig. 4(a). The $1 \rightarrow 2$, $1 \rightarrow 3$, and $2 \rightarrow 3$ transitions are labeled as $1_A \rightarrow 1_B$, $1_B \rightarrow 1_A$, $1_A \rightarrow 2_A$, and $1_B \rightarrow 2_A$ transitions in the corresponding regions in order to distinguish the interwell transition from the intrawell transitions. They are labeled according to the labeling in Fig. 2(a).

The thin barrier plays an important role for the interwell transitions. The oscillator strength versus barrier

width is shown in Fig. 4(b). For a thinner barrier the two wells are strongly coupled and the interwell wave functions have large overlap and thus large oscillator strength while for a thicker barrier the two wells are decoupled and this approaches the single-well limit.

The oscillator strength versus electric field is shown in Fig. 4(c), where the transitions are labeled according to that in Fig. 2(c). The oscillator of the interwell transitions is 1 order of magnitude smaller than that of the intrawell transitions in the present example. The interwell oscillator strength peaks at the electric field when the energy levels are mixed.

IV. STRUCTURAL CONSIDERATION

In Sec. III we have assumed a uniform electric field applied only in the well regions and thin barrier. This is a good approximation if the contact barriers are heavily doped while the wells and the thin barrier are undoped, as schematically shown in Fig. 5(a). Multiple-coupled wells are required to enhance the absorption. The contact barriers should be thick enough (≥ 100 Å) in order to decouple the individual coupled quantum wells. In this case both the blue shift and the red shift are possible.

The second possible arrangement is shown in Fig. 5(b), where the individual coupled wells are also coupled to the neighbors. The well regions should be heavily doped to ensure carriers accumulated in the ground state while the barriers are not doped. As the voltage is applied, the bands tend to align one by one,¹⁷ as is shown schematically. Thus one may not expect an energy shift of the absorption peak, but the magnitude of the peak will drop since the number of absorbent wells available are decreasing as the number of aligned wells increases when the electric field is applied.

V. CONCLUSION

In conclusion, we have developed a formalism based on the transfer matrix to calculate the energies and wave functions in an arbitrary quantum-well structure. The intersubband optical transitions of the coupled quantum wells under an applied electric field are analyzed using this formalism. Very large Stark shift by the interwell transitions is predicted. However, the oscillator strength of the interwell transition is one order of magnitude smaller than the intrawell transition.

ACKNOWLEDGMENTS

The authors thank Dr. R. Karunasiri for the helpful discussions. This work is supported in part by U.S. Naval Research office, U.S. Army Research Office, and the Semiconductor Research Corporation.

¹D. A. B. Miller, D. S. Chemla, T. C. Damen, A. C. Gossard, W. Wiegmann, T. H. Wood, and C. A. Burrus, Phys. Rev. B 32, 1043 (1985).

²David A. B. Miller, Joseph S. Weiner, and D. S. Chemla IEEE

J. Quantum Electron. QE-22, 1816 (1986).

³D. A. B. Miller, D. S. Chemla, and S. Schmitt-Rink, Phys. Rev. B 33, 6976 (1986).

⁴B. Jogai and K. L. Wang, Phys. Rev. B 35, 653 (1987).

- ⁵Alex Harwit and J. S. Harris, Jr., *Appl. Phys. Lett.* **50**, 685 (1987).
- ⁶D. Ahn and S. L. Chuang, *Phys. Rev. B* **35**, 4149 (1987).
- ⁷Y. J. Chen, Emil S. Koteles, B. Elman, and C. A. Armiento, *Mater. Res. Soc. Symp. Proc.* **102**, 571 (1988).
- ⁸Amnon Yariv, Chris Lindsey, and Uri Sivan, *J. Appl. Phys.* **58**, 3669 (1985).
- ⁹Roy Lang and Kenichi Nishi, *Appl. Phys. Lett.* **45**, 98 (1984).
- ¹⁰Herbert Kroemer and Hiroshi Okamoto, *Jpn. J. Appl. Phys.* **45**, 98 (1984).
- ¹¹Perng-fei Yuh and K. L. Wang, *Phys. Rev. B* (to be published).
- ¹²Yasunori Tokuda, Teruhito Matsui, Kenzo Fujiwara, Noriaki Tsukada, and Takashi Nakayama, *Appl. Phys. Lett.* **51**, 209 (1987).
- ¹³H. Kawai, J. Kaneko, and N. Watanabe, *J. Appl. Phys.* **58**, 1263 (1985).
- ¹⁴H. Q. Le, J. J. Zayhowski, and W. D. Goodhue, *Appl. Phys. Lett.* **50**, 1518 (1987).
- ¹⁵M. O. Vassell, Johnson Lee, and H. F. Lockwood, *J. Appl. Phys.* **54**, 5206 (1983).
- ¹⁶B. F. Levine, R. J. Malik, J. Walker, K. K. Choi, C. G. Bethea, D. A. Kleinman, and J. M. Vandenberg, *Appl. Phys. Lett.* **50**, 273 (1987).
- ¹⁷K. K. Choi, B. F. Levine, R. J. Malik, J. Walker, and C. G. Bethea, *Phys. Rev. B* **35**, 4172 (1987).

INFRARED ABSORPTION IN PARABOLIC MULTIQUANTUM WELL STRUCTURES

R. P. G. Karunasiri and K. L. Wang

Device Research Laboratory
Department of Electrical Engineering
University of California
Los Angeles, CA 90024
(Received 16 October 1987)

ABSTRACT

The absorption constant for intraband transitions in parabolic multi-quantum well structures is calculated and compared with intraband absorption in a square well superlattice. The parabolic multiple quantum well structure may be used as an Infrared detector with the possibility of lower leakage current compared to one made of square wells.

Recently there have been many studies both experimentally^{1,2,3} and theoretically^{4,5,6} in the development of infrared detectors using intraband absorption in quantum well structures. In this paper, we present a theoretical calculation of intraband absorption in parabolic quantum well superlattices.

A superlattice can be fabricated as described by Miller et.al.⁷ using heterointerfaces or alternatively with *n* and *p* doped *n-i-p-i* structure as shown by Döhler⁸. Superlattices made of these parabolic quantum wells have the interesting feature that the ground state sees a wider barrier than the excited states due to the shape of the potential. This allows one to choose the device parameters so that the ground states are nearly isolated from each other and at the same time forming a band for the first excited state. Due to this isolation it is possible to populate the ground state (by doping) without producing an appreciable leakage current due to tunneling under an applied electric field. This is similar to impurity band infrared detectors⁹ where a thin intrinsic layer is used to isolate the heavily doped active region.

First we consider the absorption between two states of an isolated parabolic well as shown in Fig. 1. To a good approximation we can describe the envelope states as given by that of an infinite parabola. The Hamiltonian (*H*) of the system in the effective mass approximation (where the effect of the nearest bands are taken into account using an empirical effective mass m^* can be written as

$$H = \frac{p^2}{2m^*} + \frac{1}{2}m^*\Omega^2z^2 \quad (1)$$

Parabolic Quantum Well

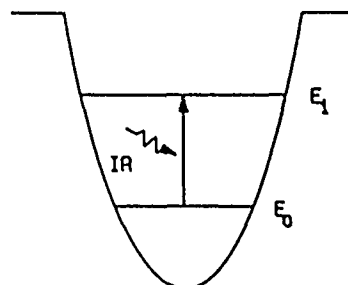


Fig.1 Schematic diagram of a parabolic quantum well showing the intraband transition.

where *z* is the growth direction and *p* is the momentum of the electron (or hole) along *z* direction. Ω is given in terms of the curvature (*K*) of the parabola by $\sqrt{K/m^*}$. Energy eigenvalues of the system (E_n) given by

$$E_n = (n + \frac{1}{2})\hbar\Omega + \frac{\hbar^2 k_{x,y}^2}{2m^*} \quad (2)$$

where $k_{x,y}$ is the wave vector of the electron (or hole) perpendicular to the growth direction and $n = 0, 1, 2, \dots$

For intraband transitions, non-zero dipole matrix elements occur when the photon interaction acts on the envelope part of the wave functions^{1,5}. The oscillator strength (*f*) corresponding to a transition between states $|n\rangle$ and $|m\rangle$ is given by¹

$$f_{m \rightarrow n} = \frac{2m_0}{\hbar^2} (E_n - E_m) |\langle n | \hat{p} | m \rangle|^2. \quad (3)$$

The matrix element $\langle n | \hat{p} | m \rangle$ can be easily obtained by writing z in terms of creation (a^+) and annihilation (a) operators¹⁰ as

$$z = \sqrt{\frac{2\hbar}{m^* \Omega}} \frac{(a^+ + a)}{2} \quad (4)$$

where a^+ and a satisfy

$$a^+ |n\rangle = \sqrt{n+1} |n+1\rangle$$

$$a |n\rangle = \sqrt{n} |n-1\rangle.$$

The matrix element can be evaluated readily using z from Eq. (4) as

$$\langle n | \hat{p} | m \rangle = \sqrt{\frac{\hbar}{2m^* \Omega}} [\sqrt{m+1} \delta_{nm+1} + \sqrt{m} \delta_{nm-1}]. \quad (5)$$

This implies that for a parabolic well, non-zero dipole matrix elements occur only between adjacent states. This is quite different from the case of a square well where the dipole matrix element is non-zero between any two states with opposite parity¹. In the case of absorption we need to consider only the first term of Eq. (5). Then the oscillator strength for the transition n to $n+1$ is given by

$$f_{n \rightarrow n+1} = \frac{m_0}{m^*} (n+1). \quad (6)$$

This may be compared with the case of a square well with an infinite barrier, where the oscillator strength for the same transition is given by¹

$$f_{n \rightarrow n+1} = \frac{64m_0}{\pi^2 m^*} \frac{(n+1)^2 (n+2)^2}{(2n+3)^3} \quad (7)$$

For the transition between the ground state and the first excited state, the oscillator strengths for parabolic and square wells are given by m_0/m^* and $0.96m_0/m^*$, respectively.

For a given interaction potential V_p the transition rate (W) is given by¹⁵

$$W = \frac{2\pi}{\hbar} \sum_F |\langle \Phi_F | V_p | \Phi_I \rangle|^2 \delta(E_F - E_I - \hbar\omega) \quad (8)$$

where E_I and E_F are the initial and final state energies, ω is the frequency of the incident photon, Φ_I and Φ_F are the initial and final state wave functions and for photon interaction V_p is given by¹¹

$$V_p = \frac{e}{m^*} \frac{\hbar}{2\epsilon_0 n_r \omega c} \hat{\epsilon} \cdot \hat{p} \quad (9)$$

where n_r is the refractive index, $\hat{\epsilon}$ and \hat{p} are the polarization of the incident photon and momentum of the electron (or hole). Evaluating the transition rate using Eq.

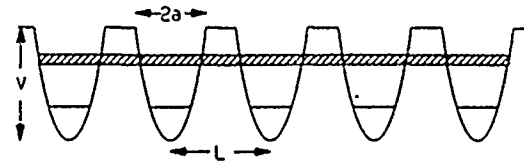


Fig.2 Parabolic well superlattice showing the isolated ground states and miniband at the first excited state.

(8) and integrating it over the incident photon energy at Brewster's angle, the fraction of energy absorbed per unit length is obtained as

$$\frac{\rho_s}{L} \frac{e^2 \hbar}{4\epsilon_0 m^* c} \frac{f}{n_r (n_r^2 + 1)} \quad (10)$$

where ρ_s is the two dimensional density of electrons (or holes) in the well.

Next, we consider an optical transition of a superlattice made of parabolic quantum wells. Fig.2 shows the schematic diagram of the superlattice, where ground states are isolated and excited states form a miniband. The analysis is very similar to the case of an impurity to band transition where a bound electron (or hole) make a transition to the conduction (or valence) band. Here, we use the tight binding method¹⁰ to find the final state wave function using infinite parabolic well wave functions as our basis set. Under these condition initial and final states wave functions can be written as

$$\begin{aligned} \Phi_I &= u_0 \frac{e^{i\vec{k}_{xy} \cdot \vec{r}}}{\sqrt{A}} \Phi_{0r}(z) \\ \Phi_F &= u_0 \frac{e^{i\vec{k}_{xy} \cdot \vec{r}}}{\sqrt{A}} \sum_n \frac{e^{iqnL}}{\sqrt{N}} \Phi_{1n}(z) \end{aligned} \quad (11)$$

where A is the area of the well, \vec{k}_{xy} , \vec{r} are the wave and the position vectors in the x, y plane, u_0 is the cell period function near the band extremum, q is the wave vector along the miniband, N is the number of wells in the superlattice (assumed very large) and Φ_{0r} and Φ_{1n} are the ground state and excited state wave functions of an infinite parabolic well at positions rL and nL , respectively.

Taking into account only the nearest-well interactions, the dispersion relation for the first excited state can be written as¹²

$$E_f = E_1 + 2t_1 \cos(qL) + \frac{\hbar^2 k_{zy}^2}{2m^*} \quad (12)$$

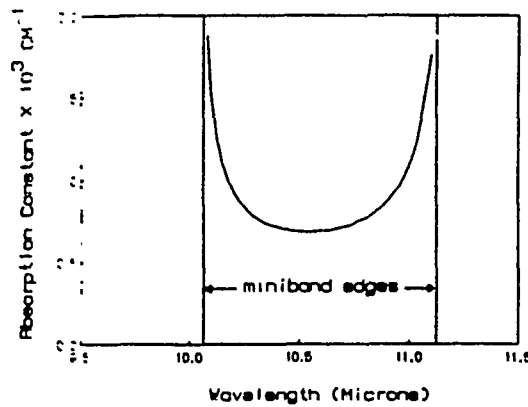


Fig.3 Absorption constant as a function of wavelength around $10.6\mu\text{m}$. Here we assumed IR incident at Brewster's angle and $L=132\text{\AA}$, $a=61\text{\AA}$, $V = 225$ meV and miniband width for the parameters used is 12 meV.

where E_1 is the first excited state energy of an isolated parabolic quantum well and t_1 is given by

$$t_1 = 2\pi\Omega^2 \sqrt{\frac{\beta^3}{\pi}} \int_{-\infty}^{\infty} z(z-L)(z^2-a^2) e^{-\beta[(z-L)^2+z^2]^{1/2}} dz \quad (13)$$

where $\beta = m^*\Omega/\hbar$. For a given parameters of the superlattice, t_1 can be easily obtained from Eq.(13) by numerical integration. Using the initial and final state wave functions we can obtain the matrix element of the transition as

$$\langle \Phi_f | \hat{e} \cdot \vec{p} | \Phi_i \rangle = \sum_n \frac{e^{-iq_n L}}{\sqrt{N}} \langle \Phi_f | \hat{e} \cdot \vec{p} | \Phi_{on} \rangle \quad (14)$$

Since Φ_{on} is localized at the n^{th} well position, the major contribution to the matrix element occurs when $n = r$. It can be easily shown using Eq. (5) that the Eq.(14) reduces to

$$|\langle \Phi_f | \hat{e} \cdot \vec{p} | \Phi_i \rangle|^2 = \frac{m^{*2}\Omega^2}{N} \frac{\hbar}{2m^*\Omega} (\hat{e} \cdot \hat{e}_r)^2. \quad (15)$$

Substituting this in the expression for the transition rate, we obtain the absorption constant as a function of photon energy ($\hbar\omega$) as

$$\alpha = \frac{e^2 \hbar}{2m^* c \epsilon_0 n_r \omega} \frac{\Omega}{\sqrt{(E_{\text{max}} - \hbar\omega)(\hbar\omega - E_{\text{min}})}} (\hat{e} \cdot \hat{e}_r)^2 \quad (16)$$

where $E_{\text{max}} = E_1 - E_0 + 2t_1$ and $E_{\text{min}} = E_1 - E_0 - 2t_1$.

Fig. 3 shows the absorption constant as a function of wavelength for a case, device parameters chosen in order to obtain response near $10\mu\text{m}$. The parabolic quantum well is assumed to contain 3×10^{17} electrons/

cm^3 . For the parameters used, Eq.(13) gives about 12 meV band width for the subband. The absorption constant shows singular behavior at the bandedges due to one dimensional van Hove singularities of the joint density of states, giving a relatively high absorption coefficient. The joint density of states has one dimensional nature since it depends only on the states in the miniband along the growth direction. The contribution to the joint density of states from the states perpendicular to the growth direction cancels due to the conservation of momentum in the process. Our value of the absorption constant is about 700cm^{-1} which is quite close to the values obtained experimentally^{1,2,3} ($600\text{--}700\text{cm}^{-1}$) for a square well superlattice with similar electron concentration in the well.

In conclusion, we have showed the possibility of using parabolic quantum well structures for infrared detector applications. Effect of the finite height of the parabolic well may be second order corrections, since the exponentially decaying tails of the wave functions are the ones that feel the finite height. Parabolic well superlattices may provide lower leakage currents due to tunneling compared to square well superlattices with the same barrier thickness, since the ground state barrier is always thicker than that of the excited state for a parabolic well superlattice. It is interesting to note that the Stark shift for a parabolic well energy state does not depend on energy of the state. Therefore, once the device parameters are optimized for a particular wavelength range it is not sensitive to the variation of the electric field present in the device. This is not true for the case of square wells for which the Stark shift is a function of the eigen state energy^{13,14}.

Acknowledgements - The authors would like to thank Professor T. W. Kang for helpful discussions. This work was supported in part by Office of Naval Research and Army Research Office.

References

- [1] L. C. West and S. J. Eglash, Appl. Phys. Lett., 46, 1156 (1985).
- [2] B. F. Levine, R. J. Malik, J. Walker, K. K. Choi, C. G. Bethea, D. A. Kleinman and J. M. Vandenberg, Appl. Phys. Lett. 50, 273 (1987).
- [3] B. F. Levine, K. K. Choi, C. G. Bethea, J. Waker and R. J. Malik, Appl. Phys. Lett. 50, 1092 (1987).
- [4] J. S. Smith, L. C. Chiu, S. Margalit, A. Yariv and A. Y. Cho, J. Vac. Sci. Technol. B1, 376 (1983).
- [5] D. D. Coon and R. P. G. Karunasiri, Appl. Phys. Lett. 45, 649 (1984).

- [6] K. W. Goossen and S. A. Lyon, *Appl. Phys. Lett.* **47**, 1257 (1985).
- [7] R. C. Miller, A. C. Gossard, D. A. Kleinman, and O. Munteanu, *Phys. Rev.* **B15**, 3740 (1984).
- [8] G. H. Döhler, *IEEE J. Quantum Electron.*, **QE-22**, 1682 (1986).
- [9] N. Sclar, *Prog. Quant. Electr.*, **9**, 149 (1984).
- [10] S. Wieder, *The Foundations of Quantum Theory*, (Academic Press, Inc., New York, 1973).
- [11] B. K. Ridley, *Quantum Processes in Semiconductors* (Oxford University, London, 1982).
- [12] P. Voisin, G. Bastard, and M. Voos, *Phys. Rev.*, **B29**, 935 (1984).
- [13] D. Ahn and S. L. Chuang, *Phys. Rev.*, **B35**, 4149 (1987).
- [14] A. Harwit and J. S. Harris, Jr., *Appl. Phys. Lett.* **50**, 685 (1987).

Formalism of the Kronig-Penney model for superlattices of variable basis

Peng-fei Yuh and K. L. Wang

Device Research Laboratory, Department of Electrical Engineering, University of California, Los Angeles, California 90024-1600

(Received 22 February 1988; revised manuscript received 7 July 1988)

A formalism of the Kronig-Penney model based on the transfer-matrix technique and the envelope-function approximation has been developed for superlattices. It can be used in handling superlattices composed of complicated bases, is easier to use than the conventional Kronig-Penney model in matching boundary conditions, and is more accurate because the effective mass and band coupling are included. The minibands of superlattices having different superlattice bases are analyzed by this new method.

I. INTRODUCTION

Superlattices are alternating ultrathin epitaxial layers, in which a one-dimensional potential is superimposed on the crystal potential of the background crystal.¹ The one-dimensional potential is formed by the band offset of the heterolayers in a compositional superlattice, or by periodically growing the *n*- and *p*-doped semiconductor layers, separated by intrinsic layers in the doped superlattice or *n-i-p-i*. While the real crystal potential has the same period as the lattice points, the period of the superlattice potential is the same as the alternating layers. For convenience, one period of the alternating layers will be called the basis of the superlattice. In the bulk semiconductor, different bases or primitive cells will result in different crystal potentials, thus different energy bands. Analogously, one may expect that the minibands in the superlattice will change as the superlattice basis changes. In the past since its inception in 1969,² the superlattice basis has always been simple barrier-well structure for simplicity of analysis. With modification of the basis, interesting effects are expected in the miniband transport and optical transitions.

The Kronig-Penney model has been applied to calculate the minibands in a superlattice with some modifications of the boundary conditions.^{3,4} Those boundary conditions are derived from the envelope function approximations.⁵ The wave equations and boundary

conditions of three commonly used models are listed in Table I for later discussion. Among them, the effective-mass model takes into account the effective-mass difference in the barrier and the well regions. The two-band model includes the coupling of the conduction band and light-hole band. While the three-band model includes further the coupling of the split-off band. Since in the *k*·*p* theory the heavy-hole band is decoupled with the other three bands,⁶ the three-band model is the most accurate of the three in treating all the four-band interactions. The modifications give simple final forms and need no more computation effort than the conventional Kronig-Penney model does.⁷ However, both the classical Kronig-Penney model and the modified ones have the fundamental limitations. First, the formalism of the Kronig-Penney model is tedious and needs to simplify the determinant of a 4×4 matrix.⁸ Secondly, it can only be used for a single square-well basis, but cannot be used for complicated bases, for example, bases with multiple layers, band-bending, or an arbitrary shape of the well by adjusting the alloy composition. With an increasing interest in applications of the novel superlattice or quantum well structures,⁹⁻¹² an accurate but simple model is necessary for theoretical predictions and explanation of experimental results.

A new formalism of the Kronig-Penney model, which uses the transfer matrix technique within the envelope-function framework is developed for general bases, and it

TABLE I. Wave equations and the boundary conditions for each of the envelope-function approximations. Those functions under the column of boundary conditions are continuous throughout the superlattice layers, and are used for Γ_1 and Γ_2 in Eq. (1).

| Model | Wave equation | Boundary conditions Γ_1, Γ_2 |
|----------------|---|--|
| Effective mass | $(E - V_1)\psi(z) + \frac{\hbar^2}{2} \left[\frac{\psi(z)'}{m^*} \right]' = 0$ | $\psi(z), \frac{\psi(z)'}{m^*}$ |
| Two band | $(E - V_1)\psi(z) + \frac{1}{2}P^2 \left[\frac{1}{E - V_p} \psi(z)' \right]' = 0$ | $\psi(z), \frac{1}{E - V_p} \psi(z)'$ |
| Three band | $(E - V_1)\psi(z) + \frac{1}{2}P^2 \left[\left[\frac{2}{E - V_p} + \frac{1}{E - V_0} \right] \psi(z)' \right]' = 0$ | $\psi(z), \left[\frac{2}{E - V_p} + \frac{1}{E - V_0} \right] \psi(z)'$ |

reduces to the earlier classical and modified Kronig-Penney models for simple structures in a simpler and more systematic way as far as the matching of boundary condition is concerned. Isolated quantum wells of an arbitrary potential profile can be calculated using the transfer matrix method as a special case of the superlattice, namely, with a very thick barrier between the bases.⁵ In Secs. II and III, we describe the new Kronig-Penney models, beginning with a general theory, following by implement of envelope-function approximations, in which different potential profiles are taken into account. Finally a comparison of the three different commonly used models is made. In Secs. IV and V, the new treatise is applied to a few superlattice structures having various superlattice bases, which are important in fundamental quantum physics and device applications.

II. GENERAL THEORY

The transfer matrix technique was employed by Vassell *et al.* for calculating the transmission coefficient of resonant tunneling structures.¹³ It is briefly reviewed here. Assuming that there are n layers in a tunneling structure with an active length L , the final wave function $\Gamma(z=L)$ and the initial wave function $\Gamma(z=0)$ have the relation

$$\Gamma(z=L) = S\Gamma(z=0), \quad (1)$$

where

$$\Gamma(z) = \begin{pmatrix} \Gamma_1(z) \\ \Gamma_2(z) \end{pmatrix}$$

is a 2×1 matrix, with $\Gamma_1(z)$ representing the envelope function and $\Gamma_2(z)$ the derivative of $\Gamma_1(z)$ times a coefficient such that $\Gamma_2(z)$ is continuous throughout the active layer. $\Gamma_2(z)$ depends on the kind of models used and are listed in Table I under the column of boundary conditions. The 2×2 transfer matrix S is given by $S = S_n S_{n-1} \cdots S_1$. Each of its multiplicand S_i 's is the transfer matrix of the i th single layer, and $S_i = [\Gamma^{(1)}(z=L_i), \Gamma^{(2)}(z=L_i)]$, where $\Gamma^{(1)}(z), \Gamma^{(2)}(z)$ are two particular solutions of Γ with initial boundary conditions $\Gamma^{(1)}(z=0) = \begin{pmatrix} 1 \\ 0 \end{pmatrix}$ and $\Gamma^{(2)}(z=0) = \begin{pmatrix} 0 \\ 1 \end{pmatrix}$, respectively. The thickness of the i th layer is given by L_i .

When applying to superlattices, the transfer matrix S should be for one period of the superlattice layers or the superlattice basis, and is obtained by multiplying the transfer matrices of each single layer in the basis. If d is the period of the superlattice or the length of the basis, one has

$$\Gamma(z+d) = S\Gamma(z) \text{ and } \Gamma(z+nd) = S^n\Gamma(z). \quad (2)$$

The eigenvalues of S are obtained by solving

$$\Gamma(z+d) = S\Gamma(z) = \lambda\Gamma(z). \quad (3)$$

As $n \rightarrow \pm \infty$, the limit of S^n should exist, and this implies $|\lambda| = 1$ for an oscillatory wave solution. Considering also translational symmetry, acceptable values of λ are $\lambda = e^{\pm iqd}$, which define the superlattice wave vector q .

The above statements illustrate the well-known Bloch theory since from Eq. (3) $\Gamma_1(z+d) = e^{\pm iqd}\Gamma_1(z)$.

Expanding the 2×2 determinant $\det(S - \lambda I) = 0$ from Eq. (3), the superlattice dispersion relation can be obtained. The summation of the two roots of λ is

$$S_{11} + S_{22} = e^{iqd} + e^{-iqd} = 2 \cos qd,$$

and the dispersion relation becomes

$$\cos qd = \frac{1}{2}(S_{11} + S_{22}). \quad (4)$$

The superlattice wave functions are the eigenfunctions in Eq. (3). The ratio of Γ_1 and Γ_2 at an arbitrary point z_0 is

$$\frac{\Gamma_1(z_0)}{\Gamma_2(z_0)} = \frac{S_{12}}{\lambda - S_{11}}. \quad (5)$$

The wave function at z_1 can be constructed from an initial point z_0 by

$$\begin{aligned} \Gamma(z=z_1) &= S(z_1, z_0)\Gamma(z=z_0) \\ &= S(z_1, z_0) \begin{pmatrix} S_{12} \\ \lambda - S_{11} \\ 1 \end{pmatrix} \times \text{const}, \end{aligned} \quad (6)$$

where S_{11}, S_{12} are the elements of $S(d+z_0, z_0)$ and $S(z_1, z_0)$ is the transfer matrix from z_0 to z_1 . Although there are two wave functions for $\lambda = e^{\pm iqd}$, their absolute values, i.e., the square root of probability densities, are equal.

In the derivations below GaAs/Al_xGa_{1-x}As will be taken as an example. All the energy levels are referenced to the valence-band maximum in GaAs.

III. IMPLANTATION OF THE ENVELOPE-FUNCTION APPROXIMATIONS

A. One-band effective-mass Kronig-Penney model

For the effective-mass model, the wave equation of the conduction-band envelope function from Table I can be reduced to

$$\psi''(z) + k^2\psi(z) = 0, \quad (7)$$

where $k^2 = (2m^*/\hbar^2)(E - V_i)$, and all the notations are defined in Table II. For a constant potential, V_i is a constant. If Γ is chosen to be

$$\Gamma = \begin{pmatrix} \psi \\ \frac{\psi'}{m^*} \end{pmatrix}, \quad (8)$$

then the transfer matrix after solving the two particular solutions $\Gamma^{(1)}(z)$ and $\Gamma^{(2)}(z)$ becomes

$$S = \begin{pmatrix} \cos kz & \frac{m^*}{k} \sin kz \\ -\frac{k}{m^*} \sin kz & \cos kz \end{pmatrix}. \quad (9)$$

TABLE II. Notations and band parameters. The 0.6:0.4 rule is used for the band offset in the conduction and the valence bands. $\text{Al}_{0.3}\text{Ga}_{0.7}\text{As}$ is used for the barrier, and $\text{Al}_{0.1}\text{Ga}_{0.9}\text{As}$ is used for the second barrier in a step-well basis.

| Notations | |
|-----------|--|
| m_0 | Free electron mass |
| m_0^* | The effective mass of GaAs |
| $m^*(z)$ | The effective mass at z , $m^* = 0.067(1-x) + 0.15x$ for $\text{Al}_x\text{Ga}_{1-x}\text{As}$ |
| E_{G0} | Energy band gap of GaAs |
| $E_G(z)$ | Energy band gap of $\text{Al}_x\text{Ga}_{1-x}\text{As}$, $E_G = 1.519 - 5.405 \times 10^{-4} T^2/T + 204 + 1.247x$ |
| ψ | Conduction-band envelope function |
| E | The electron energy when transverse wave vectors are zeros, i.e., $k_x = k_y = 0$ |
| $V_1(z)$ | The conduction-band minimum at z referred to the valence-band maximum of GaAs |
| $V_p(z)$ | The light-hole band maximum at z referred to the valence-band maximum of GaAs |
| $V_0(z)$ | The split-off band maximum at z referred to the valence-band maximum of GaAs |
| p^2 | $\frac{3\hbar^2}{4} \left[\frac{1}{m_0^*} - \frac{1}{m_0} \right] E_{G0}$ for two-band model |
| p^2 | $\frac{\hbar^2}{2} \left[\frac{1}{m_0^*} - \frac{1}{m_0} \right] \frac{E_{G0}(E_{G0} + \Delta)}{E_{G0} + 2/3\Delta}$ for three-band model |
| Δ | The split-off band maximum to the light-hole band maximum in GaAs; $\Delta = 0.35$ |

If $k^2 \geq 0$, the energy E is above the barrier V_1 , and physically it is an oscillatory wave solution. While for $k^2 < 0$, it is an evanescent wave solution. Equation (9) is still valid if one substitutes $k = i\kappa$ and uses the equalities, $\cos i\kappa z = \cosh \kappa z$ and $\sin i\kappa z = i \sinh \kappa z$. Using Eq. (4), one may easily verify that for the superlattice with a simple basis consisting of A and B layers, with layer thicknesses L_A and L_B , respectively, the dispersion relation is

$$\cos q(L_A + L_B) = \cos k_A L_A \cos k_B L_B - \frac{1}{2} \left[\beta + \frac{1}{\beta} \right] \sin k_A L_A \sin k_B L_B, \quad (10)$$

where

$$\beta = \frac{k_A}{k_B} \frac{m_B^*}{m_A^*},$$

$$k_A = \left[\frac{2m_A^*}{\hbar^2} (E - V_{1A}) \right]^{1/2},$$

and

$$k_B = \left[\frac{2m_B^*}{\hbar^2} (E - V_{1B}) \right]^{1/2}.$$

For a tilted potential, as in the case of applied field, $V_1(z) = V_1 - eFz$, Eq. (7) can be changed to

$$\psi''(\xi) - \xi \psi(\xi) = 0, \quad (11)$$

with

$$\xi = - \left[\frac{2m^* eF}{\hbar^2} \right]^{1/3} \left[z + \frac{E - V_1}{eF} \right].$$

and Eq. (8) is also changed to

$$\Gamma = \begin{bmatrix} \psi(\xi) \\ - \left[\frac{2eF}{\hbar^2 m^{*2}} \right]^{1/3} \psi(\xi)' \end{bmatrix}, \quad (12)$$

where m^* is the average value through the interesting layer. The transfer matrix is found to be

$$\begin{aligned} S_{11} &= \pi [B_i'(\xi_0) A_i(\xi) - A_i'(\xi_0) B_i(\xi)], \\ S_{12} &= \pi \left[\frac{2eF}{\hbar^2 m^{*2}} \right]^{-1/3} [B_i(\xi_0) A_i(\xi) \\ &\quad - A_i(\xi_0) B_i(\xi)], \\ S_{21} &= -\pi \left[\frac{2eF}{\hbar^2 m^{*2}} \right]^{1/3} [B_i'(\xi_0) A_i'(\xi) \\ &\quad - A_i'(\xi_0) B_i'(\xi)], \\ S_{22} &= -\pi [B_i(\xi_0) A_i'(\xi) - A_i(\xi_0) B_i'(\xi)], \end{aligned} \quad (13)$$

where $\xi_0 = \xi(z=0)$ and A_i and B_i are two linearly independent Airy functions,¹⁴ which are solutions of Eq. (11).

In reality, the potential profile within one monolayer (one layer of As atoms and one layer of Ga/Al atoms) is linear due to the discreteness in crystal growth. Thus an arbitrary potential profile in the basis can be approximated by a piece-wise linear potential. For this case, the basis is divided into several layers. Each one has either a constant or tilted potential. The smallest possible division is the length of the monolayer. The procedure follows that first the transfer matrix in each divided layer is found, then the total transfer matrix is given by multiplying all these transfer matrixes. Finally the dispersion relation is obtained by Eq. (4).

$$\begin{pmatrix} X_1(z) \\ X_2(z) \end{pmatrix}_{z=0^+} = \begin{pmatrix} X_1(z) \\ X_2(z) \end{pmatrix}_{z=0^-} + \begin{pmatrix} 0 & 0 \\ \frac{2\alpha}{\hbar^2} & 0 \end{pmatrix} \begin{pmatrix} \Gamma_1(z) \\ \Gamma_2(z) \end{pmatrix}_{z=0^-}, \quad (22)$$

where

$$X = \begin{pmatrix} X_1 \\ X_2 \end{pmatrix}$$

is a 2×1 wave-function matrix for the X minimum, analogous to Γ in Eq. (1). The coupling coefficient α having a typical value 0.1 eV \AA characterizes the intervalley transfer potential as discussed in Ref. 19. If S_Γ and S_X are denoted for the uncoupled transfer matrices for the Γ and X minima, respectively, and the notations

$$S_{\Gamma X} = S_{X\Gamma} = \begin{pmatrix} 0 & 0 \\ \frac{2\alpha}{\hbar^2} & 0 \end{pmatrix}$$

are used, then the 4×1 wave function $\begin{pmatrix} \Gamma \\ X \end{pmatrix}$ after advancing one single layer L , has the relation

$$\begin{pmatrix} \Gamma \\ X \end{pmatrix}_{z+L} = \begin{pmatrix} S_\Gamma & S_{\Gamma X} \\ S_{X\Gamma} & S_X \end{pmatrix} \begin{pmatrix} \Gamma \\ X \end{pmatrix}_z, \quad (23)$$

where the transfer matrix $S(z+L, z)$ becomes a 4×4 matrix. The allowed minibands occur at the energies where the eigenvalues of $S(z+L, z)$ have absolute values equal to one. Our calculation for AlAs/GaAs superlattices shows that for $\alpha \leq 0.1$, the miniband structures are similar to the uncoupled ones. The coupling comes into play when $\alpha \gg 0.1$ and when there is large overlap between the uncoupled Γ and X minibands. The effect of strong coupling is to diminish the original uncoupled minibands because electrons lose energy in transferring between the Γ and X minima via the overlapped minibands.

D. Comparison

The miniband energies versus well thickness are shown in Figs. 1(a)–1(c) for these three models, respectively. The barrier width is fixed to be 31 \AA (or 11 monolayers). The band parameters we used are again listed in Table II. The general trend for all the three models is that the miniband energies decrease as the width of the well increases. Also the lower the miniband energies are, the smaller their bandwidths become due to higher barriers. The two-band and three-band models give the same result in predicting the minibands for the AlGaAs system while the effective-mass model predicts too high the energy when the well is wide.

In contrast, the miniband versus barrier width of a constant well width of 130 \AA is shown in Fig. 2. It indicates that the miniband location is a strong function of the well width while the miniband bandwidth is a strong function of the barrier width in this case. The minibands become discrete energy levels as the barrier become very

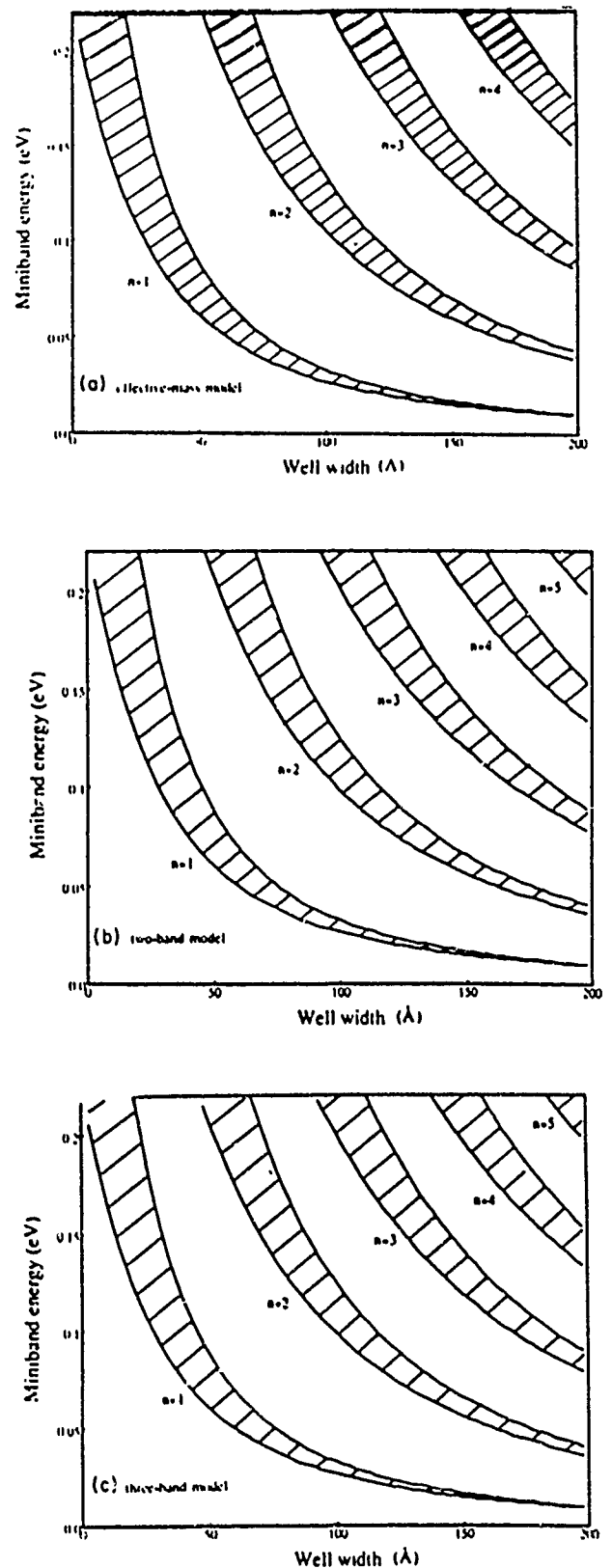


FIG. 1. The miniband energies vs well width by (a) effective-mass model, (b) two-band model, and (c) three-band model at 77 K. The barrier width is fixed to 31 \AA , corresponding to 11 monolayers. Shaded areas indicate the allowed minibands. The miniband energies fall when the well width increases. The energies of the two band or three band are lower than those of the effective-mass model. The differences of the two-band and three-band models are very small.

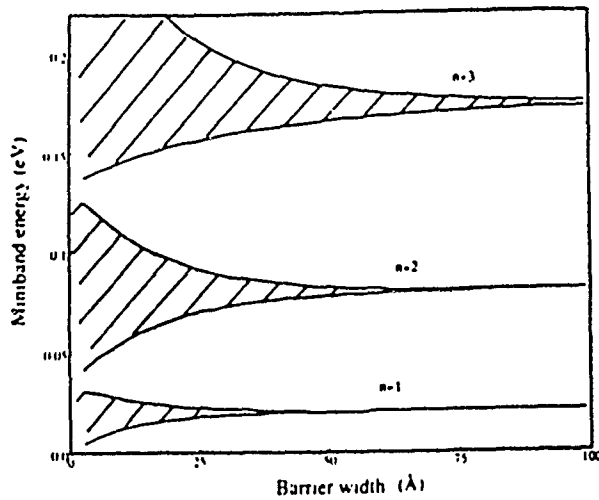


FIG. 2. The miniband energies vs barrier width by effective-mass model at 77 K. The well width is fixed to 130 Å, corresponding to 46 monolayers. The miniband width decreases when the barrier width increases while the center of the miniband is basically unchanged. As the barrier becomes very thick, the minibands of the superlattice approach discrete energy levels of isolated quantum wells.

thick in the quantum wells limit.

The advantage of the two-band or three-band model is that it includes the nonparabolicity of the bands while the limitation is that the momentum matrix element P should be a constant throughout the superlattice.⁷ We have fitted P to the effective mass of GaAs but it is not accurate for AlGaAs. The accurate determination of the mini-bands location is limited by many factors, such as the error in the choice of the percentage of band offset, the inclusion of the transverse part of the energy, and the uncertainty in determining the alloy compositions and well-barrier thickness. By and large, the trend is the same and there is little difference in the result for all the three models used here. The effective-mass model is used for the following calculations.

IV. APPLICATION TO SINGLE-WELL BASIS

A. Parabolic quantum well

Although the parabolic well is usually the building block of the doping superlattices or $n-i-p-i$,²⁰ the growth of it by grading the alloy composition is also possible.^{11,21,22} Theoretical calculations for a parabolic well under an applied electric field were done analytically²³ or numerically²⁴ just recently. Using our method, the minibands of a superlattice made of parabolic basis are shown in Fig. 3. Also shown are the minibands of the $n-i-p-i$ structure which has a constant effective mass otherwise the same potential in the conduction band. Our new model is especially useful when the carrier injection needs to be considered as in $n-i-p-i$ structures for current controlled band tuning applications.²⁰

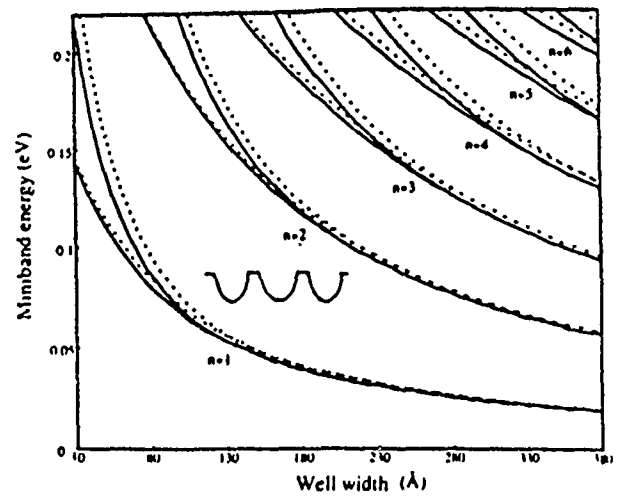


FIG. 3. Comparison of the minibands of the same parabolic well. The dotted lines indicate edges of the minibands for $n-i-p-i$, which has a constant effective mass, and the solid lines are for the compositionally graded well whose effective mass is changing with the barrier height. The maximum barrier height is $\text{Al}_{0.3}\text{Ga}_{0.7}\text{As}$. The barrier between each basis is 28 Å of the $\text{Al}_{0.3}\text{Ga}_{0.7}\text{As}$, corresponding to 10 monolayers.

B. Triangular well

The miniband energies in a rectangular-well superlattice can be simply estimated as $E_n \propto n^2$, where n denotes the n th miniband. For the applications of band-aligned superlattices (BAS),¹⁰ sometimes it is necessary to use a different kind of superlattices in order to provide a miniband discontinuity. This dissimilar superlattice has the miniband energy $E_n \propto n^a$, where $a < 2$. The parabolic well in the previous case has $a \approx 1$. Another example is the triangular well with $a < 1$ as shown in Fig. 4. The bandwidth of the triangular well superlattice decays faster than the parabolic well or the rectangular well since the barrier increases very fast. Also the ground-state band has higher energy than the other wells due to the narrowing toward the bottom of the well.

It should be noted that the channel of the high-electron-mobility transistor (HEMT) is often approximated as a triangular potential well. The exact calculation of the energy levels is possible in our treatise to include doping and the carrier accumulation effects on the potential shape.

C. Step-well superlattice

The step-well shown in the inset of Fig. 5 also falls into the superlattice group with $a < 2$. With the change of the alloy composition and the width of the well, the step well is more flexible than the parabolic well or triangular well in the BAS application. Our recent calculation also shows that the step quantum well has large intersubband Stark shift in that the energy levels in the small and big wells have different dependence on the electric field. A

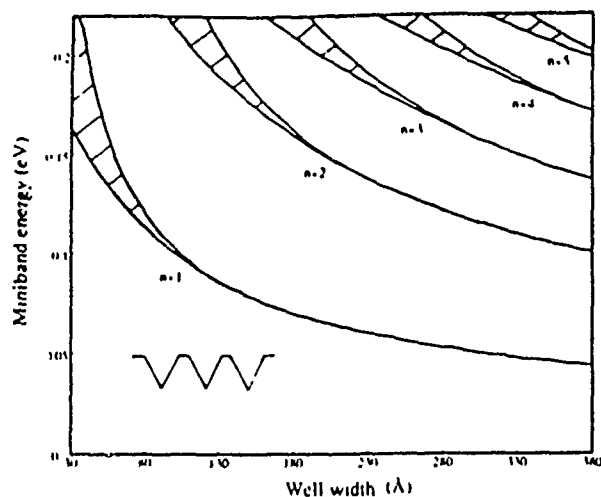


FIG. 4. The minibands of a triangular-well superlattice. The structure of a triangular-well superlattice is shown in the inset. The maximum barrier height is $\text{Al}_{0.3}\text{Ga}_{0.7}\text{As}$. The barrier between each basis is 28 \AA of the $\text{Al}_{0.3}\text{Ga}_{0.7}\text{As}$, corresponding to 10 monolayers. The gaps between minibands are decreasing toward the top of the barrier.

plot of E - k dispersion relation is shown in Fig. 5 for the rectangular well, parabolic well, triangular well, and step well, respectively, where the lower bands are deliberately chosen to be aligned, thus a miniband discontinuity is formed for the upper band. The triangular well and step well have the most desired features.

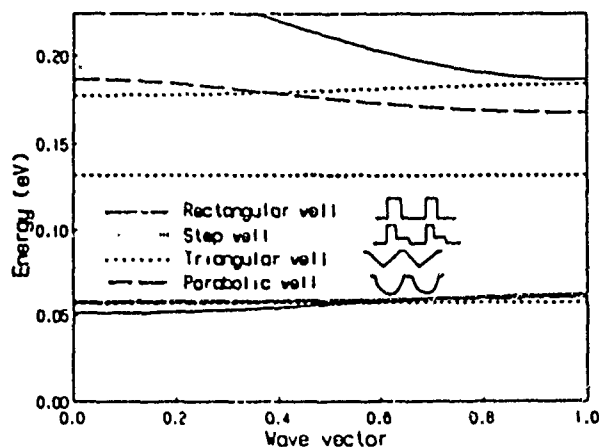


FIG. 5. Comparison of the E - k dispersion relation for the rectangular well, parabolic well, triangular well, and the step well. The structures are shown in the inset. The barrier and well widths used in the calculation are 40 \AA , 62 \AA , for the rectangular well; 40 \AA , 74 \AA (the second barrier), 34 \AA for the step well; 14 \AA , 246 \AA for the triangular well; and 28 \AA , 116 \AA for the parabolic well, respectively. We assume $\text{Al}_{0.3}\text{Ga}_{0.7}\text{As}$ for the barrier and $\text{Al}_{0.1}\text{Ga}_{0.9}\text{As}$ for the second barrier of the step well. The lower minibands are deliberately chosen to be aligned. The upper minibands of the triangular well and the step well are the lowest.

V. APPLICATION TO MULTIPLE-LAYER BASIS

A. Two-well coupling

The coupling of two quantum wells is found to have more energy levels than the single quantum well of the same dimensions.²⁵ Large Stark shift has been found in coupled quantum wells.^{9,26,27} Our theoretical calculation of the minibands is shown in Fig. 6 for a superlattice basis consisting of two rectangular wells, one of the well widths is fixed (90 \AA) and the other varied. Compared to Fig. 1(a), it is clear that in the two-well case the minibands are mixed from those of its original wells. The two horizontal bands in Fig. 6 indicate the energy levels for the 90 \AA well. While the four falling bands are the minibands of the variable well. The miniband bandwidth is narrow in this case because the other well acts as a barrier when one looks from one well.

B. Band-aligned basis

The cross points in Fig. 6 are where the minibands of the two wells are aligned. The first cross point occurs when the varied well width is 25 \AA , where its only miniband is aligned with the upper miniband of the 90 \AA well. The aligned bands have much larger bandwidth than the nonaligned bands which are bound states in nature, since the nonsymmetrical well acts as a barrier for the nonaligned minibands.

One application of the band-aligned basis is to use the bound state to miniband transition which has a significant effect in improving the dark current for the photo detectors.¹² The major advancement in using intersubband transition for $8\text{--}12 \mu\text{m}$ detection is the reduction of dark current.^{28,29} If thicker barriers are used, the

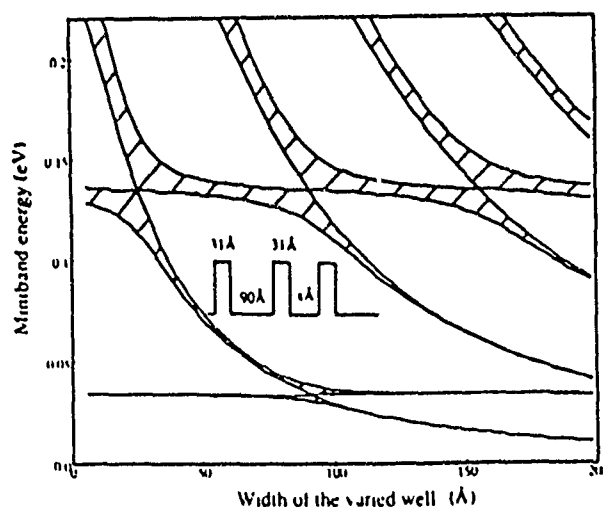


FIG. 6. The minibands of a superlattice with the basis consisting of two coupled wells. One of the well is fixed to be 90 \AA , and the other is changed as a parameter. The two barriers in the basis are fixed to be 31 \AA . It superimposes the minibands originated from each well. As the bands cross over, band alignment occurs, but are soon split off.

photocurrent will decrease due to the same reason of a low dark current. The employment of band-aligned basis will reduce the dark current because of the bound-state nature of the lower nonaligned band while the conductivity is large in the upper aligned band.

Another application of the band-aligned basis is the tuning of the mobility or the effective-mass ratio of the upper to the lower miniband. The effective mass m_z of the miniband is related to the miniband bandwidth B by $m_z = 2\hbar^2/Bd^2$, where d is the length of the basis. This relation is easily obtained by taking the second derivative of the miniband dispersion relation $E = E_0 + \frac{1}{2}B \cos qd$. Thus for a band-aligned basis, the effective-mass ratio of an aligned band to the bound state is significantly different from the conventional structures. For the rectangular-well superlattice the bandwidth ratio for the second band to the ground band is on the orders of 5–10, but for the case of band-aligned basis, it can be more than 10^3 . To reduce this bandwidth ratio, one may choose to align to the lower band instead of the upper band. An example is shown in Figs. 7(a) and 7(b) for the band alignment in the upper and the lower bands, respectively. The bandwidth ratio is about unity in the latter.

C. Perturbation of degenerate states in quantum wells

The crosspoints in Fig. 6 reveal that the bands only align in one point; beyond that point of the well width the

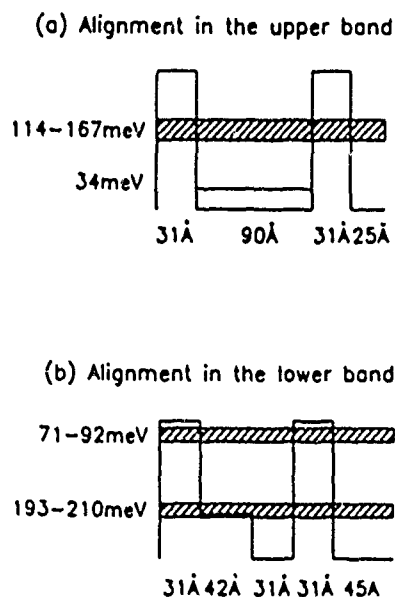


FIG. 7. Structures of band-aligned bases; alignment can be done either (a) in the upper band or (b) in the lower band. In (a), the widths of the two coupled wells are 90 Å, 25 Å, respectively. The barrier width is 31 Å. In (b), the basis consisting of a step well and a rectangular well. The alloy compositions and the layer widths are 0.3, 0.1, 0, 0.3, and 0 and 31 Å, 42 Å, 31 Å, 31 Å and 45 Å, respectively. The bandwidth in the lower band is about equal to that in the upper band.

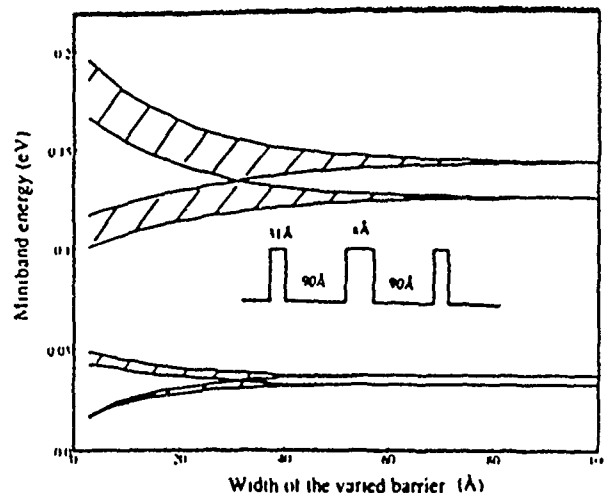


FIG. 8. The demonstration of perturbation of two degenerate minibands in the superlattice. The basis consists of two identical wells with width 90 Å, one fixed barrier with a 31 Å width and the other barrier with varied width as a parameter. The original miniband has split into two because of the perturbation.

aligned bands will split into two. The same energy tends to repel one from the other.

For further investigations, the two coupled well basis is again used as an example. This time the two wells are identical, with one variable barrier width. As shown in Fig. 8 the original states of either of the wells have two minibands, the lower one is 31–39 meV and the upper one is 119–151 meV. The variable barrier perturbs the degenerate states and each of the minibands will split into two.

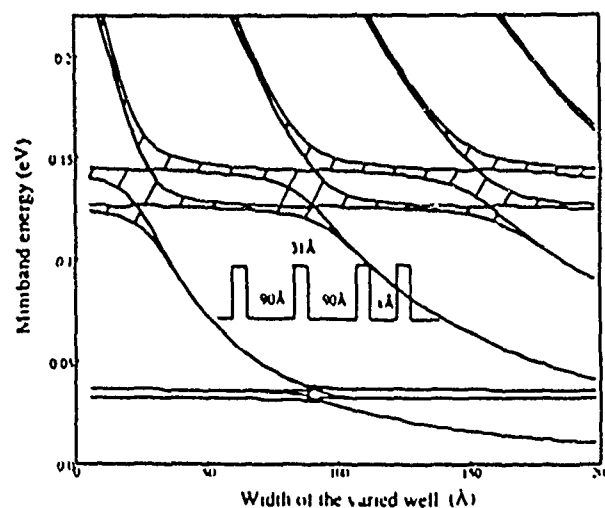


FIG. 9. The miniband structures of a basis with three coupled wells. Two of the wells are identical and fixed, with the other changed. The fixed wells have a width of 90 Å. All the barriers are fixed to be 31 Å. The band structures result from superpositions of all the minibands originated from the single well basis, with the repulsion effect taken into consideration.

D. Multiple well coupling

Physically, the miniband structures of a multiple layer basis can be treated as a mixture or superposition of the states originated from the single-well basis, with the perturbation taken into account if the energy levels are too close to each other. The wave functions are oscillatory in its own original well and decaying in all the other wells and barriers. In the case of three-well coupling, we choose two identical wells and one varied well as shown in Fig. 9. Each of the original minibands of the identical wells split into two bands because the varied well is a perturbation for the degenerate minibands, otherwise all the bands retain their original shapes.

VI. CONCLUSION

In the first part of the paper, a new formalism of the Kronig-Penney model has been developed which incorporates the transfer matrix technique and the envelope-function approximations. This new approach has several advantages over the other methods. First, its formalism by transfer matrix is much easier and more systematic than the conventional Kronig-Penney model as far as the boundary condition matching is concerned. Second, it can calculate for complicated multiple layer bases and arbitrary potential profiles result from change of alloy composition, doping or carrier accumulation. Third, it is accurate and without excessive computation cost since the

effective-mass difference, nonparabolicity and band coupling of the bulk bands are included by the envelope function in a natural way.

In the second part of the paper, our new approach is applied to some specific superlattice bases. The finite parabolic well case is solved in a simpler and more accurate way. The triangular well and step well which belong to the superlattices with $E_g \propto n^a, a < 2$, which are useful in the BAS applications can also be easily worked out. The minibands of a superlattice with the basis consisting of multiple layers can be considered as a superposition of all the minibands originated from their simple single-well basis, with the repulsion effect taken into account. The method offered to us explains readily the coupling of wells in the basis for tuning the energy levels. The splitting of minibands, the band-aligned basis, the overlapping of the wave functions originated from different wells, and the effective-mass tuning in superlattices are among the examples.

ACKNOWLEDGMENT

The authors are indebted to Dr. J. Schulman in the discussion of the envelope-function approximations. The discussions with Dr. R. Karunasiri and Mr. Y. Mii are also helpful. This work is supported in part by Office of Naval Research, Army Research Office, and Semiconductor Research Corporation.

- ¹Leo Esaki, IEEE J. Quantum Electron. QE-22, 1611 (1986).
- ²L. Esaki and R. Tsu, IBM J. Res. Dev., Jan. 1970, p. 61.
- ³G. Bastard, Phys. Rev. B 24, 5693 (1981).
- ⁴G. Bastard and J. A. Brum, IEEE J. Quantum Electron. QE-22, 1625 (1986).
- ⁵G. Bastard, in *Molecular Beam Epitaxy and Heterostructures*, Vol. 87 of *NATO Advanced Study Institute Series E*, edited by L. L. Chang and K. Ploog (Martinus Nijhoff, Dordrecht, 1985), pp. 381-423.
- ⁶E. O. Kane, J. Phys. Chem. Solids 1, 249 (1957).
- ⁷Joel N. Schulman, Mater. Res. Soc. Symp. Proc. 56, 279 (1986).
- ⁸Hung-Sik Cho and Paul R. Prucnal, Phys. Rev. B 36, 3237 (1987).
- ⁹H. Q. Le, J. J. Zayhowski, and W. D. Goodhue, Appl. Phys. Lett. 50, 1518 (1987).
- ¹⁰Peng-fei Yuh and K. L. Wang, Appl. Phys. Lett. 51, 1404 (1987).
- ¹¹Susanta Sen, Federico Capasso, Arthur C. Gossard, Richard A. Spah, Albert L. Hutchinson, and S. N. G. Chu, Appl. Phys. Lett. 51, 1428 (1987).
- ¹²K. K. Choi, B. F. Levine, C. G. Bethea, J. Walker, and R. J. Malik, Phys. Rev. Lett. 59, 2459 (1987).
- ¹³M. O. Vassell, Johnson Lee, and H. F. Lockwood, J. Appl. Phys. 54, 5206 (1983).
- ¹⁴*Handbook of Mathematical Functions*, edited by M. Abramowitz and I. A. Stegun (National Bureau of Standards, Washington, D. C., 1964).
- ¹⁵I. Hase, H. Kawai, K. Kaneko, and N. Watanabe, J. Appl. Phys. 59, 3792 (1986).
- ¹⁶E. E. Mendez, W. I. Wang, E. Calleja, and C. E. T. Goncalves da Silva, Appl. Phys. Lett. 50, 1263 (1987).
- ¹⁷A. C. Marsh, IEEE J. Quantum Electron. QE-23, 371 (1987).
- ¹⁸A. R. Bonnefoi and T. C. McGill, Phys. Rev. B 37, 8754 (1988).
- ¹⁹H. C. Liu, Appl. Phys. Lett. 51, 1019 (1987).
- ²⁰Gottfried H. Döhler, IEEE J. Quantum Electron. QE-22, 1682 (1986).
- ²¹R. C. Miller, A. C. Gossard, D. A. Kleinman, and O. Munteanu, Phys. Rev. B 29, 3740 (1984).
- ²²S. Y. Chou and J. S. Harris, Jr., Appl. Phys. Lett. 52, 1422 (1988).
- ²³R. P. Karunasiri and K. L. Wang, Superlatt. Microstruct. (to be published).
- ²⁴Yang Chu-liang and Yang Qing, Phys. Rev. B 37, 1364 (1988).
- ²⁵Herbert Kroemer and Hiroshi Okamoto, Jpn. J. Appl. Phys. 23, 970 (1984).
- ²⁶Y. J. Chen, Emil S. Koteles, B. Elman, and C. A. Armiento, Mater. Res. Soc. Symp. Proc. 102, 571 (1988).
- ²⁷Peng-fei Yuh and K. L. Wang, Phys. Rev. B 38, 8377 (1988).
- ²⁸B. F. Levine, K. K. Choi, C. G. Bethea, J. Walker, and R. J. Malik, Appl. Phys. Lett. 50, 1092 (1987).
- ²⁹K. K. Choi, B. F. Levine, C. G. Bethea, J. Walker, and R. J. Malik, Appl. Phys. Lett. 50, 1814 (1987).

Growth and characterization of Ge/Si strained-layer superlattices

S. J. Chang, C. F. Huang, M. A. Kallel, and K. L. Wang

Device Research Laboratory, Electrical Engineering Department, University of California, Los Angeles, California 90024

R. C. Bowman, Jr. and P. M. Adams

The Aerospace Corporation, P. O. Box 92957, Los Angeles, California 90009

(Received 8 July 1988; accepted for publication 30 August 1988)

Ultrathin Ge/Si strained-layer superlattices (SLS's) with periodicities of a few monolayers have been successfully grown and characterized by Raman scattering spectroscopy. Structures with alternating Ge and Si layers were grown on Si substrates of different orientations. A thick 200 nm $\text{Ge}_{0.4}\text{Si}_{0.6}$ buffer layer was grown prior to the growth of the superlattice to make the strain distribution of the superlattice symmetrical and thus to maintain the pseudomorphic growth of the superlattices. Folded acoustic phonon peaks observed from these Ge/Si SLS samples can be used to determine the superlattice periodicity. The observed optical phonon frequencies were found to depend strongly on superlattice periodicity. A quantitative interpretation of this phenomenon was presented. Subsequent annealing of these samples reveals that the transition from pure Ge and/or Si layers to $\text{Ge}_x\text{Si}_{1-x}$ alloy becomes more pronounced as the annealing time and temperature increase.

Recently, much attention has been focused on Ge/Si strained-layer superlattices (SLS's), both theoretically¹⁻⁴ and experimentally,^{5,6} due to their unusual optical and electrical properties. However, due to the large 4.2% lattice mismatch between Ge and Si, pure Ge can only be commensurately grown on a Si substrate up to six monolayers (~ 0.9 nm).⁶ In order to have a larger superlattice thickness, Kasper *et al.* had demonstrated the growth of symmetrically strained Ge/Si superlattices using an appropriate $\text{Ge}_y\text{Si}_{1-y}$ buffer layer.⁷ In this work, we studied the phonon behaviors of these Ge/Si SLS's as well as the interdiffusion of Ge and Si atoms due to thermal treatment.

Samples used in this work were grown in a Si molecular beam epitaxy chamber equipped with two electron beam evaporators for Si and Ge separately, a quadrupole mass spectrometer for residual gas analysis, and a reflection high-energy electron diffraction (RHEED) system for *in situ* characterization of the epilayer. The base and growth pressures were $\sim 7\text{--}8 \times 10^{-11}$ and $\sim 5\text{--}9 \times 10^{-9}$ Torr, respectively, and the fluxes for Ge and Si sources were monitored by an Inficon Sentinel III deposition controller. Prior to loading the Si substrates into the chamber, they were chemically precleaned by Shiraki's method.⁸ In the final step, a protective thin SiO_2 film (~ 1.5 nm) was grown chemically in a solution of $3\text{HCl}:\text{1H}_2\text{O}_2:\text{1H}_2\text{O}$ for 10 min. The protective oxide layer was then removed *in situ* by the Si beam at a substrate temperature of 700 °C. The growth temperature was kept at 400 °C, and the growth rate was 2.75×10^{14} $\text{cm}^{-2} \text{ s}^{-1}$ for Si layers and 2.2×10^{14} $\text{cm}^{-2} \text{ s}^{-1}$ for Ge layers. RHEED patterns observed from the top Si layers of these SLS samples indicate good epilayer crystallinity.

In this study, Raman experiments were performed at room temperature with near-backscattering geometry. Samples were kept in vacuum to avoid scattering from the air. Various lines (457.9, 488.0, 514.5 nm) of an argon ion laser were used for excitation. The laser light was focused with a

cylindrical lens and the power was kept under 75 mW to prevent sample heating and any possible annealing effect. Scattered light was analyzed with a Spex 1404 double spectrometer and an EG&G 941 photon counter.

All samples used in this study have a thick $\text{Ge}_{0.4}\text{Si}_{0.6}$ buffer layer and the thickness ratio of Ge and Si layers is $d_{\text{Ge}}:d_{\text{Si}} = 2:3$. Assuming that the thick buffer layer is completely relaxed, the strain on Ge and Si layers, ϵ_{Ge} and ϵ_{Si} , could be calculated to be -2.4% and $+1.7\%$, respectively.⁷ In this case, the strains of the bilayer cancel each other and, as long as the thickness of each layer does not exceed its critical thickness, no dislocations are generated at the superlattice/buffer interface. Table I is a summary of the samples used in this work, where d_n is the nominal superlattice periods and d_{RS} is the superlattice periods obtained from Raman scattering. Figure 1 shows the Raman spectra ($\lambda = 514.5$ nm) of samples H38, H41, and H56 all with the same (100) sample orientation but with different superlattice periods. Broad folded longitudinal acoustic (LA) phonons were observed at 189, 97, and 48 cm^{-1} for each sample. However, it was not observed for sample H52 with $d_n = 0.7$ nm due to its extremely small superlattice period. The nature of the broad folded LA peak and the reason that it is unable to resolve the LA phonon doublet⁹ is probably due to a slight broadening of the layer interfaces at the growth tempera-

TABLE I Summary of the Ge/Si SLS samples used in this study. All samples were grown with a 200 nm $\text{Ge}_{0.4}\text{Si}_{0.6}$ buffer layer and with the Ge and Si thickness ratio $d_{\text{Ge}}:d_{\text{Si}} = 2:3$.

| Sample | d_n (Å) | d_{RS} (Å) | No. of periods | Substrate orientation |
|--------|--------------|------------------------|-------------------|--------------------------|
| H38 | 14 | 11.6 | 150 | (100) |
| H41 | 28 | 22.5 | 120 | (100) |
| H52 | 7 | ... | 300 | (100) |
| H56 | 56 | 45.4 | 40 | (100) |

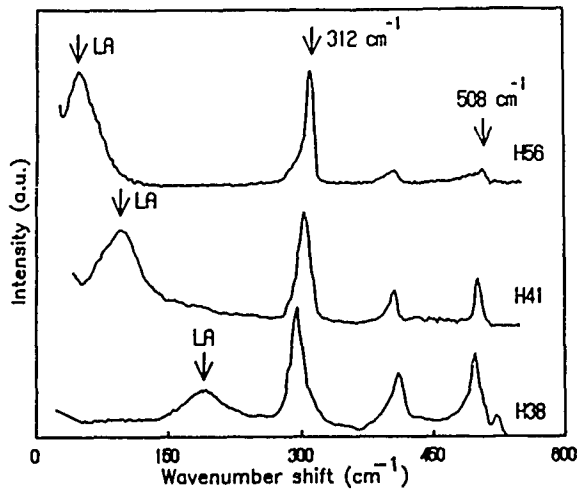


FIG. 1. Raman spectra of samples H38, H41, and H56, all with the same (100) sample orientation but different superlattice periodicities. The laser was operated at 514.5 nm.

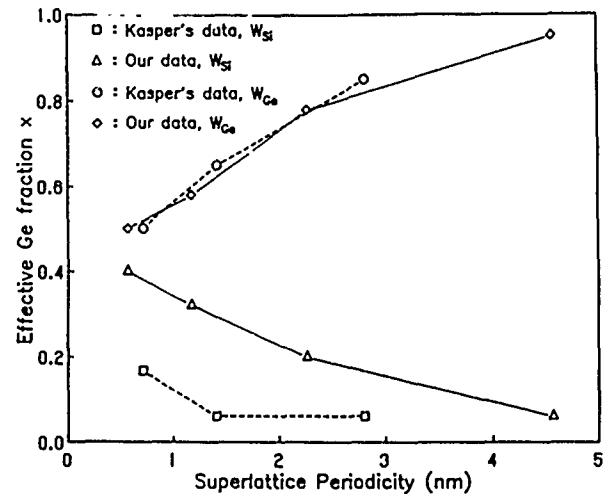


FIG. 2. Effective Ge fraction x , as obtained from the Ge-Ge and Si-Si optical phonon vibration frequencies of the Ge/Si SLS. Also shown are Kasper's data⁷ for comparison.

ture. This is evidenced from the observed increase of folded LA phonon full width at half maximum as the superlattice period becomes smaller.

Following Rytov's elastic continuum model for vibrations in layered media, we can calculate d_{RS} by¹⁰

$$\cos(qd_{RS}) = \cos\left(\frac{\omega d_{Ge}}{v_{Ge}}\right) \cos\left(\frac{\omega d_{Si}}{v_{Si}}\right) - \frac{1}{2}\left(R + \frac{1}{R}\right) \sin\left(\frac{\omega d_{Ge}}{v_{Ge}}\right) \sin\left(\frac{\omega d_{Si}}{v_{Si}}\right), \quad (1)$$

where $R = \rho_{Si}v_{Si}/\rho_{Ge}v_{Ge}$, v_{Ge} , v_{Si} are the sound velocities and ρ_{Ge} , ρ_{Si} are the densities of Ge and Si, respectively. The values of d_{RS} obtained from Eq. (1) are listed in Table I and they are consistently 20% smaller than expected from the growth parameters. The optical phonon peaks due to the vibrations of Ge-Ge, Ge-Si, and Si-Si pairs are also observed. Ge-Si vibrations can only come from layer interfaces, since the layers are pure Ge and Si. Samples with larger periods (i.e., less interfaces) will therefore have a smaller Ge-Si Raman signal, as observed in Fig. 1. The strain-induced frequency shifts $\delta\omega$ for both Ge-Ge and Si-Si vibrations could be calculated by¹¹

$$\delta\omega = \frac{p}{2\omega_0} \epsilon_{xx} + \frac{q}{2\omega_0} (\epsilon_{xx} + \epsilon_{yy}), \quad (2)$$

where ω_0 is the nonstrained phonon frequency, ϵ_{ij} are the components of the strain tensor, and p and q are phenomenological parameters. For samples grown on (100) substrates, the optical phonon frequencies for Si and Ge layers in this case are predicted to be at 508 and 312 cm^{-1} , respectively.⁷ However, all the observed frequencies are lower than their expected values, and the frequencies for samples having larger periods have phonon energies closer to the expected values. This can be explained by the fact that the Si and/or Ge atoms at layer interfaces see two neighboring Si atoms and two neighboring Ge atoms such that the local bonding is identical to a $\text{Ge}_{0.5}\text{Si}_{0.5}$ alloy.¹² Therefore, samples with smaller periods (i.e., more interfaces) will have more atoms

behaving like a weakly strained alloy. As a result, the smaller periodicity samples will have both Si-Si and Ge-Ge peak frequencies located at lower energies. Similar trends were also observed for samples grown on (110) and (111) substrates. Using Eq. (2) and the known values of Ge-Ge and Si-Si Raman energies of the unstrained $\text{Ge}_x\text{Si}_{1-x}$ alloy,¹³ we can define quantitatively the degree of alloy mixing of these Ge/Si SLS's by the effective Ge fraction x for both Ge-Ge and Si-Si phonon vibrations. These results are shown in Fig. 2. Also shown in Fig. 2 are Kasper's data⁷ for comparison.

Interface mixing due to Ge and Si interdiffusion was also studied by annealing the samples at various temperatures. Figure 3 shows the Raman spectra ($\lambda = 457.9 \text{ nm}$) of sample H56 annealed at 726 °C with different annealing times. As the annealing time increased, we can observe (1) that the relative intensity of Ge-Si phonon vibration increased and (2) a large red shift of the Ge-Ge Raman peak. Similar trends were observed as the annealing temperature increased. Figure 4 shows the effective Ge fraction x of sample H56 as a function of annealing time and temperature, obtained from their Ge-Ge Raman peak positions. We can

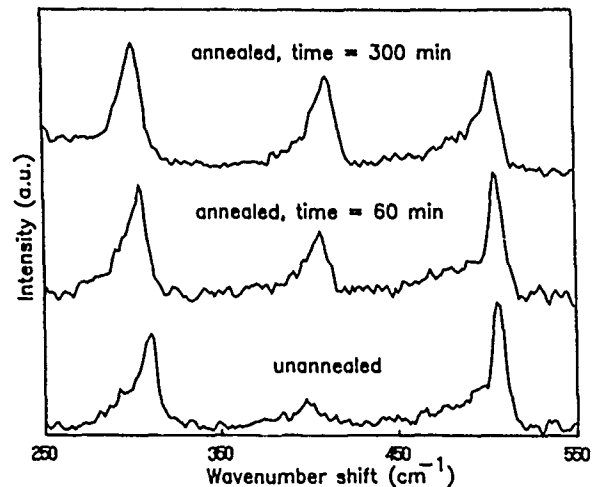


FIG. 3. Raman spectra of sample H56 after being annealed at 726 °C with different annealing times. The laser was operated at 457.9 nm.

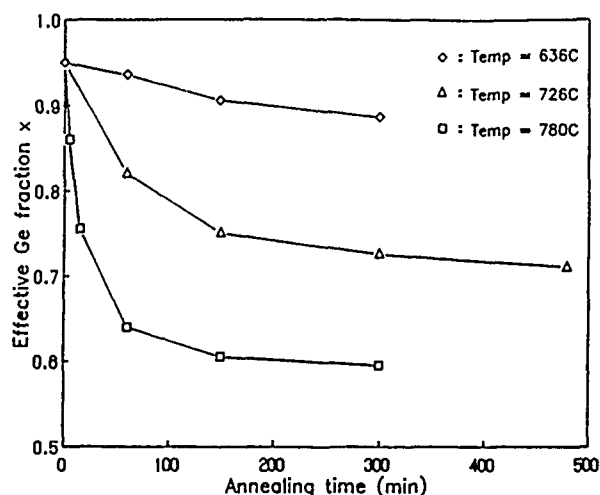


FIG. 4. Effective Ge fraction x obtained from the Ge-Ge Raman peak positions of sample H56 after being annealed at different times and temperatures.

clearly see that a transition from pure Ge and/or Si layers to $\text{Ge}_x\text{Si}_{1-x}$ alloy occurred, and this transition becomes more pronounced as the annealing time and temperature increased. The Si-Si Raman peak, however, only has a smaller red shift due to the larger Si layer thickness. When the 514.5 nm laser line, which gives a deeper penetration, was used for excitation, the intensity of Si Raman peak (at 520 cm^{-1}) from the substrate increased as the annealing time and temperature increased. Similar results were reported by Kasper *et al.*⁷ In their experiment, Ge/Si SLS's with the same overall superlattice thickness but different period lengths were compared. It was found that smaller period (i.e., more interfaces) samples are more transparent in the green spectra region. This good agreement indicates that interface mixing is indeed very important in such ultrathin Ge/Si SLS's. We also used x-ray diffraction spectroscopy to study these sam-

ples before and after annealing. The decay of the low-angle x-ray diffraction peak from the superlattice structure, as annealing time and temperature increase, confirms the interdiffusion of Ge and Si caused interface smearing. A more detailed study of x-ray diffraction will be reported later.

In summary, ultrathin Ge/Si SLS samples have been grown and characterized. It has been found that the phonon behaviors depend strongly on interface mixing and thus superlattice periodicity. The effective Ge fraction x of the Ge-Ge and Si-Si phonon vibrations can be determined by their respective Raman peak positions. The annealing effect of these Ge/Si superlattices was also studied.

The authors would like to thank Dr. E. Kasper of AEG Research for his interesting discussion and V. Arbet for his assistance in growing part of the samples. The work at the University of California, Los Angeles is supported by the Office of Naval Research and the Army Research Office. R. C. Bowman, Jr. and P. M. Adams would like to acknowledge the support of the Aerospace Sponsored Research program.

- ¹S. Froyen, D. M. Wood, and A. Zunger, *Phys. Rev. B* **36**, 4547 (1987).
- ²C. G. Van de Walle and R. M. Martin, *J. Vac. Sci. Technol. B* **3**, 1256 (1985).
- ³C. G. Van de Walle and R. M. Martin, *Phys. Rev. B* **34**, 5621 (1986).
- ⁴M. S. Hybertsen and M. Schluter, *Phys. Rev. B* **36**, 9683 (1986).
- ⁵T. P. Pearsall, J. Berk, L. C. Feldman, A. Ourmezd, J. M. Bonar, and J. P. Mannaerts, *Phys. Rev. Lett.* **58**, 729 (1987).
- ⁶J. Berk, J. P. Mannaerts, L. C. Feldman, B. A. Davison, and A. Ourmazd, *Appl. Phys. Lett.* **49**, 286 (1986).
- ⁷E. Kasper, H. Kibbel, H. Jorke, H. Brugger, E. Friess, and A. Abstreiter, *Phys. Rev. B* **38**, 3599 (1988).
- ⁸A. Ishizaka and Y. Shiraki, *J. Electrochem. Soc.* **133**, 666 (1986).
- ⁹H. Brugger, G. Abstreiter, H. Jorke, H. J. Herzog, and E. Kasper, *Phys. Rev. B* **33**, 5928 (1986).
- ¹⁰M. Rytov, *Sov. Phys. Acoust.* **2**, 68 (1956).
- ¹¹E. Anastassakis, A. Pinczuk, E. Burstein, F. H. Pollak, and M. Cardona, *Solid State Commun.* **8**, 133 (1970).
- ¹²J. C. Tseng, S. S. Iyer, and S. L. Delage, *Appl. Phys. Lett.* **51**, 21 (1987).
- ¹³W. J. Brya, *Solid State Commun.* **12**, 253 (1973).

Theory and Applications of Band-Aligned Superlattices

KANG L. WANG, SENIOR MEMBER, IEEE AND PERNG-FEI YUH

Abstract—A general new device concept based on the miniband junctions formed in multiple superlattices is described. As heterojunctions play an important role in bulk semiconductor devices, the miniband junctions have potential applications for new superlattice devices. In the band-aligned structures, the aligned minibands function as an energy filter, which ensures efficient injection of monoenergetic carriers, while the miniband offsets can block the carrier flow similarly to the band discontinuity in bulk heterostructures. By engineering the alloy composition, the layer width, the doping, and the applied electric field, several examples of band-aligned superlattices are analyzed for applications in miniband transport and intersubband transitions.

I. INTRODUCTION

ALMOST all of the semiconductor devices are made by doped p-n junctions and/or heterojunctions. Those junctions which make up the diverse device world have one thing in common; that is, they connect two semiconductor layers with different bands. The bands of a p-n junction are controlled by the dopants, while the bands of a heterojunction are changed by the alloy compositions.

The superlattice is made of periodic junctions such that the bands connected by the junctions form a one-dimensional periodic potential [1]. Because of this one-dimensional potential superimposed on the real crystal potential, minibands are formed within the conduction and valence bands. To explore the concept of semiconductor junction further, the question raised is what will be the junction which connects two superlattices having different minibands. By analogy with the junction devices, this new superlattice junction formed by stacking different types of superlattices can afford yet another dimension in the device world.

Usually, a superlattice is composed of a period of a simple element, e.g., square shape or a triangle potential. This, however, need not be the case. The building block of the superlattice can be any arbitrary potential well, and in addition, many different superlattices can be put together to form a device structure. We refer to the latter as a multiple superlattice, where "junctions" can be readily formed. The junctions between multiple superlattices can be divided into two categories: band alignment, where the minibands in both sides are partly or totally aligned, and

band offset or band stop, where the miniband on one side of the junction becomes an evanescent state on the other. For convenience, the name band-aligned superlattice (BAS) is used to refer to this new multiple superlattice [2], where the minibands are purposely aligned or not aligned, and a superjunction is the junction formed by such multiple superlattices.

The methods we use to investigate the BAS's are described in Section II. Several structures are analyzed with these methods in Sections III and IV for new infrared detector and laser applications.

II. METHODS

For an ideal superlattice, where an infinite number of periodical layers is assumed, the Kronig-Penney model [3] can be used to determine the minibands and wave functions. For a finite superlattice, on the other hand, realistic calculations must be done for transmission coefficient and current, wave functions, and carrier density. The former model has been well established in the formulation of resonant-tunneling diodes [4], [5]. The latter has been developed previously by us [6] and also by some other authors in self-consistent calculations [7], [8]. However, all the previous formalisms consider only the energies above the conduction-band edge. For energies below the conduction-band edge, evanescent waves exist, and the carrier density due to these evanescent waves cannot be simply neglected, especially for the analysis of BAS's. Thus, in what follows, we will cite only the results for the oscillatory wave solutions and describe in detail the evanescent wave case. The GaAs/AlGaAs material system is used as an example in the following calculations, and extension to other semiconductor systems is straightforward.

A. Transmission Coefficient and Current

Fig. 1 shows the conduction-band edge of a superlattice consisting of a finite number of layers with a total length L . The conduction band envelope functions along the z direction, denoted by Ψ_l and Ψ_r for the left and right hand contacts, respectively, are

$$\Psi_l = \begin{cases} A_+ e^{ik_l z} + A_- e^{-ik_l z} & \text{for oscillatory wave} \\ A_+ e^{\kappa_l z} & \text{for evanescent wave,} \end{cases} \quad z \leq 0$$

Manuscript received March 9, 1988; revised August 9, 1988. This work was supported in part by the SDI Science Innovation Program monitored by the Office of Naval Research and the Army Research Office.

The authors are with the Device Research Laboratory, Department of Electrical Engineering, University of California, Los Angeles, CA 90024
IEEE Log Number 8824436.

By assuming that $\kappa_r = \kappa_l = \kappa$ and $\gamma_r = \gamma_l = \gamma$, (8) can be reduced to

$$\tan \frac{ka}{2} = -\frac{\gamma k}{\kappa}, \quad \tan \frac{ka}{2} = \frac{\kappa}{\gamma k}, \quad (10)$$

which are the well-known dispersion relations for an isolated square quantum well.

In Cases 1 and 2, the carrier density can be determined after the wave function is obtained, and the formula is given in [6].

III. BAND-ALIGNED STRUCTURES BY ENGINEERING THE LAYER WIDTH AND ALLOY COMPOSITION

A. BAS Detector

The simple band-aligned structure shown in Fig. 2 is composed of two superlattices (S1 and S2). The ground miniband of the narrow-well superlattice (S2) is aligned with the upper band of the wide-well superlattice (S1), so that the transport in the upper band can occur continuously at the junction (J). On the other hand, the transport in the lower band stops at the junction (J). When the structure is used as an infrared detector, the miniband stop can prevent flowing of the dark current in the lower band, while the miniband alignment can allow the photocurrent to flow in the upper band. In other words, the narrow-well superlattice (S2) acts as an energy filter, which selects only the hot electrons transported in the upper band.

For convenience of analysis, we will denote each layer in the superlattice as $(M_x)_d^r$ where M is the number of monolayers and is related to the layer width L by $L = 2.83M \text{ \AA}$, x is the fraction of Al composition, r is the number of repetitions of this layer, and d denotes the doping type with $d = n, p, i$ to indicate the n-doped, p-doped, and intrinsic layers, respectively.

The transmission coefficient of a BAS detector consisting of $(11_0.335_0)_n^2(11_0.311_0)_n^2$ is shown in Fig. 3. For comparison, the coefficient of a simple superlattice $(11_0.335_0)_n^3$, which has the same dimension but without the energy filter, is also shown in Fig. 3. The transmission coefficient for the lower band of the BAS detector is significantly reduced (a factor of 10^{-3}) by the energy filter, while that in the upper band is almost not affected. This implies that the dark current of the BAS detector is reduced, while the photocurrent transport in the upper band is not affected. To investigate this further, three-dimensional plots of the wave function versus energy and location are shown in Fig. 4. The wave functions are high and oscillatory within the minibands and decay elsewhere in energy. More interesting is that the wave function in the lower band oscillates inside the $(11_0.335_0)$ superlattice, but decays rapidly in the $(11_0.311_0)$ superlattice, as the latter filters out the lower-energy waves.

There are several nonideal factors which may cause problems of miniband alignment. First of all, the well width variations may cause a shift of miniband energies. For example, a two-monolayer (or 5.8 \AA) change in a $(11_0.335_0)$ well (or 100 \AA) may cause 2 and 10 meV

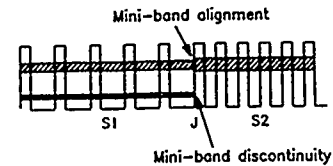


Fig. 2. Band-aligned structure for detector application. It consists of two kinds of superlattices. The wide-well superlattice (S1) on the left has two minibands, where the upper one is aligned with the ground miniband of the narrow-well superlattice (S2) on the right. Current transport in the lower band (usually dark current) is blocked by the miniband stop at the junction (J), while the current in the upper band (usually photocurrent) is not affected due to the aligned bands.

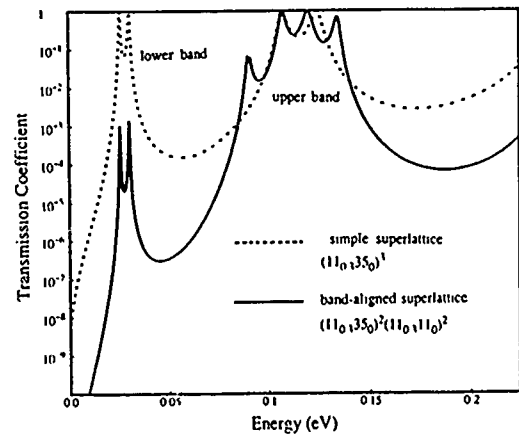


Fig. 3. Comparison of transmission coefficients of a BAS detector $(11_0.335_0)_n^2(11_0.311_0)_n^2$ and a simple superlattice detector $(11_0.335_0)_n^3$ which has the same dimensions. The lower peak is significantly reduced in the BAS detector, which implies that the current transport in the lower band is suppressed. The upper peak has the same magnitude except for the splitting, which is characteristic of aligned bands.

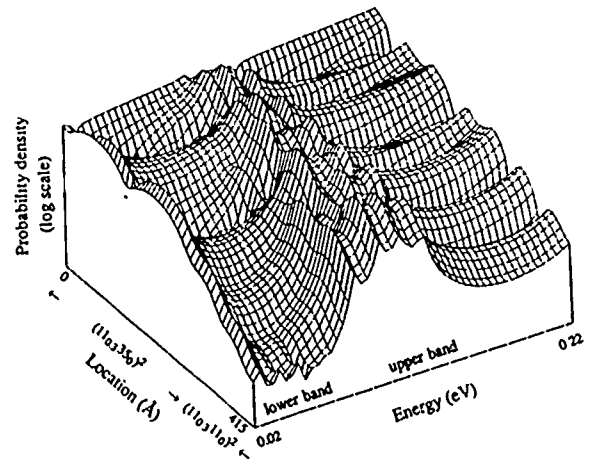


Fig. 4. The left-to-right wave function as a function of location and energy for a BAS detector consisting of $(11_0.335_0)_n^2(11_0.311_0)_n^2$. The wave functions are large and oscillatory within the minibands and decay elsewhere in energy.

shifts of the lower and upper bands, respectively. To minimize the band misalignment caused by well-width variation, thinner barriers are required so that the wells are strongly coupled and the minibands can overlap appreciably. The choice of an $(11_0.3)$ barrier has miniband bandwidths of 7 and 30 meV, respectively, for the lower and upper bands.

Second, the flat-band condition shown in Fig. 2 is not realistic when there is a band bending caused by doping and free carrier distribution. In the absence of an applied electric field, the miniband misalignment caused by band bending can be overcome by modulation doping. To estimate the doping density required for the wide-well (N_{ww}) and narrow-well (N_{nw}) superlattices, we first notice that the carrier concentration N for the two-dimensional electron gas in a miniband is [2]

$$\frac{4\pi m^*}{h^2 d} kT \ln(1 + e^{-(E_0 - E_f)/kT}), \quad (11)$$

which defines a quasi-Fermi level E_f , where E_0 is the center of the miniband and d is the superlattice period. The doping in each superlattice should be equal to the corresponding free carrier concentration for the flat-band condition to be valid. We estimate that $N_{ww} = 1.5 \times 10^{17} \text{ cm}^{-3}$ and $N_{nw} = 1.2 \times 10^{16} \text{ cm}^{-3}$ for $E_f = 0$ (relative to the GaAs conduction-band edge) and $T = 300 \text{ K}$ in $(\text{Al}_{0.35}\text{Ga}_{0.65})_n(\text{Al}_{0.3}\text{Ga}_{0.7})_n$.

In the presence of an applied electric field, additional band bending may be formed by the distribution of injected carriers. In the proposed structure shown in Fig. 2, the carriers transporting in the lower band will first accumulate at the junction (J), forming a high-field domain. The applied voltage will mostly drop at the junction and cause a band bending. With this consideration, the operating voltage should be limited by the separation of the lower- and upper-band energies, in this case being 90 mV.

B. BAS Laser

The BAS laser [2] shown in Fig. 5 consists of three superlattices (S1, S2, and S3). With the central one (S2) as the active region, the right and left ones (S1 and S3) function as the energy filters allowing carriers to be injected only into the upper band and to flow out only through the lower band. The transmission coefficient of the BAS laser consisting of $(\text{Al}_{0.3}\text{Ga}_{0.7})_n(\text{Al}_{0.3}\text{Ga}_{0.7})_n(\text{Al}_{0.3}\text{Ga}_{0.7})_n$ is shown in Fig. 6. The lower two peaks, corresponding to the lower and the upper aligned minibands indicate that currents transporting in the lower and upper bands are small, where the peak transmissions are about 10^{-3} . The wave functions from left to right and from right to left are plotted for the lower and upper bands in Fig. 7. Carriers injected from the left through the aligned lower band and those injected from the right through the upper band have large probability densities, which are about three orders of magnitude larger than those injected from the wrong directions.

The injection current density is limited by the current transported in the lower band, which is essential to provide an empty lower band for population inversion. The largest current density which can be accommodated by the miniband transport can be simply estimated by the tunneling current [5], assuming that the transmission coefficients are unity inside the miniband. In the present case, the current density is limited to $3 \times 10^6 \text{ A/cm}^2$ for a

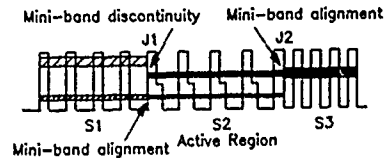


Fig. 5 Band-aligned structure for intersubband laser application. It consists of three kinds of superlattices. The central one is the active region, where its upper band is aligned to the right and its lower band is aligned to the left. Current injected from the right is trapped in the upper band because of band alignment on the right and band discontinuity on the left. Upon lasing, the carriers in the lower band flow out of the active region via the aligned bands.

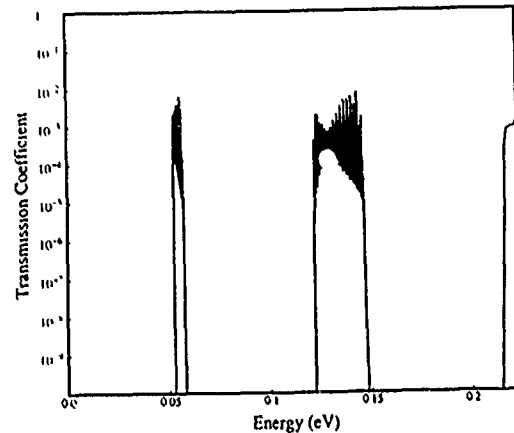


Fig. 6. Transmission coefficient of the BAS laser consisting of $(\text{Al}_{0.3}\text{Ga}_{0.7})_n(\text{Al}_{0.3}\text{Ga}_{0.7})_n(\text{Al}_{0.3}\text{Ga}_{0.7})_n$. The lowest two peaks, which are related to the minibands of the active region, are much smaller than unity.

miniband bandwidth of 3 meV, which suffices in most applications.

This novel structure provides a way of carrier injection for possible intersubband lasing. To be practical, one has to take into consideration the intersubband relaxation processes. For the nonradiative intersubband relaxation process in a quantum well, the lifetime due to longitudinal optical (LO) phonon scattering at room temperature is on the order of 10 ps for a subband splitting 150 meV [11], [12] (larger than the LO phonon energy of 36.7 meV), and that due to acoustic phonon scattering is 300 ps for a subband splitting 27 meV at 5 K [13] (less than the LO phonon energy). For lasing, it is essential to have a low nonradiative recombination rate. For the subband splitting larger than the LO phonon energy, we have performed a theoretic calculation based on the formulation of Riddoch and Ridley [14], and the results indicate that several means may be used to reduce the intersubband LO phonon scattering rate. First, lowering the temperature from 300 to 77 K can increase the lifetime by a factor of two since the phonon number is reduced at low temperature. Second, a narrower well has a longer lifetime since the narrower well has a larger splitting of the subband energies, and by the requirement of momentum conservation, a larger splitting implies that only long-wave-vector phonons (which have a smaller strength) participate in this intersubband scattering process. Our calculation shows that the scattering rate is approximately propor-

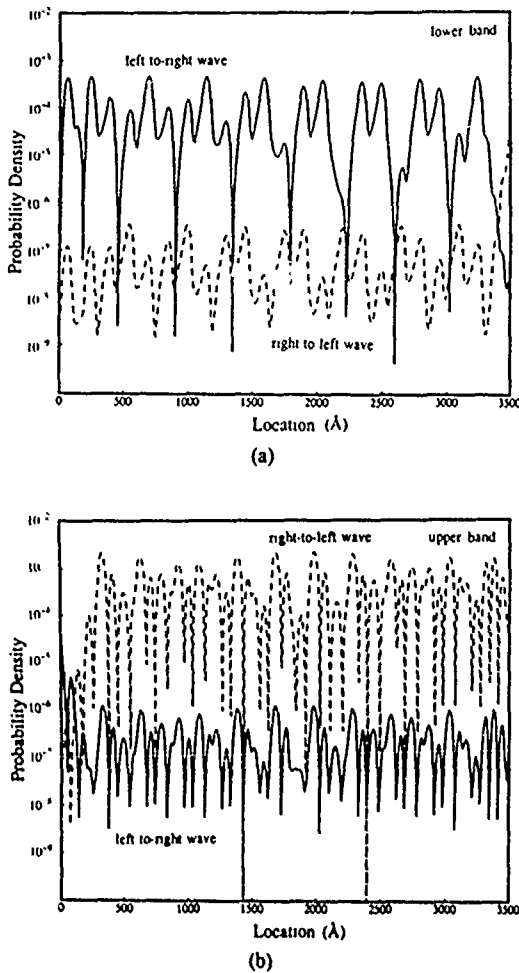


Fig. 7. Probability density (the square of the absolute value of the wave function) of the $(110.3210)^3(110.3260,160)^{20}(110.3110)^3$ BAS structure as a function of location. (a) For the lower band, where the energy is $E_L = 0.054$ eV. The transmission coefficient is 1.593×10^{-4} . (b) The upper band, where the energy is $E_U = 0.135$ eV and the transmission coefficient is 2.096×10^{-3} . The solid line indicates the left-to-right wave, and the dashed line indicates the right-to-left wave.

tional to the well width. Third, a material having a light effective mass has a long lifetime, and the scattering rate is approximately proportional to the effective mass. Fourth, a lower LO phonon energy has a smaller scattering rate, but this effect is small. To eliminate the effect of the LO phonon, subband splitting less than the LO phonon energy should be employed and operate at very low temperature. For a superlattice, there may be an additional nonradiative process for electrons to undergo intersubband Auger recombination [15]. The lifetime of Auger recombination is on the order of 100 ps and can be reduced by using a narrower miniband bandwidth, although the narrower bandwidth may limit the injected current density. For the radiative spontaneous emission process, the recombination lifetime is on the order of 6×10^{-8} ps [16] for a subband splitting 150 meV. A factor of one-third has been taken into account for the spontaneous emission rate since the intersubband transition allows only light which has an electric field component in the z -direction to be emitted. In short, the nonradiative recombination processes are usually dominant over the radiative

processes, and their effects should be evaluated for realization of intersubband lasing.

To pump carriers into the ground miniband of the narrow-well superlattice on the right, a variable space superlattice energy filter (VSSEF) [17] can be used. However, other simple structures are possible and are presented in the following section.

IV. BAS BY DOPING AND ELECTRIC FIELD

A. Resonant Injector (Emitter)

A BAS device incorporating a resonant-tunneling injector is shown in Fig. 8(a). An example of this structure is $(110.3200110.3)_i(350110.3)_{n^+}(200)_i$. From left to right, the first part of the structure is a typical undoped resonant-tunneling diode, followed by several periods of the n^+ -doped active layer, which consists of two minibands, and a thin undoped GaAs spacer at the end. Both contacts are assumed to be n^+ -GaAs, and thus the voltage drop in the contacts can be neglected.

To describe the working principle of the resonant injector BAS, we will assume that the voltage drop is sustained only by the intrinsic regions, i.e., the resonant injector and the spacer in the present structures. Detailed analysis should incorporate a self-consistent calculation with the Poisson equation, but will probably show the same principle.

When a positive bias ($eV_a < 0$) is applied on the right contact as shown in Fig. 8(b), the quasi-bound state of the injector is raised and finally aligned with the upper band of the active layer. When there is no recombination, the electron population in the upper band increases due to injection from the left contact through the aligned bands, while there is no carrier injection into the lower band from the left contact, as was discussed in Case 3 of Section II-B. However, the lower band can have a relatively large population due to the injection from the right contact since the energy of the band is low and near the Fermi level of the right contact. For laser applications, however, population inversion must be attained. To this goal, a spacer is used to depress further the Fermi level below the lower band, thus reducing the population in the lower band.

The carrier concentrations in the upper and lower bands are shown in Fig. 9 with or without the spacer. In the calculation, we have assumed coherent transport (i.e., no scattering) and no recombination¹ (i.e., the condition before lasing). The applied voltage is chosen so that the current is at its peak value when band alignment occurs.

To illustrate the relation of population inversion and the quasi-Fermi levels for lasing in BAS, we notice that the inverted electron population ΔN can be derived from (11):

$$\Delta N = N_U - N_L = \frac{4\pi m^*}{h^2 d} kT \ln \frac{1 + e^{-(E_U - E_{F_U})/kT}}{1 + e^{-(E_L - E_{F_L})/kT}} \quad (12)$$

where U and L denote the upper and lower bands, respectively. The condition for lasing is $\Delta N > 0$, which implies

¹We note that the radiative and nonradiative carrier lifetimes are important considerations for lasing, as discussed in Section III-B.

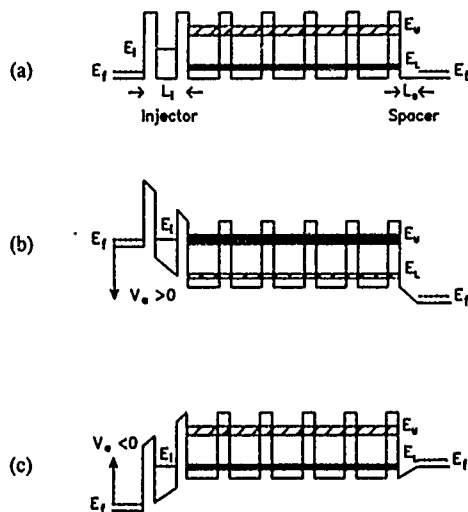


Fig. 8. BAS incorporating a resonant-tunneling injector in the emitter and a spacer in the collector. (a) For the flat-band condition. (b) For positive applied voltage, where the upper band, the quasi-bound state of the injector, and the Fermi level of the left contact are aligned together. (c) For negative applied voltage, where the lower band, the quasi-bound state of the injector, and the Fermi level of the right contact are aligned together.

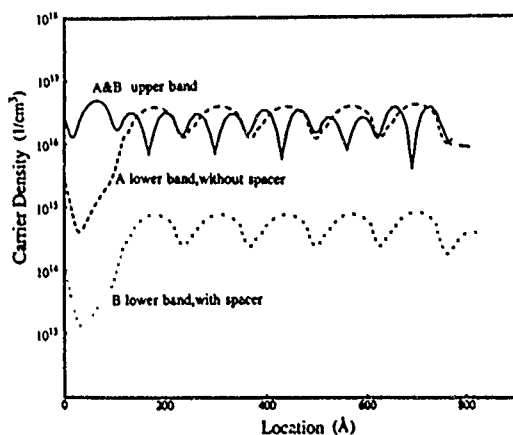


Fig. 9. Carrier densities versus location for the upper and lower bands for A, $(11_0.320_011_0.3)_i(35_011_0.3)_n$ (without spacer), and B, $(11_0.320_011_0.3)_i(35_011_0.3)_n(20_0)_i$ (with spacer). The carrier densities in the upper band for both A and B are the same as indicated by the solid line. The carrier densities in the lower band for A, indicated by the short-dashed line, are much higher than those for B, indicated by the dotted line. The applied voltage is 0.11 V for A and 0.162 V for B such that the electric fields in the injector are the same for both cases.

$E_{fU} - E_{fL} \geq E_U - E_L$, and is similar to the case of conventional junction lasers.

The current-voltage relation in the absence of recombination and scattering is shown in Fig. 10. The peak in the positive voltage corresponds to band alignment in the upper band, while the peak in the negative voltage corresponds to band alignment in the lower band. The latter situation is schematically shown in Fig. 8(c). The spacer now raises the Fermi level of the right contact to launch electrons into the lower band. While current in the positive bias is transported by the upper band, in the negative bias it is transported mainly by the lower band. Thus, the resonant injector BAS also provides a way to study miniband transport in superlattices.

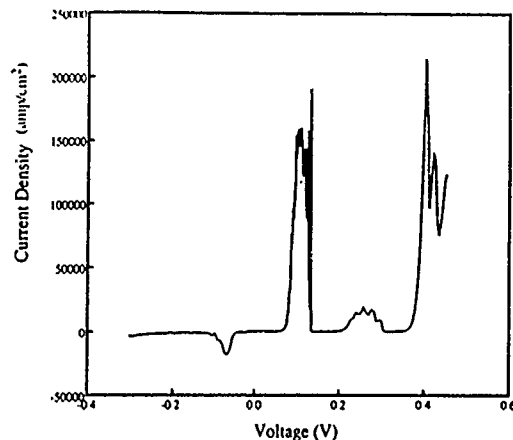


Fig. 10. Current-voltage relation for $(11_0.320_011_0.3)_i(35_011_0.3)_n$ BAS. The peak current in the positive polarity indicates where the upper band is aligned with the quasi-bound state of the injector, while that in the negative polarity occurs when the lower band is aligned with the quasi-bound state of the injector.

Finally, for device application, the first-order design principle is described below, ignoring space charge effects and assuming all energies are referred to the conduction-band edge at flat-band condition. As illustrated in Fig. 8(a), first the lower-band energy E_L and the upper-band energy E_U are selected by the transition frequency desired. The voltage drop in the injector is made to $qV_i = E_U - E_L$ in order to ensure that the Fermi level at the left contact is aligned with the upper band. The quasi-bound state energy of the injector should be $E_i = (qV_i)/2$ in order that the quasi-bound state be aligned with the upper band when the voltage drop across the injector is V_i . The well width of the injector can be determined from its known quasi-bound state. To have band alignment in the lower band as the voltage polarity changes, the thickness of the spacer L_s should be chosen as $L_s = (L_i(E_L - E_f))/(2(E_i - E_L))$ where L_i is the injector width shown in Fig. 8(a). The applied voltage to have the upper band aligned is

$$V_a^+ = V_i \left(\frac{L_s + L_i}{L_i} \right), \quad (13)$$

and for lower-band alignment, it is

$$V_a^- = (E_f + E_L - 2E_i)/q. \quad (14)$$

Obviously, the effects of space charges and contact resistance should be taken into consideration to determine the actual V_a 's.

B. Resonant Collector

Although the resonant injector BAS can achieve a high population inversion, it also has a high threshold current since the current transport in the upper band will leak to the right contact instead of falling down to the lower band. To block the upper band current flowing into the right contact and at the same time to sustain the lower-band current, one may employ another resonant-tunneling structure in the collector, referred to as the resonant collector, and its band structure is schematically shown in

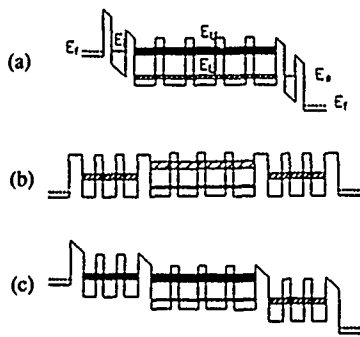


Fig. 11. (a) BAS incorporating a resonant-tunneling structure in the emitter and a resonant-tunneling structure in the collector. It is shown for a positive bias such that the upper band, the quasi-bound state of the injector, and the Fermi level of the left contact are aligned, while at the same time the lower band, the quasi-bound state of the collector, and the Fermi level of the right contact are also aligned. The threshold current is expected to be lower than that of a BAS without a collector. (b) The BAS incorporating both a superlattice injector and a superlattice collector in the flat-band condition. (c) The same structure as in (b) except being under applied bias. The desired band alignment is achieved as the voltage drop occurs mostly in the thick barriers inserted among the strongly coupled superlattices.

Fig. 11(a) when the bands are aligned. By proper design, as the upper band is aligned with the quasi-bound state of the injector, the lower band is aligned with the quasi-bound state of the collector, thus forming a channel for carrier in-and-out. The energy states in an infinite square well have the characteristics $E_n \propto n^2$ where n is the n th subband. Thus, when the lower band is aligned with the first state of the collector, the upper band should be lower than the second state of the collector so that the carriers transported in the upper band are blocked by the collector. A design example is $(11_{0.3}20_{0.3})_1(35_{0.1}11_{0.3})_n^+(16_{0.1}11_{0.3})_1$. The population distribution for the resonant collector case is shown in Fig. 12 under the same applied electric field as in the previous case without the resonant collector. The current density is 3×10^4 A/cm² in this case, compared to the previous case, which has a peak current of 1.5×10^5 A/cm², while the carrier densities are comparable.

The choice of resonant collector is not as critical as that of injector. In reality, the lower band will tend to align with the quasi-bound state of the collector since under bias the voltage drop occurs at the junction that self-adjusts the band alignment. That is, if they are not aligned, the conductivity is low and the voltage tends to drop in this highly resistive region. The voltage drop persists until the bands are aligned. The upper band tends to be aligned with the quasi-bound state of the injector too, but the current injector will not be optimized unless the Fermi level at the left contact is also aligned with the quasi-bound state of the injector.

C. Superlattice Emitter and Collector

The resonant emitter and collector can be replaced by strongly coupled superlattices [18], with thicker barriers inserted in between to sustain the voltage drop, as shown in Fig. 11(b). The minibands in the strongly coupled wells are aligned, giving high conductivity, whereas the space charge will accumulate near the thicker barriers, where

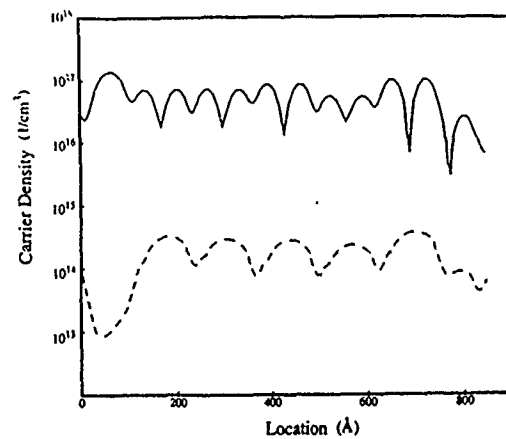


Fig. 12. Carrier densities versus location for the upper and lower bands of $(11_{0.3}20_{0.3})_1(35_{0.1}11_{0.3})_n^+(16_{0.1}11_{0.3})_1$ (with both the resonant emitter and the collector). The carrier density in the upper band is indicated by the solid line, and that in the lower band is indicated by the dashed line. The applied voltage is 0.181 V, such that the electric field of the injector are the same as in the case of Fig. 9.

the conductivity is low. Thus, the voltage drops mostly in the thicker barriers, and the miniband alignment is established as shown in Fig. 11(c). The strongly coupled superlattice was first demonstrated by Davies *et al.* [18] as an alternative approach of the resonant-tunneling structures, and we have adopted it here for the emitter and collector of the BAS. It is noticed by us that a possible intersubband laser structure was also recently proposed by Liu [19] and a similar structure in Fig. 8 was studied by England *et al.* for superlattice transport [20].

V. CONCLUSION

In conclusion, we have described a new device concept based on superjunctions between multiple superlattices. Miniband alignments and discontinuities are formed at the superjunctions. The applications of the BAS's are demonstrated in the miniband transport and the intersubband transition. For miniband transport, the BAS can inject carriers in either the upper or the lower band. The resonant injector or superlattice injector acts as a dynamic energy filter that ensures efficient currents of monoenergetic carriers. It is recognized that the analysis presented here ignores the inelastic and elastic scatterings in the subband. For intersubband transitions, new types of infrared laser and photodetectors of low dark current are proposed based on the fact that the BAS can effectively control the carrier flow in the minibands. Although examples are given for AlGaAs/GaAs superlattices, the concept is readily applicable to all other indirect as well as direct gap semiconductor systems. The BAS concept should stimulate device applications of superlattices.

ACKNOWLEDGMENT

The authors wish to thank Y. J. Mii for helpful discussions. One of them (K. L. Wang) also acknowledges the support of a Guggenheim Fellowship.

REFERENCES

- [1] L. Esaki, "A bird's-eye view on the evolution of semiconductor superlattices and quantum wells," *IEEE J. Quantum Electron.*, vol. QE-22, p. 1611, 1986.

- [2] P. Yuh and K. L. Wang, "Novel infrared band-aligned superlattice laser," *Appl. Phys. Lett.*, vol. 51, pp. 1404, 1987.
- [3] —, "Formalism of the Kronig-Penney model for superlattices of variable basis," *Phys. Rev. B*, Dec. 1988.
- [4] R. Tsu and L. Esaki, "Tunneling in a finite superlattice," *Appl. Phys. Lett.*, vol. 22, p. 562, 1973.
- [5] M. O. Vassell, J. Lee, and H. F. Lockwood, "Multibarrier tunneling in $\text{Ga}_{1-x}\text{Al}_x\text{As}$ heterostructures," *J. Appl. Phys.*, vol. 54, p. 5206, 1983.
- [6] B. Jogai, K. L. Wang, and K. W. Brown, "Free-electron density and transit time in a finite superlattice," *J. Appl. Phys.*, vol. 59, p. 2968, 1986.
- [7] H. Ohnishi, T. Inata, S. Muto, N. Yokoyama, and A. Shibatomi, "Self-consistent analysis of resonant tunneling current," *Appl. Phys. Lett.*, vol. 49, p. 1248, 1986.
- [8] M. Cahay, M. McLennan, S. Datta, and M. S. Lundstrom, "Importance of space-charge effects in resonant tunneling devices," *Appl. Phys. Lett.*, vol. 50, p. 612, 1987.
- [9] C. S. Lent, "The resonant hot electron transfer amplifier. A continuum resonance device," *Superlattices Microstructures*, vol. 3, p. 387, 1987.
- [10] L. D. Landau and E. M. Lifshitz, *Quantum Mechanics*, Vol. III. New York: Pergamon, 1958.
- [11] A. Seilmeier, H. J. Hubner, G. Abstreiter, G. Weimann, and W. Schlapp, "Intersubband relaxation in $\text{GaAs-Al}_x\text{Ga}_{1-x}\text{As}$ quantum well structures observed directly by an infrared bleaching technique," *Phys. Rev. Lett.*, vol. 59, p. 1345, 1987.
- [12] F. H. Julien, J. M. Lourtioz, N. Herschkorn, D. Delacourt, J. P. Pocholle, M. Papuchon, R. Planel, and G. Le Roux, "Optical saturation of intersubband absorption in $\text{GaAs-Al}_x\text{Ga}_{1-x}\text{As}$ quantum wells," *Appl. Phys. Lett.*, vol. 53, p. 116, 1988.
- [13] D. Y. Oberli, D. R. Wake, M. V. Klein, J. Klem, T. Henderson, and H. Morkoc, "Time-resolved Raman scattering in GaAs quantum wells," *Phys. Rev. Lett.*, vol. 59, p. 696, 1987.
- [14] F. A. Riddoch and B. K. Ridley, "On the scattering of electrons by polar optical phonons in quasi-2D quantum wells," *J. Phys. C*, vol. 16, p. 6971, 1983.
- [15] P. Yuh and K. L. Wang, "Intersubband Auger recombination in a superlattice," *Phys. Rev. B*, vol. 37, no. 15, p. 1328, 1988.
- [16] A. Yariv, *Quantum Electronics*, 2nd ed. New York: Wiley, 1975, ch. 8.
- [17] C. J. Summers and K. F. Brennan, "Variably spaced superlattice energy filter, a new device design concept for high energy electron injection," *Appl. Phys. Lett.*, vol. 48, p. 806, 1986.
- [18] R. A. Davies, M. J. Kelly, and T. M. Kerr, "Tunneling between two strongly coupled superlattices," *Phys. Rev. Lett.*, vol. 55, p. 1114, 1985.
- [19] H. C. Liu, "A novel superlattice infrared source," *J. Appl. Phys.*, vol. 63, p. 2856, 1988.
- [20] P. Englund, J. R. Hayes, J. P. Harbison, D. M. Hwang, and L. T. Florez, "Tunneling measurement of the density of states of a superlattice," *Appl. Phys. Lett.*, vol. 53, p. 391, 1988.



Kang L. Wang (S'68-M'70-SM'78) received the M.S. and Ph.D. degrees in electrical engineering from the Massachusetts Institute of Technology, Cambridge, in 1967 and 1970, respectively.

He was with M.I.T. from 1970 to 1972 as an Assistant Professor, while he worked in the research areas of applying electron and ion beams to semiconductor device testing and other surface phenomena. He joined the General Electric Corporate Research and Development Center in late 1972. Since then he has engaged in the development of charge-injection device imagers and in research in the area of device physics. He has worked in ion implantation, MOS technology, and defects in silicon and GaAs using deep-level transient spectroscopy. More recently, he was involved in the development of monolithic InSb charge-injection device infrared imagers. In addition, he has been in charge of all ion-implantation and beam-annealing projects. During his tenure with General Electric, he was also an adjunct professor with the Department of Physics, State University of New York at Albany. In 1979, he joined the faculty of the Department of Electrical Engineering, University of California, Los Angeles. At present, he is a Professor of Engineering and Applied Science and is continuing his studies of device physics and concepts. He is currently involved with molecular beam epitaxy growth of artificially structured materials and is investigating electrical transport and optical properties of these structures. In the device physics area, he is studying superlattices, multiple quantum wells, and tunneling devices for very high-frequency and high-speed electronics and optoelectronics applications. He has published more than 120 papers in various areas related to MBE, electrical and optical properties of superlattices, device physics, and processing technology.

Dr. Wang is a member of Sigma Xi, the American Institute of Physics, and the Electrochemical Society, and a Guggenheim Fellow.



Perng-Fei Yuh was born in Taiwan, Republic of China, in 1961. He received the B.S. degree in electrical engineering from National Taiwan University in 1983. After two years of military service in the Army, he continued his studies at the University of California, Los Angeles, where he received the M.S. degree in electrical engineering in 1986.

His current research interests include the study of transport and optoelectronic properties of semiconductor quantum wells and superlattices, and the development of novel device concepts based on those properties.

Large Stark Effects for Transitions from Local States to Global States in Quantum Well Structures

P. F. YUH AND K. L. WANG

Abstract—We discuss the electric-field dependence of the optical absorption for a particular type of quantum well structures, in which one or more small wells are embedded in a big well. In such structures, local energy states confined by the small well(s) and global states confined by the big well have different electric field dependence while their wave functions remain overlapped. Thus, a large Stark effect (large energy shift and oscillator strength) can be achieved for the optical transition from a local state to a global state. This concept of using the local and global states can be applied to both interband and intersubband transitions. For intersubband transitions, a typical 10–20 meV shift is predicted, compared to a reported 1.1 meV blue shift at the field 30 kV/cm. For interband transitions, the Stark shift is also larger than that in the single quantum wells.

I. INTRODUCTION

QUANTUM well structures have found important applications in optoelectronics. When an external electric field is applied, the shape of the quantum well potential deforms and the transition energies of the sublevels change accordingly. The quantum confined Stark effect [1] is referred to the shift of the transition energy in a quantum well as a function of the electric field. This Stark effect has been observed for both interband (from valence to conduction band) and intersubband (or intraband) transitions.

Several quantum well structures have been examined previously. Among them are the isolated wells, coupled wells, and superlattices. For a simple isolated well or weakly coupled multiple-well structure, the intersubband Stark shift of 1.6 meV blue shift (or higher energy shift) is reported for a 120 Å GaAs quantum well at an applied field of 36 kV/cm [2]. The interband Stark shift [3] is in reality the shift of the exciton transition energy under the field. The exciton shift is the sum of two components: a blue shift of the binding energy, which saturates at high electric field, and a red shift (or lower energy shift) of the level-to-level energy, which continues to increase at high field [4]. Typical interband Stark shift is only 10 meV red shift at a high operating field of 100 kV/cm. Consequently, large intersubband and interband Stark shifts usually require operating at very high electric field, which can result in undesirable high leakage current, early

breakdown, and long charging time. Other isolated well systems have been studied. The compositionally graded well shows an enhanced Stark shift [5], while the parabolic well shows no shifts at all [6]. It is also possible to have a transition from the bound state to the above-barrier unconfined state [7]–[9], but the electric field-induced effect has not been explored in this case.

Coupled quantum well structures, usually consisting of two wells separated by a thin (≤ 30 Å) barrier, prove to have a Stark shift larger than the single quantum well for both interband [10]–[12] and intersubband [13] transitions. However, the transitions which have large energy shifts usually have small oscillator strengths because wave functions of the states involved in the transitions are localized in different wells. This type of transitions is referred to as “interwell transitions” [12] or “oblique transitions” in real space [14].

For superlattices, which consist of a large number of coupled wells, recent theoretical and experimental results have shown that the interband absorption edge effectively blue shifts when an electric field is applied [14], [17]. This mechanism is different from that of an isolated well in that the superlattice minibands become ladder-like discrete energy levels under a strong electric field, that is, the miniband bandwidth shrinks, and the effective bandgap of the superlattices increases.

In this paper, we shall discuss another type of quantum well structures, which are constructed by embedding small well(s) in a big well. Large Stark energy shifts as well as large oscillator strengths can both be achieved for transitions from the local states in the small wells to the global state in the big well. This new type of transitions is referred as the local state-to-global state (LOG) transition. Several possible structures are described in Section II, and detailed calculations of eigenstates, wave functions, and oscillator strengths as a function of the applied field are presented in Section III.

II. WAVE-FUNCTION ENGINEERING OF A WELL-INSIDE-WELL STRUCTURE

In this section, first we will define the notations and review the simple isolated well results. Then the concept of using local states and global states to achieve a high Stark shift and oscillator strength is described and illustrated. Finally, the LOG transition is compared to other types of transitions such as the bound-to-unconfined transition in other quantum well systems.

Manuscript received August 23, 1988; revised February 10, 1989. This work was supported in part by the U.S. Office of Naval Research and the U.S. Army Research Office.

The authors are with the Device Research Laboratory, Department of Electrical Engineering, University of California, Los Angeles, CA 90024.
IEEE Log Number 8927996

A. Notations and Review

The $\text{Al}_x\text{Ga}_{1-x}\text{As}/\text{GaAs}$ heterosystem with a 0.6:0.4 conduction-to-valence band offset ratio is used. Only the transitions involving the conduction and the heavy hole valence bands near the Γ point are considered. Each of the quantum well layers is denoted by the short-hand symbol (M_x) where M is the number of monolayers (one monolayer = 2.83 Å) and x is the Al mole fraction in $\text{Al}_x\text{Ga}_{1-x}\text{As}$. For example, the structure (50_1) ($25_0 15_{0.2} 25_0$) (50_1) consists of two 25-monolayer (70 Å) GaAs wells with a 15-monolayer (42 Å) $\text{Al}_{0.2}\text{Ga}_{0.8}\text{As}$ barrier inserted in between. The whole structure is clad inside two thick AlAs barriers of 50 monolayers (142 Å). Later, the symbol (50_1) will be dropped for convenience. Two different compositions of Al are usually required and are usually accomplished using two Al (or Ga) crucibles in molecular beam epitaxy (MBE) systems. For illustration, all the structures for intersubband transitions are designed for a central transition energy 0.124 eV or 10 μm in wavelength. The eigenenergies and wave functions are calculated by a transfer matrix method within the framework of envelope function approximations. This method has been used in a previous paper [13], and the formula of oscillator strength and absorption coefficient for intersubband transitions is defined therein. Throughout this paper, the sublevel energies are calculated in reference to the center of the well. As an example, the energies of the first two conduction sublevels (1_c , 2_c) and the ground heavy hole sublevel (1_h) are shown in Fig. 1 as a function of the applied electric field for a simple quantum well structure (33_0). At low electric field (≤ 30 kV/cm), all the energies of the states are basically constant (with respect to the well centroid) since the electrons or holes see an equal average depth of the square or trapezoid potential. At high electric field (≥ 30 kV/cm), the lowest states (1_c and 1_h) see a triangular potential, and their wave functions shift to the deep side of the triangular well, lowering the energies with respect to the well center. The lower the energy level is, the easier it can be affected by the electric field. A simple guideline for a single well under an applied bias can be concluded as follows. *The bound state energy is a constant with respect to the well centroid as long as the potential drop across the well is smaller than the bound state energy.*

B. Examples of LOG Transitions

A step well structure ($37_{0.2} 26_0$) as shown in Fig. 2(a) can be considered as one small well (26_0) inside a big well ($(37 + 26)_0$). The ground conduction sublevel (1_c) at 47.4 meV is inside the small well and its wave function is localized therein, while the second state (2_c) at 163.0 meV is above the barrier (barrier height of 149.6 meV) and its wave function is oscillatory over the entire big well; hence, we have the name "global state." With an applied field of 30 kV/cm, the 1_c state tracks the center of the small well, while the 2_c state tracks the center of the big well as in a single well case. Our calculation shows

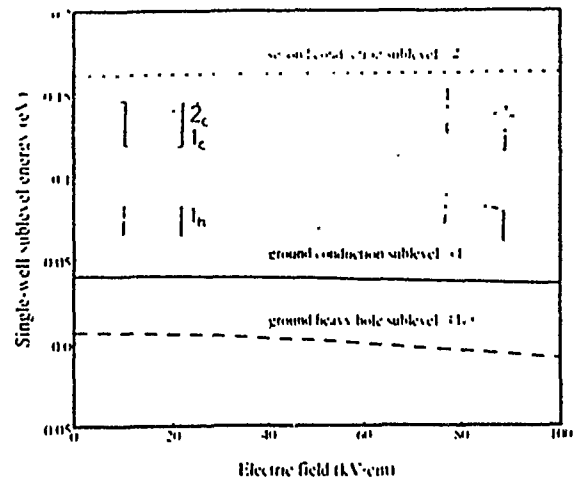


Fig. 1. Sublevel energies of a single quantum well structure (33_0) as a function of the electric field for the first two conduction sublevels 1_c and 2_c , and the ground heavy hole sublevel 1_h . Shown in the insets are the band diagram at the flat band (left) and under bias (right), respectively. The energies of the conduction and heavy hole sublevels are referenced to the centroids of the wells in the conduction and valence band edges, respectively. All the levels are constant at low field and drop at high field. The lower the sublevels are, the more sensitive they are to the applied field.

Conduction band edge of the well-inside-well structures

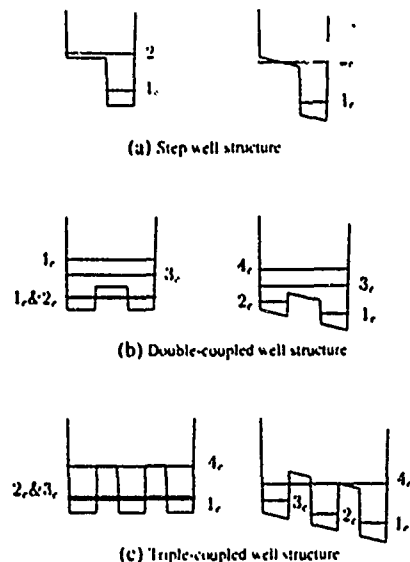


Fig. 2. Quantum well structures for LOG transitions. The conduction band edges and sublevels of three well-inside-well structures are shown in flatband condition (left) and under 30 kV/cm field (right). The three structures are (a) step well ($37_{0.2} 26_0$), (b) double coupled well ($26_0 30_0 26_0$), and (c) triple coupled well ($25_0 20_0 25_0 20_0 25_0$). In the flatband condition, the 1_c and 2_c states in the double well case and the 2_c and 3_c states in the triple well case are too close to be distinguished in our plot.

that the centers of these two wells have a potential drop 15.7 meV while the calculated Stark shift is 10.1 meV, and the oscillator strength remains large from 0.65 to 0.81 (typical of 1 for a simple well). Unlike the interwell transition in a coupled well structure where only the tails of the wave functions are overlapped, the global wave function for the LOG transition covers the entire local wave function, thus maintaining a high oscillator strength.

TABLE I
SUMMARY OF LOG TRANSITIONS FOR SEVERAL STRUCTURES. THE TRANSITION ENERGY (E) AND OSCILLATOR STRENGTH (OS) OR OVERLAP INTEGRAL (OI) ARE CALCULATED FOR FLATBAND CONDITION ($F = 0$) AND UNDER AN APPLIED FIELD 30 kV/cm ($F = 30$ kV/cm), RESPECTIVELY

| Structures | Transition Type | Initial State | $F = 0$ | $F = 30$ kV/cm | Stark Shift |
|--------------------------------|---------------------------------------|---------------|---|---|------------------------|
| $37_0, 26_0$ | $1_c \rightarrow 2_c$ intersubband | 47.4 meV | $E = 0.1156$ eV $OS = 0.65$ transparent | $E = 0.1257$ eV $OS = 0.81$ opaque | 10.1 meV blue shift |
| $26_0, 30_0, 26_0$ | $1_c \rightarrow 4_c$ intersubband | 37.7 meV | $E = 0.1242$ eV $OS = 0.54$ opaque | $E = 0.1426$ eV $OS = 0.24$ transparent | 18.4 meV blue shift |
| $23_0, 20_0, 23_0$ | $2_c \rightarrow 3_c$ intersubband | 58.4 meV | $E = 0.1234$ eV $OS = 1.14$ opaque | $E = 0.1068$ eV $OS = 0.50$ transparent | 16.6 meV red shift |
| $27_0, 17_0, 27_0$ | $1_c \rightarrow 3_c$ intersubband | 42.4 meV | $E = 0.1141$ eV $OS = 0$ transparent | $E = 0.1237$ eV $OS = 0.75$ opaque | 9.6 meV blue shift |
| $23_0, 21_0, 23_0$ | $1_c \rightarrow 3_c$ intersubband | 48.4 meV | $E = 0.1119$ eV $OS = 0$ transparent | $E = 0.1229$ eV $OS = 0.48$ opaque | 11.0 meV blue shift |
| $29_0, 22_0, 29_0$ | $1_c \rightarrow 4_c$ intersubband | 36.7 meV | $E = 0.1248$ eV $OS = 0.66$ opaque | $E = 0.1477$ eV $OS = 0.12$ transparent | 22.9 meV blue shift |
| $25_0, 20_0, 25_0, 20_0, 25_0$ | $1_c \rightarrow 4_c$ intersubband | 41.4 meV | $E = 0.1045$ eV $OS = 0.54$ transparent | $E = 0.1250$ eV $OS = 0.47$ opaque | 20.5 meV blue shift |
| $11_0, 35_0, 11_0$ | $1_b \rightarrow 1_c$ interband | | $E = 1.608$ eV $OI = 0.78$ transparent | $E = 1.585$ eV $OI = 0.22$ opaque | 16 meV red shift |

More than one small well can be embedded in a big well. Examples are given for double coupled well and triple coupled well structures as shown in Fig. 2(b) and (c). For the case of double (triple) coupled wells, the 1_c and 2_c (1_c , 2_c , and 3_c) states are localized to the small wells, while the 3_c and 4_c (4_c , 5_c , etc.) states are above the barriers and are global states belonging to the big well. When the electric field is applied, the 1_c and 2_c states track the centroids of the right and left wells, respectively, while the 3_c and 4_c states track the centroid of the big well. Thus, both blue and red shifts are possible for the optical transitions from the 1_c and 2_c states to the 3_c and 4_c states, respectively, as shown in Fig. 2(b). The energies of the shifts are approximately equal to the relative potential difference of the centroids of the respective small wells and big well. The results are summarized in Table I. Typical Stark shift is about one order of magnitude larger than that in the single quantum well case, while the oscillator strength is still about half of the single well value. Physically, the local wave function, which is confined in one small well, is overlapped by about half of the global wave function, which runs through its entire structure.

More subwells can be used to provide a larger Stark shift, but at the expense of having a smaller oscillator strength. The largest energy shift results when the wave function of the small well is localized in either the leftmost or the rightmost well. In cases, the potential drop is the largest relative to the centroid of the big well. There are two reasons for which an oscillator strength becomes smaller as the number of the subwells increases. First, suppose that there are N coupled quantum wells, each of

the local states can share only a $1/N$ of the global states. Thus, the oscillator strength is expected to drop to $1/N$ the value of the single well structure. Second, as the number of wells increases, the boundaries of the big well (the A1As well) become far apart, i.e., the big well width becomes wider. This causes a lowering of the global state energies and the global states can be easily affected by the applied field. From another point of view, the global states are affected partly by the boundaries of the big wells, and partly by the small wells. As the boundaries of the big well become far apart, the small wells play a more important role. When electric field is applied, the global states above the central barrier move down and become localized to the small wells. When this occurs, the feature of LOG transitions is lost.

The concept of using local states and global states for a large Stark effect is also applicable for the interband transitions. For such applications, the barrier height and well width of the step and coupled quantum well structure should be chosen so that the ground heavy hole state is localized while the ground conduction state is a global one. This condition is usually satisfied since the heavy hole has a much heavier effective mass than the electron and is easily confined.

C. Relation to Other Types of Transitions

In the following, we will compare the LOG transitions to the transitions in single well and simple conventional coupled well structures. First, we will show that the transition in a single quantum well under a strong electric field, which has a large Stark shift, is a LOG type of tran

sition. As the electric field increases, the bottom of a square well becomes tilted. Referring to the right inset of Fig. 1, the 1_h state first senses this triangular potential because the 1_h state has a lower energy resulting from a heavier effective mass. As the wave function of the 1_h state becomes localized to the deep (left) side of the triangular well, the 1_h state energy will track the deep side instead of the center of the well. As long as the 1_c state remains global, the $1_h \rightarrow 1_c$ interband transition has a typical feature of a LOG transition. When the electric field is increased further, the 1_c state also becomes a local state. The $1_c \rightarrow 2_c$ intersubband transition is then a LOG type of transition and has a large Stark shift. The $1_h \rightarrow 1_c$ transition under such a large field is no longer a LOG transition, but rather an interwell transition characterized by a drop of the oscillator strength since the deep sides of the triangular potential for the conduction and valence bands are located on the opposite sites of the well. The step well structure discussed in Section II-B is a modification of this triangular potential. Since the step well has a local and global state even in the flatband condition, the step well can have a large Stark shift at low bias. Another modification of this tilted potential for a single well under bias is the graded gap quantum well proposed in [5], which follows the same principle of the LOG transition.

Second, we will see the relation of a LOG transition to the conventional coupled well transition. Although most of the structures for LOG transitions employ a coupled well structure, the LOG transition is different from the conventional coupled well transitions in two aspects. First, as far as the nature of transition is concerned, the LOG transition occurs between the local state and the above-barrier global state, whereas the conventional transitions occur between two local states. Second, concerning the structure, the coupled quantum well structures for LOG transitions usually have a thick and low barrier, whereas those for conventional coupled-well transitions usually employ a thin barrier [13]. The LOG transition requires a clear distinction of the local and global states, whereas conventional transitions require all the states to be strongly coupled.

The LOG transition is also different from the bound-to-unconfined state transition although both involve the below- and above-barrier states. For the latter, the unconfined states in a superlattice are generated by the below-barrier potential, whereas the global states in a LOG transition are generated and confined by the big well. The global states of LOG transitions are usually high in energy and thus insensitive to the applied electric field, whereas the unconfined states are easily localized.

However, all conventional transitions referred to above can be in some sense treated as a LOG transition under strong electric field as the initial state becomes more localized than the final state. This correspondence is applicable to both interband and intersubband optical transitions.

In summary, the features of the LOG transition are as follows.

1) The quantum well structures consist of small well(s) embedded in a big well.

2) The local states are those states confined by the small wells. Under applied field, their wave functions become localized in the small wells and their energies track the centroids of those small wells.

The global states are the states confined by the big well and their wave functions distribute throughout the whole big well, even under applied field. The global states track the centroid of the big well.

3) The number of the small wells is limited to only a few (one-four) so that the local state can share a significant portion of the global state and thus maintain a large oscillator strength. There must be a distance between the centroids of the big and small wells in order to have a relative potential drop between these centroids and thus to achieve a large energy shift by applying an electric field.

III. THEORETICAL RESULTS

We will restrict our discussion to the case of two wells embedded in one well, the structure $(26_0 30_{0.1} 26_0)$ in Fig. 2(b). The analysis of other structures is similar and the results are summarized in Table I. Our discussion is presented in four parts: wave functions, sublevel energies, oscillator strengths, and a brief discussion of the design.

A. Wave Function

The wave functions of the lowest four states are calculated for two bias conditions as shown in Fig. 3. Fig. 3(a) shows the wave functions without applied field. In Fig. 3(b), the 1_c and 2_c wave functions become localized to the right and left wells, respectively, under a 30 kV/cm electric field, while the 3_c and 4_c wave functions are less affected by the electric field. The sublevel energies of the local states 1_c and 2_c seem to track the centroids of the right and left wells, respectively, whereas the global states 3_c and 4_c track the centroid of the big well (or equivalently, the centroid of the central barrier).

B. Sublevel Energy

Fig. 4 shows the sublevel energies as a function of the electric field. The 1_c and 2_c states are coupled states and have the following characteristics. At low field, their energies have a quadratic dependence on the electric field, which can be explained by perturbation theory [18], [19]. As the field increases to a point such that the potential drop across the well is on the order of the coupled-state splitting energy ($1_c \rightarrow 2_c$ transition energy), the field dependence of the sublevel energy becomes linear and their wave functions begin to be localized [19] to the right and left small wells, respectively. In the present case, the critical field for localizing the 1_c and 2_c states is about 3 kV/cm.

On the other hand, the 3_c and 4_c states result from single well confinement, characterized by their energies being independent of the electric field. If, however, one were to consider the 3_c and 4_c states as coupled states, their splitting energy ($3_c \rightarrow 4_c$) is about 50 meV and the critical field for localization would be 22 kV/cm. Since they remain constant even at the field 100 kV/cm, they are more like single well states than coupled well states.

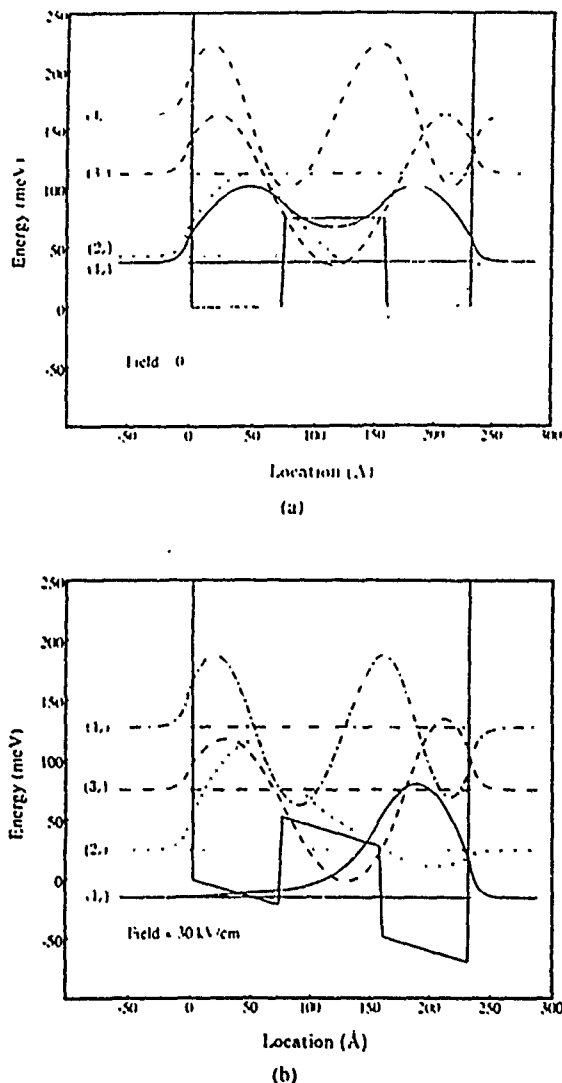


Fig. 3. Wave functions of the lowest four conduction sublevels for the double well structure (26,30,126) (a) in flatband condition, and (b) under 30 kV/cm. When the field is applied, the ground and second states become localized, while the third and fourth states do not. It is also noted that the ground and second states track the centroids of the right and left small wells, respectively, whereas the third and fourth states track the centroid of the big well (or the central barrier).

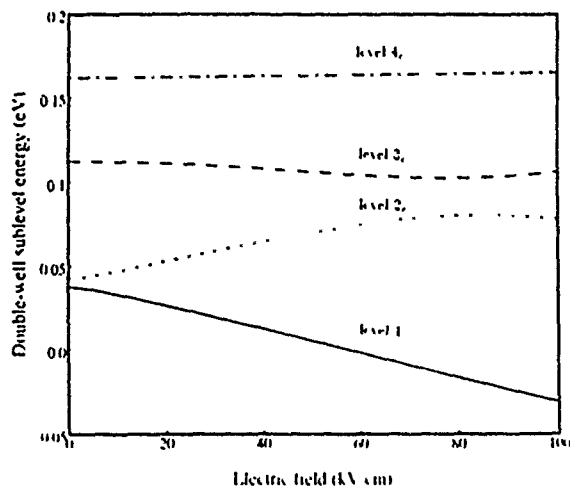


Fig. 4. Sublevel energies as a function of applied field for the lowest four conduction sublevels of the same double well structure in Fig. 3. The lowest two sublevels are sensitive to the applied field, whereas the third and fourth levels are not. Optical transitions from the lower to the upper two states are thus electric-field tunable.

It is noted that for conventional coupled well structures, the 3_c and 4_c states are usually below the barrier and are coupled well states, having a typical splitting energy five times larger than the $1_c \rightarrow 2_c$ splitting energy. When the applied field lies between the critical fields of localizing the lower states (1_c and 2_c) and upper states (3_c and 4_c), the lower states are localized and the upper ones remain global, and the transitions from lower states to upper states can be treated as in a LOG type of transition. However, when the applied field goes beyond the critical field of localizing the upper states, all the states involving the transitions become localized and the strength of transition drops because there is less overlap between the states localized in different wells.

C. Oscillator Strength

The oscillator strength, which indicates whether the transition is allowed or forbidden, is an important parameter for choosing which transition to use. For N identical coupled wells (i.e., finite superlattice) in a structure, the subbands, each of which consists of a group of N sublevels, are formed. The allowed transitions from any sublevel in the ground subband to a sublevel in the second subband are $i \rightarrow 2N - i + 1$ where $1 \leq i \leq N$ is the index for the sublevels. However, this selection rule is relaxed when an electric field or well asymmetry is introduced. The oscillator strength will decrease for the initially allowed transitions, but increase for the initially forbidden transitions, and the sum of all the oscillator strengths remains unchanged (the Sum rule). This situation is illustrated in Fig. 5 for the oscillator strengths of the $1_c \rightarrow 2_c$, $3_c \rightarrow 4_c$ transitions. The $1_c \rightarrow 4_c$ and $2_c \rightarrow 3_c$ are allowed transitions at zero electric field and their strengths drop as the field increases. The $1_c \rightarrow 3_c$ and $2_c \rightarrow 4_c$ are initially forbidden and their strengths increase as the field increases up to about 40 kV/cm.

D. Design Consideration

We briefly discuss the design of an LOG transition by a double coupled well structure. First of all, in choosing the transitions, the ground state 1_c is preferred as the initial state for intersubband absorptions since the ground state is heavily occupied. In choosing the final state, it is noted that the 4_c energy is higher than the 3_c , and thus is less affected by the applied field. But since the 4_c state is only weakly interactive with the 1_c state, the $1_c \rightarrow 4_c$ oscillator strength is small.

Second, the effect of the well width is considered. A wider well has a lower ground state and thus has large carrier accumulation in the ground state for intersubband transitions. But the well cannot be too wide to have the upper levels dropping below the barrier and becoming localized. On the other hand, a narrower well is preferred for interband transitions to ensure that the ground conduction sublevel is above the small barrier. But the well cannot be so narrow that the ground heavy hole sublevel also becomes delocalized.

Third, the effects of the barrier width and height are considered. A wider barrier is desired to have a high degree of localization of the small well state, but it should

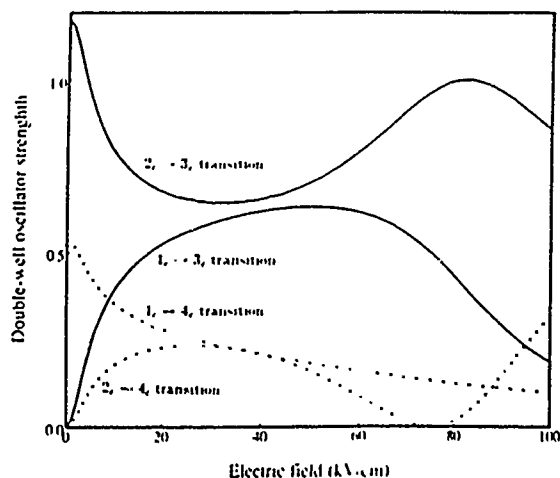


Fig. 5. Electric field dependence of the oscillator strength for the same structure in Fig. 3. At zero field, only $1 \rightarrow 4$ and $2 \rightarrow 3$ transitions are allowed. This selection rule is relaxed when the field is applied.

not be so wide that the big well states are lowered to become localized. A lower (but not too low) barrier is needed to have a clear distinction of the below-barrier local state and the above-barrier global state for a given transition energy.

Finally, the well asymmetry has the effect similar to that of applying a small electric field, i.e., the initial state (the local state) is localized even in the absence of an applied field [20]. This asymmetry will affect the oscillator strength in the zero-field condition, but it has little effect when the electric field is applied. The effect of the well asymmetry for some transitions may not be important as explained below. For example, the $1_c \rightarrow 4_c$ oscillator drops, while the $2_c \rightarrow 4_c$ strength increases when a small well asymmetry is introduced (see Fig. 5). Because the sum of these two strengths nearly conserves and their transition energies are close to each other, the overall strength in the neighborhood of the transition energy should remain unchanged.

IV. CONCLUSION

In conclusion, we have reexamined the optical transitions in semiconductor quantum well structures under an applied electric field. The LOG type of transition, i.e., transitions from local states to global states, is introduced and shown to have both a large Stark shift and oscillator strength. Many structures have been found to have a LOG type of transition, among them are the step quantum well and the coupled well structures with two or more small wells embedded in a big well. The basic feature of these structures is to embed small well(s) in one big well, and there must be a relative distance among the centroids of the small wells and the big well. Calculated results of the Stark effect for some of the structures are summarized in Table I. Although an $\text{Al}_x\text{Ga}_{1-x}\text{As}/\text{GaAs}$ system is used to illustrate this concept, the LOG transition is applicable to any general quantum well structure.

While the oscillator strength decreases by about 50 per cent, the Stark shift in LOG transitions is orders of magnitude larger than the conventional transitions in quantum wells. Thus, the LOG transition can find applications in low-current and high-speed optoelectronic devices.

ACKNOWLEDGMENT

The authors thank Dr. R. Karunasiri for helpful discussions.

REFERENCES

- [1] D. A. B. Miller, D. S. Chemla, T. C. Damen, A. C. Gossard, W. Wiegmann, T. H. Wood, and C. A. Burrus, "Band-edge electroabsorption in quantum well structures: The quantum-confined Stark effect," *Phys. Rev. Lett.*, vol. 53, pp. 2173-2176, 1984.
- [2] A. Harwit and J. S. Harris, Jr., "Observation of Stark shift in quantum well intersubband transitions," *Appl. Phys. Lett.*, vol. 50, pp. 685-687, 1987.
- [3] D. A. B. Miller, J. S. Weiner, and D. S. Chemla, "Electric-field dependence of linear optical properties in quantum well structures: Waveguide electroabsorption and sum rules," *IEEE J. Quantum Electron.*, vol. QE-22, pp. 1816-1830, 1986.
- [4] D. A. B. Miller, D. S. Chemla, T. C. Gossard, W. Wiegmann, T. H. Wood, and C. A. Burrus, "Electric field dependence of optical absorption near the band gap of quantum-well structures," *Phys. Rev. B*, vol. 32, pp. 1043-1060, 1985.
- [5] K. Nishi and T. Hiroshima, "Enhancement of quantum confined Stark effect in a graded gap quantum well," *Appl. Phys. Lett.*, vol. 51, pp. 320-322, 1987.
- [6] R. P. G. Karunasiri and K. L. Wang, "Infrared absorption in parabolic multiquantum well structures," *Superlattices Microstruct.*, vol. 4, pp. 661-663, 1988.
- [7] A. Ya. Shik, "Optical properties of semiconductor superlattices with complex band structures," *Fiz. Tekh. Poluprov.*, vol. 6, pp. 1268-1277, 1972 (*Sov. Phys.—Semicond.*, vol. 6, pp. 1110-1117, 1973).
- [8] B. F. Levine, C. G. Bethea, K. K. Choi, J. Walker, and R. J. Malik, "Bound-to-extended state absorption GaAs superlattice transport infrared detectors," *J. Appl. Phys.*, vol. 64, pp. 1591-1593, 1988.
- [9] Y. S. Yoon, "Optical studies of unconfined energy states and characterizations of $\text{GaAs}/\text{Al}_x\text{Ga}_{1-x}\text{As}$ superlattices," Ph.D. dissertation, Univ. Southern California, Los Angeles, 1988.
- [10] H. Kawai, J. Kaneko, and N. Watanabe, "Doublet state of resonantly coupled $\text{AlGaAs}/\text{GaAs}$ quantum well grown by metalorganic chemical vapor deposition," *J. Appl. Phys.*, vol. 58, pp. 1263-1269, 1985.
- [11] H. Q. Le, J. J. Zayhowski, and W. D. Goodhue, "Stark effect in $\text{Al}_x\text{Ga}_{1-x}\text{As}/\text{GaAs}$ coupled quantum wells," *Appl. Phys. Lett.*, vol. 50, pp. 1518-1520, 1987.
- [12] Y. J. Chen, E. S. Koteles, B. S. Elman, and C. A. Armiento, "Effect of electric fields on excitons in a coupled double-quantum-well structure," *Phys. Rev. B*, vol. 36, pp. 4562-4565, 1987.
- [13] P. Yuh and K. L. Wang, "Intersubband optical absorption in coupled quantum wells under an applied electric field," *Phys. Rev. B*, vol. 38, pp. 8377-8382, 1988.
- [14] P. Voisin, J. Bleuse, C. Bouche, S. Gaillard, C. Alibert, and A. Regreny, "Observation of the Wannier-Stark quantization in a semiconductor superlattice," *Phys. Rev. Lett.*, vol. 61, pp. 1639-1642, 1988.
- [15] J. Bleuse, G. Bastard, and P. Voisin, "Electric-field-induced localization and oscillatory electro-optical properties of semiconductor superlattices," *Phys. Rev. Lett.*, vol. 60, pp. 220-223, 1988.
- [16] E. E. Mendez, F. Agulló-Rueda, and J. M. Hong, "Stark localization in $\text{GaAs}/\text{GaAlAs}$ superlattices under an electric field," *Phys. Rev. Lett.*, vol. 60, pp. 2426-2429, 1988.
- [17] J. Bleuse, P. Voisin, M. Allovon, and M. Quillec, "Blue shift of the absorption edge in $\text{AlGaInAs}/\text{GaInAs}$ superlattices: Proposal for an original electro-optical modulator," *Appl. Phys. Lett.*, vol. 53, pp. 2632-2634, 1988.
- [18] E. J. Austin and M. Jaros, "Carrier lifetimes and localisation in coupled $\text{GaAs}/\text{GaAlAs}$ quantum wells in high electric fields," *J. Phys. C*, vol. 19, pp. 533-541, 1986.
- [19] P. W. A. Mollroy, "Effect of an electric field on electron and hole wave functions in a multiquantum well structure," *J. Appl. Phys.*, vol. 59, pp. 3532-3536, 1986.
- [20] R. Lang and K. Nishi, "Electronic state localization in semiconductor superlattices," *Appl. Phys. Lett.*, vol. 45, pp. 98-100, 1984.

P. F. Yuh, photograph and biography not available at the time of publication.

K. L. Wang, photograph and biography not available at the time of publication.

Optical transitions in a step quantum well

P. F. Yuh and K. L. Wang

Device Research Laboratory, Department of Electrical Engineering, University of California, Los Angeles, Los Angeles, California 90024-1600

(Received 12 September 1988; accepted for publication 30 January 1989)

We have theoretically studied the field-dependent optical properties of a step quantum-well structure, which consists of a small well inside a big well. The wave functions of the small and big wells overlap and their eigenenergies have different field dependencies. The transition from a small-well state to a big well state thus gives a large Stark shift at low applied field without degrading the oscillator strength. Another advantage is to allow optical transitions that are forbidden in simple single-well structures. This relaxation of the selection rule makes it possible to provide optical pumping for intersubband lasing. Also, since the step well is asymmetric, many nonlinear properties are expected.

I. INTRODUCTION

Optical transitions in a square quantum well have been studied for possible applications in optical switching. The energy shift of the interband¹ or intersubband² transition under an applied electric field (the Stark shift) is usually small. In coupled quantum wells,³⁻⁵ on the other hand, the Stark shifts are large but the oscillator strengths are small since these shifts are caused by an "interwell" type of transitions.⁴ There seems to be a tradeoff for achieving both large shifts and strengths in the above-mentioned cases.

In this paper, we discuss an alternative quantum-well structure—the step quantum well. For such a step well, both large Stark shift and oscillator strength can be achieved.

II. ANALYTIC DISPERSION RELATION

First we will derive an analytic dispersion relation for a step quantum well. The step-well structure consists of two layers A and B with layer widths L_A and L_B bounded by two thick barriers as shown in Fig. 1. To analyze this structure we note that the energy states and wave functions for quantum-well structures of arbitrary potential shapes have been derived using a transfer matrix method.⁵ The energy states are found by

$$-\frac{m_r^*}{\kappa_r} = \frac{S_{11} + \kappa_l/m_l^* S_{12}}{S_{21} + \kappa_l/m_l^* S_{22}}, \quad (1)$$

where S is a 2×2 transfer matrix of the well region and is explicitly given in Ref. 6. The well region, which may have any arbitrary potential profile, is assumed to be bounded by two flat-band barriers with potential V_l and V_r (for left and right). The wave vectors for the corresponding left and right barriers are

$$\begin{aligned} \kappa_l^2 &= -2m_l^*/\hbar^2(E - E_{||} - eV_l), \\ \kappa_r^2 &= -2m_r^*/\hbar^2(E - E_{||} - eV_r), \end{aligned}$$

where E is the total energy and $E_{||} = \hbar^2 k_{||}^2/2m^*$, $k_{||}$ is the wave vector parallel to the quantum-well layers, and m^* 's are the effective masses in the corresponding regions.

For infinite barrier height approximation, one may assume $V_l, V_r \rightarrow \infty$ or $\kappa_l, \kappa_r \rightarrow \infty$ and Eq. (1) reduces to S_{12}

= 0. For a step-well structure referring to Fig. 1, Eq. (1) can be analytically expressed as

$$\begin{aligned} \frac{\kappa_l}{m_l^*} + \frac{\kappa_r}{m_r^*} + \left(\frac{\kappa_l \kappa_r}{k_A} \frac{m_A^*}{m_l^* m_r^*} \right) \tan k_A L_A + \left(\frac{\kappa_l \kappa_r}{k_B} \frac{m_B^*}{m_l^* m_r^*} \right) \\ \times \tan k_B L_B + \left(\frac{k_B \kappa_l}{k_A} \frac{m_A^*}{m_B^* m_l^*} + \frac{\kappa_A \kappa_r}{k_B} \frac{m_B^*}{m_A^* m_r^*} \right) \\ \times \tan k_A L_A \tan k_B L_B = 0, \end{aligned} \quad (2)$$

where the wave vectors in layers A and B are $k_A^2 = 2m_A^*/\hbar^2(E - E_{||} - eV_A)$, $k_B^2 = 2m_B^*/\hbar^2(E - E_{||} - eV_B)$, and m_A^*, m_B^*, V_A, V_B are the effective masses and potential heights in the two regions.

For the infinite barrier approximation, Eq. (2) is reduced to

$$\frac{m_A^*}{k_A} \tan L_A k_A + \frac{m_B^*}{k_B} \tan L_B k_B = 0. \quad (3)$$

After the energy levels are determined from Eq. (2), the wave functions can be constructed from any initial point, usually the well boundary, by the transfer matrix method.⁶ Explicitly the wave function is

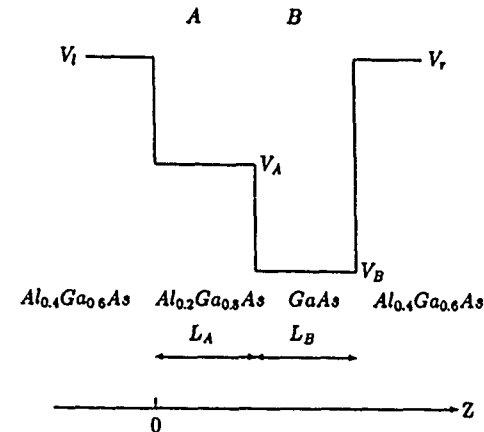


FIG. 1. A step quantum well consisting of two layers. A: $\text{Al}_{0.2}\text{Ga}_{0.8}\text{As}$. B: GaAs bound by two thick $\text{Al}_{0.4}\text{Ga}_{0.6}\text{As}$ barriers. The layer thicknesses of A and B are denoted by L_A and L_B , respectively.

$$\psi(z) = \begin{cases} Ce^{\kappa z} & z < 0 \\ C \left(\cos k_A z + \frac{\kappa_A}{k_A} \frac{m_A^*}{m_I^*} \sin k_A z \right) & 0 \leq z \leq L_A \\ \psi(L_A) \cos k_B (z - L_A) + \frac{\psi'(L_A)}{k_B} \frac{m_B^*}{m_A^*} \sin k_B (z - L_A) & L_A \leq z \leq L_A + L_B \\ \psi(L_A + L_B) e^{-\kappa_B (z - L_A - L_B)} & L_A + L_B \leq z \end{cases} \quad (4)$$

where C is a normalization constant.

Under applied field, the elements of the transfer matrix consist of Airy functions,⁶ and the dispersion relation is basically expressed by Eq. (1), although the exact form is more cumbersome.

III. LINEAR OPTICAL ABSORPTION UNDER A FIELD

The intersubband transitions under an applied field are discussed first. The similar analysis is then applied to interband transitions and the results will be briefly discussed later.

A. Intersubband transitions

The wave functions and energy states for the lowest three conduction-band sublevels (1_c , 2_c , and 3_c) are shown in Fig. 2 under different electric fields. This step-well structure consists of two layers A and B bounded by two thick ($>200 \text{ \AA}$) $\text{Al}_{0.4}\text{Ga}_{0.6}\text{As}$ barriers. Layer A (the shallow side of the step well) is 120-\AA $\text{Al}_{0.2}\text{Ga}_{0.8}\text{As}$ (or 42 monolayers), and layer B (the deep side) is 70-\AA GaAs (or 25 monolayers). Later we will use the notation $(42_{0.2}25_0)$ to represent the above structure and similar notations for other step-well structures. The (25_0) well or the deep side of the step

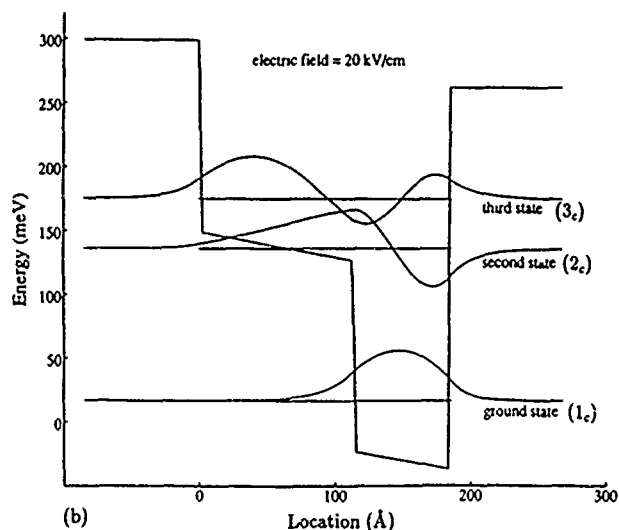
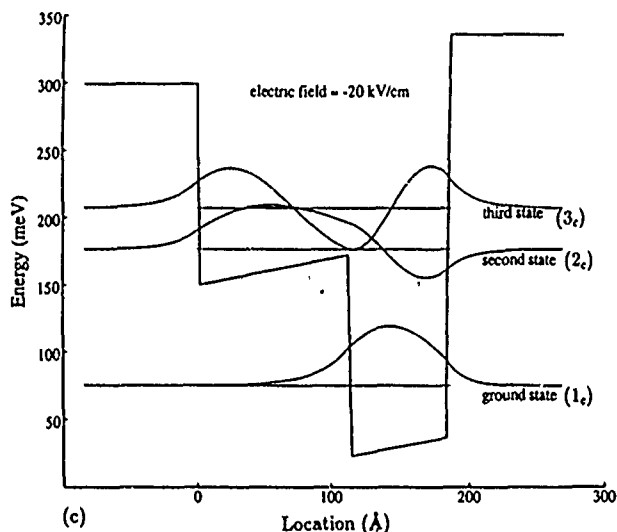
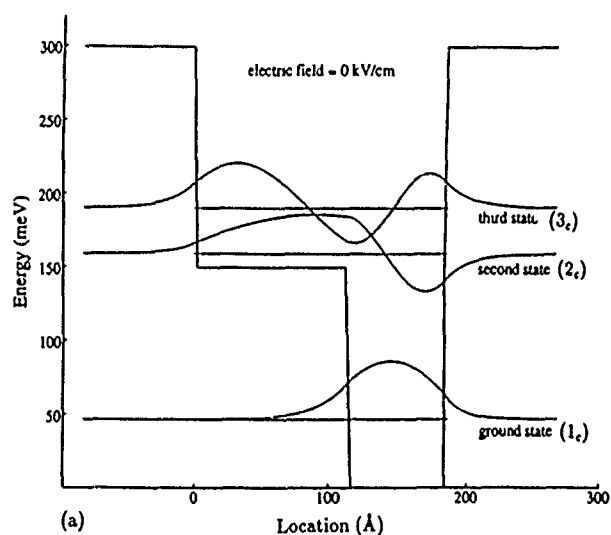


FIG. 2. Wave functions and energy states for the lowest three conduction-band sublevels of a step quantum well $(42_{0.2}25_0)$ under different applied electric fields.

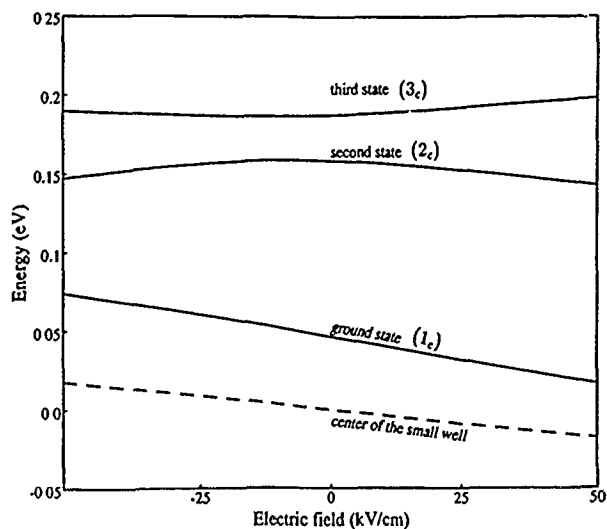


FIG. 3 Electric field dependence of the lowest three states. The energy is referred to the center of the whole step well. The ground state tracks the center of the small well, indicated by the dashed line. While the higher states are approximately constant.

well is referred to as the small well, and an imaginary $[(42 + 25)_{0.2}]$ well is the big well. The results of wave functions and eigenenergies have several unique features. First, the wave functions can be engineered by the step potential to have a localized ground state and delocalized excited states. The ground state 1_c has energy below the $\text{Al}_{0.2}\text{Ga}_{0.8}\text{As}$ barrier, and its wave function is localized in the small well, while the excited states 2_c and 3_c belong to the big well and their wave functions oscillate globally in the big well. Second, the sublevel energies of different wells have different field dependencies. The 1_c state seems to track the center of the small well while the 2_c and 3_c states track the center of the big well. Third, because of the nonsymmetric nature of the structure, the sublevel energies can move close or far apart depending on the direction of the applied field. Thus, both red and blue shifts (shift to longer and shorter wavelengths, respectively) can be obtained by simply changing the bias direction.

To further illustrate the second and third results discussed above, we have shown in Fig. 3 the electric field dependence of the lowest three conduction-band states. The energy is referred to the center of the entire step-well structure. The second and third states (2_c and 3_c) are nearly

constant, while the ground state (1_c) shifts linearly with respect to the step-well center. To illustrate that the ground state actually tracks the center of the small well, we have also plotted the center of the small well as the field changes in dotted line. From Fig. 3 we observe that the $1_c \rightarrow 2_c$ and $1_c \rightarrow 3_c$ intersubband transitions have large Stark shifts, typically one order of magnitude larger than that of the single-quantum-well case. A comparison of the intersubband Stark effect for a step well and a simple square well is made in Table I. It is noticed from the table that both red and blue shifts are possible, depending upon the polarity of the field. In addition to the large Stark shifts, the oscillator strengths, which indicate whether a transition is allowed or forbidden, also retain comparable to that of single-well case. The oscillator strength as a function of the applied field is plotted in Fig. 4(a). The $1_c \rightarrow 3_c$ transition has a comparable strength as the $1_c \rightarrow 2_c$ transition for this case. Unlike the coupled quantum-well case in which wave functions belonging to different wells overlap only by their tails,⁵ in the step well given here the wave function localized in the small well can overlap appreciably with those in the big well. Thus, large Stark shifts as well as large oscillator strengths can be achieved in the step quantum well. The oscillator strength is also investigated as a function of the layer width L_A of the shallow well (or the width of $\text{Al}_{0.2}\text{Ga}_{0.8}\text{As}$ layer) as shown in Fig. 4(b). The deep well, or the GaAs layer width L_B , is fixed at 70 Å. In the limit when $L_A \rightarrow 0$, step well approaches the single-well case in which the $1_c \rightarrow 3_c$ transition is not allowed. As the big well expands, the strength of $1_c \rightarrow 3_c$ increases to about 0.5 and becomes an allowed transition.

B. Interband transitions

For interband transitions, we first notice that the heavy hole is more easily confined than the electron. Thus, it is possible to have the ground heavy-hole sublevel (1_h) inside the deep side while the ground electron sublevel (1_c) is in the shallow side of the step well. Since the sublevels in different wells track different centroids of the wells and have different field dependencies, the $1_h \rightarrow 1_c$ transition can have a large Stark shift, meanwhile, a large strength is retained due to a large overlap of the wave functions just like the intersubband case discussed earlier. The fundamental absorption

TABLE I Comparison of intersubband Stark effect in a step quantum well and a simple square well. The transition energy (E) and oscillator strength (OS) are calculated for a step quantum well $(42_{0.2}25_0)$ under different electric fields (F)

| Structures | Transition | $F = 0$ | $F = +36 \text{ kV/cm}$ | $F = -36 \text{ kV/cm}$ | Stark shift (meV) |
|--------------|-----------------------|-------------------------|-------------------------|-------------------------|-------------------|
| Step well | $1_c \rightarrow 2_c$ | $E = 112.0 \text{ meV}$ | $E = 123.2 \text{ meV}$ | $E = 86.5 \text{ meV}$ | + 11.2 |
| | | $OS = 0.62$ | $OS = 0.87$ | $OS = 0.22$ | - 25.5 |
| Step well | $1_c \rightarrow 3_c$ | $E = 141.0 \text{ meV}$ | $E = 169.8 \text{ meV}$ | $E = 121.9 \text{ meV}$ | + 28.8 |
| | | $OS = 0.30$ | $OS = 0.08$ | $OS = 0.63$ | - 19.1 |
| Square well* | $1_c \rightarrow 2_c$ | $E = 89.2 \text{ meV}$ | $E = 90.8 \text{ meV}$ | | + 1.6 |
| | | $OS = 0.96$ | $OS = 0.95$ | | |

*From Ref. 2 for a 120-Å well bound by $\text{Al}_{0.5}\text{Ga}_{0.5}\text{As}$ barriers.

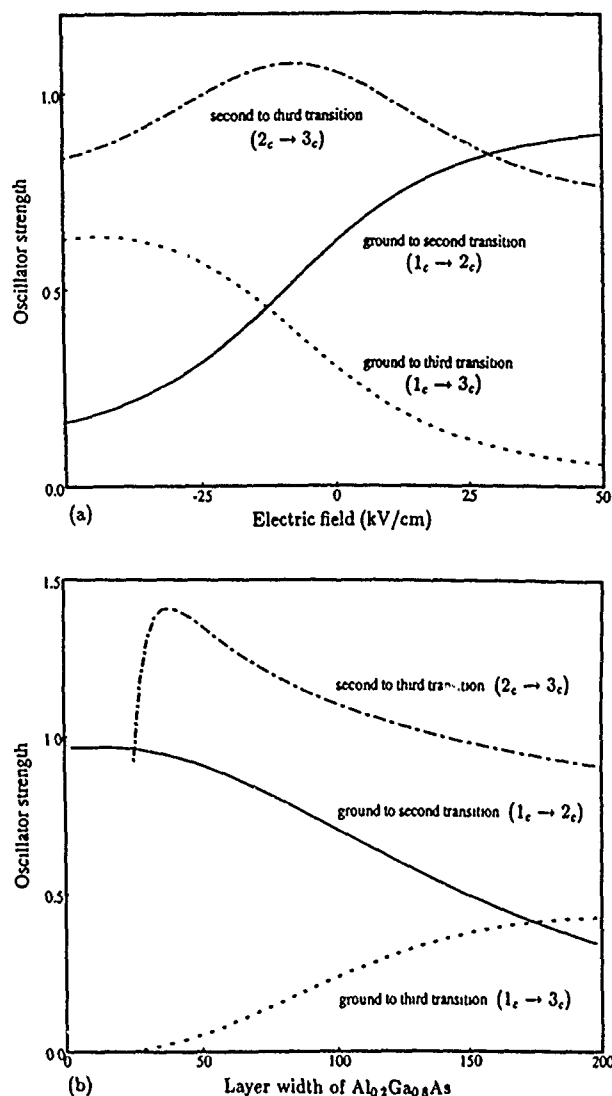


FIG. 4 Oscillator strength as a function of (a) the applied field and (b) the layer width L_A , or the $\text{Al}_{0.2}\text{Ga}_{0.8}\text{As}$ barrier. It is noted that both $1 \rightarrow 2$ and $1 \rightarrow 3$ transitions are allowed and their strengths can be adjusted by applying an electric field or engineering the layer widths.

neglecting the exciton effects for a $(45_{0.1}11_0)$ step well is shown in Fig. 5 under different applied fields. The $1_h \rightarrow 1_c$ transition has a 6-meV blue shift at a +30-kV/cm field and a 13-meV red shift at a -30 kV/cm field. In both cases the oscillator strengths remain large. A similar calculation for a square well (17_0), which has a transition energy of 1.608 eV, shows only a 0.2-meV red shift at a field of 30 kV/cm. Unlike the interband transition in a single well or coupled wells, where only a red shift is present, the transition in a step well can have a blue shift as well. In addition, due to the asymmetry of the step well, its electric field dependence is asymmetric.

IV. OTHER APPLICATIONS

A. Intersubband laser

Recently there is an increasing interest in the infrared light emission from intersubband transitions in semiconductor quantum-well structures. Most of the structures proposed⁷⁻⁹ or demonstrated¹⁰ use current injection for pump-

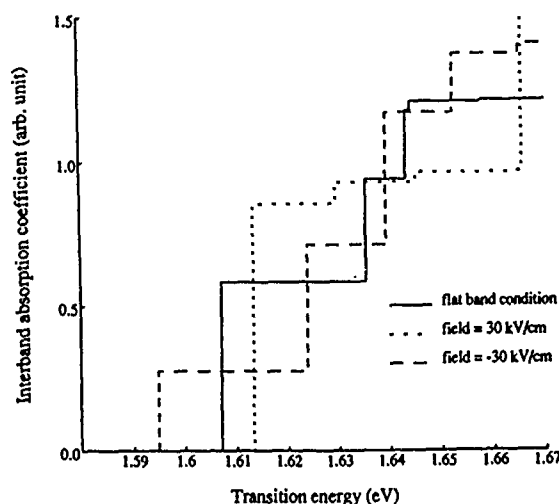


FIG. 5. Fundamental absorption neglecting the exciton effects for a $(45_{0.1}11_0)$ step well under different applied fields. Both red and blue shifts are possible depending on the polarity of the bias.

ing. Here we discuss the possibility of optical pumping using one of the unique features of the step quantum well, i.e., the selection rule is tunable.

We consider the lowest three conduction sublevels in a $(45_{0.17}26_0)$ step well. The energy levels are designed such that we have $E_{31} \approx 124$ meV which can be pumped by a CO_2 laser; $E_{32} \approx 28$ meV which is smaller than the longitudinal optical phonon energy E_{LO} (36 meV for GaAs); and $E_{21} \approx 96$ meV which is bigger than E_{LO} . We assume that the structure is doped and the ground state is occupied while the other higher states are empty in thermal equilibrium. Since the $1 \rightarrow 3$ transition is allowed in this step-well structure having an oscillator strength of 0.4, carriers can now be effectively pumped to the third level by a CO_2 laser. The $3 \rightarrow 2$ transition has a large oscillator strength of 1.1, which implies a high radiative recombination rate. And it is expected to have a long nonradiative recombination lifetime caused only by acoustic phonon scattering (~ 300 ps) because $E_{32} < E_{\text{LO}}$ and the optical phonon scattering is suppressed.¹¹ Therefore, the $3 \rightarrow 2$ is efficient for lasing action. While the $2 \rightarrow 1$ transition has a very short lifetime caused by optical phonon scattering (~ 10 ps),^{12,13} a fast depopulation of level 2 is ensured. The population inversion can be estimated by a simple rate equation,

$$\Delta N = N_3 - N_2 = \frac{[1 - (\tau_{21}/\tau_{32})]N}{[2 + (\tau_{21}/\tau_{32})] + (1/cI)[(1/\tau_{31}) + (1/\tau_{32})]}, \quad (5)$$

where N is the total population, N_i is the population in level i , τ_{ij} is the nonradiative lifetime between levels i and j , $R = cI(N_1 - N_3)$ is the pump rate of the CO_2 laser, I is the laser intensity, and c is a constant proportional to the $1 \rightarrow 3$ oscillator strength. If the laser intensity is high enough, then the population inversion becomes $\Delta N \approx N/2$, since $\tau_{21}/\tau_{32} < 0.1$ for this design $E_{21} > E_{\text{LO}} > E_{32}$. If, however, $E_{32} > E_{21} > E_{\text{LO}}$, we still can have population inversion since

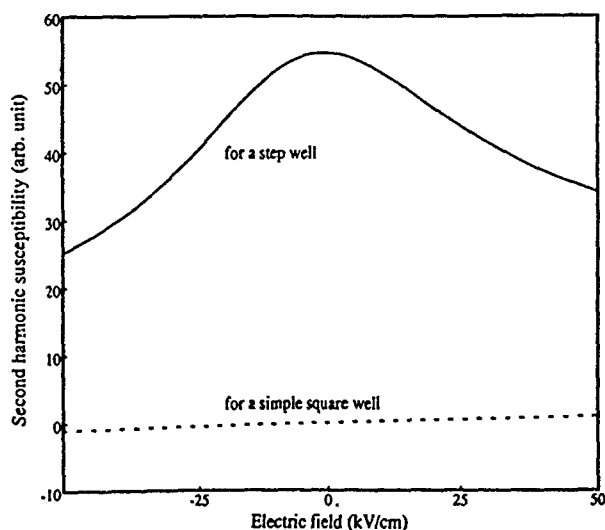


FIG. 6. Calculated second harmonic susceptibility vs field for a step quantum well ($42_0 \rightarrow 25_0$) and a simple square well (31_0), which has the same $1_c \rightarrow 2_c$ transition energy 112 meV. The unit of susceptibility is normalized to the single-well case at a field 50 kV/cm.

a larger energy separation usually has a longer lifetime even involving optical phonon scattering.⁹ This three-level system is not feasible for a simple square well structure since the transition from the ground to the third or higher levels is forbidden.

B. Second-order nonlinear properties

Another advantage of using step-well structures is to have a high optical nonlinearity for interband and intersubband transitions. The second-order susceptibility for intersubband transitions has been calculated for several asymmetric quantum-well structures, for example, a Morse potential well¹⁴ and a square well under applied field^{15,16}, and it has also been calculated for interband transitions for an asymmetric coupled well.¹⁷ We have calculated for a step well the second-harmonic susceptibility, which is proportional to $|M_{21}|^2(M_{11} - M_{22})$ for a two-level system, and M_{ij} is the dipole matrix element for transition between levels i and j . The result as a function of electric field is shown in Fig. 6 in comparison with a square well case. It is noted that the step well has a much larger second-order susceptibility than the single-well case calculated in Ref. 15.

V. SUMMARY

In summary, we have derived analytic solutions of the energy states and wave functions for a step quantum well, which consists of a small well inside a big well. Optical transitions from the states in the small well to the states in the big well show large Stark shifts, and at the same time retain large strengths. This result can be applied to a low current, fast electro-optical effect utilizing interband or intersubband transitions in a step quantum well. Other special features are that the selection rule is different from the simple square well case and can be applied to efficient optical pumping for light emission by intersubband transitions, and that the well asymmetry introduces a large second-order susceptibility.

ACKNOWLEDGMENT

This work is supported in part by U.S. Office of Naval Research and U.S. Army Research Office.

- ¹D. A. B. Miller, J. S. Weiner, and D. S. Chemla, *J. Quantum Electron.* **QE-22**, 1816 (1986).
- ²A. Harwit and J. S. Harris, Jr., *Appl. Phys. Lett.* **50**, 685 (1987).
- ³H. Q. Le, J. J. Zayhowski, and W. D. Goodhue, *Appl. Phys. Lett.* **50**, 1518 (1987).
- ⁴Y. J. Chen, E. S. Koteles, B. S. Elman, and C. A. Armiento, *Phys. Rev. B* **36**, 4562 (1987).
- ⁵P. Yuh and K. L. Wang, *Phys. Rev. B* **38**, 8377 (1988).
- ⁶P. Yuh and K. L. Wang, *Phys. Rev. B* **38**, 13307 (1988).
- ⁷P. Yuh and K. L. Wang, *Appl. Phys. Lett.* **51**, 1404 (1987).
- ⁸H. C. Liu, *J. Appl. Phys.* **63**, 2856 (1988).
- ⁹K. L. Wang and P. Yuh, *J. Quantum Electron.* **25**, 12 (1989).
- ¹⁰M. Helm, E. Colas, P. England, F. DeRosa, and S. J. Allen, Jr., *Appl. Phys. Lett.* **53**, 1714 (1988).
- ¹¹D. Y. Oberli, D. R. Wake, M. V. Klein, J. Klem, T. Henderson, and H. Morkoç, *Phys. Rev. Lett.* **59**, 696 (1987).
- ¹²A. Seilmeier, H. J. Hübner, G. Abstreiter, G. Weimann, and W. Schlapp, *Phys. Rev. Lett.* **59**, 1345 (1987).
- ¹³F. H. Julien, J. M. Lourtioz, and N. Herschler, *Appl. Phys. Lett.* **53**, 116 (1988).
- ¹⁴M. K. Gurnick and T. A. Detemple, *J. Quantum Electron.* **QE-19**, 791 (1983).
- ¹⁵L. Tsang, D. Ahn, and S. L. Chuang, *Appl. Phys. Lett.* **52**, 697 (1988).
- ¹⁶Z. Ikonić, V. Milanović, and D. Tjapkin, *J. Quantum Electron.* **25**, 54 (1989).
- ¹⁷J. Khurgin, *Appl. Phys. Lett.* **51**, 2100 (1987).

Si/Ge_xSi_{1-x}/Si resonant tunneling diode doped by thermal boron source

S. S. Rhee, R. P. G. Karunasiri, C. H. Chern, J. S. Park, and K. L. Wang

Device Research Laboratory, Electrical Engineering Department,
University of California, Los Angeles, California 90024

(Received 22 September 1988; accepted 22 September 1988)

A study of resonant tunneling of holes in a Si/Ge_xSi_{1-x}/Si double barrier structure doped by a thermal boron doping source is presented. The source consists of a pyrolytic boron nitride crucible and uses filament heating. Sharp and constant doping levels between 1×10^{17} and 4×10^{19} cm⁻³ are obtained with a maximum *K*-cell temperature of $\sim 1560^\circ\text{C}$. The double barrier tunneling devices realized by this source shows 2.1/1 peak-to-valley ratio at 4.2 K in current-voltage characteristics. Magnetotunneling measurements confirm that both the light and heavy holes participate in the resonant tunneling.

Recently, strained layer GeSi heterostructures have attracted considerable attention due to possible Si-based quantum well and superlattice device application.¹⁻³ The devices engineered using the valence band of the GeSi system have advantages both due to the large band offset as well as the small light-hole mass. However, realization of such devices in this system has been hampered mainly due to difficulties of achieving desired doping concentrations with sharp profiles. In Si molecular-beam epitaxy (Si MBE) Ga and B are normally used as *p*-type dopants. Ga which has a relatively higher vapor pressure than B has a serious problem in controlling the doping profile. The difficulties come from the long residence time at low substrate temperature (*T_s*) as well as the low sticking coefficient at high *T_s*.⁴ For a typical GeSi growth temperature which is lower than 550°C , this results in serious smearing of the doping profiles. Also, the higher ionization energy of Ga further imposes limitation on the achievable carrier concentrations.

It has been reported that B has a very short residence time, no surface segregation^{5,6,7} and unity sticking coefficient. However, B has a low vapor pressure⁸ and high temperatures (1300 – 2000°C) are needed to obtain an appreciable doping concentration.^{5,7,9} In order to obtain high boron source temperatures, Kubiak *et al.*⁵ employed a direct heating method by passing electric current through conductive crucibles such as graphite or refractory metals. Recently, Andrieu *et al.*⁹ reported a technique combining electron bombardment and radiative heating in boron doping. However, these methods have several drawbacks arising from the complicated cell structures necessary to obtain such high temperatures. Several groups have also experimented with boron compounds such as B₂O₃ (Refs. 6,10,11) and HBO₂ (Ref. 12) in lieu of pure boron for producing boron at lower *K*-cell temperatures. Even though the sticking coefficient seems to be independent of the growth temperature in the case of B₂O₃, the incorporation of oxygen into the epitaxial film at low growth temperature and surface segregation of B due to chemical reaction have been observed.¹³ In this paper, we present characteristics of doping profiles achieved by a conventional *K*-cell designed specifically for moderately high-temperature operation and the results of resonant tunneling of Si/GeSi/Si double barrier diodes doped using such a source.

In the experiment, samples were grown in a Si MBE chamber with a base pressure of 7×10^{-11} Torr. The samples were chemically cleaned by the Shiraki method⁴ and the protective oxide was removed *in situ* by heating the substrate at 950°C for ~ 10 min. The performance of the boron source was characterized for both Si and GeSi epitaxial films grown at different cell temperatures. The doping profile and the concentration were obtained from spreading resistance (SR) and secondary ion mass spectrometry (SIMS) measurements.

First we estimated the temperature range for the necessary boron fluxes to obtain the required doping concentrations using the equation¹⁵

$$I = 1.118 \times 10^{22} PA / l^2 \sqrt{MT}$$

where *I* is the flux at the sample surface in molecules/cm² s, *P* is the partial pressure in Torr, *A* is the area of the source opening, *l* is the distance between the source and the sample, *M* is the molecular weight and *T* is the temperature of the cell

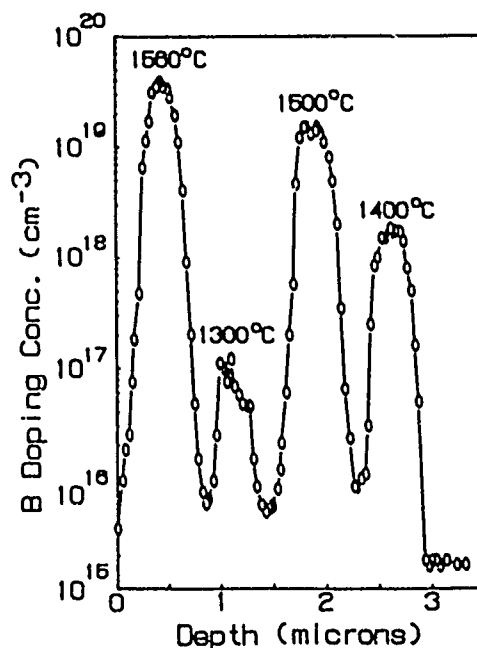


FIG. 1. Spreading resistance measurement of a B doped Si MBE film. Different B doping cell temperatures are shown. Si flux used was 160 \AA/m .

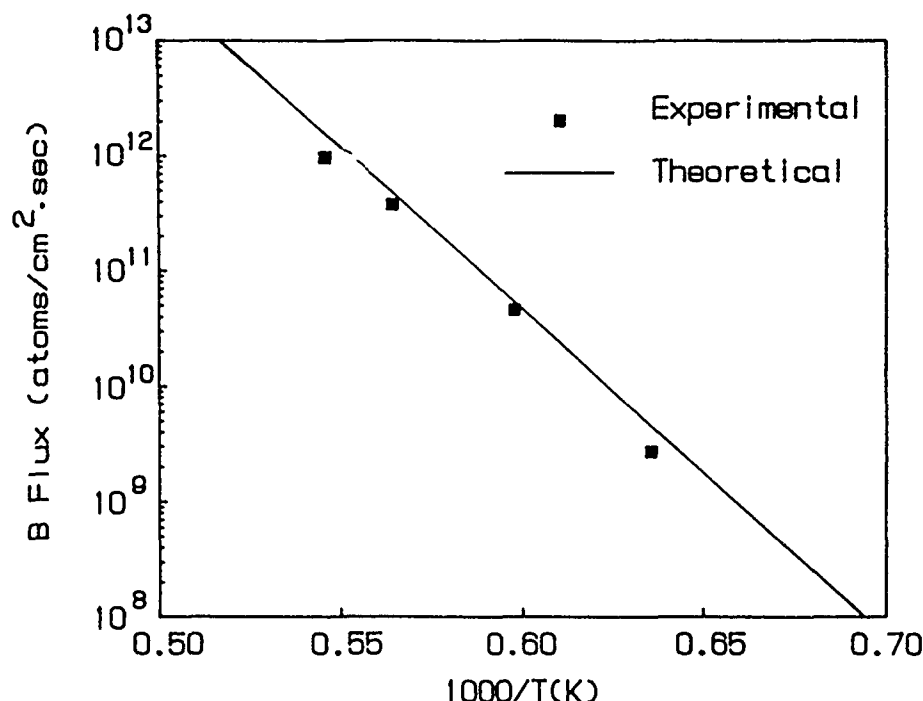


FIG. 2. Experimental and theoretical flux rates as a function of temperature of the thermal boron source.

in Kelvin. For the system we used, $A = 0.73 \text{ cm}^2$ and $l = 15 \text{ cm}$. the vapor pressure of B was obtained from Ref. 8.

Figure 1 shows SR measurement data of a boron doped Si film grown at 700°C substrate temperature and the growth rate was maintained at 160 Å/min throughout the growth. The boron cell temperature was varied from 1300 – 1560°C and the power rating of the cell is 280 W at $\sim 1560^\circ\text{C}$. The SR data exhibits a well-controlled doping profile in the range of 1×10^{17} to $4 \times 10^{19} \text{ cm}^{-3}$. Doping concentration changes more than one decade per 1000 Å as seen in the SR data. It is noted that the boron cell temperature of only 1400°C is needed to obtain the 10^{18} cm^{-3} doping level for a reasonable growth rate of 2 – 3 Å/s . The background doping level is $\sim 1 \times 10^{16} \text{ cm}^{-3}$. Figure 2 shows the experimentally observed doping concentrations as a function of temperature compared with the data calculated from the above equation and good agreement is seen. The actual abruptness of the doping profile should be better than that shown in Fig. 1 due to the inherent limitations of the SR measurement.

In order to obtain a better estimate for the abruptness of the doping profile, different samples were grown for the SIMS measurement. The structure consists of four periods of intrinsic Si and boron doped Si layers. The growth rate of Si was 48 Å/min and substrate temperature was kept at 530°C . The boron cell temperature of 1325°C was used to dope the p -Si layers. Thicknesses for each layer of a period were 100 , 250 , 500 , and 1000 Å , beginning from the surface. The SIMS data in Fig. 3 show an abruptness of \sim one decade/ 200 Å . However, the slope of the doping profile should be even better considering smearing effects from the ion mixing and incomplete coverage of primary ions over the surface. Considering these effects together with the background signal in the SIMS system, the actual doping profile should have an abruptness better than the SIMS data as shown in Fig. 3. A high doping concentration of $\sim 5 \times 10^{17} \text{ cm}^{-3}$ in

undoped layers seems to be mainly from the background of the SIMS system.

To investigate the performance of devices, using the above boron source, we have fabricated a Si/Ge_{0.4}Si_{0.6}/Si double barrier tunneling structure on a low resistivity ($0.01 \Omega \text{ cm}$) Si(100) wafer. Ge was evaporated from a conventional Knudsen cell. The growth temperature was 530°C . The Si and Ge deposition rates were 45 and 30 Å/min , respectively. The structure of the sample consists of a double barrier structure sandwiched between a 7000-Å Ge_{0.4}Si_{0.6} buffer

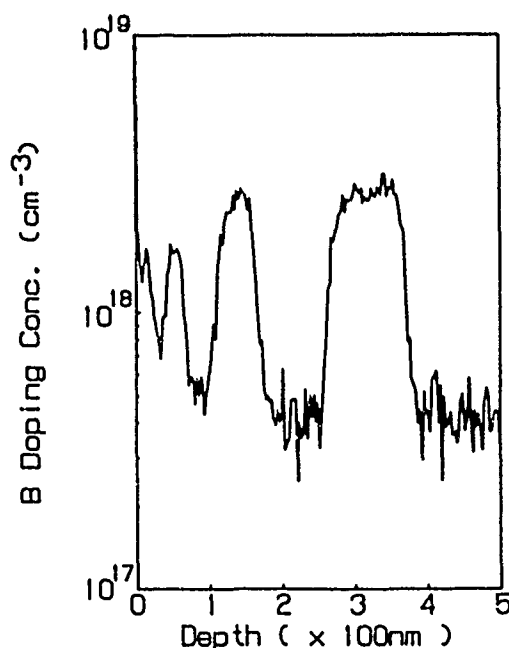


FIG. 3. SIMS doping profile of a Si film doped using the thermal boron source at 1325°C . Sharpness of the profile is better than a decade/ 200 Å . Si flux was 48 Å/min .



FIG. 4. TEM picture of the double barrier resonant tunneling structure. It shows 43-Å well and two 50-Å Si barriers. All the layers are Ge_{0.4}Si_{0.6}, except Si barriers.

and a cap layers. Both layers were doped to $5 \times 10^{18} \text{ cm}^{-3}$. The double barrier structure was composed of an undoped 43-Å Ge_{0.4}Si_{0.6} quantum well between 50-Å Si barriers. Outside the two Si barriers, two 150-Å Ge_{0.4}Si_{0.6} layers were undoped to prevent the diffusion of dopants into the active region. In the structure, only the Si barriers are strained and all the Ge_{0.4}Si_{0.6} layers are unstrained. Figure 4 shows a transmission electron microscopy (TEM) image of the double barrier structure used in the experiment and the thickness obtained from TEM is in good agreement with the thickness that is estimated from the flux rates. We have also used x-ray diffraction to determine the lattice constant of the substrate (a_{Si}), and the relaxed buffer and contact layers (a_{GeSi}). The measurement yields $a_{\text{Si}} = 5.4236 \text{ Å}$ and $a_{\text{GeSi}} = 5.5213 \text{ Å}$ along the growth direction for the Si substrate and unstrained GeSi layers, respectively. We have calculated the percentage of the lattice mismatch $\epsilon = (a_{\text{GeSi}} - a_{\text{Si}})/a_{\text{Si}}$ to be 1.8%, for a completely relaxed Ge_{0.4}Si_{0.6} layer, we have $\epsilon = 1.6\%$ using the lattice constants of Si and Ge.¹⁶ This indicates that the buffer and contact layers are not completely relaxed and a small amount of residual strain remains even though the film thickness is well above the critical thickness.

Figure 5 shows splitting of the light- and heavy-hole bands together with the valence-band offset for strained films on a

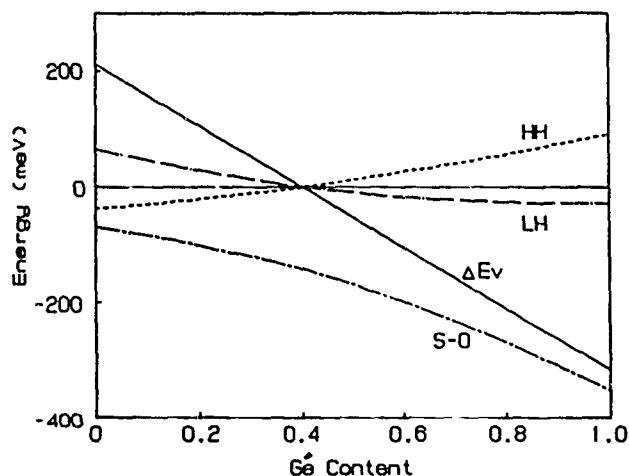


FIG. 5. Heavy (HH), and light-hole (LH) band-edge splitting and the valence-band offset (ΔE_v) for strained Ge_xSi_{1-x} film grown on Ge_{0.4}Si_{0.6} buffer layer.

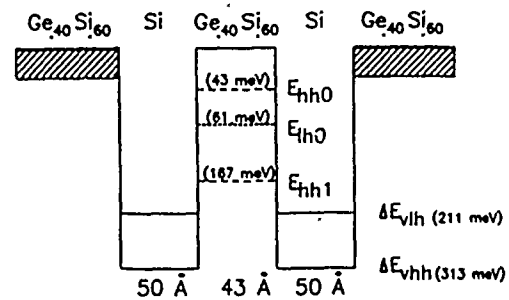


FIG. 6. Band diagram of the resonant tunneling structure used in the experiment. The heavy- and light-hole band edges are degenerated in unstrained Ge_{0.4}Si_{0.6} layers.

completely relaxed Ge_{0.4}Si_{0.6} buffer layer. The valence-band offset was obtained from the self-consistent *ab initio* pseudopotential results of Van de Walle *et al.*¹⁷ The light- and heavy-hole band splitting due to strain was obtained using an empirical deformation potential theory.^{18,19} In order to calculate the bound state energies in the quantum well for the light and heavy holes, the envelop function approximation using different masses for the well and barriers was used. The effective masses of the light and heavy holes were estimated using a linear interpolation of (001) masses of the warped bulk Si and Ge valence band and the calculated masses for a relaxed Ge_{0.4}Si_{0.6} layer are $0.08 m_e$ and $0.26 m_e$, respectively. Figure 6 shows the band diagram of the double barrier structure. For the heavy hole, there are two bound states in the quantum well at energies $E_{\text{hh0}} = 43 \text{ meV}$ and $E_{\text{hh1}} = 167 \text{ meV}$ and for the light hole only the ground state at $E_{\text{lh0}} = 61 \text{ meV}$ is obtained. Tunneling diodes were fabricated by a conventional lift-off technique and electrical measurement data were obtained for 50-μm diam diodes. The *I-V* characteristics of the diode at 4.2 K, 77 K and room temperature are shown in Fig. 7. Inset of the Fig. 7 shows the 77-K measurement for higher bias. At 77 K there are two resonant peaks at 270 and 900 mV due to the light-hole ground state (E_{lh0}) and the heavy-hole first excited state (E_{hh1}), respectively. Another resonance feature is observed from the d^2I/dV^2 data at 170 mV (see Fig. 8) and is believed to be due to the heavy hole ground state (E_{hh0}). As seen in Fig. 5 the light- and heavy-hole bands are degenerated in Ge_{0.4}Si_{0.6} layers and light-hole tunneling current is dominant due to the smaller mass and lower barrier.

In order to identify whether the resonant tunneling is due to light or heavy holes, we have carried out magnetotunneling experiments with a magnetic field applied parallel to the interfaces. According to a theoretical estimation²⁰ the peak shift is proportional to B^2 and the gradient of the peak shift vs B^2 is inversely proportional to the effective mass. Figure 9 shows the peak shift vs B^2 for the two peaks at 170 and 270 mV. The ratio of the slopes of two lines gives $m_{\text{hh}}/m_{\text{lh}} = 3.9$ as compared with the theoretically estimated value of 3.3. This indicates that the peak at 170 mV is due to the heavy hole and the one at 270 mV comes from the light hole. The effect of the series resistance of the device on the peak voltage shift may be small since the peak resonant tunneling current remains the same as the magnetic field is changed.³ The for-

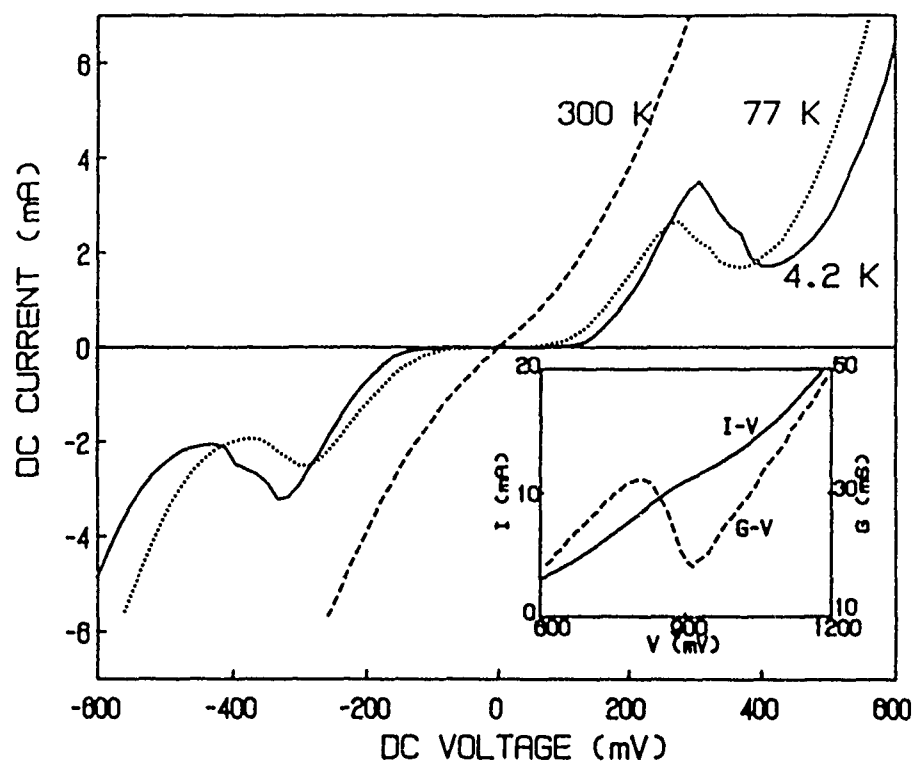


FIG. 7. I - V characteristics of a 50- μ m diameter resonant tunneling diode at 4.2 K, 77 K, and room temperature. Inset shows the I - V and conductance measurement of an additional peak for high bias at 77 K.

mation of Landau levels in the emitter region may be ignored due to ionized impurity scattering of carriers.²⁰

In conclusion, we have demonstrated the use of a conventional K -cell for pure boron doping in Si MBE and sharp doping profiles with concentrations needed for device applications are obtained. A resonant tunneling structure was

fabricated using the boron source and both light- and heavy-hole tunnelings were observed. The dominant types of tunneling carriers corresponding to the different peaks were identified using the voltage shift of the resonant tunneling current peaks in the presence of a strong magnetic field applied parallel to the interfaces.

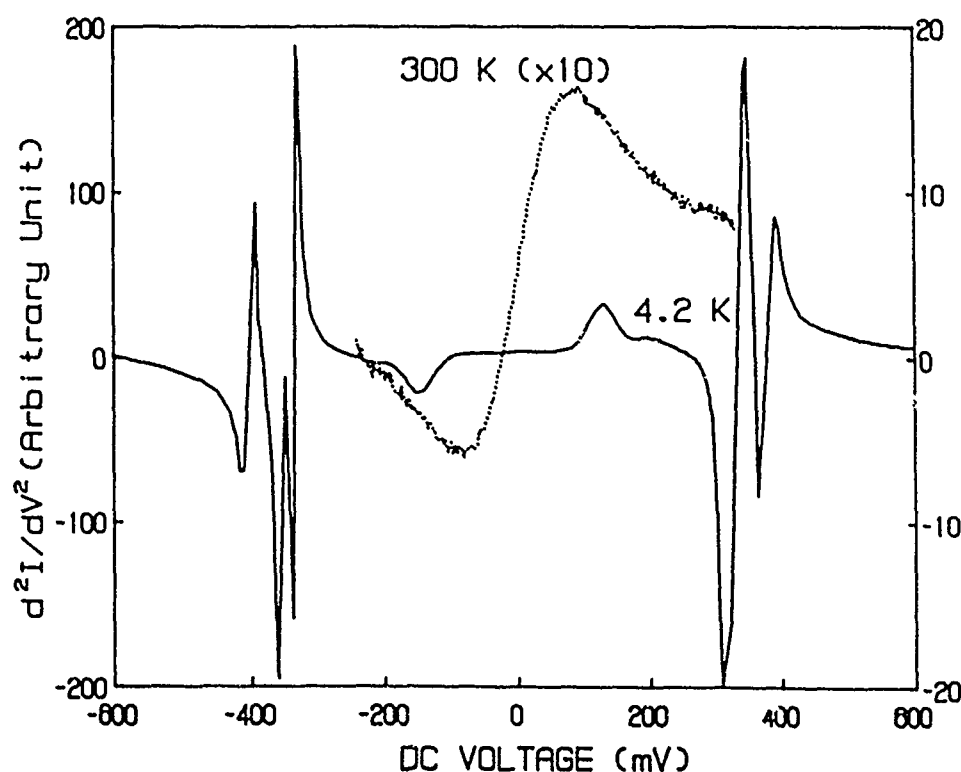


FIG. 8. Second derivative of $I(V)$ at 4.2 K and room temperature showing the tunneling due to the heavy-hole ground state.

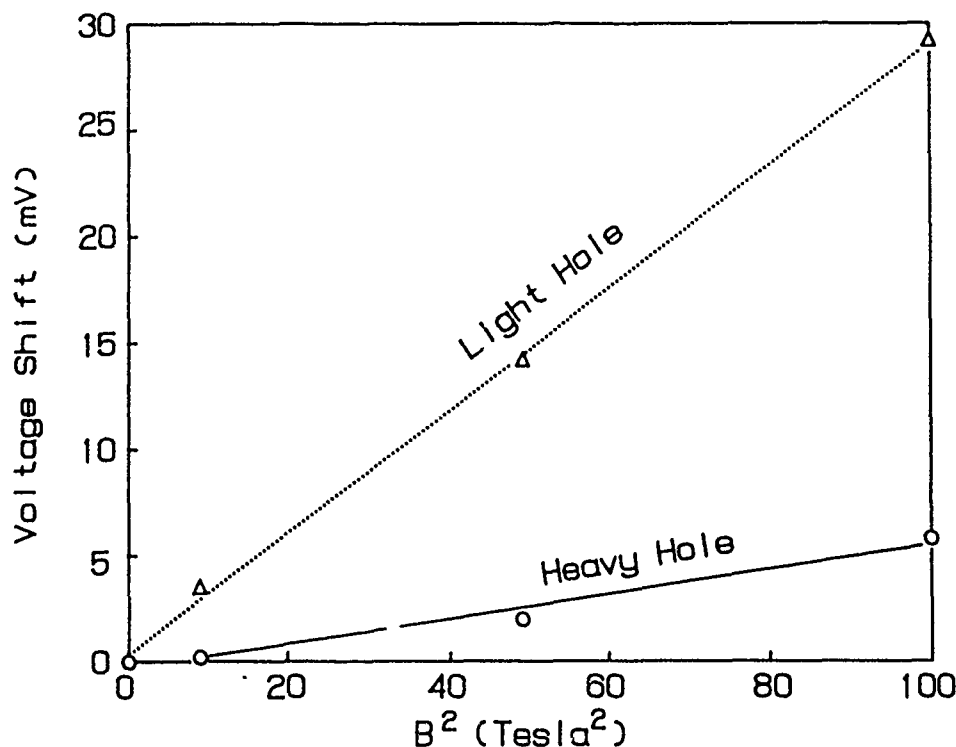


FIG. 9. Peak voltage shift vs B^2 for the peaks at 270 mV (dashed curve) and at 170 mV (solid curve) for the magnetic field parallel to the interfaces.

ACKNOWLEDGMENTS

The authors would like to acknowledge the support of SRC, ONR, and ARO.

¹S. S. Rhee, J. S. Park, R. P. G. Karunasiri, Q. Ye, and K. L. Wang, *Appl. Phys. Lett.* **53**, 204 (1988).

²H. C. Liu, D. Lanheer, M. Buchanan, and D. C. Houghton, *Appl. Phys. Lett.* **52**, 1809 (1988).

³K. L. Wang, R. P. Karunasiri, J. Park, S. S. Rhee, and C. H. Chern, *Superlattices and Microstructures* (to be published).

⁴S. S. Iyer, R. A. Metzger, and F. G. Allen, *J. Appl. Phys.* **52**, 5608 (1981).

⁵R. A. A. Kubiak, W. Y. Leong, and E. H. C. Parker, *J. Vac. Sci. Technol. B* **3**, 592 (1985).

⁶N. Aizaki and T. Tatsumi, *Extended Abstracts of the 17th Conference on Solid State Devices and Materials* (The Japanese Society of Applied Physics, Tokyo, 1985), p. 297.

⁷R. A. A. Kubiak, W. Y. Leong, and E. H. C. Parker, *Appl. Phys. Lett.* **44**, 878 (1984).

⁸R. E. Honig and D. A. Kramer, *RCA Rev.* **30**, 285 (1969).

⁹S. Andrieu, J. A. Chroboczek, Y. Campidelli, E. Andre, and F. A. d'Avitya, *J. Vac. Sci. Technol. B* **6**, 835 (1988).

¹⁰R. M. Ostrom and F. G. Allen, *Appl. Phys. Lett.* **48**, 221 (1986).

¹¹E. de Fresart, S. S. Rhee, and K. L. Wang, *Appl. Phys. Lett.* **49**, 847 (1986).

¹²T. Tatsumi, H. Hirayama, and N. Aizaki, *Appl. Phys. Lett.* **50**, 1234 (1987).

¹³E. de Fresart, K. L. Wang, and S. S. Rhee, *Appl. Phys. Lett.* **53**, 48 (1988).

¹⁴A. Ishizaka and Y. Shiraki, *J. Electrochem. Soc.* **133**, 666 (1988).

¹⁵N. F. Ramsey, *Molecular Beams* (Oxford University, New York, 1963), p. 11.

¹⁶S. M. Sze, *Physics of Semiconductor Physics* (Wiley, New York, 1981), p. 850.

¹⁷C. G. Van de Walle and R. M. Martin, *J. Vac. Sci. Technol. B* **3**, 1256 (1985).

¹⁸W. H. Kleiner and L. M. Roth, *Phys. Rev. Lett.* **2**, 334 (1959).

¹⁹R. People and J. C. Bean, *Appl. Phys. Lett.* **48**, 538 (1986).

²⁰L. Eaves, K. W. H. Stevens, and F. W. Sheard, *The Physics and Fabrication of Microstructures and Microdevices*, edited by M. J. Kelly and C. Weisbuch (Springer-Verlag Berlin, 1986).

STUDY OF ULTRA-THIN Ge/Si STRAINED LAYER SUPERLATTICE

S.J. CHANG, C.F. HUANG, M.A. KALLEL and K.L. WANG

Device Research Laboratory, Electrical Engineering Department, University of California, Los Angeles, California 90024, USA

and

R.C. BOWMAN, Jr. and P.M. ADAMS

The Aerospace Corporation, P.O. Box 92957, Los Angeles, California 90009, USA

Ultra-thin Ge/Si strained layer superlattices (SLSs) with periodicities of a few monolayers (MLs) have been successfully grown and characterized by Raman scattering spectroscopy. Structures with alternating Ge and Si layers were grown on Si substrates of different orientations. A thick 200 nm $\text{Ge}_{0.4}\text{Si}_{0.6}$ buffer layer was grown prior to the growth of the superlattice to make the strain distribution of the superlattice symmetrical and thus to maintain the pseudomorphic growth of the superlattices. Folded acoustic phonon peaks observed from these Ge/Si SLS samples can be used to determine the superlattice periodicity. The observed optical phonon frequencies were found to depend strongly superlattice periodicity. A quantitative interpretation of this phenomena was presented. Subsequent annealing of these samples reveals that the transition from pure Ge and/or Si layers to $\text{Ge}_x\text{Si}_{1-x}$ alloy becomes more pronounced as the annealing time and temperature increase.

Recently, much attention has been focused on Ge/Si SLSs, both theoretically [1-4] and experimentally [5,6] due to its unusual optical and electrical properties. However, due to the large 4.2% lattice mismatch between Ge and Si, pure Ge can only be commensurately grown on Si substrate up to 6 ML (~ 0.9 nm) [6]. In order to have a larger superlattice thickness, Kasper et al. had demonstrated the growth of symmetrically strained Ge/Si superlattices using an appropriate $\text{Ge}_y\text{Si}_{1-y}$ buffer layer [7]. In this work, we studied the phonon behavior of these Ge/Si SLS, as well as the inter-diffusion of Ge and Si atoms due to thermal treatment.

The samples used in this work were grown in a Si-MBE chamber equipped with 2 electron beam evaporators for Si and Ge separately, a quadrupole mass spectrometer for residual gas analysis and a reflection high energy electron diffraction (RHEED) system for in-situ characterization of the epi-film. The base and growth pressures were $\sim (7-8) \times 10^{-11}$ and $\sim (5-9) \times 10^{-9}$ Torr respectively, and the fluxes from Ge and Si sources were

monitored by an Inficon Sentinel III deposition controller. Prior to loading the Si substrates into the chamber, they were chemically pre-cleaned by Shiraki's method [8]. In the final step, a protective thin SiO_2 film (~ 1.5 nm) was grown chemically in a solution of 3 HCl:1 H_2O_2 :1 H_2O for 10 min. The protective oxide layer was then removed in-situ by the Si beam at a substrate temperature of 700°C. The growth temperature was kept at 400°C, and the growth rates were $2.75 \times 10^4 \text{ cm}^{-2} \text{ s}^{-1}$ for Si layers and $2.2 \times 10^{14} \text{ cm}^{-2} \text{ s}^{-1}$ for Ge layers, respectively. RHEED patterns observed from the top Si layers of these SLS samples indicate good epi-film crystallinity.

In this study, Raman experiments were performed at room temperature with near-back-scattering geometry. Samples were kept in vacuum to avoid scattering from the air. Various lines (457.9, 488.0 and 514.5 nm) of an argon ion laser were used for excitation. The laser light was focused with a cylindrical lens and the power was kept under 75 mW to prevent sample heating and any possible annealing effect. Scattered light was

Table 1

Summary of the Ge/Si SLS samples used in this study. All samples were grown with a 200 nm $\text{Ge}_{0.4}\text{Si}_{0.6}$ buffer layer and with the Ge and Si thickness ratio $d_{\text{Ge}}:d_{\text{Si}} = 2:3$

| Sample | d_n (Å) | d_{RS} (Å) | Number of periods | Substrate orientation |
|--------|--------------|------------------------|----------------------|--------------------------|
| H38 | 14 | 11.6 | 150 | (100) |
| H41 | 28 | 22.5 | 120 | (100) |
| H52 | 7 | - | 300 | (100) |
| H56 | 56 | 45.4 | 40 | (100) |

analyzed with a Spex 1404 double spectrometer and an EG&G 941 photon counter.

All samples used in this study have a thick $\text{Ge}_{0.4}\text{Si}_{0.6}$ buffer layer and the thickness ratio of Ge and Si layers is $d_{\text{Ge}}:d_{\text{Si}} = 2:3$. Assuming the thick buffer layer is completely relaxed, the strain on Ge and Si layers, ϵ_{Ge} and ϵ_{Si} could be calculated to be -2.4% and $+1.7\%$ respectively [7]. In this case, the strains of the bilayer cancel each other and as long as the thickness of each layer does not exceed its critical thickness, no dislocations are generated at the superlattice/buffer interface. Table 1 is a summary of the samples used in this work, where d_n is the nominal superlattice periods and d_{RS} is the superlattice periods obtained from Raman scattering. Fig. 1 shows the Raman spectra ($\lambda = 514.5$ nm) of samples H38, H41 and H56, all with the same (100) sample

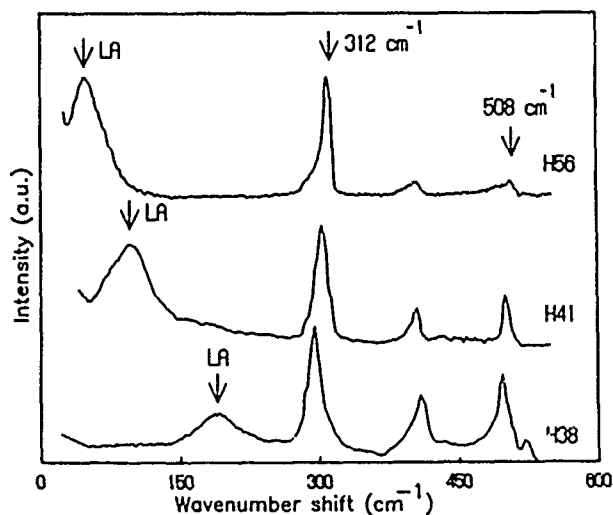


Fig. 1. Raman spectra of samples H38, H41 and H56, all with the same (100) sample orientation but different superlattice periodicities. The laser was operated at 514.5 nm.

orientation but different superlattice periods. Folded longitudinal acoustic (LA) phonons were observed at 189, 97 and 48 cm^{-1} for each sample. However, it was not observed for sample H52 with $d_n = 0.7$ nm due to its extremely small superlattice period.

Following Rytov's elastic continuum model for vibrations in layered media, we can calculate d_{RS} , by [9]:

$$\cos(qd_{\text{RS}}) = \cos\left(\frac{\omega d_{\text{Ge}}}{v_{\text{Ge}}}\right) \cos\left(\frac{\omega d_{\text{Si}}}{v_{\text{Si}}}\right) - \frac{1}{2} \left(R + \frac{1}{R}\right) \sin\left(\frac{\omega d_{\text{Ge}}}{v_{\text{Ge}}}\right) \sin\left(\frac{\omega d_{\text{Si}}}{v_{\text{Si}}}\right), \quad (1)$$

where $R = \rho_{\text{Si}}v_{\text{Si}}/\rho_{\text{Ge}}v_{\text{Ge}}$, v_{Ge} and v_{Si} are the sound velocities, and ρ_{Ge} and ρ_{Si} are the densities of Ge and Si, respectively. The values of d_{RS} obtained from eq. (1) are listed in table 1, and they are consistently 20% smaller than expected from the growth parameters. The optical phonon peaks due to the vibrations of Ge-Ge, Ge-Si and Si-Si pairs are also observed. Ge-Si vibrations can only come from layer interfaces, since the layers are pure Ge and Si. Samples with larger periods (i.e. less interfaces) will therefore have a smaller Ge-Si Raman signal, as observed in fig. 1. The strain induced frequency shifts, $\delta\omega$, for both Ge-Ge and Si-Si vibrations could be calculated by [10]:

$$\delta\omega = \frac{P}{2\omega_0} \epsilon_{zz} + \frac{q}{2\omega_0} (\epsilon_{xx} + \epsilon_{yy}), \quad (2)$$

where ω_0 is the non-strained phonon frequency, ϵ_{ij} are the components of the strain tensor, and p and q are phenomenological parameters. For samples grown on (100) substrates, the optical phonon frequencies for Si and Ge layers in this case are predicted to be at 508 and 312 cm^{-1} , respectively [7]. However, all the observed frequencies are lower than their expected values, and the frequencies for samples having larger periods have phonon energies closer to the expected values. This can be explained by the fact that the Si and/or Ge atoms at layer interfaces see 2 neighboring Si atoms and 2 neighboring Ge atoms such that the local bond-

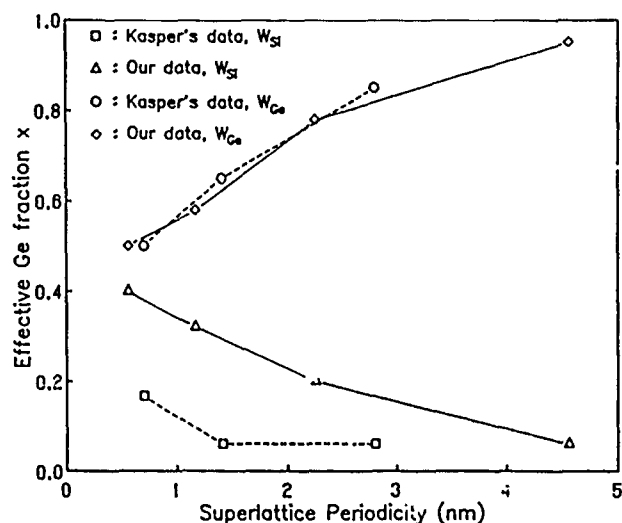


Fig. 2. Effective Ge fraction x , as obtained from the Ge-Ge and Si-Si optical phonon vibration frequencies of the Ge/Si SLs; also shown are Kasper et al.'s data [7] for comparison.

ing is identical to a $\text{Ge}_{0.5}\text{Si}_{0.5}$ alloy [11]. Therefore, samples with smaller periods (i.e. more interfaces) will have more atoms behaving like a weakly strained alloy. As a result, the smaller periodicity samples will have both Si-Si and Ge-Ge peak frequencies located at lower energies. Similar trends were also observed for samples grown on (110) and (111) substrates. Using eq. (2) and the known values of Ge-Ge, Si-Si Raman energies of unstrained $\text{Ge}_x\text{Si}_{1-x}$ alloy [12], we can define quantitatively the degree of alloy mixing of these Ge/Si SLs by the effective Ge fraction x for both Ge-Ge and Si-Si phonon vibrations. These results are shown in fig. 2. Also shown in fig. 2 are Kasper et al.'s [7] data for comparison.

Interface mixing due to Ge and Si interdiffusion was also studied by annealing the samples at various temperatures. Fig. 3 shows the Raman spectra ($\lambda = 457.9$ nm) of sample H56 annealed at 726°C with different annealing times. As the annealing time increased, we can observe (1) the relative intensity of Ge-Si phonon vibration increased, and (2) a large red shift of the Ge-Ge Raman peak. Similar trends were observed as the annealing temperature increased. Fig. 4 shows the effective Ge fraction x of sample H56 as a function of annealing time and temperature, obtained from their Ge-Ge Raman peak positions. We can clearly see a transition from pure Ge and/or Si

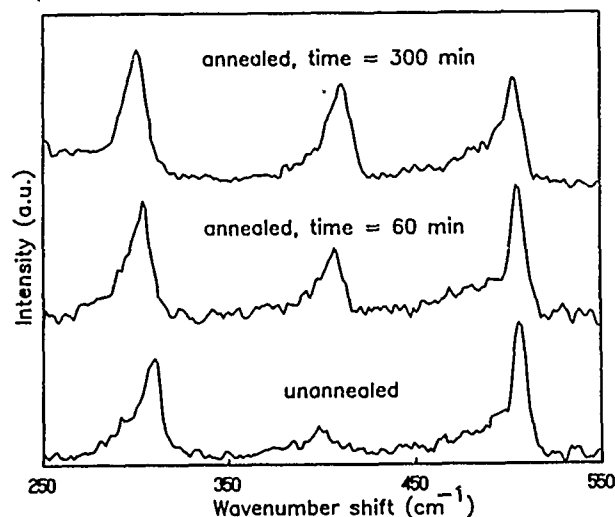


Fig. 3. Raman spectra of sample H56 after annealed at 726°C with different annealing time. The laser was operated at 457.9 nm.

layers to $\text{Ge}_x\text{Si}_{1-x}$ alloy, and this transition became more pronounced as the annealing time and temperature increased. The Si-Si Raman peak, however, only has a smaller red shift due to the larger Si layers thickness. When the 514.5 nm laser line which gives a deeper penetration, was used for excitation, the intensity of Si Raman peak (at 520 cm^{-1}) from the substrate increased as the annealing time and temperature increased. Similar results were reported by Kasper et al. [7]. In their

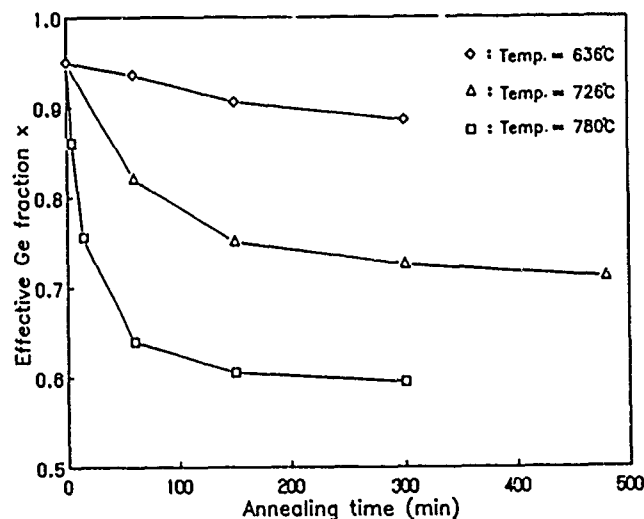


Fig. 4. Effective Ge fraction x obtained from the Ge-Ge Raman peak positions of sample H56 after annealed at different time and temperature.

experiment, Ge/Si SLSs with the same overall superlattice thickness but different period lengths were compared. It was found that smaller period (i.e. more interfaces) samples are more transparent in the green spectra region. This good agreement indicates that interface mixing is indeed very important in such ultra-thin Ge/Si SLSs. We also used X-ray diffraction spectroscopy to study sample H56 before and after annealing. The decay of the low angle X-ray diffraction peak from the superlattice structure, as annealing time and temperature increase, confirms the interdiffusion of Ge- and Si-caused interface smearing. A more detailed study of X-ray diffraction will be reported later.

In summary, ultra-thin Ge/Si SLS samples have been grown and characterized. It has been found that the phonon behavior depends strongly on interface mixing and thus on superlattice periodicity. The effective Ge fraction x of the Ge-Ge and Si-Si phonon vibrations can be determined by their respective Raman peak positions. The annealing effect of these Ge/Si superlattices was also studied.

The authors would like to thank Mr. V. Arbet for his assistance in growing part of the samples. The work at UCLA is supported by the Office of

Naval Research and the Army Research Office, R.C.B. and P.M.A. would like to acknowledge the support of The Aerospace Sponsored Research program.

References

- [1] S. Froyen, D.M. Wood and A. Zunger, *Phys. Rev.* B36 (1987) 4547.
- [2] C.G. Van de Walle and R.M. Martin, *J. Vacuum Sci. Technol.* B3 (1985) 1256.
- [3] C.G. Van de Walle and R.M. Martin, *Phys. Rev.* B34 (1986) 5621.
- [4] M.S. Hybertsen and M. Schluter, *Phys. Rev.* B36 (1986) 9683.
- [5] T.P. Pearsall, J. Berk, L.C. Feldman, A. Ourmezd, J.M. Bonar and J.P. Mannaerts, *Phys. Rev. Letters* 58 (1987) 729.
- [6] J. Berk, J.P. Mannaerts, L.C. Feldman, B.A. Davison and A. Ourmazd, *Appl. Phys. Letters* 49 (1986) 286.
- [7] E. Kasper, H. Kibbel, H. Jorke, J. Brugger, E. Friess and G. Abstreiter, private communication, and to be published.
- [8] A. Ishizaka and Y. Shiraki, *J. Electrochem. Soc.* 133 (1986) 666.
- [9] M. Rytov, *Soviet Phys.-Acoust.* 2 (1956) 68.
- [10] E. Anastassakis, A. Pinczuk, E. Burstein, F.H. Pollak and M. Cardona, *Solid State Commun.* 8 (1970) 133.
- [11] J.C. Tseng, S.S. Iyer and S.L. Delage, *Appl. Phys. Letters* 51 (1987) 21.
- [12] W.J. Brya, *Solid State Commun.* 12 (1973) 253.

Hole transport through minibands of a symmetrically strained $\text{Ge}_x\text{Si}_{1-x}/\text{Si}$ superlattice

J. S. Park, R. P. G. Karunasiri, K. L. Wang, S. S. Rhee, and C. H. Chern

Device Research Laboratory, 7619 Boelter Hall, Department of Electrical Engineering, University of California, Los Angeles, California 90024

(Received 17 November 1988; accepted for publication 2 February 1989)

The hole transport through the minibands of a $\text{Ge}_x\text{Si}_{1-x}/\text{Si}$ superlattice is observed for the first time. The symmetrically strained, short-period $\text{Ge}_x\text{Si}_{1-x}/\text{Si}$ superlattice is grown on a $\text{Ge}_{x/2}\text{Si}_{1-x/2}/\text{Si}$ buffer layer. The current-voltage and conductance-voltage characteristics show two peaks which are attributed to the conduction of light holes through the first and second light hole minibands. The light hole miniband energies are estimated by thermionic emission analysis and are in good agreement with the calculated values using effective mass approximation.

The strained-layer $\text{Ge}_x\text{Si}_{1-x}/\text{Si}$ heterostructures and superlattices have created a great deal of interest due to the potential of integration with the conventional silicon very large scale integrated technology. With the current advances in silicon molecular beam epitaxy (Si MBE) technology, device quality $\text{Ge}_x\text{Si}_{1-x}/\text{Si}$ layers with controlled strain have become possible. Several optical and electronic devices, such as modulation-doped field-effect transistors (MODFETs),^{1,2} heterojunction bipolar transistors (HBTs),^{3,4} and photodetectors^{5,6} have been demonstrated with the GeSi/Si system. Recently, resonant tunneling of holes through double-barrier diodes has been reported in variously strained $\text{Si}/\text{Ge}_x\text{Si}_{1-x}/\text{Si}$ heterostructures.⁷⁻⁹ The successful demonstrations of resonant tunneling in the GeSi/Si heterostructures indicate that the GeSi/Si interfaces are sufficiently smooth for the fabrication of quantum devices. It further suggests the possibility of superlattice devices using GeSi/Si . In this letter we report the first observation of hole transport through the minibands of a short-period $\text{Ge}_x\text{Si}_{1-x}/\text{Si}$ superlattice grown on a $\text{Ge}_{x/2}\text{Si}_{1-x/2}$ buffer layer.

The samples used in the experiments are grown in a computer-controlled Si MBE system with a base pressure of approximately 7×10^{-11} Torr. The system has two electron beam evaporators for silicon and germanium deposition, and several effusion cells for doping. For this experiment, (100) oriented p^+ ($1-5 \times 10^{-3} \Omega \text{ cm}$) Si wafers are used. The details of the sample preparation have been described elsewhere.⁸ The growth temperature and pressure are 530°C and 6×10^{-9} Torr, respectively, and the p -type doping is obtained using a thermal boron source.¹⁰ The superlattice structure is grown on a $2\text{-}\mu\text{m}$ -thick unstrained $p^+\text{Ge}_{0.2}\text{Si}_{0.8}$ buffer layer doped to $5 \times 10^{18} \text{ cm}^{-3}$. The active layers of the structure consist of 15 period superlattice of p -doped ($1 \times 10^{17} \text{ cm}^{-3}$) $\text{Ge}_{0.4}\text{Si}_{0.6}/\text{Si}$ (each layer 50 \AA thick) and 150 \AA contact layers in each side of the superlattice. The contact layers 100 \AA to the superlattice are undoped. Finally, a 7000 \AA of $p^+\text{Ge}_{0.2}\text{Si}_{0.8}$ cap layer is grown for ohmic contacts. The $\text{Ge}_{0.2}\text{Si}_{0.8}$ buffer and cap layers are unstrained, and the $\text{Ge}_{0.4}\text{Si}_{0.6}/\text{Si}$ layers in the superlattice are symmetrically strained. Due to the strain symmetrization, one can grow as many periods as desired without suffering the critical thickness limitation.¹¹ Superlattice diodes with

$450 \mu\text{m}^2$ in area are fabricated by a conventional mesa etching and lift-off technique. Al is evaporated to make ohmic contacts. Current-voltage (I - V) and conductance-voltage (dI/dV - V) are measured by a tunneling spectroscopy setup at different temperatures.

Figure 1 shows the measured I - V and dI/dV at 4.2, 35, and 77 K. Two peaks at 1.1 and 2.5 V (77 K) are present in the I - V and dI/dV . The peak at 2.5 V shows the clear negative differential resistance (NDR). As the temperature of the sample decreased, the peak-to-valley ratio of the peak at 2.5 V increases, and the peak at 1.1 V becomes more apparent from the dI/dV curve. The peak and the valley currents of the peak at 2.5 V decrease as the temperature is reduced, while the peak positions shift toward higher voltages. Above 100 K, the NDR is no longer clearly observed. No current-voltage oscillatory behavior, similar to GaAs/AlAs superlattice as demonstrated by Esaki and Chang,¹² is observed.

In order to understand the data, it is necessary to consider the band structure of the sample. The schematic band diagram of the sample is shown in Fig. 2(a). For convenience, the hole energy is taken to be positive. The barrier heights for the light and the heavy holes, measured from the respective band edges, are 215 and 302 meV. The band off-

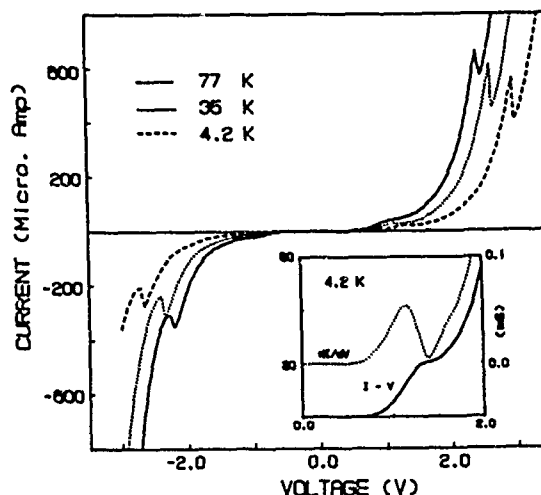


FIG. 1 Observed current voltage (I - V) at 77, 35, and 4.2 K, showing conduction through minibands in the superlattice. Inset of the figure shows the magnified I - V and dI/dV for the first peak.

sets of the $\text{Ge}_x\text{Si}_{1-x}$ films grown on relaxed $\text{Ge}_y\text{Si}_{1-y}$ buffer are obtained based on Refs. 13 and 14. In the relaxed $\text{Ge}_{0.2}\text{Si}_{0.8}$ buffer layer, both heavy and light holes are degenerated. However, the strained $\text{Ge}_{0.4}\text{Si}_{0.6}$ layers, the light hole band moves upwards in hole energy while the heavy hole band moves downwards due to the compressive strain. On the other hand in the strained Si layers, the light and the heavy hole band edges move in the opposite direction due to the tensile strain.

The energies and widths of the hole minibands are estimated using the Kronig-Penny model¹⁵ in the effective mass framework. The effective masses of light and heavy holes in $\text{Ge}_x\text{Si}_{1-x}$ are deduced from the linear interpolation of bulk Si and Ge effective masses. There are two light hole minibands at 52 and 181 meV from the light hole band edge with respective widths of 1 and 20 meV. For the heavy holes, only localized bound states are obtained due to the relatively higher barrier as well as the larger effective mass.

The measured I - V and dI/dV data can be understood quantitatively as the light hole conduction through the minibands in the superlattice. As the applied bias is increased, the light and heavy holes in the buffer layer are injected into the $\text{Ge}_{0.4}\text{Si}_{0.6}$ contact layer through the potential barrier formed at the heterojunction between the buffer and the contact layers. Since the contact layers are undoped, impurity scattering rarely occurs in the contact layers. Thus, most of the carriers injected from the emitter travel through the contact layer coherently and are incident upon the superlattice barrier. The conduction through minibands occurs when the Fermi level in the emitter region is aligned with the bottom of a miniband. The NDR shows up when the Fermi level is moved away from the minibands. Figure 2(b) shows schematically the miniband conduction process. The NDR due to conduction through the second miniband is clearly observed as shown in Fig. 1. The dI/dV data show a rather

broad first peak. Since the bandwidth of the first miniband is relatively thin, the transport through it may involve phonon-assisted processes as well as impurity scattering rather than by a simple miniband conduction. The absence of current-voltage oscillations suggests that the electric field in the doped superlattice region is small, and that localized high-field domains in the superlattice do not exist. Most of the voltage drop occurs in the undoped $\text{Ge}_{0.4}\text{Si}_{0.6}$ contact layers outside of the superlattice. The heavy hole transmission coefficient is smaller than that of the light hole due to its larger effective mass and higher potential barrier. Therefore, the heavy hole current through the superlattice is negligible compared with the light hole current.

In order to obtain the energies of the minibands, we have studied the dependence of current through the structure with temperature at low bias conditions. At low bias, thermionic emission, which is sensitive to the miniband energies of the superlattice, is the predominant component. The thermionic emission current through a miniband of bandwidth ΔH in a superlattice is described by the following equation¹⁶.

$$J = A^* T(E) T^2 \left[\exp\left(\frac{-\phi(V)}{kT}\right) - \exp\left(\frac{-\phi(V) - \Delta H}{kT}\right) \right], \quad (1)$$

where A^* is the effective Richardson constant, T is the temperature, k is the Boltzmann constant, $\phi(V)$ is the potential between Fermi level in emitter and miniband level in the superlattice, V is the bias voltage, and $T(E)$ is the tunneling transmission coefficient. The second exponential term subtracts the current component due to the carriers with energies above the miniband, which are blocked by the barrier. The total current through the structure is the sum of currents through each miniband.

If the ΔH is smaller than kT , the above equation can be simplified to

$$J = \frac{A^* T(E) \Delta H}{k} T \exp\left(\frac{-\phi(V)}{kT}\right). \quad (2)$$

Based on Eqs. (1) and (2), $\phi(0)$ can be estimated from the experimental I - V - T data by taking the slope of $\log(I/T)$ vs $1/T$ at biases greater than several kT , and then extrapolating to zero bias.¹⁶ For the sample used in the present experiment,

$\text{Ge}_{0.2}\text{Si}_{0.8} / \text{Ge}_{0.4}\text{Si}_{0.6} / \text{Ge}_{0.4}\text{Si}_{0.6} / \text{Si superlattice} / \text{Ge}_{0.4}\text{Si}_{0.6} / \text{Ge}_{0.2}\text{Si}_{0.8}$

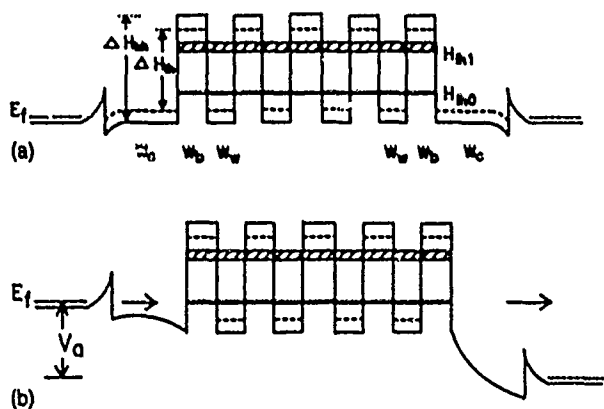


FIG. 2. Schematic band diagram of the structure used in the present experiment (a) without bias. (b) Miniband conduction process under bias. The device parameters are: number of superlattice period = 15, $x = 0.4$, $W_c = 150$ Å, $W_b = 50$ Å, $W_w = 50$ Å, ΔH_{hh} (heavy hole barrier height) = 302 meV, ΔH_{lh} (light hole barrier height) = 215 meV, and heavy hole and light hole band splitting = 39 meV. The dashed line indicates the light hole band edge.

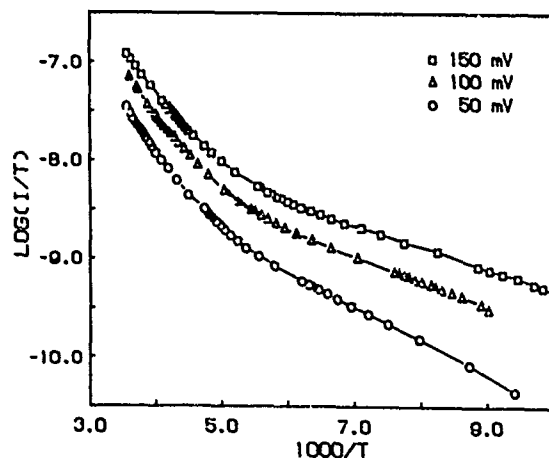


FIG. 3. Arrhenius plots for three different biases due to the thermionic emission current through minibands.

the first miniband width is negligible, and above 200 K the second miniband width is smaller than kT , thus Eq. (2) can be used. The plot of $\log(I/T)$ vs $1/T$ for the sample at different biases is shown in Fig. 3. Below 77 K the characteristics are almost independent of the temperature. This means, at small biases, below 77 K, current through the superlattice is mainly due to tunneling. This tunneling current at small biases is about two orders of magnitude smaller than the thermionic current measured in this experiment (above 100 K). Thus, we assume that tunneling current is negligible in our I - V - T measurement. For a given bias, two regions with different slopes are observed. One appears in a relatively high-temperature region (200–300 K), while the other appears in a lower temperature region (100–170 K). This observation indicates that there are two different thermionic current components (through the first and the second minibands) flowing in the superlattice, as expected. In the low-temperature region, most of the thermionic current is from the first miniband at lower energy. Whereas in the higher temperature region, the increased thermal energy allows the carriers to flow through the second miniband as well. The latter component of current is dominant because of the larger bandwidth of the second miniband. Assuming thermionic current due to the second miniband is negligible in the low-temperature region, one can estimate $\phi_1(0)$ of the first miniband from the experimentally obtained slopes. Figure 4(a) shows

the plots of $\log(I/T)$ vs $1/T$ at several biases. The slope of each plot is obtained by least-squares fitting of the data points. Figure 4(b) shows the plots of $\log(I/T)$ vs $1/T$ corresponding to the high-temperature region. In order to obtain the activation energy for the second miniband [$\phi_2(0)$], we have subtracted the current contribution of the first miniband by extrapolating the low-temperature data of the current to the high-temperature region. The experimentally obtained values for the first and second minibands are 95 and 250 meV respectively. These values are in good agreement with the calculated values of 91 and 220 meV from the emitter band edge including heavy and light hole band splitting. Here, we have assumed the Fermi level at the degenerate valence band, and ignored the band bending at the barrier interface and in the barrier.

In summary, we have demonstrated hole miniband transport in the symmetrically strained, short-period superlattice for the first time. The I - V and dI/dV data showed the NDR and peaks in dI/dV at the positions corresponding to the light hole minibands. The thermionic emission analysis was employed to estimate the energies of the minibands experimentally. The measured values are in good agreement with calculated values. The results from the experiment suggest the use of GeSi/Si superlattices for device applications, such as hot carrier and band aligned superlattice devices.¹⁷

This work is in part supported by Army Research Office, the Office of Naval Research, and Semiconductor Research Corporation.

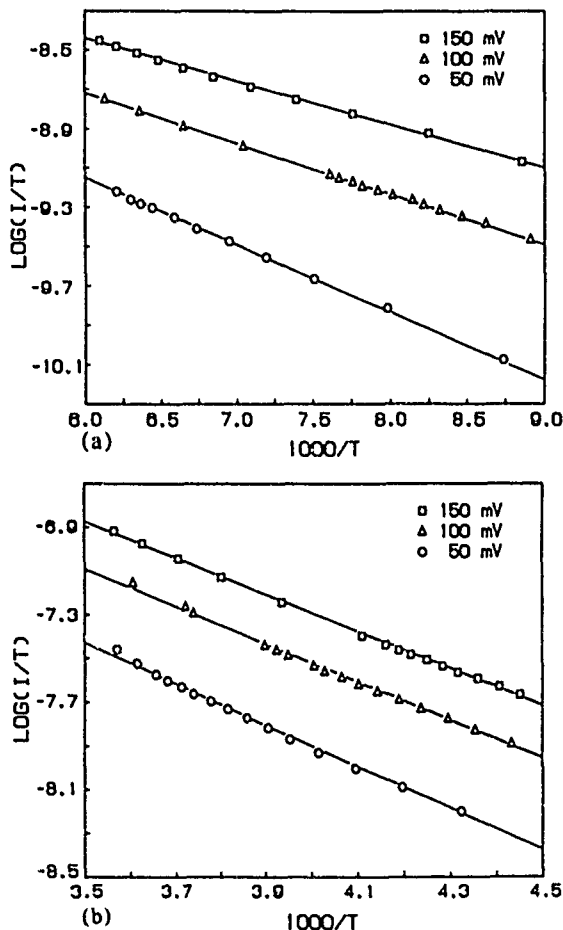


FIG. 4 Plots of $\log(I/T)$ vs $1/T$ (a) in the low temperature region (100–170 K) and (b) in the high-temperature region (200–300 K).

- ¹D. H. Daembkes, H. J. Herzog, H. Jorke, H. Kibbel, and E. Kasper, IEEE Trans. Electron Devices ED-33, 633 (1986).
- ²T. P. Pearsall, J. C. Bean, R. People, and A. T. Fiory, IEEE Electron Device Lett. EDL-7, 308 (1986).
- ³G. L. Patton, S. S. Iyer, S. L. Delaage, S. Tiwari, and J. M. C. Stork, IEEE Electron Device Lett. EDL-9, 165 (1988).
- ⁴T. Tatsumi, H. Hirayama, and N. Aizaki, Appl. Phys. Lett. 53, 165 (1988).
- ⁵S. Luryi, T. P. Pearsall, H. Temkin, and J. C. Bean, IEEE Trans. Electron Device Lett. EDL-7, 104 (1986).
- ⁶T. P. Pearsall, H. Temkin, J. C. Bean, and S. Luryi, IEEE Trans. Electron Device Lett. EDL-7, 330 (1986).
- ⁷H. C. Liu, D. Landheer, M. Buchanan, and D. C. Houghton, Appl. Phys. Lett. 52, 1809 (1988).
- ⁸S. S. Rhee, J. S. Park, R. P. G. Karunasiri, Q. Ye, and K. L. Wang, Appl. Phys. Lett. 53, 204 (1988).
- ⁹K. L. Wang, R. P. G. Karunasiri, J. S. Park, S. S. Rhee, and C. H. Chern, Superlatt. Microstruct. (1989).
- ¹⁰S. S. Rhee, R. P. G. Karunasiri, C. H. Chern, J. S. Park, and K. L. Wang, J. Vac. Sci. Technol. (to be published).
- ¹¹E. Kasper, H. J. Herzog, H. Jorke, and G. Abstreiter, Superlatt. Microstruct. 3, 141 (1987).
- ¹²L. Esaki and L. L. Chang, Phys. Rev. Lett. 33, 495 (1974).
- ¹³C. G. Van de Wall and R. M. Martin, J. Vac. Sci. Technol. B 3, 1256 (1985).
- ¹⁴R. People, Phys. Rev. B 34, 2508 (1986).
- ¹⁵P. F. Yuh and K. L. Wang, Phys. Rev. B 38, 13307 (1988).
- ¹⁶M. J. Paulus, C. I. Huzeng, C. A. Bozada, M. E. Cheney, S. C. Dudley, C. E. Stutz, K. R. Evans, and R. L. Jones, J. Vac. Sci. Technol. (to be published).
- ¹⁷K. L. Wang and P. F. Yuh, IEEE J. Quantum Electron. QE-25, 12 (1989).